Climatology of Warm Conveyor Belt Moisture Transport into the Upper Troposphere and Lower Stratosphere

Dissertation

for the award of the title

Doctor of Natural Sciences (Dr. rer. nat.)

to the faculty

Physics, Mathematics, and Computer Science

of Johannes Gutenberg University Mainz

submitted by

Ziyan Guo

born 28.02.1996 in Xi'an, China

Mainz, December 2025

JOHANNES GUTENBERG UNIVERSITÄT MAINZ

JG|U

1. Examiner:

2. Examiner:

Day of the oral examination: 21.04.2026

Declaration

I hereby declare that this dissertation was prepared independently and without unauthorized assistance. All sources and materials used are properly cited, and any content derived from published or unpublished work is clearly identified in accordance with bibliographic rules. To help with the phrasing of certain sentences, I consulted the AI-tools provided by ChatGPT. Throughout this research, I have complied with the rules of standard scientific practice as formulated in the statutes of Johannes Gutenberg-Universität Mainz.

Ziyan Guo
Mainz, November 11, 2025

Abstract

Warm conveyor belts (WCBs) are key airstreams within extratropical cyclones that transport air from the lower troposphere to the upper troposphere and lower stratosphere (UTLS). Through this ascent, WCBs influence UTLS humidity, ice cloud distribution, and radiative properties. However, their overall contribution to the extratropical UTLS moisture budget and the physical controls governing transport efficiency remain incompletely quantified from both climatological and process-based perspectives.

This thesis investigates WCB-driven moisture transport into the UTLS by combining a 10-year ERA5-based climatological analysis with process-oriented, convection-permitting simulations using the ICON model. First, a climatology of WCB outflow moisture and its impact on UTLS water content based on ERA5 is established in Chapter 3. Using Lagrangian trajectory diagnostics, WCB ascent and outflow are identified, and both moisture anomalies in the UTLS and water fluxes into a newly defined UTLS layer are quantified. Despite strong moisture loss during ascent, WCB outflow is associated with persistent ($\sim$12 h) positive anomalies in total moisture content and a negative temperature anomaly in the upper troposphere and accounts for up to $\sim$14% (mean $\sim$4%) of the total water flux and up to $\sim$23% (mean $\sim$6%) of the condensate flux into the UTLS, despite representing only about 4% of all air parcels entering this layer.

Secondly, I investigate how inflow conditions are linked to outflow properties. We hypothesize that WCB outflow characteristics are primarily controlled by the thermodynamic conditions in the inflow region and the ascent behaviour, which is shaped by both inflow conditions and the dynamical evolution of the associated extratropical cyclone. In Chapter 4, this link is established using an inflow-based WCB object framework that connects inflow conditions and outflow moisture properties in a Lagrangian framework. A strong positive relationship between inflow and outflow properties is found with moister inflow conditions leading to moister outflows and warmer inflow air masses generally remaining warmer at outflow. These results provide a physical explanation for part of the variability identified in the climatological outflow diagnostics. Next, to enable a targeted high-resolution analysis, a physical metric is developed to select a reduced subset of 50 climatologically representative WCB cases that reproduces the key variability of the full ensemble. Building on this selection, Chapter 5 presents case studies, one in summer and one in winter, which are compared directly to ERA5. These simulations show that

ascent timescale is the primary control on WCB moisture transport efficiency, while seasonally varying thermodynamic conditions and cloud microphysical processes modulate moisture loss pathways.

Finally, in Chapter 6, a small ensemble of four ICON simulations is used to evaluate the robustness of ERA5-based WCB diagnostics. While ERA5 robustly captures the mean impact of WCBs on UTLS moisture, it underrepresents variability associated with fast and slow ascent regimes. Fast WCBs with $\tau_{600} \leq 10$ h and slow WCBs with $\tau_{600} \geq 30$ h account for 12.6% and 34.2% of ICON WCB trajectories, but only 3.1% and 15.7% in ERA5, respectively, for the simulated cases.

Overall, this thesis enhances our understanding of WCB moisture transport into the UTLS by establishing a reanalysis-based climatology of the moisture transport and by integrating this climatology with high-resolution modeling, thereby clarifying both the robustness and the limitations of coarse-resolution diagnostics.

Zusammenfassung

Warm Conveyor Belts (WCBs) sind zentrale Luftströmungen innerhalb außertropischer Zyklonen, die Luft aus der unteren Troposphäre in the upper troposphere and lower stratosphere (UTLS) transportieren. Durch diesen Aufstieg beeinflussen WCBs die Feuchtigkeit der UTLS, die Verteilung von Eiswolken sowie die Strahlungseigenschaften. Ihr gesamter Beitrag zum außertropischen Feuchtehaushalt der UTLS sowie die physikalischen Steuerungsmechanismen der Transporteffizienz sind jedoch sowohl aus klimatologischer als auch aus prozessbasierter Perspektive bislang nicht vollständig quantifiziert.

Diese Dissertation untersucht den durch Warm Conveyor Belts (WCBs) getriebenen Feuchtetransport in die UTLS, indem eine 10-jährige, auf ERA5 basierende klimatologische Analyse mit prozessorientierten, konvektionsauflösenden Simulationen mit dem ICON-Modell kombiniert wird. Zunächst wird in Kapitel 3 eine auf ERA5 basierende Klimatologie der WCB-Outflow-Feuchte und ihres Einflusses auf den Wassergehalt der UTLS erstellt. Mithilfe lagrangischer Trajektoriendiagnostik werden WCB-Aufstieg und -Outflow identifiziert, und sowohl Feuchteanomalien in der UTLS als auch Wasserflüsse in eine neu definierte UTLS-Schicht quantifiziert. Trotz starker Feuchteverluste während des Aufstiegs ist der WCB-Outflow mit persistierenden ($\sim$12 h) positiven Anomalien des gesamten Feuchtegehalts sowie mit einer negativen Temperaturanomalie in der oberen Troposphäre verbunden und trägt zu bis zu $\sim$14% (im Mittel $\sim$4%) des gesamten Wasserflusses und zu bis zu $\sim$23% (im Mittel $\sim$6%) des Kondensatflusses in die UTLS bei, obwohl er nur etwa 4% aller Luftpakete repräsentiert, die diese Schicht erreichen.

Zweitens untersuche ich, wie Inflow-Bedingungen mit Outflow-Eigenschaften verknüpft sind. Wir stellen die Hypothese auf, dass die Eigenschaften des WCB-Outflows primär durch die thermodynamischen Bedingungen im Inflow-Gebiet und durch das Aufstiegsverhalten bestimmt werden, welches sowohl von den Inflow-Bedingungen als auch von der dynamischen Entwicklung des zugehörigen außertropischen Zyklons geprägt ist. In Kapitel 4 wird dieser Zusammenhang mithilfe eines inflow-basierten WCB-Objektrahmens hergestellt, der Inflow-Bedingungen und Outflow-Feuchteeigenschaften in einem lagrangischen Rahmen verknüpft. Es wird ein starker positiver Zusammenhang zwischen Inflow- und Outflow-Eigenschaften gefunden, wobei feuchtere Inflow-Bedingungen zu feuchteren Outflows führen und wärmere Inflow-Luftmassen im Allgemeinen auch im Outflow wärmer bleiben. Diese Ergebnisse liefern eine physikalische

Erklärung für einen Teil der Variabilität, die in den klimatologischen Outflow-Diagnostiken identifiziert wurde. Anschließend wird zur Ermöglichung einer gezielten hochauflösenden Analyse eine physikalische Metrik entwickelt, um eine reduzierte Teilmenge von 50 klimatologisch repräsentativen WCB-Fällen auszuwählen, die die wesentliche Variabilität des vollständigen Ensembles reproduziert. Aufbauend auf dieser Auswahl präsentiert Kapitel 5 Fallstudien, eine im Sommer und eine im Winter, die direkt mit ERA5 verglichen werden. Diese Simulationen zeigen, dass die Aufstiegszeitskala der primäre Kontrollfaktor für die Effizienz des WCB-Feuchtetransports ist, während saisonal variierende thermodynamische Bedingungen und wolkenmikrophysikalische Prozesse die Feuchteverlustpfade modulieren.

Abschließend wird in Kapitel 6 ein kleines Ensemble aus vier ICON-Simulationen verwendet, um die Robustheit der auf ERA5 basierenden WCB-Diagnostik zu bewerten. Während ERA5 den mittleren Einfluss von WCBs auf die Feuchte der UTLS robust erfasst, unterschätzt es die Variabilität, die mit schnellen und langsamen Aufstiegsregimen verbunden ist. Schnelle WCBs mit $\tau_{600} \leq 10$ h und langsame WCBs mit $\tau_{600} \geq 30$ h machen 12.6% bzw. 34.2% der ICON-WCB-Trajektorien aus, jedoch nur 3.1% bzw. 15.7% in ERA5, jeweils für die simulierten Fälle.

Insgesamt erweitert diese Dissertation unser Verständnis des WCB-Feuchtetransports in die UTLS, indem eine reanalysebasierte Klimatologie des Feuchtetransports erstellt und diese mit hochauflösender Modellierung integriert wird, wodurch sowohl die Robustheit als auch die Limitationen von Diagnostiken mit grober Auflösung aufgezeigt werden.

Contents

1 Introduction and Background

1.1 Earth's Atmospheric System

The atmosphere is a fundamental and complex component of the Earth system. It forms a thin but vital gaseous envelop of planet Earth that sustains life and governs the exchange of energy, momentum, and water between the surface and space. Through these exchanges, the atmosphere defines the planet's climate, drives the weather systems, and maintains the global energy balance. Composed primarily of nitrogen and oxygen, with trace amounts of greenhouse gases such as water vapour, carbon dioxide, and ozone, the atmosphere plays a central role in absorbing, scattering, and redistributing both solar and terrestrial radiation. The atmosphere exhibits a vertically stratified structure, commonly divided into the troposphere, stratosphere, mesosphere, and thermosphere, based on characteristic temperature and density profiles (Fig. 1.1). Among these, the troposphere and stratosphere are of particular importance for weather and climate processes, as they contain most of the atmospheric mass and involve dynamic and radiative interactions that directly influence surface weather and climate. Across all atmospheric layers, the distribution of water vapour is spatially variable and tightly coupled to temperature, circulation, and phase changes, making it a key tracer of transport and diabatic processes.

1.1.1 The troposphere

The troposphere is the lowest layer of the atmosphere (Fig. 1.1) and contains nearly 80–90 % of its total mass, including most of its water vapour and aerosols. Water vapour concentrations decrease rapidly with altitude due to cooling and condensation, with evapouration from the surface acting as the primary source and condensation and precipitation as the dominant sinks, thereby tightly linking tropospheric moisture to weather systems and vertical transport. The troposphere extends from the Earth's surface up to approximately 8–18 km, depending on latitude and season, being deepest in the tropics and shallowest near the poles (e.g. Wallace and Hobbs, 2006; UCAR Center for Science Education, 2023). The troposphere is the most active and dynamically complex region of the atmosphere, where large-scale atmospheric dynamics, radiative heating, latent heat release, and small-scale turbulent mixing interact to produce varies weather systems (e.g., Wallace and Hobbs, 2006; Holton and Hakim, 2013).

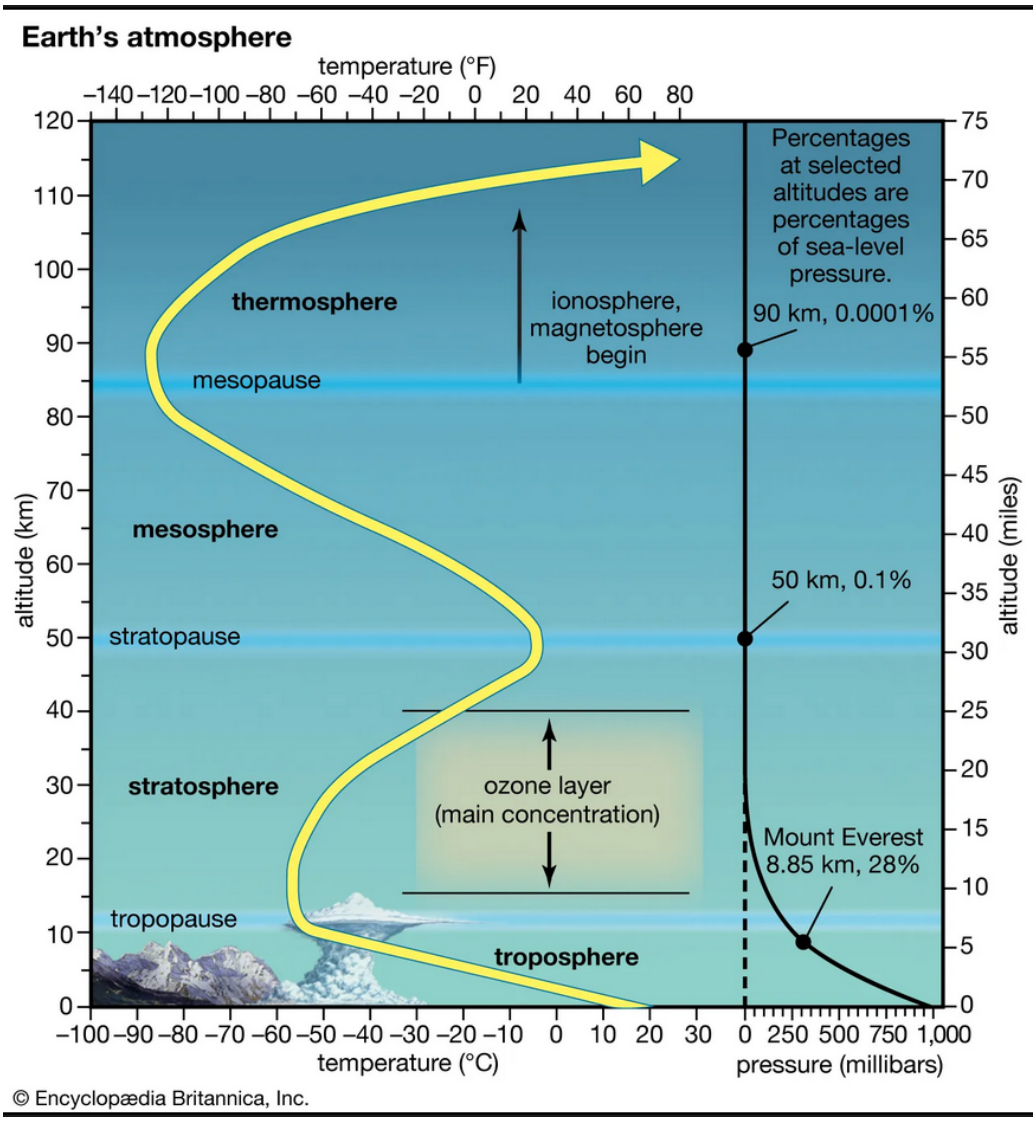

Figure 1.1: Vertical structure of the Earth's atmosphere showing temperature variation with altitude and the major layers: troposphere, stratosphere, mesosphere, and thermosphere. Adapted from Encyclopædia Britannica.

The differential heating between the equator and the poles drives large-scale circulations and jet streams, while smaller-scale processes such as convection and boundary-layer turbulence govern local energy and moisture exchange (e.g., Emanuel, 1994; Trenberth et al., 2009). The troposphere is also the region where clouds form and most precipitation occurs, providing a primary link between atmospheric dynamics, the hydrological cycle, and the Earth's surface energy balance. Through these processes, the troposphere plays a central role in regulating the transport of heat, momentum, and water vapour, forming the foundation of global weather and climate variability (e.g., Stephens, 2005; Hartmann, 2015).

1.1.2 The tropopause

The tropopause marks the boundary between the troposphere and the stratosphere, reaching altitudes of about 16–18 km in the tropics and descending to roughly 8–10 km in polar regions. This latitudinal variation reflects the large-scale circulation of the atmosphere and the influence of meridional temperature gradients, which controls baroclinicity and the regions of extratropical cyclone development (e.g., Dameris, 2015; Hu and Vallis, 2019; Hoffmann and Spang, 2021). The tropopause marks a sharp transition in temperature and stability that strongly constrains the vertical distribution of water vapour. As a result, small variations in transport across or near the tropopause can have a disproportionate impact on UTLS moisture and radiative effects. The tropopause can be defined in different ways depending on the context.

From a dynamical perspective, the tropopause is commonly defined using potential vorticity (PV). In practice, the 2 PVU surface is widely used to represent the dynamical tropopause, which acts as both a dynamical and chemical barrier that constrains vertical exchange and limits the upward transport of water vapour and trace gases (e.g., Wernli and Sprenger, 2007; Sprenger et al., 2007; Turhal et al., 2024). This definition is particularly suited to extratropical dynamics and stratosphere–troposphere exchange, and is therefore adopted throughout this thesis.

Thermally, the WMO (World Meteorological Organization, 1957) defines the tropopause as the lowest altitude where the lapse rate decreases to 2 K km^{-1} or less. While this lapse-rate-based definition performs well in the tropics, Seidel et al. (2001) showed that it is less suitable in extratropical and higher latitudes, where dynamical criteria are often more relevant. Building on PV-based concepts, Kunz et al. (2011) proposed a tropopause definition based on isentropic PV gradients, providing a refined alternative to the use of a fixed PV threshold across all isentropes and seasons.

From a chemical perspective, the tropopause can be identified by sharp vertical gradients in long-lived trace gases such as N_2O, O_3, or CO, which separate chemically distinct tropospheric and stratospheric air masses. More recently, a tropopause definition based on the vertical gradient of relative humidity with respect to ice (RHi) has been proposed (Reutter and Spichtinger, 2025), linking the tropopause structure to ice cloud formation and to both adiabatic and diabatic effects.

Regardless of the definition applied, the tropopause does not represent a fixed boundary. Processes such as deep convection, tropopause folds, and warm conveyor belts can locally enable diabatic transport of air masses and constituents between the troposphere and stratosphere

(e.g., Škerlak et al., 2015; Hitchman and Rowe, 2021; Homeyer and Bowman, 2021; Tinney and Homeyer, 2021; Gordon et al., 2024).

1.1.3 The stratosphere

Above troposphere lies the stratosphere, where temperature increases with height due to ozone absorption of ultraviolet radiation. This layer extends from the tropopause to altitudes of roughly 50 km and is characterized by strong static stability, which suppresses vertical mixing and limits the exchange of air with the troposphere (Grise et al., 2010). The presence of the ozone layer within the middle stratosphere not only shields the surface from harmful ultraviolet radiation but also plays a central role in establishing the positive temperature gradient and in shaping the radiative balance of the atmosphere (e.g., Solomon, 1999; Rowland, 2006). The stratospheric circulation is dominated by the Brewer–Dobson circulation, which transports moist air upward in the tropics and downward in the extratropics, thereby influencing the global distribution of trace gases and water vapour (e.g., Butchart, 2014).

1.1.4 The upper troposphere and lower stratosphere (UTLS)

The upper troposphere and lower stratosphere (UTLS) is a dynamically complex and chemically sensitive region of the atmosphere that plays a central role in the Earth's climate system. It locates roughly between 8–18 km in altitude (i.e. around the tropopause), depending on latitude and season, and represents the transition zone connecting the turbulent, moist troposphere with the stratified, drier and more stable stratosphere (see Fig. 1.2). There is currently no universally accepted definition of the UTLS. However, a key characteristic of the UTLS is the pronounced vertical structure associated with the tropopause. In this view, the UTLS extends several kilometres above and below the tropopause and is marked by sharp vertical gradients in temperature, water vapour, and chemical composition (e.g., Gauss et al., 2003; Riese et al., 2012). Due to the sharp gradients and the presence of air masses with different properties, transport and mixing processes can strongly modify the composition and vertical structure of the UTLS.

Even though the UTLS is only a thin layer, it has a strong influence on the global energy balance because it is located at the boundary between the warm, moist lower atmosphere and the cold, dry stratosphere. Radiation emitted from the Earth's surface and lower atmosphere must pass through this region before escaping to space. Since the UTLS is very cold and contains very little water vapour, even small changes in its temperature or humidity can strongly affect how much heat the Earth loses to space. Water vapour, ozone, and other greenhouse gases are especially effective at influencing the global energy balance when they are located near the

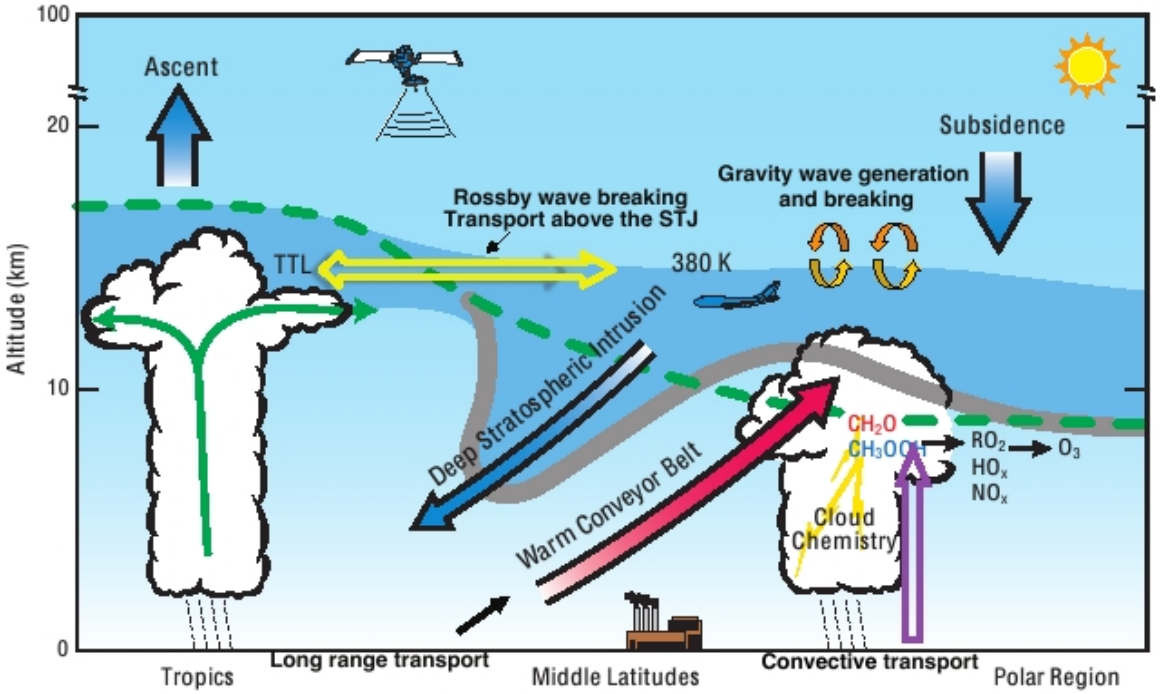

Figure 1.2: Schematic illustration of key processes influencing the composition and transport in the UTLS, including the convection, warm conveyor belts, stratospheric intrusions, and wave-driven dynamics. Adapted from the Atmospheric Chemistry Observations and Modeling (ACOM) Laboratory (National Center for Atmospheric Research (NCAR)).

tropopause, because this region lies close to the effective emission level of outgoing longwave radiation and is characterized by low temperatures and weak radiative damping (e.g., Hartmann, 2015; Riese et al., 2012; Solomon et al., 2010). As a result, even small variations in UTLS composition, such as the exchange of trace gases between the troposphere and stratosphere, can shift the radiative budget and influence global climate.

The climatological state and variability of the UTLS are shaped by a wide range of interacting physical processes, including large-scale circulation and mesoscale and synoptic-scale dynamical processes, such as gravity-wave activity and Rossby wave breaking. (e.g., Gettelman et al., 2011; Inai et al., 2019; Shangguan et al., 2019; Charlesworth et al., 2023; Turhal et al., 2024). Consequently, the UTLS exhibits pronounced spatial and temporal variability. The altitude of the extratropical tropopause varies in response to synoptic-scale activities, such as warm conveyor belts, creating a dynamically active layer in which dynamical, thermodynamical, and cloud processes interact on timescales from hours to weeks.

Water vapour is one of the most important constituents of the UTLS. Although its absolute concentration is much lower than in the lower troposphere (Fig. 1.3), water vapour exerts a

strong radiative influence in the UTLS because infrared emission is highly sensitive to changes in trace gas concentrations at cold temperatures and under conditions of low background humidity (e.g., Solomon et al., 2010; Gettelman et al., 2011). Even small variations in water vapour content can significantly modify longwave radiation fluxes, thereby affecting both regional and global climate. Furthermore, water vapour plays a central role in cirrus formation near the tropopause. These cirrus clouds modulate radiative feedbacks and provides a key pathway for dehydration of air entering the stratosphere (e.g., Jensen et al., 1996, 2013; Clark et al., 2003).

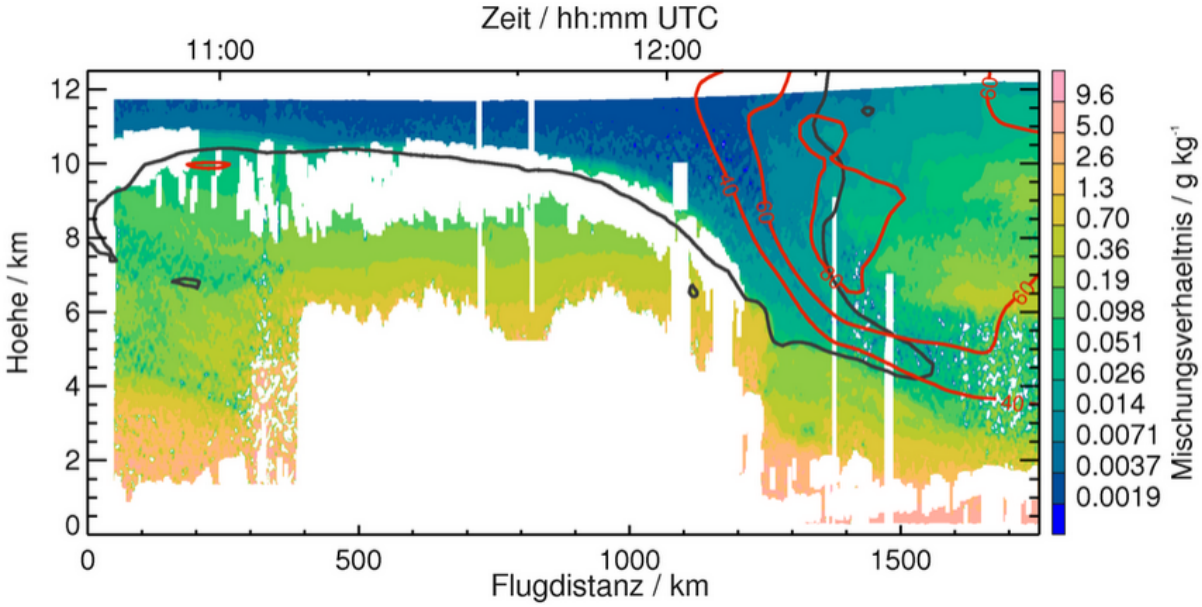

Figure 1.3: Example of a lidar cross section in the vicinity of a low-pressure system over the Atlantic, illustrating the vertical distribution of water vapour (color shading) by transport processes. Strong moisture gradients are found near the tropopause (black line) and the jet streams (red contours, m s^{-1}).
Credit: DLR (CC BY-NC-ND 3.0).

The UTLS water vapour can originate from both troposphere and stratosphere. The UTLS is strongly influenced by tropospheric processes that transport humid air upward across or near the tropopause. Deep convection can rapidly lift moist air from the boundary layer to the upper troposphere and, in some cases, transport water vapour or ice directly into the lower stratosphere (Konjari et al., 2025). In the extratropics, baroclinic weather systems and their associated WCBs act as efficient pathways for lifting moist air to the upper troposphere, where it may further mix into the lower stratosphere or spread horizontally within the upper troposphere. These tropospheric pathways represent the dominant source of UTLS moisture and largely control its spatial and temporal variability (e.g., Schwenk and Miltenberger, 2024; Catto et al., 2015).

In addition to the tropospheric moisture source, the UTLS can also be moistened by stratospheric water. Most stratospheric water vapour enters the stratosphere via slow ascent in the tropical tropopause layer (TTL), where extremely low temperatures lead to ice formation, followed by sedimentation that limits the amount of water vapour that can enter the lower stratosphere (e.g., Mote et al., 1996; Rosenlof, 2003; Jensen and Pfister, 2004; Hardiman et al., 2015). This dehydrated air forms the characteristically dry background of the lower tropical stratosphere and is subsequently transported poleward and downward by the Brewer–Dobson circulation, gradually filling much of the extratropical lower stratosphere (e.g., Randel and Park, 2019; Zahn et al., 2014; Tinney and Homeyer, 2023). Additional contributions to stratospheric water vapour arise from the oxidation of methane during long-term chemical processing in the stratosphere (e.g., Lelieveld et al., 1993). Although this source produces only a few parts per million by volume of water vapour, it nonetheless exerts a strong radiative influence and plays an important role in stratospheric ozone chemistry. (e.g., Solomon et al., 2010; Dessler et al., 2013).

The UTLS water vapour is closely linked to both cirrus cloud formation and stratosphere–troposphere exchange (STE) (e.g., Fueglistaler et al., 2009; Krämer et al., 2020). Near the tropopause slight increases in relative humidity with respect to ice (RHi) can trigger the formation of thin cirrus layers. As ice crystals grow and sediment out, they dehydrate ascending air masses in the TTL and extratropical UTLS, thereby influencing the amount of moisture entering the stratosphere (e.g., Jensen et al., 1996, 2013). At the same time, variability in UTLS moisture strongly modulates stratosphere–troposphere exchange by affecting the efficiency of mixing and cross-tropopause transport (e.g., Stohl et al., 2003; Riese et al., 2012). Consequently, RHi and cirrus microphysical processes emerge as key controls on UTLS composition and its radiative impact, underscoring the importance of understanding the processes that regulate UTLS water vapour and its sensitivity to tropospheric transport pathways.

1.1.5 Stratosphere-troposphere exchange

Stratosphere–troposphere exchange (STE) refers to the bidirectional transport of chemical constituents, trace gases, and aerosols between the two atmospheric layers. Downward transport of stratospheric air brings ozone to the upper troposphere and subsequently influences lower level air quality and the oxidative capacity of the troposphere (e.g., Kentarchos and Roelofs, 2003; Kremser et al., 2016), while upward transport of water vapour, aerosols and trace gases into the lower stratosphere modulates its radiative properties, cirrus formation and global energy budget (e.g., Corti et al., 2006; Ramanathan and Inamdar, 2006; Wang et al., 2019). Thereby these exchange processes play a central role in shaping the chemical and radiative properties of the UTLS.

STE results from a combination of large-scale circulation patterns and synoptic- to mesoscale dynamical processes, and crucially requires diabatic processes such as radiative heating and cooling or latent heat release to enable cross-tropopause tranport (e.g., Spreitzer et al., 2019). The Brewer–Dobson circulation drives the slow ascent of air through the tropical tropopause layer and its poleward and downward transport within the stratosphere, strongly influencing ozone and water vapour distributions. in the lower stratosphere. In addition to this large-scale background flow, synoptic-scale systems such as baroclinic waves, extratropical cyclones, and jet streaks create regions of strong vertical shear that can facilitate rapid and localized cross-tropopause exchange.

Quantifying water vapour exchange across the tropopause is challenging due to the complex geometry of the tropopause and the wide range of transient processes involved. However, recent advances in reanalysis products, high-resolution numerical modelling, and Lagrangian tools have substantially improved our ability to diagnose exchange pathways and estimate associated fluxes (e.g., Škerlak et al., 2014; Guo and Miltenberger, 2025).

1.1.6 The mesosphere and thermosphere

Above the stratosphere lie the mesosphere, which extends up to about 80–85 km, and the thermosphere, which occupies the region above and extends to much higher altitudes. In the mesosphere, temperatures decrease again with height, reaching the coldest values in the atmosphere near the mesopause (e.g., Lübken and Von Zahn, 1991; States and Gardner, 2000). The overlying thermosphere is characterized by strong heating from solar ultraviolet and X-ray absorption, leading to rapidly increasing temperatures and partial ionization of atmospheric constituents. Although these upper layers are thin and contain only a small fraction of the atmospheric mass, they play an important role in modulating energy deposition and radiation from the sun, influencing the propagation of atmospheric waves, and coupling the lower atmosphere to space weather processes (e.g., Beig et al., 2008; Vincent, 2015; Lübken, 2022). Through its continuous interactions with the ocean, cryosphere, and biosphere, the atmosphere both responds to and drives variability across a broad range of spatial and temporal scales, including turbulent eddies, convective systems, and planetary-scale circulation patterns (e.g., Seo et al., 2023; Boy et al., 2019; Ghil and Lucarini, 2020).

A comprehensive knowledge of the atmosphere's structure and dynamics is therefore fundamental for understanding the processes that govern the transport and distribution of heat and moisture, the formation and evolution of clouds, and the exchange between the troposphere and stratosphere. These processes form the physical basis for the investigations presented in

this thesis.

1.2 Extratropical Cyclones

Extratropical cyclones (ETCs) are large-scale weather systems that dominate mid-latitude circulation and play a key role in transporting heat, moisture, and momentum between the tropics and the poles (e.g., Seiler, 2019; Federer et al., 2025). They typically form along baroclinic zones, which are regions characterized by strong horizontal temperature gradients, where available potential energy is converted into kinetic energy through baroclinic instability. These low-pressure systems feature a characteristic frontal structure composed of warm and cold fronts, extensive cloud bands, and intense precipitation driven by vigorous ascending motions (e.g., Sinclair et al., 2020; Federer et al., 2025; Pfahl et al., 2015). The airflow within an ETC is commonly characterized by three coherent airstreams (Fig. 1.6): the warm conveyor belt (WCB), the cold conveyor belt (CCB), and the dry intrusion (DI). In particularly intense storms, an additional airstream known as the sting jet (SJ) may develop and produce extremely strong surface winds with potentially severe socio-economic impacts.

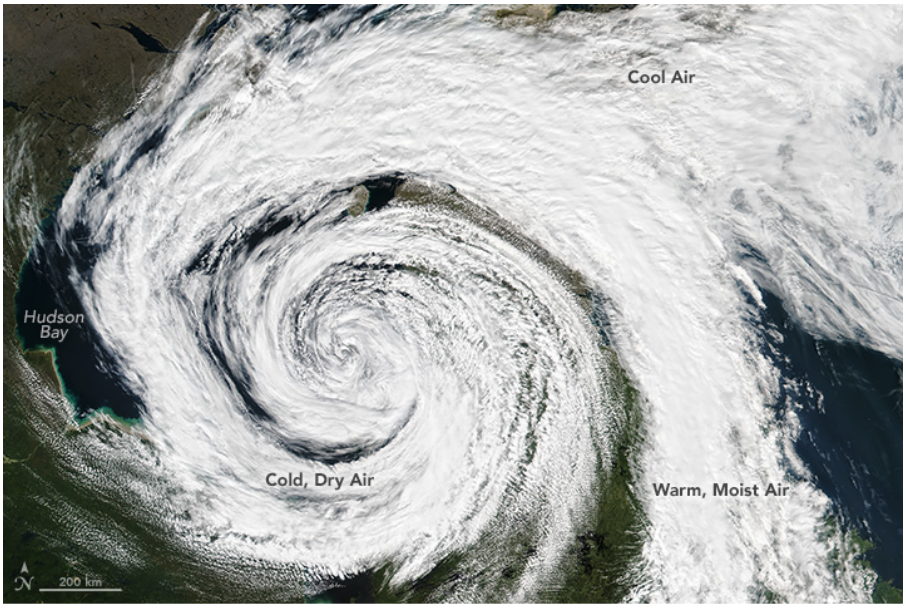

Figure 1.4: Imagery of an extratropical cyclone over Hudson Bay acquired on 10 August 2016 by the VIIRS instrument aboard the Suomi NPP satellite. The cyclone displays a well-defined structure, including a moist warm conveyor belt along its southeastern flank and cold and regions of cold, dry air wrapping around the western and northern side of the system. The figure is adapted from NASA Earth Observatory Suomi NPP VIIRS imagery.

The life cycle of an extratropical cyclone typically follows four conceptual stages: cyclogen-

esis, intensification, maturity, and decay (see in Fig. 1.5). Cyclogenesis often occurs along quasi-stationary fronts or jet stream disturbances, where upper-level divergence supports surface pressure reduction (e.g., Riehl and Teweles Jr, 1953; Parsons and Smith, 2004; Ludwig et al., 2015; Catto, 2016). During the intensification stage, the cyclone deepens as the warm and cold air masses are advected poleward and equatorward, respectively, strengthening the temperature gradient and the associated frontal zones. At maturity, the cyclone reaches its maximum intensity, often accompanied by a well-developed warm sector and strong frontal precipitation. The system then weakens during occlusion, when the warm-sector air is lifted from the surface as the cold front overtakes the warm front (Fig. 1.5d), reducing the low-level temperature gradient and leading to cyclone decay. (e.g., Schemm et al., 2018; Schultz et al., 2019).

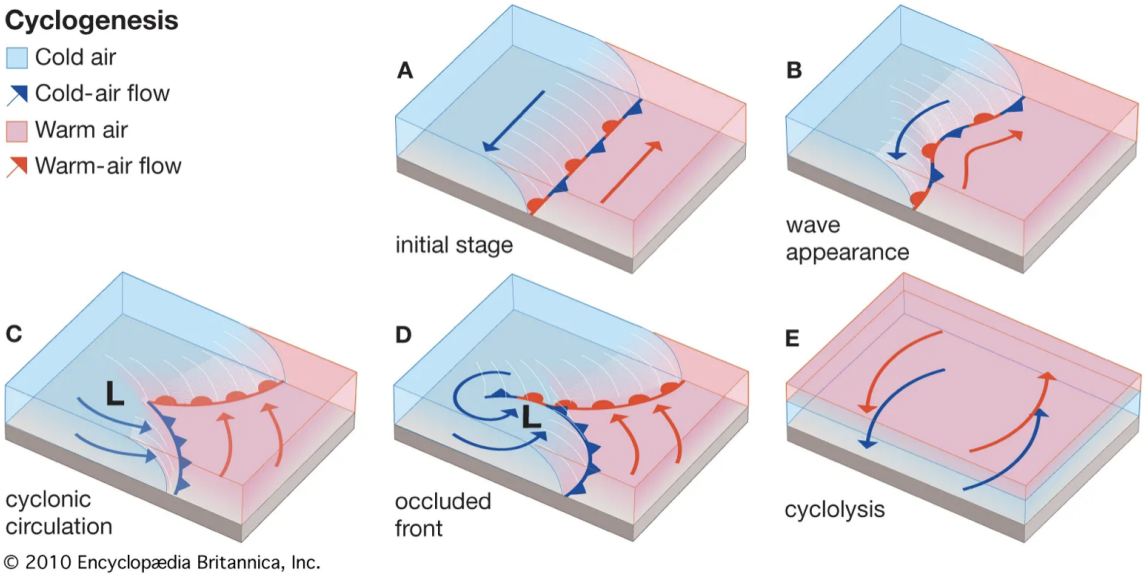

Figure 1.5: Conceptual stages of extratropical cyclogenesis over a baroclinic zone. (A) Initial state with a quasi-stationary front separating warm and cold air masses. (B) Wave disturbance forms and along-front circulations initiate ascent ahead of the warm front and descent behind the cold front. (C) Cyclonic circulation intensifies, warm and cold fronts sharpen, and a warm sector develops. (D) Occlusion begins as the cold front overtakes the warm front and a bent-back occluded front forms, near the time of peak intensity. (E) Decay as the thermal contrast weakens and frontal baroclinicity decreases. Adapted from Encyclopædia Britannica

In addition to shaping synoptic-scale weather, ETCs are critical for the vertical redistribution of moisture and energy. Embedded within these systems are coherent mesoscale flow structures such as jet streaks, fronts, and synoptic-scale conveyor belts, which shape the cloud and precipitation patterns and control the vertical and horizontal transport of air masses (e.g., Browning and Roberts, 1996; Binder et al., 2016). As the primary hosts of warm conveyor belts, ETCs

are therefore central to understanding how moisture and energy are transported to upper troposphere. Quantifying how these systems modulate UTLS water vapour forms a key objective of this thesis.

1.3 Warm Conveyor Belts

1.3.1 Definition

Warm conveyor belts (WCBs) represent one of the coherent airstreams within ETCs. WCBs can rapidly transport heat, moisture and momentum from the boundary layer to upper tropospheric levels, where the WCB outflow can substantially modify the structure of the local tropopause, forming a key link between lower atmospheric moisture, cloud and precipitation processes throughout the tropopause, and the large scale circulation. In a conceptual sense, WCBs are coherent streams of warm, moist air that originate in the warm sector of a developing cyclone and ascend ahead of the cold front, typically along and above the warm front as a result of diabatic heating (see structures in Fig. 1.6 and the warm sector at the southern part of the cyclone in satellite image Fig. 1.4). As they rise, air parcels typically undergo a deep, quasi-continuous ascent of several kilometres within 1-2 days, potentially making them an efficient pathways for vertical mass transport in the midlatitudes.

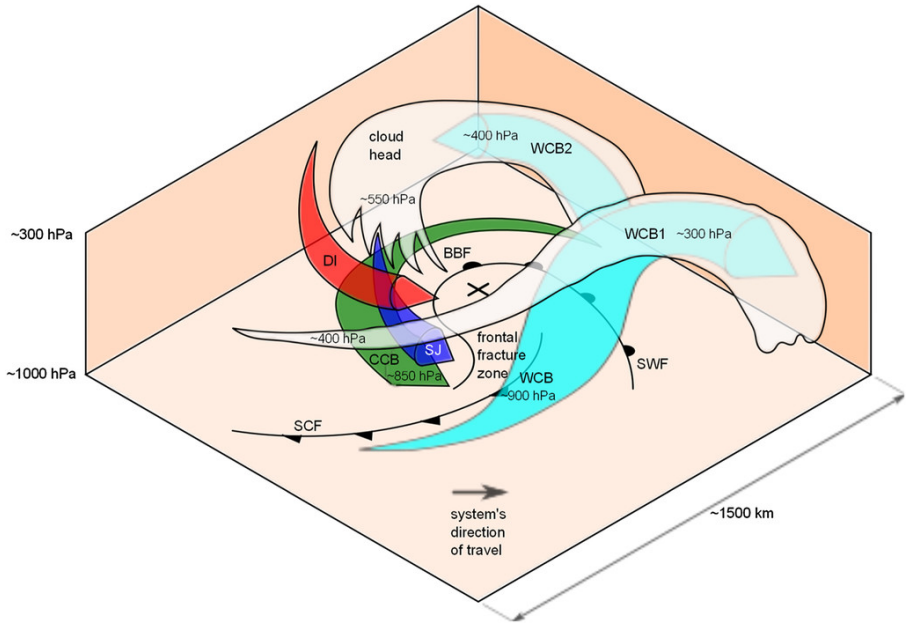

Figure 1.6: Illustration of a Shapiro-Keyser cyclone structure, including the warm conveyer belt (WCB), cold conveyor belt (CCB), dry intrusion (DI) and sting jet (SJ). Adapted from Martínez-Alvarado et al. (2014).

WCBs were first conceptualized in the late 1970s and early 1980s as part of the three-airstream

model of ETCs (e.g., Harrold, 1973; Carlson, 1980; Neiman and Shapiro, 1993), which also includes the CCB and the DI. In this early framework, the WCB was described as a deep, poleward airstream originating in the warm sector of a developing cyclone. Modern studies have refined this definition in a Lagrangian sense as ensemble of air parcels that ascend more than 600 hPa in 48 hours, typically from the lower troposphere ahead of the cold front to the upper troposphere in the vicinity of a cyclone (e.g., Wernli, 1997; Madonna et al., 2014). This ascent criterion has become the standard diagnostic in modelling, and climatological studies, which is also applied in this thesis.

1.3.2 Kinematic structure

Warm conveyor belts are synoptic-scale airstreams within ETCs that contain embedded mesoscale processes, which strongly control their thermodynamic evolution and moisture transport characteristics. Embedded convection can locally dominate WCB ascent through intense diabatic heating and strong vertical velocities, processes that are poorly represented at coarse resolution and therefore motivate the use of high-resolution simulations in this thesis.

WCB trajectories follow a characteristic three-phase structure: inflow, ascent, and outflow (e.g., Madonna et al., 2014; Oertel et al., 2019; Heitmann et al., 2024), with their corresponding positions and heights shown in Fig. 1.7 for a real case based on data from a CALIPSO overpass. The inflow region marks the origin of the WCB trajectories and is typically located below about 800 hPa in Lagrangian analyses (e.g., Madonna et al., 2014; Heitmann et al., 2024; Guo and Miltenberger, 2025). These inflow air masses differ from the surrounding environment by their high moisture content and low static stability, which facilitate rapid ascent. The ascent phase is characterized by coherent upward motion, with most WCB parcels rising several kilometres within 1-2 days. This ascent is driven by a combination of frontal lifting, large-scale quasi geostrophic forcing and latent heat release (e.g., Barry and Chorley, 2009; Joos and Wernli, 2012). Latent heating is particularly important because it amplifies vertical motion, intensifies cyclone development, and shapes the diabatic heating profiles that influence downstream flow (e.g., Danard, 1964; Kuo, 1965; Chang et al., 1982; Ahmadi-Givi et al., 2004). WCB outflow occurs near the tropopause, typically ahead of or downstream of the cyclone center and often along the poleward flank of the jet stream (e.g., Browning and Roberts, 1994; Grams et al., 2011). In this region, WCB air parcels spread mostly horizontally, forming extensive upper-level clouds and influencing upper-tropospheric potential vorticity (PV) distribution and jet stream structure. The outflow air frequently interacts with the upper-level jet, where diabatic PV modification associated with latent heating contributes to jet acceleration and the development of jet streaks (e.g., Grams et al., 2011; Wernli and Gray, 2023; Oertel et al., 2020). Portions of the outflow may cross the dynamical tropopause, leading to intrusions of moist air

into the lower stratosphere and further shaping the UTLS moisture distribution (e.g., Stohl et al., 2003; Eckhardt et al., 2004; Oertel et al., 2019, 2021; Heitmann et al., 2024; Guo and Miltenberger, 2025).

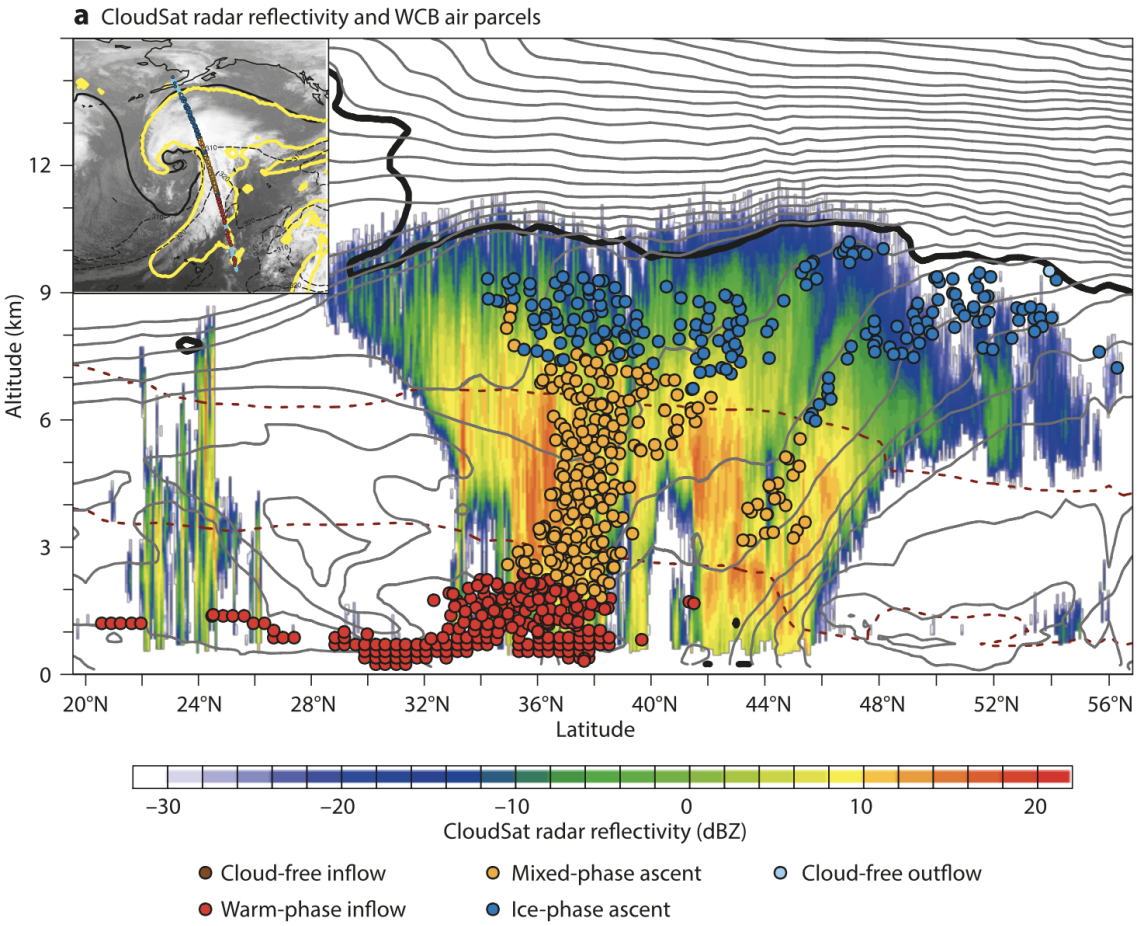

Figure 1.7: Illustration of WCB parcel positions and heights along an atmospheric cross section for a midlatitude cyclone at 00 UTC on 3 January 2014, with the location of the section indicated in the satellite image (upper left). Shading shows CloudSat radar reflectivity, with ECMWF operational analyses of equivalent potential temperature (black contours, 5 K spacing), temperature (red dashed contours at 0 °C and –23 °C), and the dynamical tropopause represented by the 2 PVU surface (thick black line). Coloured dots mark WCB air parcels located within 20 km of the CloudSat track, with colours indicating their cloud phase. Figure adapted from Binder (2017), as reproduced in ECMWF Newsletter (2018).

1.3.3 Dynamical role

Beyond their Lagrangian definition and trajectory structure, WCBs exert a strong dynamical influence through the way diabatic heating modifies potential vorticity (PV). PV is a quantity that combines the effects of rotation and stratification. In the atmosphere, PV values are typ-

ically low in the well-mixed troposphere and high in the more stably stratified stratosphere, with the dynamical tropopause often marked by the 2-PVU surface.

As WCB air rises and experiences intense latent heating, the vertical changes in heating systematically modify PV along the airstream (e.g., Wernli, 1997; Joos and Wernli, 2012). In the lower and middle troposphere, heating tends to increase PV, creating positive PV anomalies that can strengthen the low-level circulation of a developing cyclone (e.g., Binder et al., 2016; Martínez-Alvarado et al., 2016). At upper levels, where heating weakens, PV is reduced, producing very low-PV air in the WCB outflow (Fig. 1.8 b). This negative PV anomaly is dynamically important: it helps build and amplify upper-level ridges, sharpens the tropopause, and can accelerate the jet stream downstream of the cyclone (e.g., Grams et al., 2011; Joos and Wernli, 2012; Oertel et al., 2020).

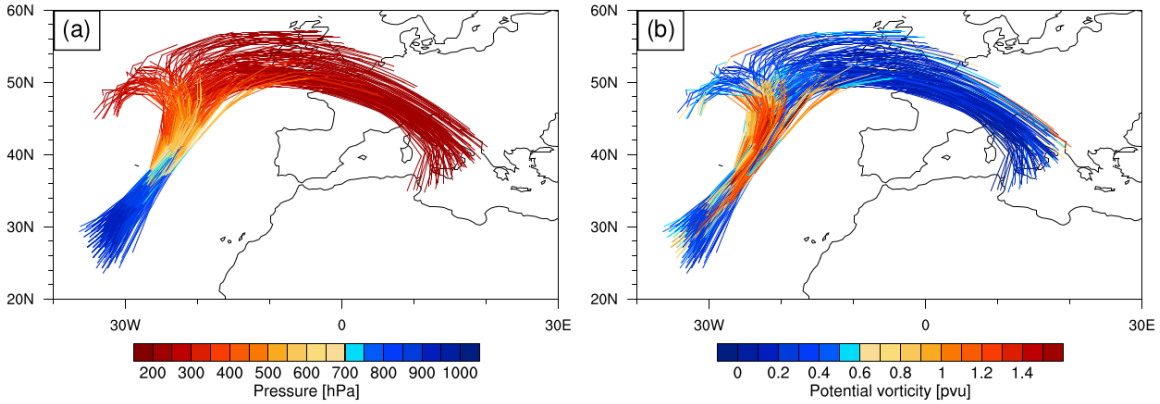

Figure 1.8: Evolution of (a) pressure (hPa) and (b) potential vorticity (pvu) along 48-hour WCB trajectories initiated at 18 UTC on 5 October 2012. Adapted from Binder (2017).

Together, these diabatically produced PV anomalies modify the vertical coupling between the lower and upper troposphere and thereby influence the evolution and intensification of extratropical cyclones (e.g., Wimmer et al., 2022; Wernli and Gray, 2023). Through this PV-based pathway, WCBs play a central role in shaping the structure of the jet stream, modulating Rossby-wave propagation, and contributing to variations in midlatitude predictability on synoptic to subseasonal timescales (e.g., Grams et al., 2018; Wernli, 1997; Madonna et al., 2014).

1.3.4 Microphysical role

WCBs are associated with extensive cloud structures that shape much of the cloud and precipitation pattern of extratropical cyclones (e.g., Browning, 1990). These cloud systems usually include deep layers of mixed-phase microphysics, where condensation, freezing, deposition and

riming governs precipitation development. Microphysical processes along the ascent strongly influence precipitation efficiency, cloud lifetime, and the vertical distribution of latent heating, thereby shaping both the thermodynamic and dynamical evolution of the WCB (e.g., Joos, 2019; Oertel et al., 2023; Schwenk and Miltenberger, 2024). At upper levels, the WCB outflow is frequently associated with ice supersautration and layers of enhanced UTLS humidity, while thin cirrus formation typically occurs above the outflow (e.g., Stohl et al., 2003; Eckhardt et al., 2004; Oertel et al., 2019; Heitmann et al., 2024; Lüttmer et al., 2025). These upper-level cloud features not only trace the final stages of WCB ascent but also play an important role in modulating radiative effects and providing a pathway for dehydration and cloud microphysical processing of air in the UTLS.

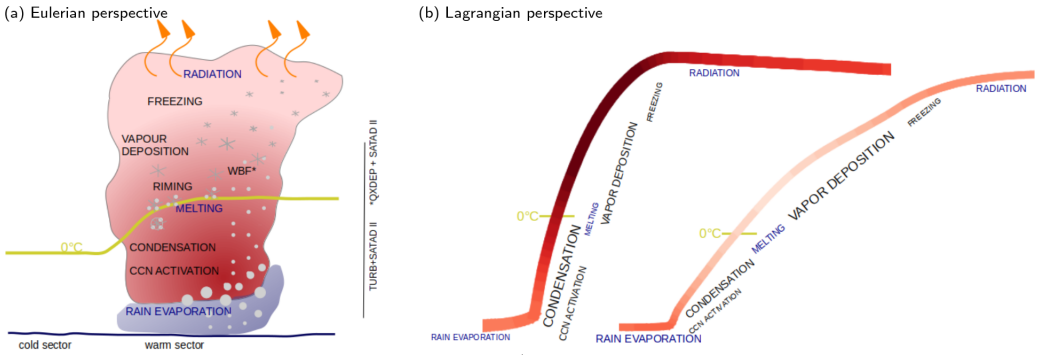

Figure 1.9: Illustration of WCB ascent microphysical processes from (a) Eulerian perspective and (b) Lagrangian perspective. (a) also indicates the Bergeron–Wegener–Findeisen process within the mixed-phase cloud, describing how ice crystals grow at the expense of supercooled liquid droplets because the saturation vapour pressure over ice is lower than over liquid water. As vapour deposits onto ice and droplets evaporate, ice particles rapidly grow and contribute to precipitation formation. (b) The shading along the fast-rising and slow-rising trajectories illustrates the cumulative diabatic heating experienced during ascent, with stronger heating shown by deeper colors. Adapted from Oertel et al. (2023).

In summary, WCBs represent an important link between lower-tropospheric moisture, diabatic ascent as well as upper-tropospheric dynamical evolution. They restructure moisture, clouds, and PV on synoptic scales makes them essential in shaping the cyclone development and mid-latitude UTLS moisture distribution. At the same time, the complexity of their thermodynamic and microphysical pathways highlights the need for detailed investigation. These considerations motivate the scope and methodological choices in the following sections, where reanalysis data and high-resolution model simulations are used to quantitatively characterize WCB behaviour and its broader atmospheric impacts.

1.4 Literature Review on WCB Climatologies

This section reviews existing climatological studies of WCBs, with a focus on how their occurrence, structure and thermodynamic evolution have been characterized in reanalysis data, models and observations. Emphysis is placed on trajectory-based climatologies, which form the basis of most current knowledge on WCB statistics and variability, as well as on complementary Eulerian and modelling approaches. Together, these studies provide the context for the climatological analysis presented in this thesis.

Trajectory-based WCB climatologies reveal three doninant centres of activity, located over the North Atlantic, North Pacific and Southern Hemisphere storm track (e.g., Madonna et al., 2014; Eckhardt et al., 2004; Binder et al., 2016). These regions coincide with the frequent ETC development, where strong baroclinicity and frontal ascent favour the formation of WCBs. Catto et al. (2015) point out that WCB inflow is strongly associated with the warm sector of ETCs and is located ahead of the cold front. As shown in Fig. 1.10, WCB inflow often originates in warm and moist maritime regions. Eckhardt et al. (2004) produced the first global 15-year WCB climatology using 355 million trajectories from ERA-15. They showed that WCBs typically ascend from the boundary layer to the upper troposphere within 2 days, originate most frequently between 25-45° N/S, and contain 7-12 $\mathrm{g\,kg^{-1}}$ of moisture that is almost entirely precipitated out, warming parcels by 15-22 K in potential temperature. WCB trajectories generate 4-6 times more precipitation that non-WCB trajectories and occur predominantly near cyclone centres, with WCB occurrence being nearly an order of magnitude more frequent in winter than in summer. The WCB distribution can also be modulated by climate modes: during positive NAO (The North Atlantic Oscillation), WCBs are ∼12% more frequent with outflow shifted ∼10° poleward and ∼20° eastward, while ENSO phases affect WCB frequency in South hemisphere around Australia (e.g., Madonna et al., 2014; Hoskins and Hodges, 2005; Grams et al., 2011, 2018). ENSO also affects WCB behavior in other regions, with enhanced WCB frequency and moisture transport over Asia and southwest Asia during El Niño (Breeden et al., 2023), and stronger Pacific WCB activity during La Niña events as shown for subseasonal MJO–WCB modulation (Quinting et al., 2024).

Beyond WCB occurrence statistics, Madonna et al. (2014) provides key climatological insights into the thermodynamic and dynamical evolution of WCB air parcels using ERA-Interim. The study shows that cloud liquid and ice water contents peak near 700 hPa and 550 hPa, respectively, consistent with strong latent heating of more than 20 K in potential temperature during ascent. This diabatic heating leads to characteristic PV signatures along the airstream, with positive PV anomalies in the lower and middle troposphere and pronounced negative PV anomalies in the upper troposphere (Fig. 1.8b). WCB outflow typically resides in the upper

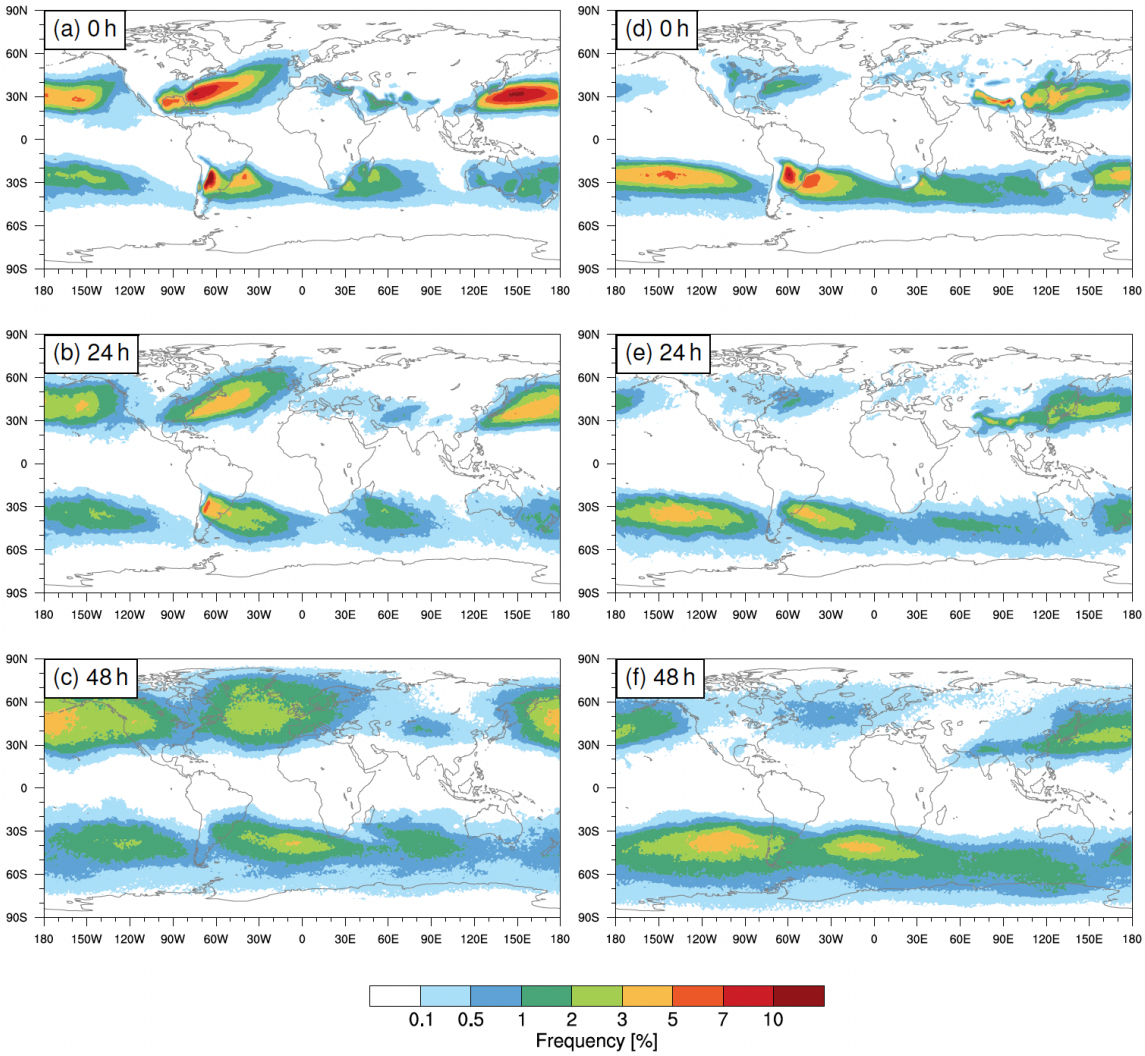

Figure 1.10: Climatological distribution of WCB activity from 1979 to 2014, displayed for DJF (a–c) and JJA (d–f). The panels show the relative frequency (%) of WCB trajectories (a, d) at the starting location, (b, e) after 24 h, and (c, f) after 48 h. Adapted from Madonna et al. (2014), reproduced by Binder (2017).

troposphere and lower stratosphere and is characterized by low PV values resulting from this diabatic ascent (e.g., Wernli and Davies, 1997; Madonna et al., 2014). The climatological outflow PV patterns (Fig. 1.11) are dynamically important, as they influence downstream flow evolution and the amplitude of upper-level ridges (e.g., Wernli, 1997; Madonna et al., 2014; Binder, 2017). The magnitude of the diabatic PV modification also varies systematically with latitude (Fig. 1.11). Low-latitude WCBs ($< 40°$) undergo intense latent heating but produce weak PV anomalies due to small background planetary vorticity, whereas higher-latitude WCBs generate larger PV anomalies due to stronger vertical heating gradients and higher ambient absolute vorticity (e.g., Madonna et al., 2014; Binder, 2017).

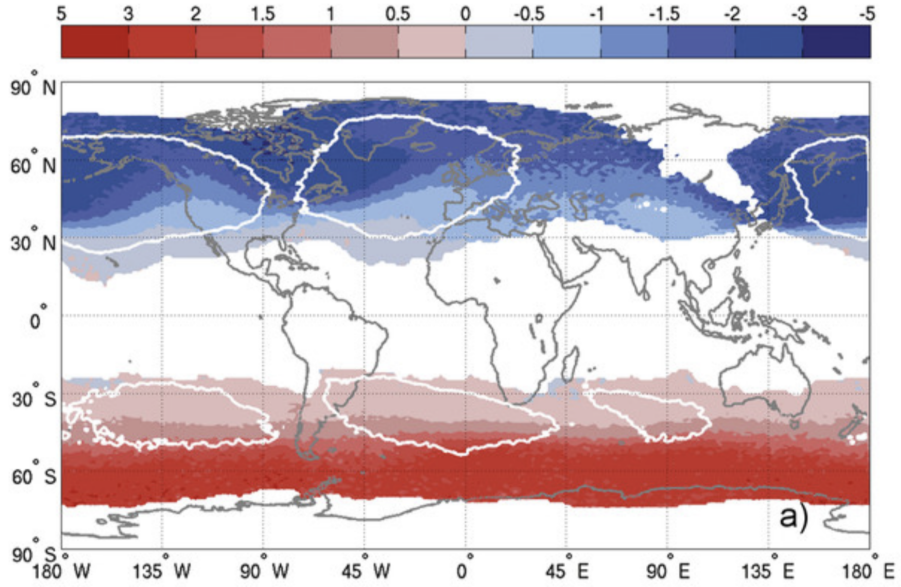

Figure 1.11: Spatial distribution of PV anomalies in the DJF WCB outflow, computed by averaging all trajectories found between 340 and 280 hPa at t = 48 h. White contours mark areas in which the relative occurrence of WCB trajectories at t = 48 h is greater than 1%. Adapted from Madonna et al. (2014).

Extending previous climatological work, Heitmann et al. (2024) use a new ERA5-based trajectory dataset (1980–2022) and construct two-dimensional Eulerian masks from Lagrangian trajectories that separately represent WCB inflow, ascent, and outflow regions, providing the first climatological perspective on how WCB characteristics evolve from cyclone genesis through intensification to maturity. They analyse roughly 5000 North Atlantic winter cyclones and show that during cyclone intensification, diabatic PV production in the WCB ascent region leads to a strengthening positive PV anomaly in the lower troposphere, whereas the upper-level negative PV anomaly linked to the WCB outflow remains nearly constant. The cyclonic branch, which outflows at lower altitudes, produces weaker negative PV anomalies than the higher-ascending anticyclonic branch. This contrast aligns with their finding that the cyclonic WCB branch strengthens as the surrounding cyclonic wind field intensifies during the cyclone's development.

In addition to the present-day characteristics summarized above, Joos et al. (2023a) provides new insight into how WCBs respond to warming climate. Using CESM1 RCP8.5 simulations, the study shows that inflow moisture increases by up to ∼33%, leading to stronger WCB-related precipitation and enhanced mid-tropospheric diabatic heating. These changes also raise the WCB outflow level, which in turn intensifies the interaction of WCBs with the upper-level Rossby waveguide. The simulations also reveal regional shifts in WCB occurrence consistent with storm-track changes, including a northward shift over the North Pacific and enhanced activity in parts of the Southern Hemisphere. Complementing these results, Joos et al. (2023b)

shows that cyclone deepening rates correlate strongly with WCB strength, with the strongest response in the Southern Hemisphere. These results further indicate that future explosive cyclones are linked to stronger WCBs, enhanced diabatic PV production, and more intense PV towers.

From a numerical modelling perspective, and beyound Eulerian- and Lagrangian-based climatological analyses, the simulated behaviour of WCBs is highly sensitive to model resolution and physical parameterizations. Choudhary and Voigt (2022) investigated how the representation of the WCB in North Atlantic cyclone Vladiana responds to changes in grid spacing, convective parameterization, and cloud microphysics in a set of 18 ICON simulations spanning resolutions from 80 to 2.5 km. As the grid spacing is refined, the WCB becomes more dynamically realistic: the number of identified trajectories increases (Fig. 1.12), ascent becomes stronger and reaches higher altitudes, vorticity intensifies, and diabatic heating is enhanced. At convection-permitting scales (< 10 km), these sensitivities are further amplified but become largely insensitive to additional grid refinement. By contrast, Mazoyer et al. (2021, 2023) demonstrate that differences in the representation of mixed-phase and ice microphysical processes strongly modulate WCB diabatic heating and ascent characteristics. These differences further impact on WCB outflow structure and downstream ridge amplification.

Oertel et al. (2025) construct a high-resolution 70-member perturbed-parameter ensemble (PPE) and show that uncertainty in WCB behaviour is dominated by variations in the inflow conditions, which exert strong control over ascent strength, total precipitation, and the ridge amplitude. Microphysical perturbations also influence the large-scale flow pattern, but their impact is weaker than the changes in inflow conditions. Schwenk et al. (2025) further analyse this 70-member PPE ensemble and show that microphysical parameter perturbations affect the amount of ice and water vapour in the UTLS. Although these perturbations have little impact on the thermodynamic state of the WCB outflow, they substantially modify the UTLS ice mass mixing ratio and relative humidity, particularly in fast-ascending parcels, mainly driven by the capacitance of ice and ice-nucleating particle number concentration.

In addition to these modelling studies, observational data from field campaigns also complement our understanding of how WCBs shape the UTLS moisture distribution. Using coordinated aircraft, lidar, and radar measurements, Boettcher et al. (2020) show that ensemble analyses exhibit a moist bias in parts of the WCB inflow but capture cloud water species well during the ascent phase. Complementary evidence from IAGOS measurements demonstrates that reanalysis data (ERA5) reproduces the occurrence frequency of ice supersaturated regions (ISSRs) in the upper troposphere (e.g., Driver et al., 2025), but not in regions associated with the dry intrusion. Consistent with this, Reutter et al. (2020) further showed that temperature and water

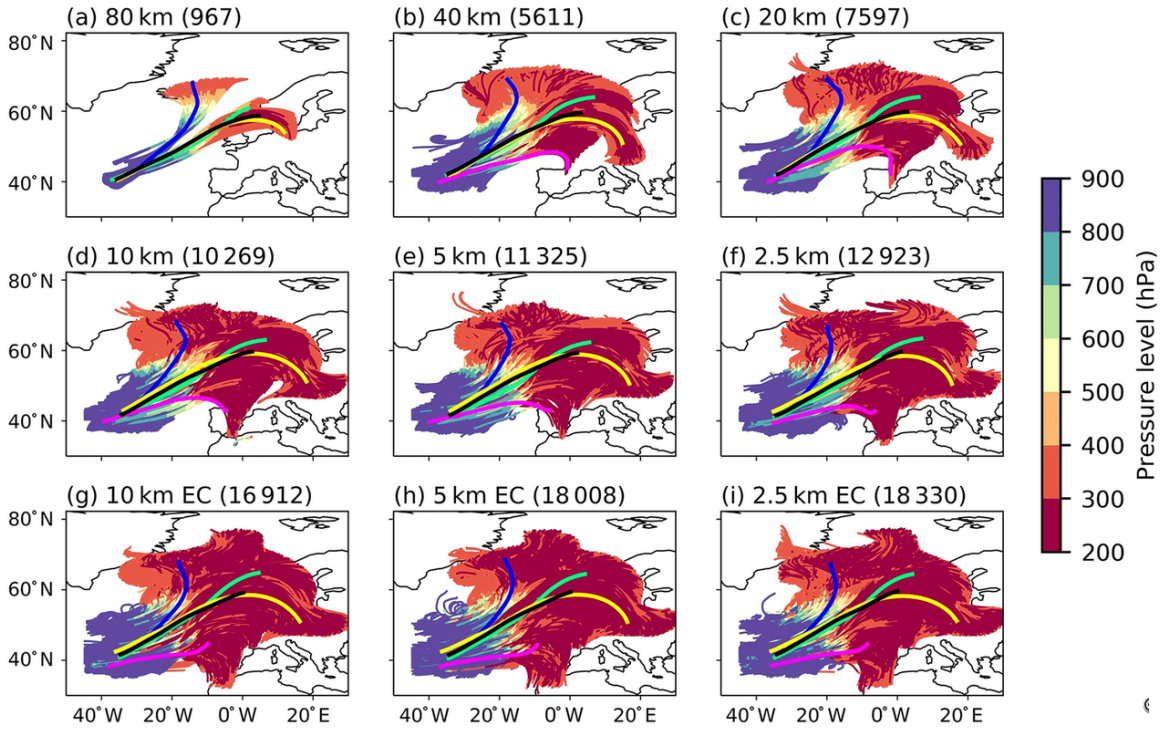

Figure 1.12: WCB trajectories from 48-h forward simulations with two-moment cloud microphysics. The lower panels (g-i) show the simulations for explicit convection. Trajectories are coloured by pressure, and mean pathways of four subclasses (blue, green, yellow, magenta) and the overall mean (black) are indicated. Adapted from Choudhary and Voigt (2022).

vapour agree well between in situ measurements and ERA-Interim. However, the comparison of ISSR pathlengths reveals that ERA-Interim exhibits a significantly smaller number of small ISSRs compared to IAGOS.

Limitations

Despite the progress achieved by previous studies, several limitations remain that are directly relevant for the present work. First, the identification of WCBs can vary depending on the choice of trajectory criteria, temporal window, and vertical coordinate, which affects how many WCBs are detected and how their ascent pathways are characterized (e.g., Pfahl et al., 2014; Madonna et al., 2014; Heitmann et al., 2024). As a result, climatologies derived using different definitions or identification algorithms are not always directly comparable, complicating attempts to synthesise findings across datasets or methodologies.

A second limitation arises from uncertainties in the underlying datasets. Reanalysis products differ in spatial resolution, vertical-motion characteristics, and humidity biases (e.g., Kunz et al., 2014; Krüger et al., 2022). While such differences are known to affect UTLS moisture dis-

tribution, their impact on the diagnosed structure, frequency, and moisture transport associated with WCBs has not yet been systematically quantified. Likewise, model-based studies depend on microphysical and convective parameterizations that influence condensation processes, precipitation efficiency, and the partitioning between hydrometeor species (e.g., Morrison et al., 2020; Choudhary and Voigt, 2022; Mazoyer et al., 2021; Schwenk and Miltenberger, 2024). These dataset uncertainties may lead to systematic discrepancies in the representation of WCB ascent and associated moisture fluxes.

While field campaign observations are invaluable for process understanding but they offer only limited constraints on WCB climatology. Aircraft measurements and remote-sensing instruments provide detailed snapshots of individual WCB cases, but their spatial and/or temporal coverage is inherently restricted. Measurement campaigns are typically confined to specific seasons or geographic regions and sample only a small number of events. Consequently, while they provide rich process-level insight, they cannot capture the full variability of WCB behaviour necessary for robust climatological generalization (e.g., Rolf et al., 2018; Tinney and Homeyer, 2023).

Together, these limitations highlight persistent uncertainties in how WCBs are detected, represented, and interpreted across different methodologies and datasets. Addressing these challenges is essential for improving our understanding of WCB dynamics and their climatological impacts.

1.5 Research Questions

As introduced and reviewed in previous sections, WCBs are key contributor to the extratropical UTLS moisture budget and thereby influence cloud formation and radiative processes. Water vapour in the extratropical UTLS is controlled by a combination of dynamical and microphysical processes. Besides upward transport within extratropical cyclones and deep convection (Zahn et al., 2014), additional contributions arise from isentropic mixing across the subtropical jet, vertical transport within the South Asian Monsoon Anticyclone (e.g., Rolf et al., 2018; Brunamonti et al., 2019), and tropical moisture transported poleward by the Brewer–Dobson circulation (Zahn et al., 2014). Against this diverse background, WCBs have been proposed as a potentially efficient extratropical pathway for transporting water vapour and condensate into the UTLS, but their quantitative contribution remains constrained.

Despite the recognised importance of WCBs, several knowledge gaps remain from a climatological perspective. Existing studies have largely focused on the dynamical impact of WCB

outflow in the UTLS, in particular its role in shaping PV anomalies and the large-scale circulation. In contrast, comparatively few studies have examined the associated moisture anomalies and their dependence on inflow characteristics and ascent behaviour. Factors such as initial moisture availability, ascent timescale, latent-heating intensity, and microphysical conversions are rarely examined systematically in a climatological context. Moreover, there is still no solid quantification of the water transported by WCBs into the UTLS or of their overall impact on UTLS moisture content from a climatological perspective. In addition, it remains unclear how long WCB-related moisture anomalies persist in the UTLS after ascent has ceased, and to what extent such anomalies contribute to the long-term UTLS water vapour budget.

To address these gaps, the first part of the thesis is guided by the following research questions.

1. How strongly do WCB outflows contribute to UTLS moisture anomalies?

2. How long do WCB outflow-related moisture anomalies persist in the UTLS after ascent?

3. How significantly do WCBs affect the UTLS moisture flux?

These questions are answered in Chapter 3, where ERA5 reanalysis data and LAGRANTO trajectories are used to construct a climatology of WCB outflow and its impact on UTLS moisture. A new definition of the UTLS boundary is introduced, and both mass and water fluxes across this layer are quantified to assess the contribution of WCBs to the total transport.

Building on the climatological quantification of WCB moisture transport into the upper troposphere and its lasting impact on UTLS moisture anomalies, the next step is to understand the underlying moisture transport pathways and controlling processes across different seasons and individual cases. Such process-level insight is essential for improving UTLS water-vapour climatologies and their representation in climate models. The second part of the thesis therefore addresses the following research questions:

4. How does variability in the WCB inflow environment influence the moisture transport into the UTLS?

5. To what extent do mesoscale processes resolved in high-resolution ICON simulations affect UTLS moisture transport in detailed case studies compared to ERA5?

6. How robust are comparisons between ERA5-based diagnostics of WCB moisture transport from multiple high-resolution ICON simulations?

Research questions 4-6 are addressed sequentially in Chapters 4, 5, and 6 through a combination of reanalysis data and high-resolution modelling. Chapter 4 examines variability in the WCB inflow environment within extratropical cyclones and assesses how differences in inflow thermodynamic conditions and ascent characteristics influence WCB outflow moisture properties. Using a newly developed Eulerian inflow mask applied to ERA5, this chapter characterizes statistically representative inflow conditions associated with WCBs and quantifies their relationship with outflow moisture. The resulting framework further provides a physically consistent basis for selecting representative cases for subsequent high-resolution ICON simulations.

Chapter 5 presents a detailed analysis of two contrasting cases, one representative of boreal summer (JJA) and one of winter (DJF). For these cases, inflow environments and outflow characteristics are compared with ERA5, and relationships between inflow and outflow thermodynamic diagnostics are analysed. High-resolution ICON output is further employed to explore the microphysical pathways that control ascent behaviour and moisture transport.

Finally, Chapter 6 synthesises the ERA5-based climatology with the ICON ensemble simulations to assess the consistency between reanalysis-derived analysis and high-resolution model results, thereby diagnosing the reliability of reanalysis-based WCB climatologies.

1.6 Outline

In summary, this chapter has outlined the current understanding of WCB dynamics, reviewed the methodologies used to construct WCB climatologies, and identified key limitations that motivate this thesis.

The thesis is structured as follows. Chapter 1 introduces the fundamental concepts, scientific background, and the motivation and research questions addressed in this thesis. Chapter 2 describes the data sets and methods used throughout the thesis. Chapter 3 presents a 10-year ERA5-based climatological analysis of WCB outflow and its contribution to UTLS moisture. Chapter 4 focuses on WCB inflow properties and introduces an algorithm to identify and track inflow objects in ERA5. Chapter 5 analyses two contrasting WCB events using high-resolution ICON simulations, with emphasis on ascent behaviour and microphysical processes. Finally, Chapter 6 synthesises the reanalysis and high-resolution perspectives to compare ERA5 against ICON and to assess the robustness of reanalysis-based representations of WCB climatology, with a particular focus on the role of embedded convection.

2 Data and Methods

2.1 ERA5

Reanalysis datasets provide a physically consistent reconstruction of the historical atmospheric state by combining numerical weather prediction (NWP) models with a wide range of observations through data assimilation. In climate and weather research, ERA5 represents the global reanalysis produced by the European Centre for Medium-Range Weather Forecasts (ECMWF). ERA5 is based on a high-resolution version of the Integrated Forecasting System (IFS), with a horizontal grid spacing of approximately 31 km and 137 vertical levels extending up to 0.01 hPa. The temporal resolution is also improved from 6-hourly to hourly analyses, allowing more detailed sampling of rapidly evolving atmospheric features. ERA5 employs an upgraded 4D-Var assimilation system together with higher-quality observational input, including reprocessed satellite data and additional data types not assimilated in ERA-Interim. As a result, ERA5 provides more accurate representations of key atmospheric variables (e.g. temperature, humidity, winds) and improves the reliability of trajectory-based analysis (e.g., Hersbach, 2019; Hersbach et al., 2020; Hoffmann et al., 2019).

2.2 LAGRANTO

Air parcel trajectories have been used in meteorology since the early 20th century (e.g., Shaw, 1903; Shaw and Lempfert, 1906). Nowadays, this Lagrangian perspective has been further advanced through the development of dedicated computational tools. LAGRANTO (Lagrangian Analysis Tool) is one of the most widely used software packages for computing and analysing air parcel trajectories in NWP and reanalysis datasets. LAGRANTO was originally developed by Wernli (1997) for diagnosing coherent airstreams in extratropical cyclones, it has been extended and modernized in the second version described in detail by Sprenger and Wernli (2015). The tool provides a flexible and efficient framework for calculating both forward and backward trajectories, interpolating meteorological fields in space and time, and deriving a broad range of dynamical and thermodynamic diagnostics along parcel paths (e.g. wind components, water vapour, condensate, potential vorticity). It supports multiple input formats, including ECMWF datasets such as ERA-Interim and ERA5, making it well suited for climatological and case-

study applications.

LAGRANTO has become a standard tool for investigating atmospheric transport processes, including stratosphere–troposphere exchange and warm conveyor belts or dry intrusions. It is particularly well suited for studying the three-dimensional evolution of airstreams in complex synoptic systems (e.g., Sprenger and Wernli, 2015; Wernli, 1997; Raveh-Rubin, 2017), benefiting from its robustness, computational efficiency, and extensive diagnostic capabilities (e.g. tracing variables). In the first part of this thesis, LAGRANTO, together with ERA5, serves as the primary tool and dataset for computing and identifying WCB trajectories and for quantifying their climatological impact on moisture transport into the UTLS.

2.3 ICON model

ICON (ICOsahedral Nonhydrostatic) is an atmospheric modelling framework jointly developed by the German Weather Service (DWD) and the Max Planck Institute for Meteorology (MPI-M) to provide a unified system for numerical weather forecasts and simulations (Zängl, 2013). Unlike conventional latitude–longitude grids, ICON solves the non-hydrostatic equations on a spherical icosahedral grid (Fig. 2.1; Prill et al. 2023), which provides quasi-uniform horizontal resolution, eliminates polar singularities, and prevents severe grid distortions at high latitudes.

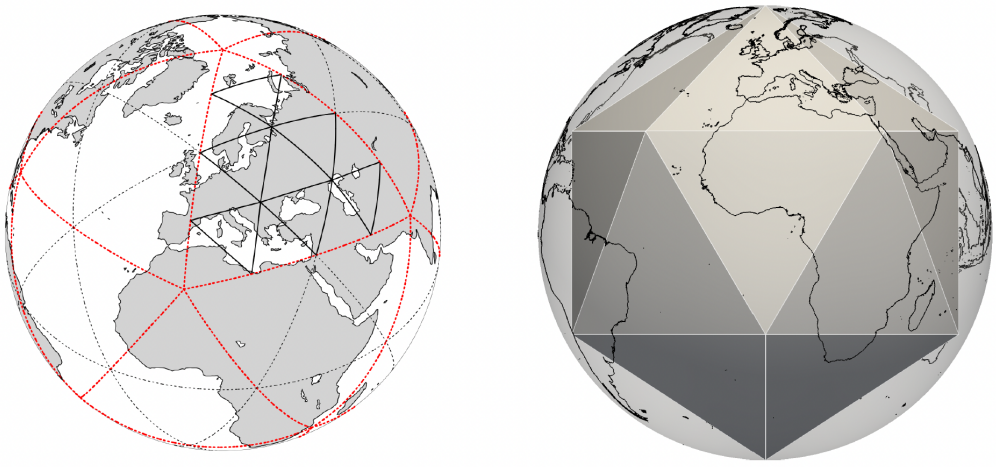

Figure 2.1: Illustartion of ICON grid generation. The left panel shows the geometric construction of the grid from a spherical icosahedron through refinement steps, while the right panel shows the example of 12 pentagon points. Adapted from Prill et al. (2023).

2.3.1 Two-way nesting

As shown in Fig. 2.1 (left panel), ICON supports a two-way grid-nesting approach in which each child cell is uniquely and fully associated with a single parent cell due to its triangular mesh, thereby reducing ambiguities in parent–child mappings within the nested grid hierarchy (Zängl, 2013). Local grid refinement is achieved by overlaying a higher-resolution child domain on a coarser parent domain within the icosahedral mesh. At each time step, the parent domain supplies dynamically consistent lateral boundary conditions to the child domain, in return, the prognostic variables in the parent domain are relaxed towards the corresponding child-grid averages within a feedback zone covering the nested area (for details of the procedure, see in Fig. 2.2).

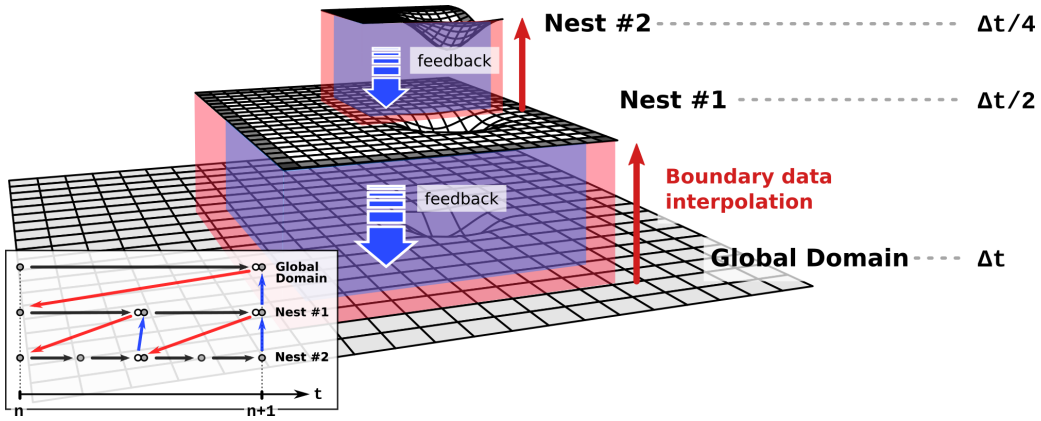

Figure 2.2: Illustartion of the ICON two-way nesting procedure, showing the configuration of multiple nested domains within a global (or limited area) base domain, together with the time integration sequence used for advancing all domains from one time step to the next. Adapted from Zängl et al. (2022).

This two-way coupling allows small-scale features resolved in the nest to influence the larger-scale flow in the parent domain, so that the nested domain effectively behaves as a locally refined part of a single, unified model. In contrast, reanalysis data such as ERA5 are produced on a single coarse-resolution grid without interactive local refinement, so the ICON two-way nesting framework provides a more advanced representation of regional, kilometre-scale WCB dynamics and cloud processes while retaining global consistency.

For the high-resolution simulations presented in this thesis, we use version 2.6.2 of the ICON model in the NWP configuration. The convection scheme is parametrized following Tiedtke (1989) and cloud microphysical processes are represented using the two-moment microphysics scheme by Seifert and Beheng (2006). Radiative transfer is computed with the Rapid Radiative Transfer Model. Non-orographic gravity wave drag, subgrid-scale orographic drag (e.g., Lott and Miller, 1997; Orr et al., 2010), and turbulence are parameterized using the standard ICON

schemes on all domains. A detailed description of the ICON model setup, including grid nesting and domain configuration, is given in Section 5.2.1.

2.3.2 Convection scheme

The high-resolution simulations conducted in this study are specifically designed to capture embedded convection within WCBs and the associated microphysical processes along the ascent, which are not resolved in reanalysis datasets. Therefore, the convection and cloud microphysics schemes are described in more detail below, as they directly govern vertical transport and the evolution of water during WCB ascent. Convection typically occurs on spatial scales of a few kilometers or less, so it can only be resolved when the model's horizontal and vertical grid spacing are sufficiently small. In NWP this generally requires grid spacings of order 1-3 km for deep convection and even finer resolutions for shallow convection. Such high-resolution simulations remain computationally demanding, especially for global domains, and are therefore not yet feasible for long-term climate simulations. Consequently, most operational NWP and climate models employ coarser horizontal resolutions and must parameterise convection rather than resolve it explicitly.

Convection in ICON's NWP physics package is represented by a bulk mass-flux parametrisation based on the Tiedtke–Bechtold scheme originally developed for the ECMWF IFS (e.g., Tiedtke, 1989; Bechtold et al., 2001, 2008). In this scheme, both shallow and deep convection are simulated as updraft and downdraft plumes that interact with the ambient large-scale flow. Convection is diagnosed at each grid column and time step by evaluating the environmental thermodynamic state, including measures of atmospheric instability such as CAPE (convective potential available energy), the depth and buoyancy of clouds, and the large-scale moisture convergence that sustains plume development. This mass-flux framework enables ICON to represent the effects of subgrid-scale convection on the resolved atmospheric state in coarse-resolution configurations.

At the 3.3 km grid spacing of the nested ICON domain used in this study, the model operates in a convection-permitting regime. Accordingly, parameterized deep convection is disabled, and the convection scheme is configured to represent shallow convection only. In this configuration, the strongest and most organised deep convective updrafts associated with WCBs are at least partly resolved by the model dynamics and microphysics, while the Tiedtke–Bechtold scheme mainly accounts for the remaining unresolved convective transport. The parameterization is therefore predominantly active for shallow and weakly organised convection in the boundary layer and lower troposphere, where individual plumes still remain subgrid at 3.3 km. These tendencies therefore complement the resolved convective motions and must be considered

when comparing the high-resolution ensemble results with the fully parameterized convection in ERA5.

2.3.3 Microphysical scheme

Cloud microphysical processes in the ICON simulations are represented by a bulk two-moment microphysics scheme. (Seifert and Beheng, 2006). In this framework the model predicts both the mass mixing ratio and the number concentration for several hydrometeor categories (cloud water, cloud ice, rain, snow and graupel), rather than only the mass as in traditional one-moment schemes. This double-moment formulation allows for a more accurate representation of microphysical processes, including the influence of varying hydrometeor number concentrations and aerosol variability on phase changes and precipitation formation. The scheme includes parameterized processes such as condensation and deposition, aggregation and riming, melting, evaporation and sublimation, as well as the sedimentation of precipitating species, and is applied consistently across the different ICON domains used in this study.

2.3.4 Online trajectory

Except for LAGRANTO, which is effectively an offline tool in today's terminology, another concept so called "online trajectories" was introduced in the early 1990s (Rössler et al., 1992), who embedded trajectory calculations directly into a NWP model so that trajectories used the instantaneous model wind field without temporal interpolation. This idea was later further developed and generalized, for example in the COSMO online-trajectory module (e.g., Miltenberger et al., 2013), and more recently adapted to the ICON model (e.g., Miltenberger et al., 2020; Oertel et al., 2023; Schwenk and Miltenberger, 2024), which is also used for the high-resolution ensemble study in this study in the second part.

The trajectory equation in ICON is integrated using a Petterssen predictor–corrector scheme at the model time step (e.g., Petterssen, 1956; Miltenberger et al., 2013). The Petterssen predictor–corrector scheme can be interpreted as approximating the trajectory velocity by the mean wind between two consecutive trajectory positions. In ICON, the wind components required to integrate the trajectory equation are estimated at the parcel position by horizontal interpolation on the triangular grid and linear interpolation in the vertical from the Eulerian wind fields. In addition, tendencies from the microphysics, radiation, and turbulence schemes are interpolated to the parcel position at each model time step, enabling detailed diagnostics of individual process contributions along the trajectories. Moreover, in two-way nested ICON

simulations, it is not sufficient to follow WCBs only in the finest domain. Therefore, the ICON online trajectory tool was further developed by Oertel et al. (2023) to support nesting, allowing trajectories to cross between nests such that air parcels are always advanced with the wind field and time step of the highest-resolution domain available at their current location.

2.4 WCB computation and identification

The identification and analysis of warm conveyor belt (WCB) events presented in this thesis are based on ERA5 reanalysis data from the European Center for Medium-Range Weather Forecasts (ECMWF) (Hersbach et al., 2020). ERA5 provides a consistent, high-resolution representation of the global atmospheric state, available from 1979 to the present. In this analysis, we specifically utilize data from the period 2010–2019 at a horizontal resolution of 0.25° and hourly temporal resolution. Vertically, the ERA5 dataset comprises 137 levels extending from the Earth's surface up to approximately 1 hPa. In the extratropical tropopause region, the vertical resolution is approximately 300–400 meters, providing sufficient detail for capturing upper-tropospheric dynamics relevant to WCB analysis. The quality of ERA5 is critical for accurately characterizing WCB outflow and its impact on UTLS moisture. Two notable biases have been studied in the ERA5 lower-stratospheric data: (i) a cold temperature bias, which has been addressed in ERA5.1 version (Simmons et al., 2020), and (ii) a systematic moist bias in the specific humidity around 1 2 km above the thermal tropopause (Krüger et al., 2022). Since this study primarily focuses on the upper troposphere, the potential influence of these lower stratospheric biases is expected to be minor and does not significantly affect the key conclusions.

The WCB identification follows a Lagrangian approach commonly employed in previous studies (e.g., Madonna et al., 2014; Oertel et al., 2019). Forward trajectories are initialized every 6 hours, covering the entire Northern Hemisphere. Trajectories extending 48 hours forward in time are initialized every 6hours, covering the entire Northern Hemisphere. The trajectory starting points are spaced horizontally at intervals of 0.25° and vertically every 20 hPa between 1050 hPa and 790 hPa, resulting in over 790,000 trajectories per initiation time. These trajectories are computed kinematically using the LAGRANTO tool (Sprenger and Wernli, 2015), based on ERA5 wind fields at resolved scales, with trajectory positions and tracer variables available at hourly intervals. WCB trajectories are identified based on two criteria: (i) the air parcel must ascend at least 600 hPa within 48 hours, and (ii) this ascent must intersect with an extratropical cyclone. Cyclones are identified following the method of Wernli and Schwierz (2006), which detects the largest closed sea-level pressure contours surrounding local pressure minima. While this identification method is widely applied, this selection may underestimate the total number of WCB trajectories, particularly those ascending near but outside the main

cyclone region (Heitmann et al., 2024). Consequently, the estimates of WCB-related moisture transport and its associated anomalies in this study should be considered lower bounds of the actual WCB influence on the UTLS.

To characterize the WCB ascent and to define the WCB outflow locations, we initially identify the fastest 600 hPa ascent segment along each selected trajectory. The shortest trajectory segment required for achieving this 600 hPa ascent is referred to as the ascent timescale, τ_{600}, in line with previous literature (Oertel et al., 2019). This identified ascent period (τ_{600}) is then extended both forward and backward, provided the parcel's vertical ascent velocity remains greater than 8 hPa h^{-1}. The last point of this extended ascent segment is defined as the beginning of the WCB outflow, which is denoted as $t = 0$ h. The total duration of the extended ascent is denoted as the WCB ascent timescale τ_{WCB} in the following.

Fig. 2.3 illustrates this selection procedure, showing pressure changes over time for two example WCB trajectories. The fastest ascent periods (τ_{600}) are highlighted with warm colors, and the extended ascent segments are shown as thicker, cooler-colored lines. The rationale behind extending the ascent beyond the fastest ascent segment is that many trajectories continue to ascend significantly afterward, reaching higher altitudes and transporting greater quantities of condensate. For subsequent analyses, all WCB outflow points are mapped to the ERA5 grid. A grid cell is considered influenced by WCB outflow if it contains one or more trajectory points at $t = 0$ h.

To examine the evolution of the WCB outflow beyond the ascent phase (post-ascent), additional 48-hour forward trajectories are calculated from each outflow point, indicated by the red cross ("WCB outflow point") in Fig. 2.3. This 48-hours subsequent trajectory calculation is again performed using LAGRANTO with ERA5 input data. The time following the ascent phase is referred to as the WCB outflow age, denoted by t in the range 0-48 h. This allows for quantification how WCB air masses evolve within the UTLS over time after their ascent.

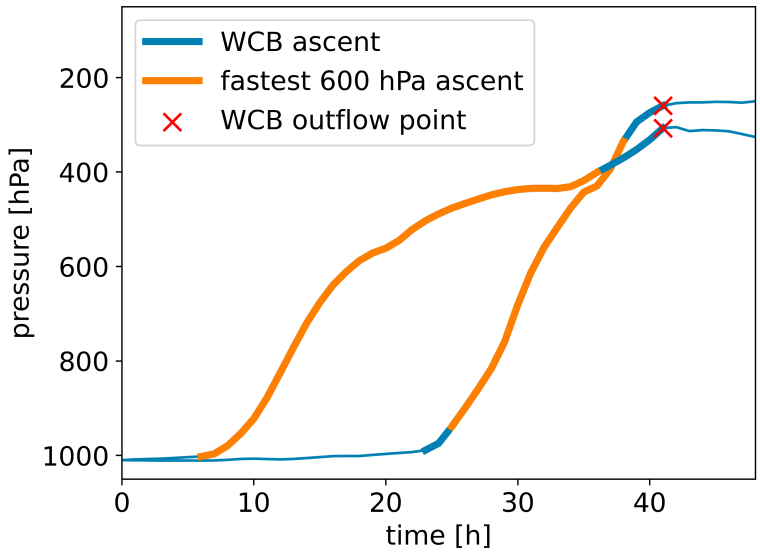

Figure 2.3: Pressure evolution of two exemplary WCB trajectories. The definition of τ_{600} and WCB ascent as described in section 2.4 is illustrated: Thin lines show the full trajectories, thick lines indicate the duration of WCB ascent (τ_{WCB}) and orange lines depict the fastest 600 hPa ascent(τ_{600}).

3 Climatological Analysis of WCB Outflow Moisture Contribution

This chapter reuses the materials from the publication in *Journal of Climate*, titled "Climatology of warm conveyor belt contributions to UTLS moisture in ERA5 between 2010 and 2019".

DOI: 10.1175/JCLI-D-25-0020.1

Author contributions: AM contributed to the conceptualization of the study and the development of the methodology. ZG and AM jointly implemented the methodology and contributed to data analysis and visualization. ZG drafted the manuscript, with revisions and improvements to the text provided by AM. Daniel Kunkel developed the scripts for computing 3D PV and for ERA5 data retrieval.

3.1 Introduction

The extratropical UTLS plays a crucial role in the climate state and future changes thereof (e.g., Riese et al., 2012; Charlesworth et al., 2023). The extratropical UTLS is characterized by the transition of thermodynamic properties and chemical composition from tropospheric to stratospheric values. The large gradients in trace gas, aerosol and cloud concentrations as well as their spatio-temporal variability have a strong impact on radiative forcing (e.g., Gauss et al., 2003; Riese et al., 2012). The climatological mean and higher-frequency variability is shaped by a multitude of physical processes, including non-linear flow dynamics(e.g. gravity or Rossby wave breaking). Given the large vertical gradients in potential temperature and potential vorticity in the tropopause region, which are an effective barrier for adiabatic transport and mixing, diabatic processes are thought to be crucial for vertical redistribution and stratosphere-troposphere exchange (e.g., Gettelman et al., 2011).

Among the trace gases with large vertical gradients in the extratropical UTLS is water vapour (e.g., Gettelman et al., 2011; Zahn et al., 2014). Water vapour in the extratropical UTLS has been suggested to be strongly controlled by upward transport in the extra-tropics within deep convection and extratropical cyclones (e.g., Zahn et al., 2014). Aside from these more "local" sources there are contributions from mixing across the sub-tropical jet, upward transport in the South Asian Monsoon Anticyclone (e.g., Rolf et al., 2018; Brunamonti et al., 2019), as well as transport from the tropics via the Brewer-Dobson circulation (e.g., Zahn et al., 2014).

The water transport from the boundary layer to the UTLS is strongly modulated by cloud processes, as it typically is thought to occur in deep convection or organized large-scale ascent associated with extratropical cyclones (the warm conveyor belt, WCB). This also implies water is transported both as vapour and in condensed form, which implies water transport is not purely thermodynamically constrained. Recent observational studies suggest a dominant role of convection in the South Asian summer monsoon and Northern hemispheric land masses in moistening the UTLS during the summer months (e.g., Rolf et al., 2018; Tinney and Homeyer, 2023). The influence of convection likely wanes into the winter month due to less favorable thermodynamic conditions. In the transition seasons and the winter months vertical transport in WCBs likely becomes more important, although the larger potential temperature and potential vorticity (PV) gradients at the tropopause and stronger stratospheric circulation in winter likely prevent the advection of the moisture beyond the lowermost stratosphere (e.g., Sprenger and Wernli, 2003; Gettelman et al., 2011; Madonna et al., 2014).

Previous studies have shown that WCBs play a significant role for upper-tropospheric cloudiness and cloud radiative forcing (e.g., Wernli et al., 2016; Joos, 2019). Furthermore, WCB

moisture transport may also be related to the occurrence of ice supersaturated regions (ISSRs), which are important determinant for the spatio-temporal distribution of natural and anthropogenic in-situ cirrus (e.g., Spichtinger et al., 2005; Hofer et al., 2024). Recent studies suggest that although the overall number of extratropical cyclones may decline in a future warmer climate (e.g., Priestley and Catto, 2021), their intensity is expected to increase. The anticipated increased boundary layer moisture content further contributes to a likely larger moisture flux into extratropical cyclones, while altered vertical temperature profiles may impact precipitation formation. Combined these changes are anticipated to enhance moisture transport into the UTLS (e.g., Joos et al., 2023a; Binder et al., 2023).

Despite the potential importance of WCB related water transport for the moisture content of the extratropical UTLS little is known about the quantitative contribution of WCBs transport. Therefore this chapter provides a quantitative analysis of the role of WCBs for extratropical UTLS moisture anomalies and water transport into the UTLS. The analysis is based on Lagrangian framework using ERA5 data. While ERA5 offers a physically consistent representation of WCB contributions to UTLS moisture content and vertical structure, it is important to consider known biases in UTLS humidity (Krüger et al., 2022). Krüger et al. (2022) identified a systematic lower-stratospheric moist bias in the ERA5 reanalysis, with a maximum overestimation of 55 % occurring approximately 1.3 km above the thermal tropopause, particularly pronounced in mixed air masses and during summer. However, the specific mixing processes and timescales responsible for the formation and vertical structure of this moist bias in ERA5 remain to be fully understood. Therefore, this chapter aims to address these gaps and uncertainties and to answer the research questions outlined in Section 1.5.

3.2 Method

3.2.1 Atmospheric background state

A central objective of this study is to investigate the influence of WCB outflows on the moisture content of the UTLS. To better assess this impact, it is essential to quantify not only the moisture content within the WCB outflows themselves but also in the surrounding atmosphric environment that not influenced by WCB outflow, referred to here as the atmospheric background. We define the atmospheric background by selecting all atmospheric columns that located within the geographic region where the climatological occurrence frequency of recent WCB outflows (age 0 h) exceeds 1 %. For the analysis outflow evolution (section. 3.4), this threshold applies to the occurrence frequency of any WCB outflow aged 0 to 48 h. In both

cases, the selected background columns are themselves not influenced by any WCB activity during or shortly before the time of analysis, specifically:

- No WCB ascent is detected within the column at any time during the identified WCB ascent period (τ_{WCB}).
- No WCB outflow aged 24 h or less is present within the column for the climatological analysis of vertical moisture anomalies in fresh WCB outflow (Section 3.3.2). For the analysis of WCB outflow evolution (Section 3.4), this criterion is extended to exclude WCB outflow aged 48 h or younger.

For the analysis of fresh WCB outflow (age 0 h), restricting the domain to regions with at least 1 % occurrence frequency is necessary to account for the strong spatial variability in atmospheric humidity, which reflects, for example, the land–sea distribution and the non-homogeneous occurrence of WCB outflow.

To effectively limit the selected profiles to the extratropics, we apply a WCB selection criterion requiring trajectories to cross a closed sea level pressure contour north of 25° N. In Section 3.3, atmospheric columns containing WCB outflow points at any age up to 24 h are excluded from the comparison of moisture anomalies between the outflow and the background columns in fresh WCB outflow. While in Section 3.4, columns containing WCB outflow points at any age up to 48 h are excluded in the analysis of the further WCB outflow evolution.

The process of excluding outflow points at different trajectory ages is geographically illustrated in Fig. 3.1. Panel (a) shows the locations of WCB trajectories immediately after they complete their ascent phase (τ_{WCB}), while panel (b) includes all outflow positions reached within the following 48 hours. The red contour outlines the region where the climatological frequency of WCB outflow exceeds 1 %. Orange dots represent specific outflow locations at each time step. For example, in Section 3.1, the background region is defined as the grid points inside the red contour that are not marked by orange points in panel (b), meaning grid points that are not associated with outflow during the 48 hour period, and these points are used to compute averaged atmospheric conditions. This distinction is used to compare environmental properties with and without the influence of WCB outflows.

Following the above criteria, approximately 20 % of all ERA5 grid points within the 30-60 ° N latitude band between 2010 and 2019 are included in our analyses, corresponding to the region outlined by the red contour in Fig. 3.1. Within this selected area, 97.15 % of grid points represent the "atmospheric background", whereas 2.85 % correspond to WCB outflow.

For the climatological analysis presented in Section 3.3, all identified background columns are considered within the 1 % occurrence frequency. While in Section 3.4, monthly averaged background conditions are utilized for the evolution analysis. Background averages are computed on either on fixed relative-tropopause altitude levels ranging from -5 km to 2 km with intervals of 200 m or at fixed pressure levels between 1000 hPa and 100 hPa with a spacing of 10 hPa.

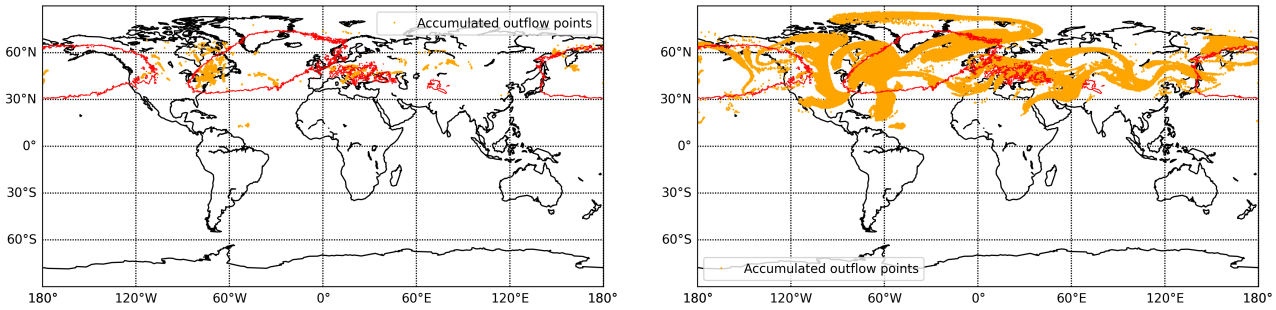

(a) WCB outflow points t=0

(b) Accumulated outflow points within 48 h

Figure 3.1: WCB outflow locations on 1 December 2010 at 10:00 UTC. Panel (a) shows the trajectories positions immediately after completing their WCB ascent (τ_{WCB}), while Panel (b) includes all outflow points, capturing both current and previously ascended parcels that propagated over the following 48 hours.

3.2.2 Definition and identification of the extra-tropical UTLS

3D label

The term upper troposphere and lower stratosphere (UTLS) generally refers to the transition region between the troposphere and the stratosphere, including the tropopause. However, a consistent and objective definition of the UTLS has yet to be established. In agreement with previous studies, the dynamic tropopause is identified here using a combination of the ±2 pvu (solid red line in Fig. 3.2 a) and the 380 K iso-surface (dahsed red line in Fig. 3.2 b) (e.g., Holton et al., 1995; Hoerling et al., 1991). The combination of PV and potential temperature ((θ)) criteria ensures a meaningful tropopause definition in the tropics, where PV values are consistently low in the upper troposphere. PV is a commonly used tracer to distinguish between tropospheric and stratospheric air, and 2 pvu is typically used as a threshold. In the Southern Hemisphere, PV is often defined with an opposite sign, using -2 pvu (also illustrated in Fig. 3.2 a). However, not all air with $|\mathrm{PV}| \geq 2$ is of stratospheric origin. Diabatic processes can generate high-PV air within the troposphere, for example within cyclone systems. Similarly, frictional effects near the surface, such as over mountains, can also create high PV anomalies. Moreover, over high-latitude continental regions such as Greenland and Antarctica, very stable air masses just above the surface also have high PV values (Škerlak et al., 2014). These non-stratospheric PV anomalies can exceed the ± 2 pvu threshold. Additionally, the

stratosphere-troposphere exchange (STE) processes can lead to high |PV| anomalies in troposphere and low |PV| anomalies in stratosphere. Therefore, using a simple threshold ($|PV| \geq 2$) may mistakenly identify tropospheric and stratospheric regions. To address this, we applied a 3D labeling algorithm (e.g., Sprenger et al., 2003; Škerlak et al., 2014) to distinguish between tropospheric and stratospheric air in a more objective and physically consistent manner.

As shown in Fig. 3.2 c, we classify the atmosphere into five distinct categories by assigning labels from 1 to 5. Firstly, all grid points with either $|PV| \geq 2$ or $\theta \geq 380$ K are flagged, capturing both stratospheric air and high-PV anomalies in the lower atmosphere. Among these, the largest contiguous grid points are identified as main stratospheric reservoir. The smaller disconnected high-PV anomalies are then assigned **label 3**, representing stratospheric cut-offs or diabatically generated PV anomalies, and **label 5**, denoting surface-bound high-PV anomalies near the ground. In the next step, grid points with $|PV| < 2$ that were not part of any previous labeled objects are considered as troposphere. The largest contiguous region of these grid points is labeled as **label 1**, representing the main tropospheric reservoir. The smaller isolated regions of low-PV air embedded in the stratosphere are assigned **label 4**, representing tropospheric cut-offs such as convective lifted air masses.

Finally, to correctly identify identify stratospheric intrusions into the troposphere, a vertical propagation is applied. Starting from the top model level, grid points within the main stratospheric reservoir are assigned as **label 2**. The stratospheric label (**label 2**) is then propagated downward and laterally connect grid points that satisfy the high-PV conditions. This step allows for multiple interfaces in the same column, enabling a physically meaningful characterization of tropopause folds. Regarding to tropopause folds, we do not extend the analysis horizontally beyond the tropopause grid point identified. In cases where the descending stratospheric reservoir is connected with surface-bound high-PV anomalies, vertical propagation was allowed to override these near-surface labels (initially assigned **label 5**). However, any remaining surface-bound PV anomalies that are not connected to the stratosphere retain **label 5**, indicating PV anomalies due to orographic effects. The final labeling scheme, as illustrated in Fig. 3.2 c, thus assigns:

- **label 1**: the main tropospheric region.
- **label 2**: stratospheric air connected to the main stratospheric reservoir.
- **label 3**: stratospheric cut-offs or high-PV anomalies that not connected to the main stratospheric reservoir.
- **label 4**: tropospheric cut-offs embedded in the stratosphere.

- **label 5**: surface-bound high-PV anomalies.

This method ensures a physically consistent, three-dimensional representation of complex atmospheric structures, including tropopause folds, cut-off systems, and STE events.

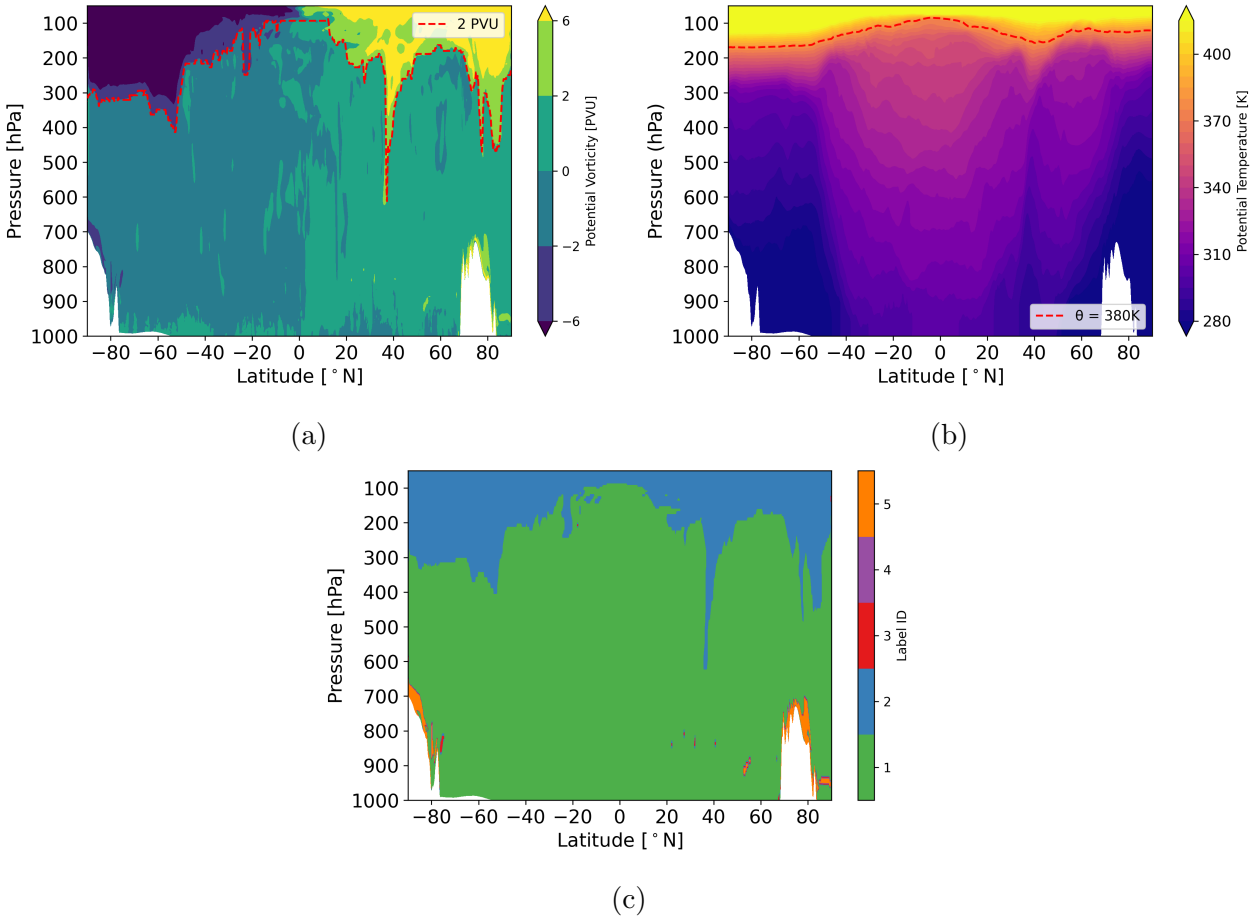

Figure 3.2: (a) Vertical cross-section of potential temperature ((θ)) on 01. January 2017 at 00 UTC along 30 ° E. The dynamical tropopause, defined by the ±2,pvu threshold, is indicated by the red dashed line. (b) Same cross-section as in (a), showing potential temperature (θ). The 380,K isentropic surface is marked by the red dashed line. (c) Example of a 3-D labeling output, as described in Section 3.2.2, for the same date and cross-section. The atmospheric region is classified into five categories (labels 1–5) based on PV and θ thresholds, combined with their spatial connectivity.

UTLS identification

In this study, we propose a quantitative definition of the UTLS layer as the vertical region extending from 50 hPa below the local dynamic tropopause to the first level above it where PV exceeds 6 pvu (indicated by blue shading in Fig. 3.3 a). To ensure that the dynamic tropopause reflects the true boundary between the main tropospheric and stratospheric air masses from

reanalysis data, we exclude isolated high-PV anomalies in the troposphere and low-PV anomalies in the stratosphere, which may lead to misidentification.

This identification is applied to each vertical column. If PV does not reach 6 pvu above a tropopause fold, the entire column within the fold is classified as UTLS. In addition, if the vertical distance between the fold and the main tropopause is less than 100 hPa, the enclosed tropospheric area is considered as UTLS.

An example of the identified UTLS layer is shown in Fig. 3.3 a. The dynamic tropopause is marked by the red solid line, and the 6 pvu iso-surface is indicated by the yellow line. The identified UTLS region is shaded in blue. The 380 K isentrope is indicated by red dashed line.

The climatological distribution of the dynamical tropopause and the UTLS layer is shown in Fig. 3.3 b. The UTLS follows the expected zonal structure, with altitude decreasing towards the pole. The highest probability of UTLS occurrence is found just above the tropopause north of 60 $^\circ N$ and south of 45 $^\circ N$. The highest occurrence probability, implying frequent occurrence in a narrow altitude range, is found just above the dynamical tropopause north of 60 $^\circ N$ and south of 45 $^\circ N$. Around the average position of the extratropical jet stream, near 50 $^\circ N$, the UTLS extends across a broad range of altitudes, reflecting a large synoptic-scale variability and complicated tropopause structure in the storm track region.

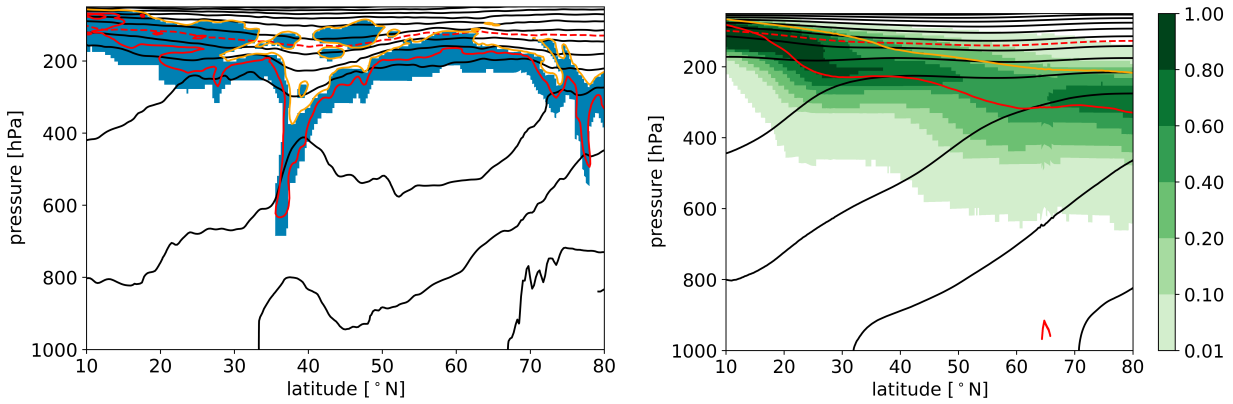

(a) (b)

Figure 3.3: (a) Example of the tropopause and UTLS structure at 30 ° E on 01 January 2017 00 UTC. The UTLS layer as defined in Section 3.2.2 is indicated by the blue shading. The dynamical tropopause is marked by the red line, the 6 pvu isoline by the orange line, and isentropes ranging from 250 K to 500 K with 20 K intervals are shown with black lines. The 380K isentrope is shown with red dashed line. (b) Climatological probability of the presence of UTLS layer at 30 ° E for DJF 2010-2019 (color shading). The average position of the dynamical tropopause is indicated by the red line, that of the 6 pvu isoline by the orange line, and the average position of the isentropes from 250 K to 500 K in 20 K steps by the black lines. The 380K isentrope is shown with red dashed line.

Sensitivity test for UTLS layer definition

As the WCB impact is likely sensitive to the placement of the lower boundary of the UTLS, we conduct a sensitivity test extending the UTLS layer to 100 hPa below the local dynamic tropopause. This alternative definition is used to evaluate how moisture flux diagnostics (see section. 3.5) respond to different UTLS layer configurations. Conducting such sensitivity test is essential for evaluating the robustness of the defined UTLS layer and understanding how moisture fluxes may vary with different UTLS lower boundaries. Further details on the sensitivity setup and results are provided in Appendix Fig. A.1.1

3.2.3 Computation of water flux into the UTLS layer

The water flux into the UTLS is quantified using a Lagrangian diagnostic inspired by Škerlak et al. (2014). They employed trajectory calculations based on ERA5-Interim data to estimate air mass and ozone fluxes arosss the tropopause. In this study, we focus on the moisture transport into the UTLS. To this end, we compute a set of 3 h backward trajectories starting within the UTLS layer, defined in Section 3.2.2, between 10° N and 80° N. Trajectories are initialized at each horizontal ERA5 grid point, with a vertical spacing of 10 hPa, and launched every 3 hours..

Trajectories that leave the UTLS layer within the initial 3-hour window are extended backward in time for another 72 hours and forward for 24 hours. To focus on long-term exchange processes and exclude short-lived transient exchange between the free troposphere and the UTLS, we apply the following criteria:

- trajectories much remain outside the UTLS for at least 9 hours during the 12 hours before crossing into the UTLS, and
- remain within the UTLS for at least 9 hours after crossing.

Although transient contributions to the UTLS may occur more frequently, they are not expected to contribute to the climatological mean state of the UTLS, unless they exhibit a systematic correlation with turbulence events. As the current approach does not allow us to quantify such correlations, we restrict our analysis to the less frequent but more persistent moisture transport events asscociated with WCBs.

Based on the selected trajectories, the mass flux to the UTLS is estimated as the sum of the mass contributions from trajectories crossing into the UTLS at the given grid point in a certain time interval. This sum is normalized by the surface area of the respective grid-point. The mass associated with each trajectory is calculated using:

$$m = \frac{\Delta p_0}{g} \cdot A_0 \tag{3.1}$$

where Δp_0 is the pressure difference between vertical levels at the trajectory starting points, g is the gravitational acceleration, and A_0 is the horizontal area of ERA5 grid point. In addition to computing the total mass flux, we distinguish between contributions from tropospheric air entering the UTLS (upward flux) and stratospheric air entering the UTLS (downward flux), and those specifically associated with WCB trajectories. The WCB trajectories are identified in the 72-hour backward-extended trajectory data-set according to the criteria introduced in Section 2.4.

Building on the mass flux, the water flux is computed by considering the specific humidity and hydrometeor mass mixing ratio of the parcel at the time and location, where it enters the UTLS. The total water mass associated with a trajectory is given by:

$$m_{q_t} \approx m \cdot q_t \tag{3.2}$$

where m_{q_t} is the total water mass associated with each trajectory. q_t is the water mass mixing ratio, defined as the sum of specific humidity and the mass mixing ratios of cloud, rain, ice,

and snow, interpolated to the trajectory position from ERA5 model-level data.

It is important to note that the flux analysis is confined to latitudes between 10° N and 80° N. Furthermore, the Lagrangian trajectories are driven by the grid-scale wind field, which does not explicitly resolve vertical motion associated with convection and turbulence. However, the effects of these unresolved processes are incorporated through parameterizations, which influence the grid-scale distribution of atmospheric properties such as moisture, temperature, and momentum, and are thus reflected in the trajectory data.

3.3 Climatology of WCB outflow and vertical moisture anomalies

3.3.1 Spatio-temporal distribution of WCB trajectories

The 10-year climatology of the geographical distribution of WCB outflow trajectories is shown in Fig. 3.4 for the beginning of the ascent (τ_{WCB}) and in Fig. 3.5 for the end of the ascent, for both DJF and JJA. The frequency indicates the fraction of considered times, during which at least one WCB trajectory finishes its ascent within a given grid box (similar as in Madonna et al., 2014). The black contour encloses the area, in which WCB ascent is expected at least for 1 % of the time. Trajectories originating below 25°N are excluded to eliminate the potential influence of tropical cyclones.

WCB origins and fresh outflow (t = 0 h)

The geographical distribution of WCB starting points, i.e. the beginning of the τ_{WCB} ascent, is shown for DJF and JJA in Fig. 3.4. WCBs occur more frequently in boreal winter than in summer, with occurrence maxima over the North Atlantic, North Pacific, Mediterranean, and the Persian Gulf. The climatology of WCB starting points exhibits distinct southwest–northeast oriented bands over the North Atlantic and North Pacific. Over the Atlantic, this band extends from the Gulf of Mexico toward northern Europe, consistent with the climatological storm track pathway. The corresponding pattern over the Pacific spans a wider longitude range, reflecting the broad storm track entry zone. These distributions are in line with cyclone climatology studies (e.g., Sickmöller et al., 2000; Wernli and Schwierz, 2006). During JJA, the frequency of WCB starting points is markedly lower than in winter. A distinct maximum appears over the United States (US), likely associated with continental convective systems enhanced by orographic lifting along the Rocky Mountains. Over northern India, maximum signal is linked to deep convection within the South Asian monsoon, fueled by strong low-level moisture inflow from the Arabian Sea and Bay of Bengal (e.g., Schott and McCreary Jr, 2001; Houze Jr et al.,

2007; Parker et al., 2016). Another maximum over the Tibetan Plateau and southern China coincides with the East Asian summer monsoon and the Meiyu–Baiu frontal zone, a quasi-stationary convergence band extending from eastern China to Japan (e.g., Xu et al., 2010; Sampe and Xie, 2010).

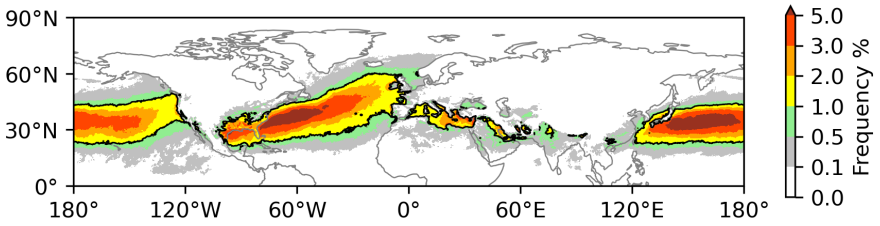

(a) DJF

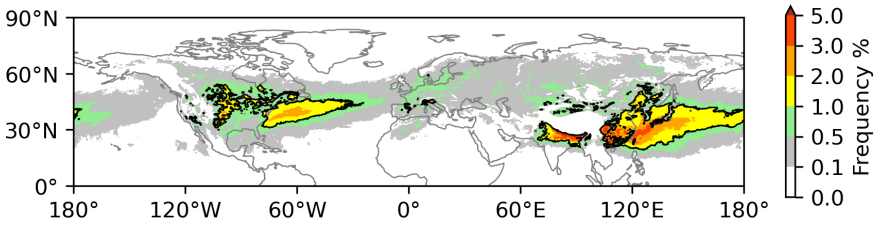

(b) JJA

Figure 3.4: Climatology of trajectory positions at the start of τ_{WCB} ascent for (a) DJF and (b) JJA (2010–2019). Shading indicates the probability (as a percentage) that at least one WCB trajectory is present in an ERA5 grid box during any 6-hour interval. The black contour denotes a WCB occurrence frequency of 1 %.

The climatological distribution of WCB outflow points, defined at the end of the τ_{WCB} ascent, is shown in Fig. 3.5 for DJF and JJA. In both seasons, the highest frequencies occur over the central and northern parts of the storm track regions. Compared to the starting points, the outflow positions are on average shifted northeastward. Over the Atlantic, the occurrence extends from the western North Atlantic to southern Greenland and northern Europe, consistent with the northeastward tilt of the storm tracks. In the Pacific, the distribution spans a broad longitude range from East Asia to the west coast of the US and Alaska. During JJA, the frequency of WCB outflows is much reduced. The main maximum is located over East Asia and the western North Pacific. A secondary maximum is found over the North Atlantic, though it is weaker and shifted southward relative to DJF.

The spatial and seasonal variability of the WCB starting and outflow distributions is consistent with earlier climatologies based on ERA-Interim (e.g., Stohl, 2001; Eckhardt et al., 2004; Madonna et al., 2014) and ERA5 (e.g., Heitmann et al., 2024). Compared to these studies, Fig. 3.5a shows a slight upstream shift, likely due to the definition of the end of ascent (on

average 15-20 h after start of ascent, Fig. 3.11 a) compared to fixed time intervals after start of ascent in earlier studies (typically 48 h).

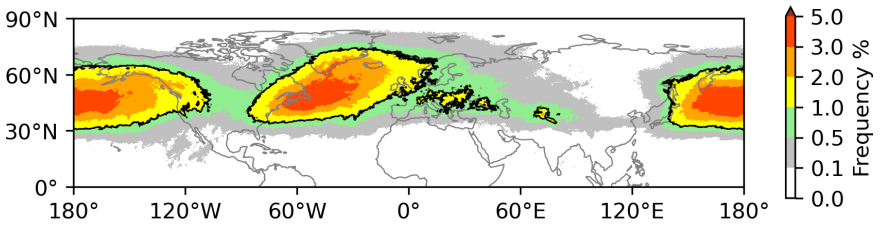

(a) DJF

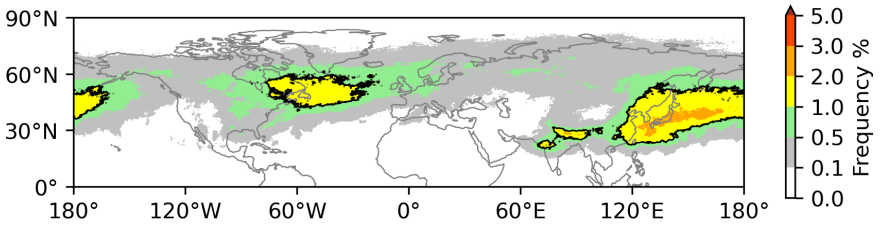

(b) JJA

Figure 3.5: Climatology of trajectory positions at the end of τ_{WCB} ascent (fresh WCB outflow at t = 0 h) for (a) DJF and (b) JJA (2010–2019). Shading indicates the probability (as a percentage) that at least one WCB trajectory is present in an ERA5 grid box during any 6-hour interval. The black contour denotes a WCB occurrence frequency of 1 %.

WCB outflow evolution (t=[0-48] h)

The climatological evolution of WCB outflow parcel positions at 6, 12, 24, and 48 h after the end of ascent is shown in Fig. 3.6 for DJF. For times shortly after the end of ascent (t = 6 h and t = 12 h) trajectories continue to move predominantly northeastward, consistent with the slantwise transport during ascent. During this stage, the WCB signals originating over continents have largely dissipated. With increasing time (t = 24 h, Fig. 3.6c), the distribution broadens and shifts eastward, while a gradual southward displacement becomes apparent. At later times, the trajectories turn more equatorward on average, and the maximum occurrence frequency at t=48 h is found at around 30 ° N, particularly over North Africa and the western US.

In the summer season JJA (Fig. 3.7), the spatial distribution of WCB outflow broadly resembles that in DJF, but with larger differences between the Pacific and Atlantic basins. Over the Atlantic, the evolution of outflow positions is similar to winter, whereas over the western Pacific a more pronounced southwestward shift is evident. Additionally, there is a notable increase in outflow activity over the Tibetan Plateau. These patterns are likely influenced by the southerly

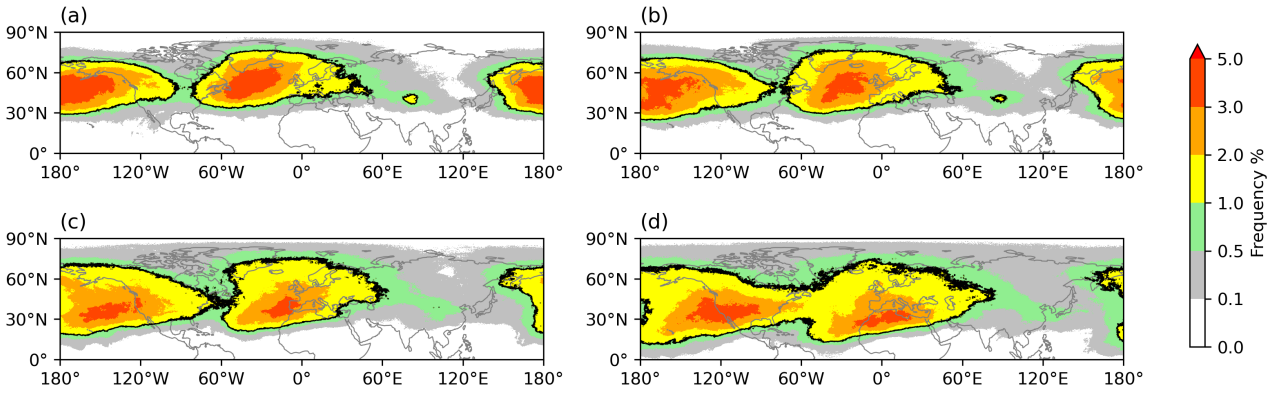

Figure 3.6: Climatology of WCB trajectory positions at t = 6 h (a), t = 12 h (b), t = 24 h (c), and t = 48 h (d) after the end of the WCB ascent for 2010-2019 DJF. The colorbar indicates the probability, expressed as a percentage, that at least one WCB outflow trajectory of a specific age is present within a grid-box for each hour. The black contour highlights the 1 % occurrence frequency of WCB outflow at each time age.

position of the storm track during summer and the effects of the Asian summer monsoon. These seasonal contrasts reflect the reduced intensity of the midlatitude storm tracks in summer and the stronger influence of convection-related systems on WCB ascent and outflow distributions.

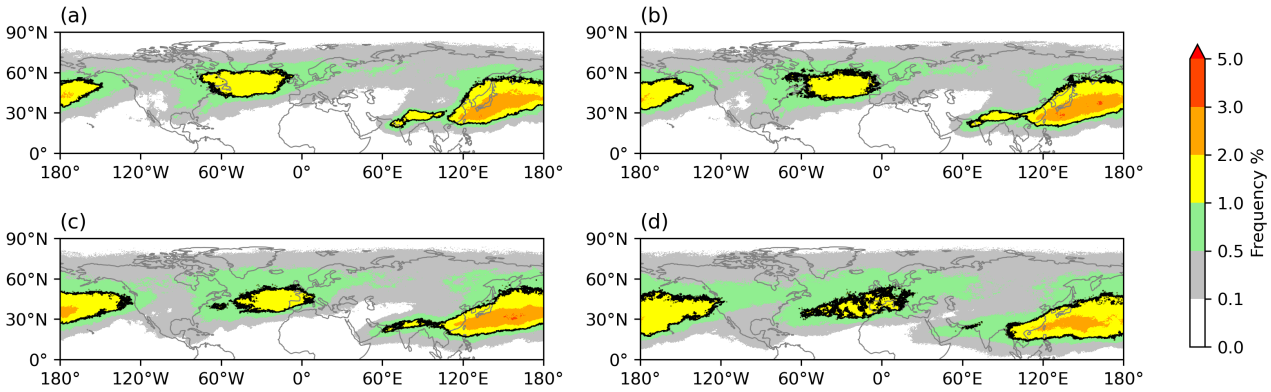

Figure 3.7: Same as Fig. 3.6 but for JJA.

3.3.2 Moisture anomaly in fresh WCB outflow (t = 0 h)

To quantify the impact of WCB transport on atmospheric moisture distribution, we compare climatology of moisture profiles in columns affected by fresh WCB outflow (t = 0 h) to the climatological background as defined in Section 3.2.1. This approach allows us to compare vertical moisture distributions in the geographic area, where WCB outflow occurs (more than 1 % of all times), at times with and without WCB influence.

The vertical position of the fresh WCB outflow points relative to the local dynamical tropopause altitude is shown in Fig. 3.8. Climatologies for the Atlantic and Pacific storm track regions have been separately constructed and are shown by solid and dashed lines, respectively. Seasonal variations are indicated by blue lines for DJF and orange lines for JJA. WCB outflow occurs mainly in the 5 km below the local tropopause and the occurrence frequency peaks at about 1 km below the local dynamical tropopause. During JJA WCB outflow maintains roughly the same altitude relative to the tropopause in the Atlantic as in DJF, but it occurs at lower relative altitude in the Pacific.

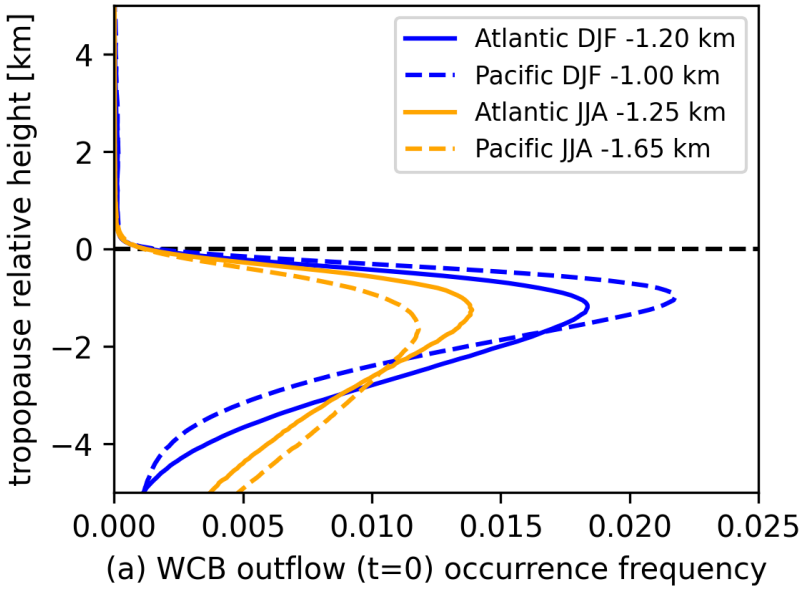

Figure 3.8: Vertical position of WCB outflow points (t = 0 h) during 2010-2019 on the Northern Hemisphere in regions with WCB outflow occurrence frequency larger than 1 %. The y-axis in all panels corresponds to the dynamical tropopause relative altitude.

The vertical structure of shifts in the distribution of moisture, hydrometeor and temperature in WCB outflow at t = 0 h and the background are shown in Fig. 3.9 a-d in a tropopause-relative coordinate system (tropopause relative height z_{rtp}). The vertical distribution of WCB outflow positions is shown in Fig. 3.8. Note these figures contain data in the entire atmospheric columns, in which WCB outflow is found, not only data-points in the WCB outflow. Blue (red) shading indicates more (less) common occurrence of a particular value in WCB outflow columns compared to the background.

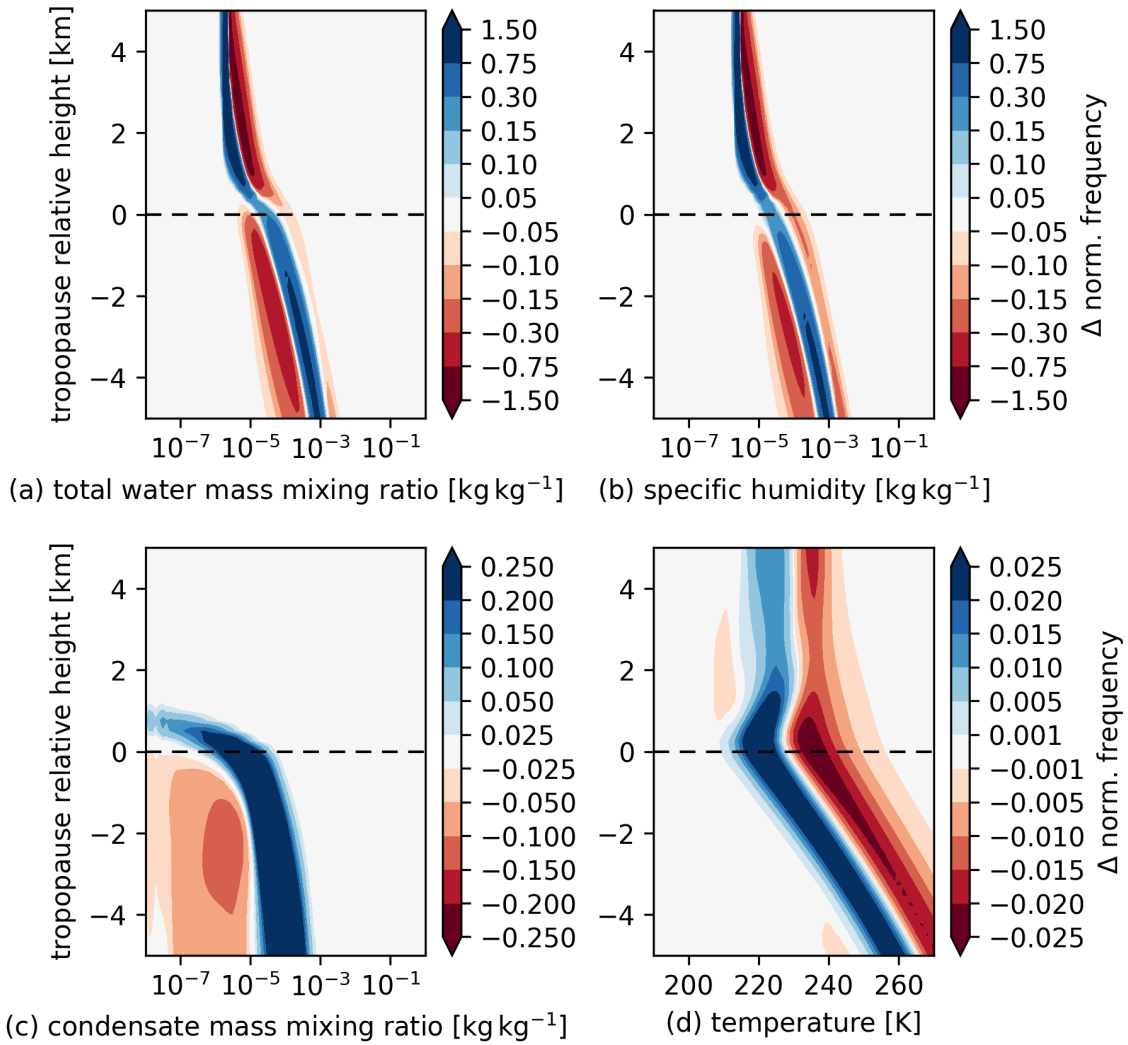

Figure 3.9: Vertical profiles of moisture and temperature anomalies in columns affected by fresh WCB outflow (t = 0 h). The data shown includes all WCB outflow points identified during 2010-2019 DJF on the Northern Hemisphere in regions with WCB outflow occurrence frequency larger than 1 %. As detailed in Section 3.2.1 the background conditions are also defined over this area, but exclude columns influenced by WCB ascent or WCB outflow with age younger than 24 h. In particular the panels (a) to (d) show: (a) total water, (b) specific humidity, (c) condensed water, and (d) temperature. The y-axis in all panels corresponds to the dynamical tropopause relative altitude. The colorbar indicates normalized frequency anomalies, calculated as WCB outflow minus background.

First, we consider the distribution of total water content (Fig. 3.9 a). Below the tropopause larger total moisture values are more commonly found in WCB outflow columns compared to background conditions. More humid conditions extend (at least) to the middle troposphere, i.e. to 5 km below the local tropopause. However, for all considered altitudes in the troposphere, there are some instances where the background is more humid than WCB outflow. More humid conditions are found on average (over $z_{rtp} = -5 - 0$ km) in 5.30 % of the time. This may be associated with air masses influenced by convection or by large-scale ascent in the vicinity of WCBs that does not fulfill the 600 hPa ascent criterion. Above the local tropopause the background air appears to be consistently more humid than WCB outflow columns. This surprising shift in the distribution of total moisture can be explained by an upward shift of the local tropopause above WCB outflow (Fig. 3.12 d). This upward shift is reflected in a substantial shift of the temperature distribution at the dynamical tropopause to colder conditions in outflow columns than found in the background (Fig. 3.9 d). This shift in tropopause altitude and thereby temperature results in consistently smaller temperatures at a particularly tropopause relative height in the background column compared to the WCB columns (Fig. 3.9 d). Particular in the (deeper) stratosphere, where a direct influence of WCB outflow is not expected, it is unlikely that there are systematic deviations in the relative humidity (RH) distribution between WCB-outflow columns and background columns. Note that in the troposphere and maybe lowermost stratosphere (relative altitude $\sim\leq$1 km) systematic shifts in the RH distribution are expected. As water vapour concentrations (at a fixed RH) are exponentially dependent on temperature, the surprising shift in the stratospheric part of the profile is likely due to the strong temperature control on specific humidity and the systematic temperature shift induced by the vertical displacement of the tropopause above WCB-outflow. This hypothesis is corroborated by analyzing the moisture anomalies in pressure instead of the tropopause-relative coordinates in Section 3.3.2.

The total water content anomaly can be divided into contributions from specific humidity and hydrometeor content: Fig. 3.9 b shows the difference in the specific humidity distribution between background and WCB outflow columns. The pattern follows closely that obtained for total water content. However, more humid conditions in the background are more common than for total water (7.7 %). Fig. 3.9 c shows the differences in the condensate content between background and WCB outflow columns. Anomalies are essentially constrained to the troposphere, where a strong increase of condensed water content in WCB outflow columns is found. Above the local tropopause, defined as the lowest 2 pvu isoline in ERA5, there is some small amount of condensate in WCB scenarios, which may be related to the occurrence of tropopause folds. At tropopause-relative altitudes above $\sim$750 m also WCB columns contain virtually no condensate (< 1 mg kg^{-1}). Only the combination of enhanced specific humidity and high condensate content explains the clearly more humid conditions (in terms of total water content)

in WCB outflow, highlighting the importance of condensate carried to upper troposphere.

During JJA cyclone activity and therefore WCB occurrence frequency reduces compared to DJF (Fig. 3.4 - Fig. 3.6), while convective activity typically increases. The enhanced moisture transport by deep convection enhances the background moisture content. Consistently, the shift in total moisture and specific humidity distributions is reduced in the ~ 1 km below the local tropopause(Fig. 3.10 a-b). A shift towards more humid conditions is only found in the middle troposphere (below 1.5 km below local dynamical tropopause), i.e. below the main outflow level of deep convection. In contrast the shift to larger condensate content remains equally large as in DJF and extends up to the local tropopause. This may be a manifestation of the representation of moisture transport and condensate detrainment in the convection parameterization used in ERA5 and should be compared with observational data in future studies.

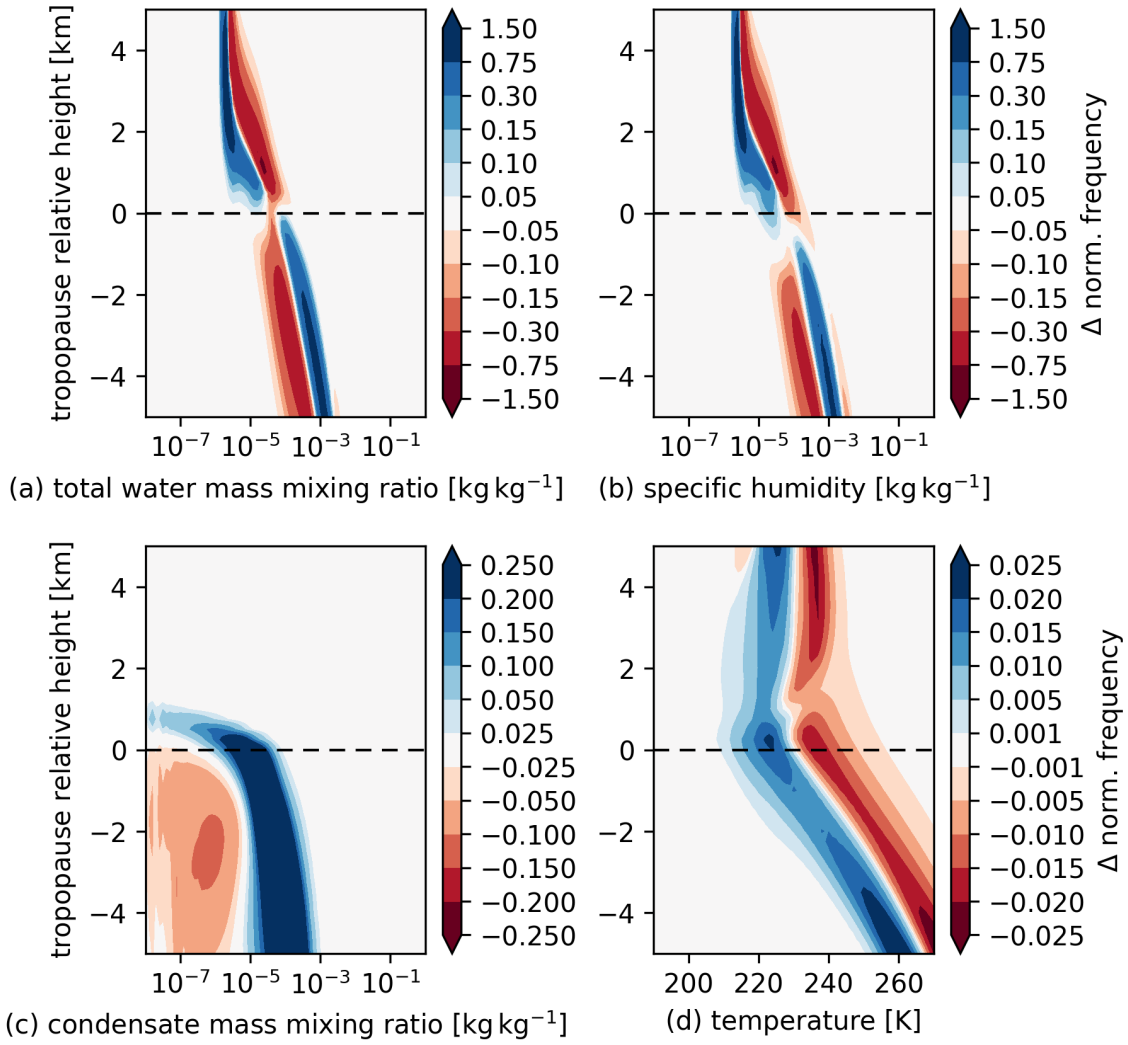

Figure 3.10: Same as Fig. 3.9 but for JJA.

Previous high-resolution modelling studies have found that the moisture transport and the cloud microphysical structure in the WCB outflow depends on the ascent timescale τ_{600} (Schwenk and Miltenberger, 2024), as it impacts the cloud microphysical evolution of WCB parcels (e.g., Oertel et al., 2019, 2023; Schwenk and Miltenberger, 2024). Substantial variations in ascent timescales within a given WCB and across different cases are documented (e.g., Oertel et al., 2019, 2023; Rasp et al., 2016) and are linked to embedded convection. Most convective activity in ERA5 is presented by the convection parameterization and therefore is not accessible by our current trajectory data, which is derived from the grid-resolved velocity field. Despite convective activity not present in our data-set, the distribution of ascent timescales, measures by τ_{600}, shows a large variability (Fig. 3.11 a). The τ_{600} distribution peaks at about 15 h in DJF and about 10 h in JJA. The reduction of τ_{600} in the summer months is most likely due to higher surface temperatures, higher moisture availability, and a less stable atmospheric state. This reduction is consistent with previous analysis of case-studies with high-resolution numerical simulations (e.g., Rasp et al., 2016). In addition to τ_{600}, Fig. 3.11 shows the climatological distribution of WCB ascent timescale τ_{WCB} (as defined in Section 2.4). The difference between τ_{WCB} and τ_{600} is slightly larger for the short timescales and the summer season. This is expected based on results from high-resolution case-study suggesting WCB trajectories with small τ_{600} rising to higher potential temperatures and lower pressure, exceeding the vertical displacement of 600 hPa used for defining τ_{600} (e.g., Oertel et al., 2023). The different ascent timescales influence the cloud microphysical processes, in particular cloud glaciation and precipitation formation, and thereby affect the moisture content in the outflow (e.g., Oertel et al., 2019, 2023; Schwenk and Miltenberger, 2024).

Fig. 3.11 b shows the normalized distribution of pressure differences for τ_{WCB} trajectory segments in DJF (blue) and JJA (orange). Both distributions exhibit a pronounced maximum at $\Delta P \approx 600\,\mathrm{hPa}$, followed by a sharp decrease, indicating that most WCB trajectories terminate their characteristic $8\,\mathrm{hPah}^{-1}$ ascent near this level. A secondary peak appears around 610–620 hPa, where the JJA distribution is slightly lower than DJF. Overall, the close overlap of the two curves indicates that the pressure difference of τ_{WCB} segments is consistent across seasons, and the seasonal dependence of ascent characteristics is weak.

Fig. 3.11 c-d show the distribution of total water and condensed water content at the end of ascent as function of τ_{600}. Trajectories completing a 600 hPa ascent in less than 10 h transport a much larger amount of total water and cloud condensate into the upper troposphere compared to the trajectories rising more slowly. This is consistent with recent results from high-resolution modelling studies (Schwenk and Miltenberger, 2024).

In summary, fresh WCB outflow columns are associated with a negative temperature anomaly

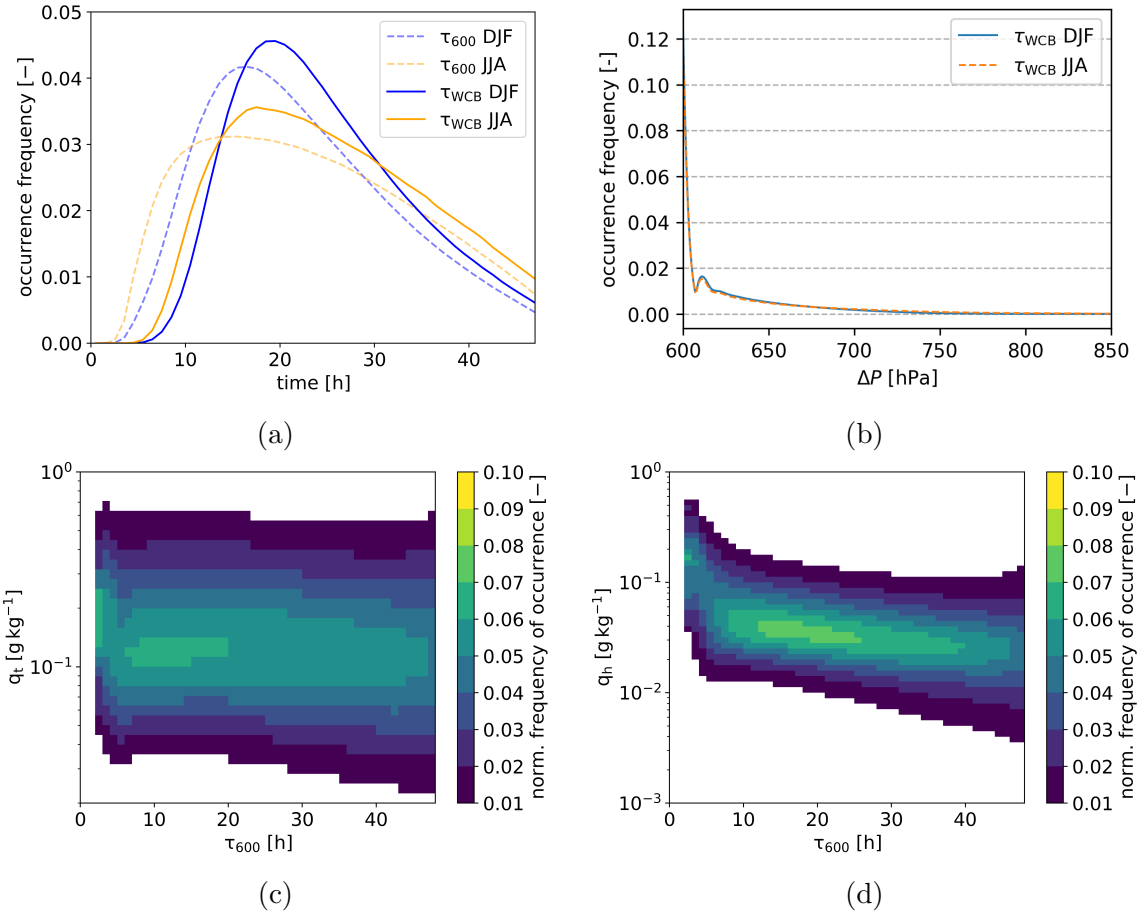

Figure 3.11: Panel (a) shows the climatological distribution of the timescale τ_{600} for the fastest 600 hPa ascent (dashed lines) and the duration τ_{WCB} of the entire WCB ascent (solid lines). Panel (b) displays the distribution of pressure differences within the τ_{WCB} segments of the trajectories. Panels (c) and (d) show the distributions of total moisture content and hydrometeor content, respectively, at the end of the WCB ascent as a function of τ_{600}. Panels (a) and (b) include both Northern Hemisphere winter (DJF, blue) and summer (JJA, orange), while panels (c) and (d) contain DJF data only.

at the dynamical tropopause and largely positive anomalies in total water and condensate content in the upper troposphere. The negative temperature anomaly arises due to a systematic upwards displacement of the dynamical tropopause. The condensate content anomaly is particularly large in quickly ascending WCB trajectories ($\tau_{600} \leq 10$ h).

Moisture anomaly in fresh WCB outflow in pressure coordinates

In pressure coordinates there is no systematic off-set in specific humidity above the local dynamical tropopause (see Fig. 3.9). Moisture anomalies (total water, specific humidity, condensates) appear as clear positive signals centered near 300–350 hPa, consistent with the maximum occurrence frequency of WCB outflow at this level (Fig. 3.12 a). This reflects that the dynamical tropopause over the WCB outflow region is systematically located at lower pressures compared to the background, leading to consistently higher moisture at the same pressure level.

In temperature, a quadrupole structure emerges that reflects a vertical shift of the tropopause and the transition between negative and positive vertical temperature gradients characteristic of the troposphere and stratosphere, respectively. This structure indicates that the tropopause is located near 300 hPa, consistent with Fig. 3.12 a. At WCB outflow points, the dynamical tropopause is mainly found between 150 and 350 hPa, with a peak near 200–250 hPa, whereas in the background it spans a broader range and can extend down to 400 hPa (Fig. 3.12 d), a level not occupied by fresh WCB outflow. Thus, in WCB outflow regions the tropopause is systematically higher, so that air parcels at a given pressure above 300 hPa are colder than in the climatological background, producing the observed anomaly pattern.

Interestingly, the moisture and temperature patterns are consistent across the two vertical coordinate systems when comparing Fig. 3.9 and Fig. 3.12. In pressure space, temperature anomalies resemble moisture anomalies in tropopause-relative space, as both highlight the upward transport of moist air below the dynamical tropopause. Conversely, moisture anomalies in pressure space align with temperature anomalies in tropopause-relative space, as both emphasize the displaced reference frame of the tropopause, which makes the outflow appear moister at fixed pressure but colder at a fixed distance from the tropopause.

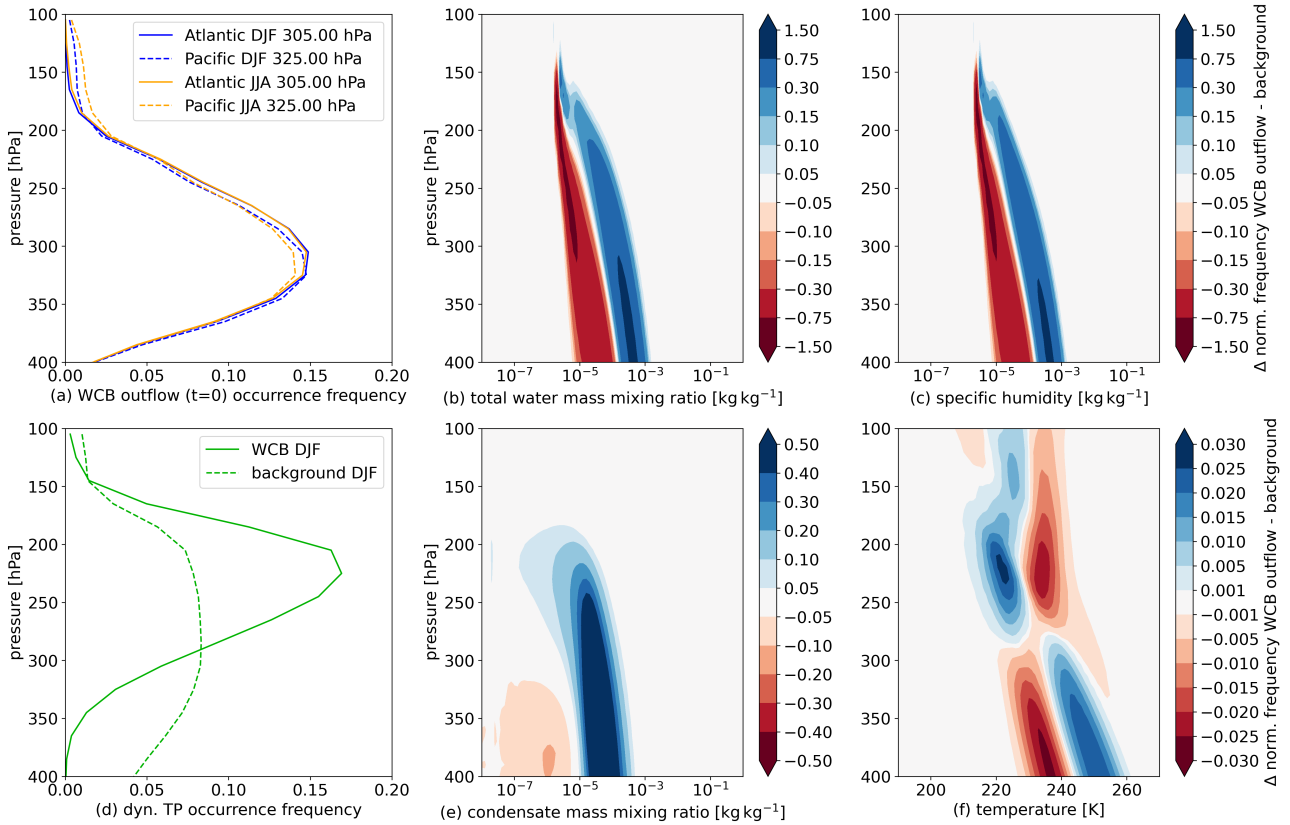

Figure 3.12: (a) Pressure of WCB outflow trajectories (t = 0 h), (d) distribution of the pressure at the dynamical tropopause (PV = 2 pvu), as well as (b,c,e,f) moisture and temperature anomalies in the columns affected by fresh WCB outflow (t = 0 h). The data shown includes all WCB outflow points identified during 2010-2019 DJF on the Northern Hemisphere in regions with WCB outflow occurrence frequency larger than 1 %. As detailed in Section 3.2.1 the background conditions are also defined over this area, but exclude columns influenced by WCB ascent or WCB outflow with age younger than 24 h. In particular the panels (b, c, e, f) show: (b) total water, (c) specific humidity, (e) condensed water, and (f) temperature. The y-axis in all panels corresponds (in contrast to Fig. 3.9) to the pressure.

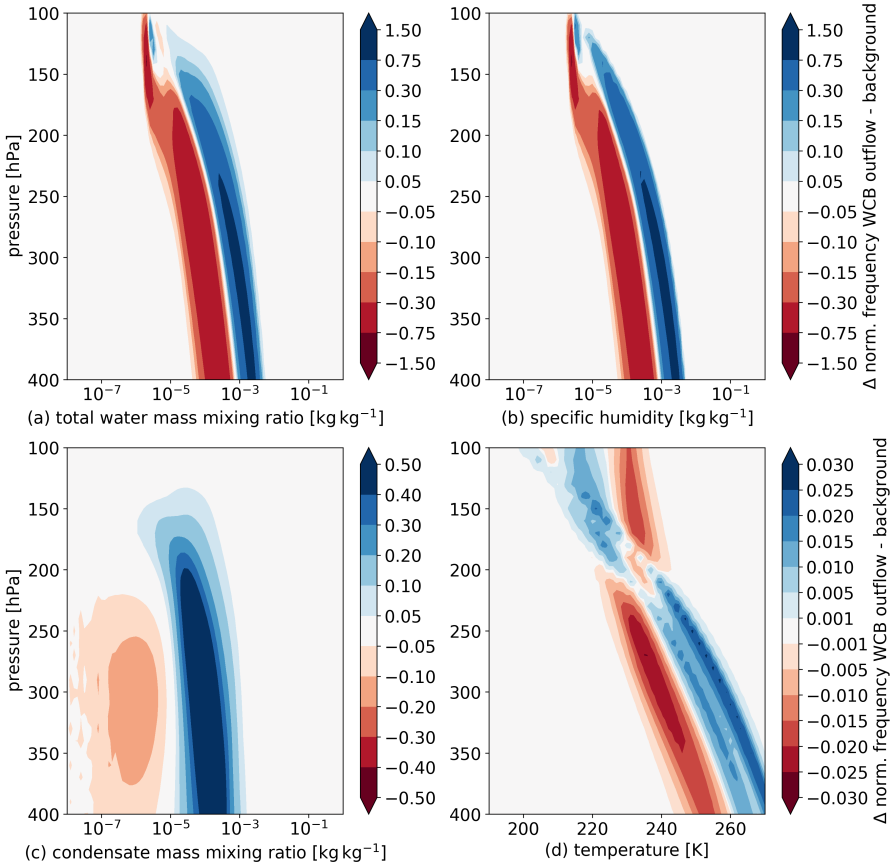

Figure 3.13: Same as Fig. 3.12 but for JJA.

3.4 Evolution of WCB outflow properties after end of ascent (t=[0-48] h)

The impact of the moisture anomaly introduced by WCB outflow in the UTLS depends significantly on its lifetime and geographic position at times after the end of the WCB ascent. To investigate the fate of WCB outflow after the end of ascent, we follow WCB outflow parcels for 48 h after completing τ_{WCB} ascent (Section 2.4).In addition to considering the evolution of thermodynamic and moisture variables along actual WCB outflow trajectories, we also consider the evolution that would arise along the WCB outflow trajectory path in background conditions, i.e. along the same longitude, latitude, tropopause-relative altitude (or pressure) path but monthly-averaged temperature and moisture fields as described in Section 3.2.1.

For full understanding the impact of WCB outflow on the UTLS, not only the properties of fresh WCB outflow are of interested but also their temporal evolution in the subsequently. First we consider the temporal evolution of the vertical (tropopause-relative) position of WCB outflow in the 48 h after end of ascent (Fig. 3.14 a), as this provides essential context for understanding the altitude of WCB induced anomalies as well as the temperature evolution and its impact on condensate content. Consistent with the southeasterly propagation, most WCB trajectories move away from the local tropopause over the 48 h after end of ascent. On average they are located about 3 km below the local tropopause after 48 h. About 10 % of the the trajectories undergo a very strong descent (for 5 % of the descent is consistent with a dry intrusion descent according to the criteria established by Raveh-Rubin (2017), not shown). Also a small fraction of trajectories continues to rise over the 48 h after end of ascent and about 5 % of trajectories are found above the local tropopause at t = 48 h.

The red lines show the tropopause relative altitude that the air parcels would have at the given location and pressure in background atmospheric conditions as defined in section. 3.2.1. At times less than about 12 h, outflow trajectories are located near the background dynamical tropopause, whereas in actual conditions they are located on average about 1.5 km below the local dynamical tropopause. This further corroborates the large vertical displacement of the tropopause above WCB outflow. After about 30 h the difference between the tropopause-relative position in actual and background atmospheric state diminishes indicating that parcels have moved away from the region with an upward shifted tropopause. Interestingly, the difference remains larger for parcels located close to the local tropopause (Fig. 3.15 a) suggesting that these parcels remain in the ridge dominated part of the flow.

Due to the systematic displacement of the dynamical tropopause in the WCB outflow region

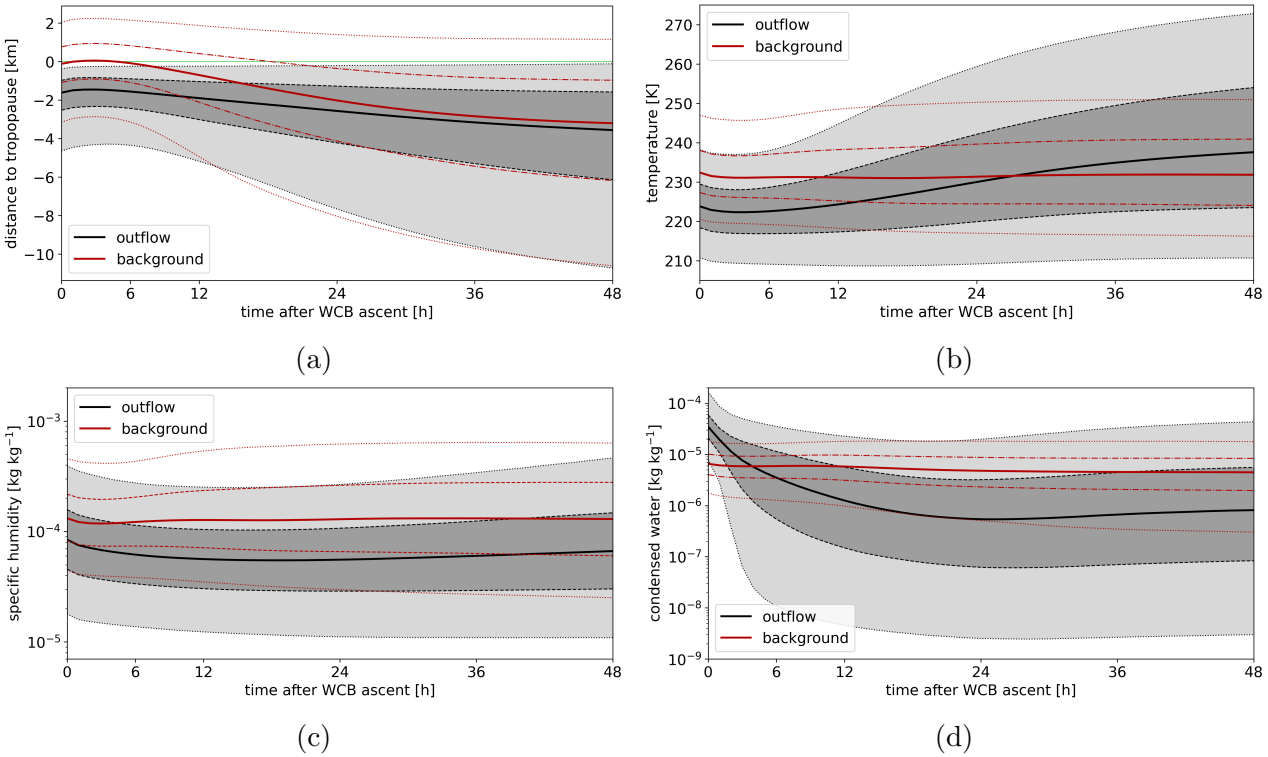

Figure 3.14: Time evolution of outflow properties over the first 48 h after end of WCB ascent for DJF from 2010 to 2019. The four panels show (a) distance to the tropopause, (b) temperature, (c) specific humidity, and (d) condensed water. Grey shading and black lines represent the evolution along outflow trajectories. The red lines represent the evolution of the monthly averaged background conditions along the outflow trajectories (according to their tropopause-relative altitude and geo-location). The solid lines represent the median, dash-dotted lines the 25$^{\text{th}}$ and 75$^{\text{th}}$ percentiles, and dotted lines the 5$^{\text{th}}$ and 95$^{\text{th}}$ percentiles.

and the strong cross-tropopause temperature and humidity gradients, the analysis of temperature and moisture evolution is performed in a tropopause-relative altitude coordinate in this subsection.

The evolution of air temperature along the WCB outflow trajectories is shown in Fig. 3.14 b: It shows a strong warming of the trajectories starting at about t = 6 h with an average warming of 14 K over the considered 48 h. This is consistent with dry adiabatic descent of about 1.6 km, i.e. comparable to the descent shown in Fig. 3.14 a. In addition, the climatological background temperature at the WCB trajectory position is shown by the red lines in Fig. 3.14 b. Initially, the WCB outflow trajectories are on average about 10 K colder than in background conditions consistent with analysis in Fig. 3.9d. The temperature difference between WCB outflow and background is consistent with the vertical displacement of the tropopause. The temperature in the background remains almost constant during the considered 48 h.

The evolution of condensed water content is shown in Fig. 3.14 d: The condensate content in fresh WCB outflow is enhanced by almost a factor 10 compared to background conditions (consistent with analysis in Section 3.3.2). The positive anomaly persists for approximately 6 h, after which the background contains more condensate than WCB. This change of sign in the anomaly is mainly due to rapid decrease of condensate content in the WCB outflow airmass likely due to ice crystal sedimentation and sublimation descending air.

The evolution of specific humidity is shown in Fig. 3.14 c: Fresh WCB outflow trajectories have a lower specific humidity compared to the same tropopause-relative position in the background. This anomaly increases slightly in the first 12 h after end of ascent and later diminishes slight. Reduced specific humidity is somewhat in contrast to results in Section 3.3.2, which is mainly due to the different geographic area considered there: While only regions affected by fresh WCB outflow are considered in Section 3.3.2, the analysis here includes regions affected by WCB outflow of any age ($\leq$ 48 h). The analysis here in particular includes more south-easterly profiles in the Mediterranean region that have likely larger UT humidity. For radiative considerations the tropopause-relative altitude may be of less importance than anomalies at the same pressure level. Therefore we also evaluate background specific humidity at WCB outflow parcel pressure positions in the following subsection.

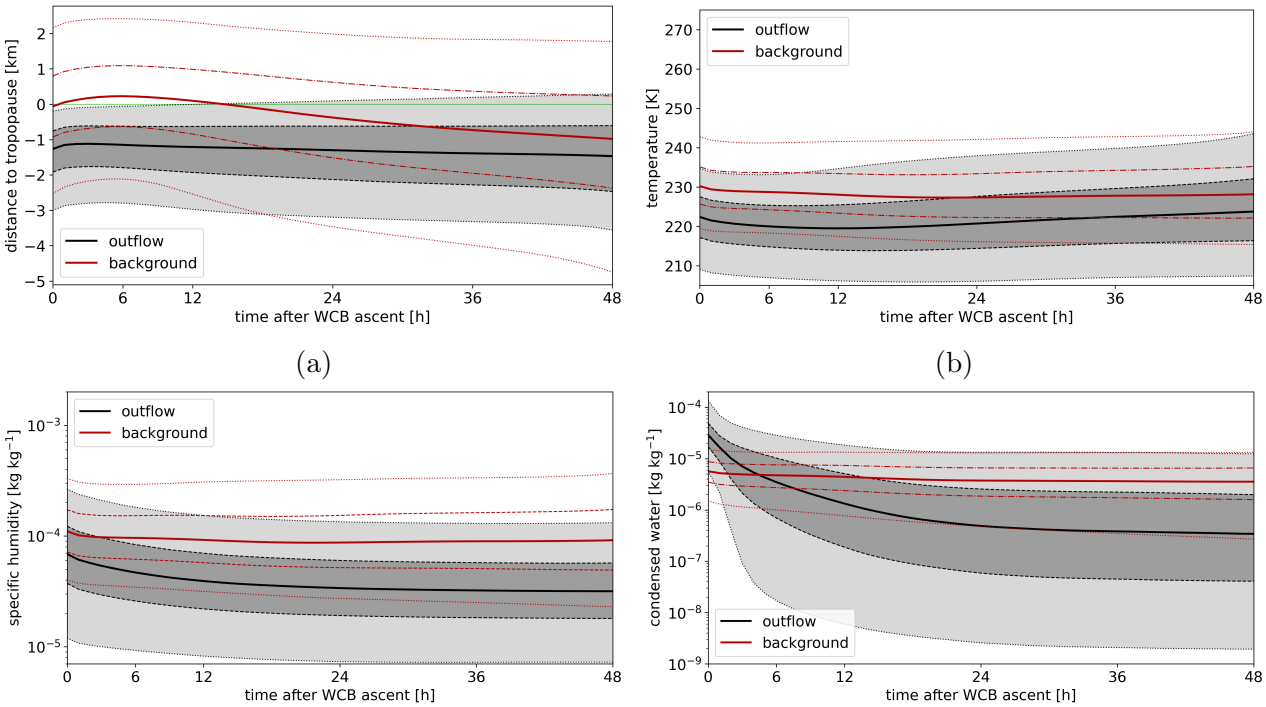

Figure 3.15: Same as Fig. 3.14, but only for trajectories staying within 4 km of the local tropopause over the considered 48 h period.

One particular interest of this study is the impact of WCB outflow on the UTLS. Therefore, we additionally discuss the evolution of air parcels that remain within 4 km of the tropopause throughout the entire 48 hour period after end of ascent. This sub-set of WCB outflow parcels remains at an almost constant altitude of approximately 1 to 1.5 km beneath the local tropopause (Fig. 3.15 a). The background shows an increasing distance to the local tropopause consistent with the trajectories moving away from the area with a large vertical displacement of the tropopause above fresh WCB outflow. The temperature of WCB outflow parcels decreases in the first 9 h, but afterwards slightly increases. The evolution of specific humidity and condensate mass mixing ratio is similar to that observed for all WCB outflow trajectories. If considering the evolution at fixed pressure instead of fixed tropopause-relative altitude, enhanced specific humidity and condensate content is maintained longer in this subset of trajectories (20 h and 12 h, respectively) compared to all WCB outflow trajectories.

In summary, WCB outflow is associated with large negative temperature anomalies and large positive condensate anomalies at about 1.5 km below the local tropopause. The WCB outflow trajectories descent on average by about 2 km in the following 48 h. The negative temperature anomaly persists for about 24 h, while the positive condensate anomaly is maintained for only 6 h. In tropopause-relative coordinates, WCB outflow is associated with a negative specific humidity anomaly throughout the considered lifetime, which is likely related to the colder temperatures and deeper ascent in the WCB outflow region. However, in pressure coordinates, WCB outflow is associated with a positive specific humidity anomaly that has a Lagrangian lifetime of about 20 h.

We additionally examine the post ascent evolution of WCB outflow properties in pressure coordinates in Appendix A.1.2. This complementary analysis is included to assess how WCB outflow influences UTLS moisture on fixed pressure levels, providing context beyond the tropopause relative framework used in the main sections.

3.5 Impact of WCBs on the water content of the UTLS

3.5.1 Mass and water flux into the UTLS

So far we have quantified the anomalies of water vapour and condensate mass mixing ratios associated with WCB outflow. To quantify the impact of these anomalies on the total water content of the UTLS, we proceed to quantify the flux of water mass to the UTLS that is associated to the WCB ascent with the Lagrangian metrics introduced in Section 3.2.3. The

climatological mass flux of dry air from the troposphere into the UTLS is shown in Fig. 3.16 a. Pronounced local maxima are found in the region of the Atlantic and Pacific storm track, the subtropical jet in the Atlantic and Pacific, the Pamir mountains, downstream of Greenland and along the west coast of Canada / Alaska. Secondary maxima are found over eastern Mediterranean as well as across the Tibetan Plateau and in southern China.

The geographical distribution of total water flux into the UTLS is shown in Fig. 3.16 b, where the relative contributions of water vapour and condensate to the total water flux are shown in Fig. 3.16 c and d, respectively. The spatial distribution of the total water flux closely mirrors that of the mass flux, though notable differences include a strong relative reduction of the amplitude of all regional maxima with the exception of those in the Atlantic and Pacific storm track regions and missing local maxima along the subtropical jet. With the exception of the Maritime continent and the adjacent region in the Pacific, the water vapour flux accounts for more than 60 % of the total water flux. We hypothesize that the water transport into the UTLS in this region is likely dominated by large-scale organized convection, which efficiently transports condensate to very cold temperatures. Secondary local minima in the contribution of water vapour flux to the total water flux are found in the Atlantic and Pacific storm track regions, over the Eastern Mediterranean and over the Tibetan plateau (Fig. 3.16 c).

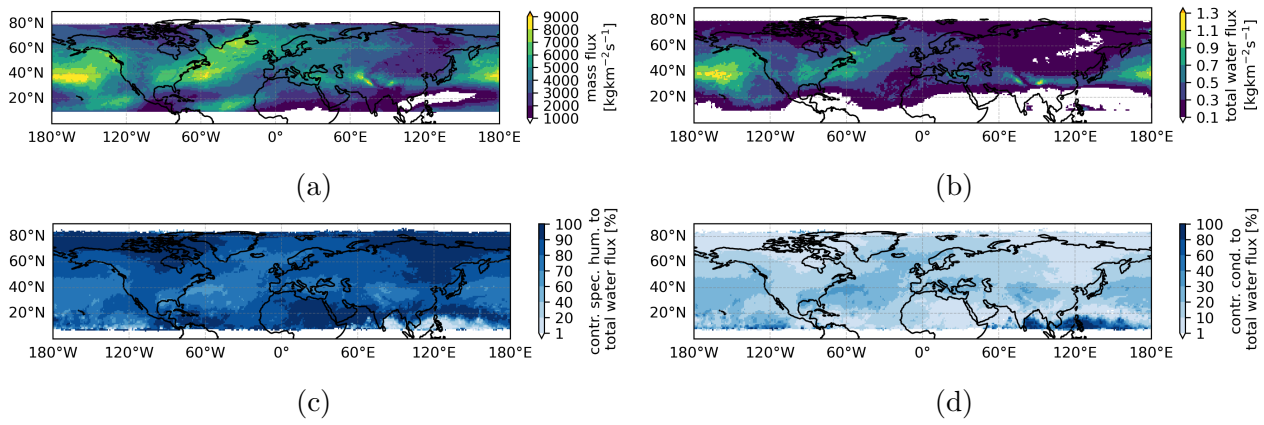

Figure 3.16: Mass flux and water flux into the UTLS from 2010 to 2019 during DJF. Trajectories enter the lower UTLS edge from below. Panel (a) shows the dry air mass flux into the UTLS, (b) illustrates the total water flux. Panel (c) shows the relative contribution of water vapour flux to the total water flux; panel (d) the relative contribution of condensate flux to the total water flux.

3.5.2 Mass and water flux from WCB

We now quantify the contribution of WCB outflow trajectories to the total water flux into the UTLS by considering only trajectories which fulfill the WCB selection criteria for the flux com-

putation (for details see Section 3.2.3). The WCB mass flux is shown in Fig. 3.17 a: The peak values are about 10 % of the maximum total mass flux values. The spatial pattern aligns well with the spatial distribution of WCB outflow as discussed Section 3.3. Notably, the primary maxima occur over the Pacific and northwest Atlantic storm tracks between 40°N and 60°N. The distribution of WCB total water flux resembles that of the WCB mass flux (Fig. 3.17 b). Interestingly the WCB total water flux is less over the North Atlantic compared to the North Pacific although the mass flux is comparable. Albeit this warrants closer investigation in future work, we hypothesize that this is related to the closer proximity of WCB outflow to the local tropopause in the Pacific compared to the Atlantic (Fig. 3.8, see discussion in Section 3.3.2).

The relative contribution of condensate and water vapour to the WCB total water flux is shown in Fig. 3.17 c and d, respectively. The water vapour flux dominates with accounting for more than 60 % of the WCB total water flux. However, the relative contribution of condensate is largest in the south of the storm track maximum in its beginning part, i.e. the western part of the ocean basins. Here, condensate contributes up to 40 % while further north and east the contribution decreases to about 10-20 %.

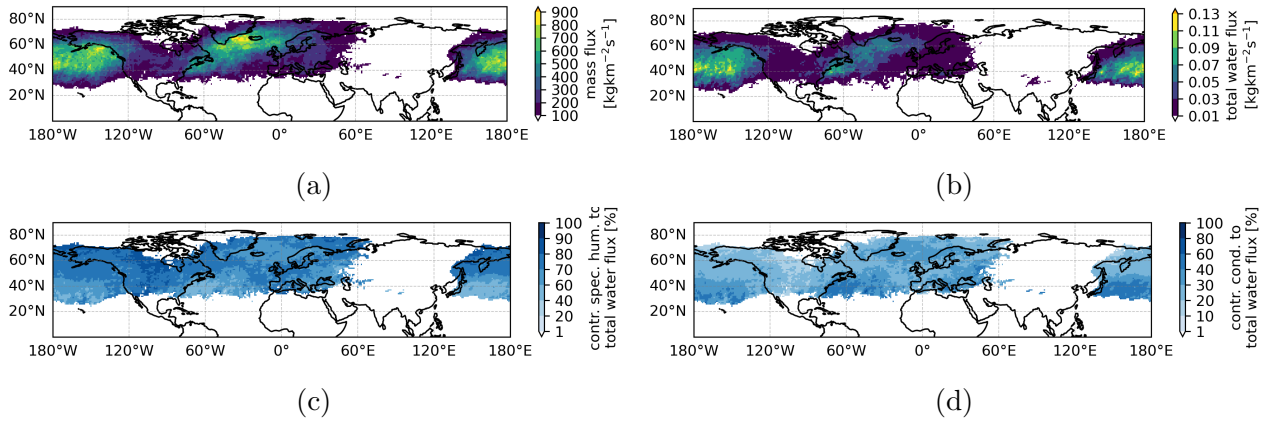

Figure 3.17: Relative contribution of WCB outflow to the total mass flux (a), total water flux (b), water vapour flux (c), and condensate flux (d) into the UTLS from 2010 to 2019 during DJF.

Finally, we quantify the relative contribution of WCBs to the dry air mass, total water, water vapour, and condensate fluxes into the UTLS. These are shown in Fig. 3.18. Unsurprisingly the largest contributions are found in the regions affected by WCB outflow. WCBs contribute up to 12.8 % of the air mass flux and an equal contribution of 13.8 % to the total water flux. The contribution over the Pacific is somewhat larger than to the fluxes into the UTLS over the Atlantic. WCBs contribute up to 11.7 % to the water vapour flux and up to 23.3% to the condensate flux into the UTLS. Averaged over the areas with non-zero WCB contribution, WCB outflow contributes 3.71 % of the total mass flux, 3.78 % of the total water flux, 3.28 %

of the water vapour flux, and 6.33 % of the condensate flux.

The analysis indicates that moisture, in particular condensate, fluxes are enhanced compared to the WCB contribution in mass flux. The enhancement is strongest for the condensate flux with an average (peak) enhancement by a factor 2.0 (16.5). This is consistent with the large positive condensate anomaly found in fresh and slightly aged (t≤6 h) WCB outflow (see Section 3.3.2 and 3.4). For total moisture flux the enhancement reduces to a factor 1.2 (8.2) in the average (peak), while the specific humidity flux is only slightly enhanced compared to the WCB mass flux (factor 1.1 and 7.7 in mean and average, respectively). In particular the on average small enhancement in specific humidity flux is consistent with the small or even negative specific humidity anomaly in fresh and slightly aged WCB outflow (see Section 3.3.2 and 3.4). The small anomalies likely arise because of the colder WCB outflow temperatures compared to background locations at a similar distance to the local tropopause. This temperature difference appears to dominate over anticipated systematic differences in relative humidity (WCB air close to saturation, on average sub-saturated conditions in the background). The latter hypothesis is consistent with results from a high-resolution WCB case study presented in Schwenk and Miltenberger (2024).

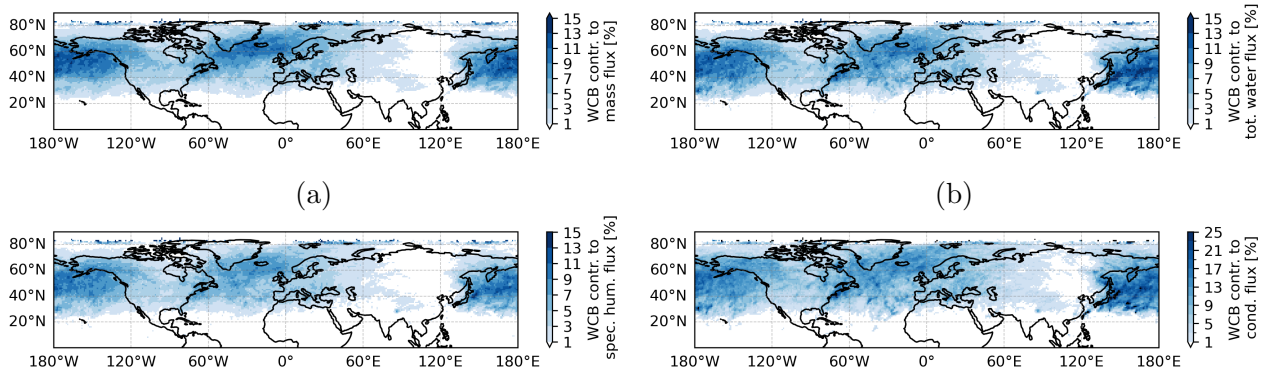

Figure 3.18: Percentage of WCB trajectories relative to total trajectories from 2010 to 2019 DJF. Panels (a) and (b) depict the percentage of WCB mass and water flux compared to the total mass and water flux, respectively. Panel (c) shows the relative contribution of WCB water vapour flux to the WCB total water flux; panel (d) the relative contribution of WCB condensate flux to the WCB total water flux.

3.6 Key findings and discussions

In this chapter, we present a 10-year climatology of Warm Conveyor Belt (WCB) outflow, its properties, and its impact on the Upper Troposphere and Lower Stratosphere (UTLS) moisture content, primarily during the winter season (DJF) based on the ERA5 reanalysis data-set. WCB ascent and outflow are identified with a Lagrangian approach, where WCB air parcels are required to ascend at least 600 hPa within 48 h near an extratropical cyclone. To take into account the evolution of WCB outflow airmasses after the end of ascent, we explore not only the moisture anomaly in fresh WCB outflow (at t = 0 h), but also the evolution of the moisture content and tropopause relative position of aged WCB outflow air for up to 48 h after the end of ascent. The main findings of this chapter on WCB outflow properties and their impact on UTLS moisture can be summarized as follows:

1. Consistent with earlier research, a high occurrence frequency of WCB outflow in the Pacific and Atlantic storm track regions is found for DJF with reduced frequency in the summer season. The outflow positions are typically found about 1 - 1.5 km below the local tropopause.

2. Over the following 48 h, the WCB outflow generally moves in a southeastwards towards the subtropics and descends again to the mid-troposphere. 15.3 % of the outflow trajectories remain within 2 km of the local tropopause, with about 5 % of all trajectories passing into the stratosphere within the first 48 h after end of ascent.

3. Despite very efficient moisture removal during WCB ascent, WCB outflow still introduces positive anomalies in total moisture content, specific humidity, and condensate content, alongside a negative temperature anomaly, which is limited mainly to the upper troposphere. Even in ERA5 with parameterized convection fast ascending trajectories requiring less than about 10 h are found to contribute the largest total water content values, which is consistent with convection-permitting case-studies (Schwenk and Miltenberger, 2024). The negative temperature anomaly of WCB outflow air is due to an upward displacement of the tropopause.

4. Positive anomalies in condensate content persist for approximately 6 h in the uppermost troposphere. In tropopause-relative coordinates WCB outflow is associated with a weak negative specific humidity anomaly, which persist up to 48 h after end of WCB ascent. In contrast, in pressure-relative coordinates WCB outflow is associated with a large positive specific humidity anomaly, which persists for up 12 h. The specific humidity signal arise most likely to the large vertical displacement of the local tropopause above WCB outflow and the associated large negative temperature anomaly at the tropopause and the WCB outflow. After the end of WCB ascent, the majority of WCB parcels descent

over a timescale of 24-48 h to the mid-troposphere, while about 5 % of all WCB outflow trajectories cross the local dynamical tropopause.

5. Lagrangian estimates of water fluxes into the UTLS and the contribution of WCB outflow to the total flux underscores the substantial contribution of WCB trajectories to UTLS moisture content. Considering all the trajectories entering the UTLS, only ≈4 % of them are identified as WCBs, but WCBs directly account for up to 13.8 % (mean: 3.71 %) of the total water flux into the UTLS and up to 23.3 % (mean: 6.33 %) of the condensate flux. Notably, the WCB-associated condensed water flux is predominantly found south of the storm track in the western part of the Atlantic and Pacfic ocean basins. Note that fluxes are limited mostly to the upper troposphere with few WCB outflow trajectories crossing into the lower stratosphere.

Despite elucidating and quantifying some key aspect of the role of WCBs for extratropical UTLS moisture content, there are a few limitations to the study that need to be discussed here. ERA5 has known issues in its representation of UTLS moisture content (e.g., Krüger et al., 2022), which will impact some of the results in our analysis in particular the moisture anomalies in columns with fresh WCB outflow (Section 3.3.2). However, Krüger et al. (2022) found the largest moisture biases in the 1-2 km above the thermal tropopause, particularly in mixed air masses and during summer, i.e. outside the region directly influenced by WCB outflow. We therefore expect no major impact of the reported biases on our analysis, where we focus directly on WCB outflow. However, the identified signals should be verified with the (limited) observational data available in a future study.

Another issue with the data and methodology used is the representation of convection. While earlier convection-permitting simulations of individual cases have highlighted the role of embedded convection and fast ascent for microphysical and dynamical aspects of WCB ascent (e.g., Oertel et al., 2023) as well as the associated moisture transport (Schwenk and Miltenberger, 2024), convection is parameterized in ERA5. Furthermore, the airmass trajectories used in this study are based on the resolved wind-field meaning that they do experience additional ascent in regions with parameterized convection. However, as far as it is represented by the underlying convection representation, the input of condensate and water vapour into the UTLS will be seen along the trajectories as increase in the trajectories water content. As we focus on the winter season where convection is limited, we nonetheless expect the key conclusions of the paper to be qualitatively robust.

In addition, the used criteria for identifying WCB ascent, albeit shared with many previous studies on WCB, focus on the most strongly ascending airstream and might miss less strong ascending parcels in the vicinity of the core WCB ascent or vertically displaced airmasses above

the WCB that despite not being identified as WCB might contribute to the WCB associated water transport into the UTLS. We therefore view the WCB mass and water flux into the UTLS as lower boundaries of the actual contribution. Finally, while the choice of trajectory starting points and choices in the flux estimation (e.g. definition of lower edge of UTLS layer, length of original trajectory segment for identifying trajectories passing into the UTLS, residence time in the UTLS) may affect the absolute values, sensitivity tests (shown in Appendix. A.1.1) indicate that these factors have only a minor impact on the overall qualitative conclusions. In light of these limitations and the known bias in ERA5 UTLS moisture, subsequent chapters therefore investigate how variability in WCB inflow conditions influences the diagnosed outflow properties and assess the robustness of the key quantitative conclusions using high-resolution modelling studies.

4 WCB Inflow Variability and Its Link to Outflow Moisture Properties

4.1 Introduction

Chapter 3 quantified the climatological influence of warm conveyor belts (WCBs) on upper troposphere and lower stratosphere (UTLS) moisture using ERA5 reanalysis data. The analysis revealed that WCBs generate pronounced positive moisture anomalies in the upper troposphere and contribute substantially to the total moisture flux into the UTLS. These results establish WCBs as a key component of the large-scale UTLS moisture budget and highlight the importance of their outflow characteristics from a climatological perspective.

While this climatological analysis provides a robust assessment of the mean contribution of WCBs to UTLS moisture, it does not address how variability in WCB inflow conditions modulates the resulting outflow moisture properties. In particular, WCBs originate from a wide range of inflow environments that differ in moisture availability, thermodynamic conditions, and large-scale flow characteristics. How this inflow variability influence the outflow moisture signal remains insufficiently quantified. Understanding this relationship is essential for interpreting the spread in WCB outflow moisture signals identified in Chapter 3.

Motivated by this knowledge gap, the present chapter focuses on the characterization of WCB inflow variability and its statistical linkage to outflow moisture properties. Specifically, this chapter develops and validates comprehensive framework to identify inflow tracks, and select representative WCB cases in order to address the research question proposed in Section 1.5: *How does variability in the WCB inflow environment influence the moisture transport into the UTLS?*

To this end, WCB inflow tracks are objectively identified and analysed with respect to their geometric pathways and initial thermodynamic conditions. This framework further provides an objective basis for selecting a limited number of meteorologically diverse yet climatologically representative WCB cases, which form the foundation for the targeted simulations presented

in the subsequent chapters.

4.2 Method

4.2.1 WCB inflow track construction

Inflow object definition

In this section, we describe in detail the methodology used to define and track the inflow region of WCBs. The approach is based on the Eulerian WCB mask framework introduced by Heitmann et al. (2024), in which the WCB inflow region is defined as a two-dimensional Eulerian mask constructed from the positions of WCB trajectories residing at pressures above 800 hPa, providing a phase-based, climatological representation of low-level WCB air masses. The present study adapts this concept to focus explicitly on inflow properties and their relationship to subsequent moisture transport into the UTLS. To this end, only the inflow point marking the start of ascent is retained for each WCB trajectory, and these inflow points are tracked forward in time to reconstruct the full life cycle of individual WCB cases. As outlined in Section 2.4, we define the ascent segment and ascent time scale of each WCB, as the portion of the trajectory where the parcel's vertical ascent rate exceeds 8hPa h^{-1}. In previous analysis, the final point of this ascent segment was used to characterize the WCB outflow. In contrast, the present section focuses on the WCB inflow here, defined as the first point of the τ_{WCB} segment.

To construct continuous and spatially representative Eulerian WCB inflow masks, each inflow point is inflated to a circle with a 100 km radius, as also done by Heitmann et al. (2024). Without this inflation, the masks would consist of mostly isolated points, leading to discontinuous patterns of the inflow objects. The inflation helps to avoid artificial gaps particularly in regions where only a few inflow points are detected. By spatially extending each inflow point, the resulting two-dimensional masks more realistically capture the footprint of WCB inflows. To capture the temporal variability of inflow occurrence, inflow points are sampled at an hourly resolution.

Figure 4.1 shows identified WCB inflow objects on 1 February 2010 at 05:00 UTC, with each object displayed in a different color. Each inflow object represents a cluster of inflow points that have been inflated with a 100 km radius and are spatially and temporally close, likely belonging to the same WCB object. The location of each inflow object is defined by the centroid latitude and longitude. To avoid artificial discontinuities in the inflow objects over the Pacific Ocean, the longitude is shifted to center at 60°E. This choice has only a negligible impact on WCB inflow tracks entering North America from the Pacific, as inflow occurrence in this region is

predominantly confined to the ocean and rarely originates over the North American continent (see Fig. 3.4a).

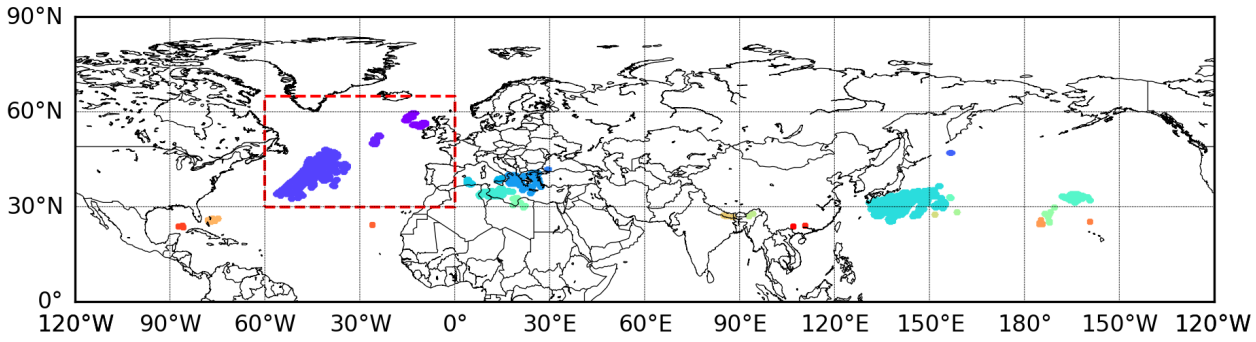

Figure 4.1: Example of WCB inflow objects on 1 February 2010 at 05:00 UTC. Each inflow object, identified as described in Section 4.2.1, is shown in a different color. The red dashed line indicates the region used for visualizing the tracking algorithm in Section 4.2.1.

As an initial characterization of these inflow objects, Figure 4.2 presents a histogram of their spatial extent, quantified by the number of grid points contained within each detected inflow object for boreal winter (DJF) of the year 2010. The histogram demonstrates a clear peak in the bin ranging from 50 to 100 grid points, indicating that most inflow objects fall within this spatial scale, corresponding to areas of order 10^4–$10^5\,\mathrm{km}^2$ at ERA5 resolution. Based on this distribution, objects with fewer than 50 grid points are discarded from subsequent analysis, which excludes approximately 13% of all detected inflow objects and primarily removes very small structures that are likely to correspond to minor features separating from the developing main inflow object rather than constituting new independent inflow regions.

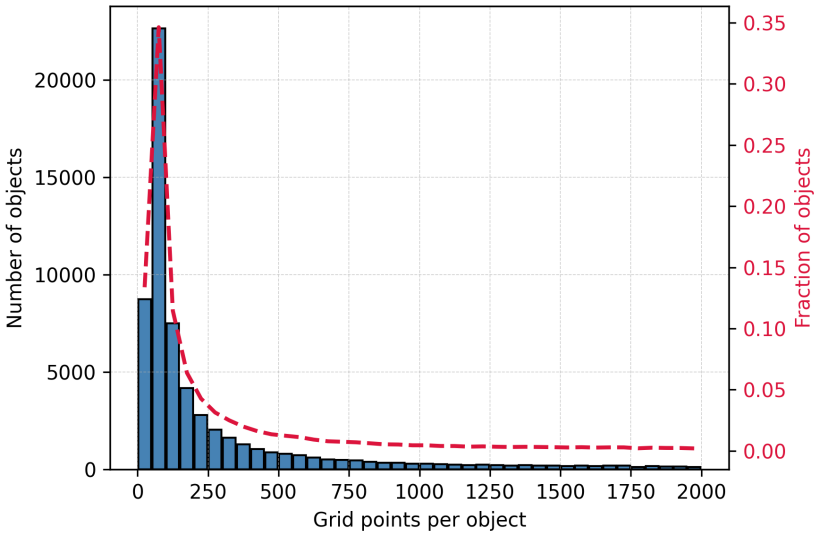

Figure 4.2: Histogram showing the distribution of the spatial extent of inflow objects identified during DJF 2010, summed by the number of grid points contained within each object. Blue bars represent the raw object counts per bin, and the red dashed line indicates the corresponding fraction of the total number of identified objects.

Tracking algorithm

After identifying the inflow objects, we developed a tracking algorithm to follow the propagation of these structures in time, which we refer to as *inflow tracks*. For the selected objects, we track their motion using an overlap-based tracking function defined as follows:

$$\text{Overlap} = \frac{\text{Number of pixels in the intersection}}{\text{Number of pixels in the union}} \tag{4.1}$$

Here, the intersection and union are computed between inflow objects identified at two consecutive time steps. The overlap is evaluated in grid-point space, with all grid points weighted equally and no explicit latitudinal weighting applied, as the metric is designed to ensure object continuity rather than represent physical area. Figure 4.3 illustrates the fundamental concept of this overlapping method. The blue contour represents an object identified at time $t = 0$, while the green contour corresponds to the same object at the subsequent time step $t = 1$. The union is the area enclosed by both contours (blue and green), and their intersection is highlighted in red, indicating the region where they overlap. Through this computation, we can continuously track the evolution of large, coherent inflow objects over time. If an object in the subsequent time step does not sufficiently overlap with any existing object from the current time step, it is classified as a new object and initiates a new tracking sequence from that point onward. To assess the sensitivity of the response to this threshold, we tested overlap ratios ranging from 0.1 to 0.6, as shown in Appendix Fig. A.10). An overlap threshold of 0.3 was ultimately selected,

as sensitivity tests indicate that this value yields the largest number of consistently tracked inflow objects while preserving the expected spatial coherence of inflow track evolution.

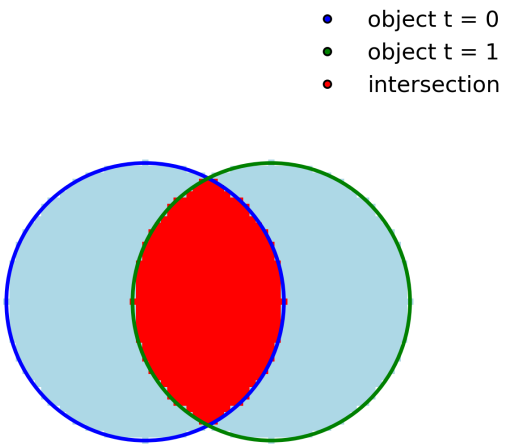

Figure 4.3: Conceptual visualization of the overlap-based tracking method, showing the object contours at two consecutive time steps (blue contour at $t = 0$, green contour at $t = 1$) and their intersection region (red).

A real-case application of this tracking procedure is presented in Figure 4.4. In this example, inflow objects identified at 05:00 UTC on 01 February 2010 are shown in red. The blue contours represent the positions of the objects one hour later,i.e. at 06:00 UTC. Their position at 07:00 UTC is outlined in cyan, and that at 08:00 UTC is indicated by yellow contours. This sequence demonstrates how the overlap-based tracking method captures the temporal evolution and structural continuity of the inflow objects over time.

In this real-case demonstration, the largest inflow object in the lower-left quadrant and the feature centered near 25°W, 50°N are tracked continuously at every time step, satisfying the 0.3 overlap threshold. The two small, closely spaced objects in the upper-right quadrant show how the algorithm handles merging and splitting events. At the second time step, they merge into a single object (blue contour). The fragment with the greater overlap retains its original ID, while the other one becomes `inactive`. When the object divides again at the third time step, the fragment with the greater overlap continues the original track, and the other fragment receives a new ID, starting a new track. This tracking behavior, including the handling of merging and splitting objects, is implemented explicitly within the tracking algorithm developed in this study.

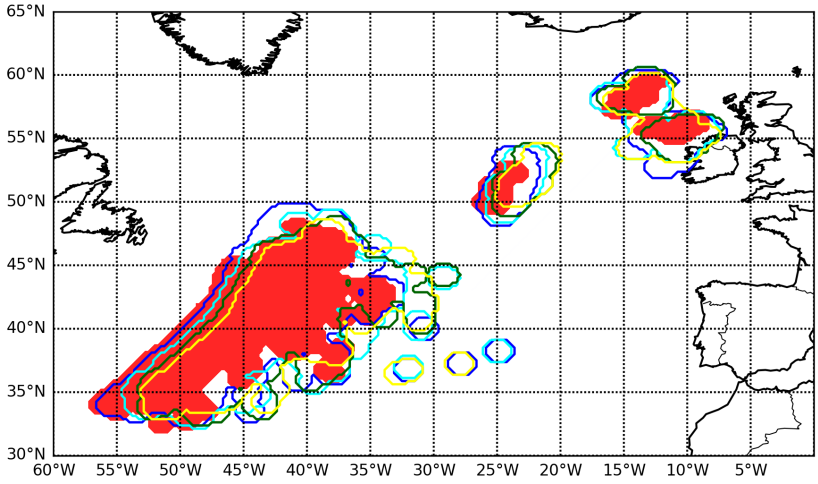

Figure 4.4: Example of overlap-based object tracking starting at 01 February 2010, 05:00 UTC. Inflow objects identified at the initial time are shown in red shading. Their positions at 06:00 UTC, 07:00 UTC, and 08:00 UTC are outlined in blue, cyan, and yellow contours, respectively.

From a climatological perspective, the tracking and filtering strategy employed here is designed to retain only physically meaningful WCB inflow events while excluding short-lived or weakly developed structures. A subset of infow obkects appear only briefly and is subsequently filtered out by the applied size and lifetime criteria. These short-lived objects often represent minor features that separate from or merge into a dominant inflow structure. Taking such features as independent climatological events would therefore overestimate the number of distinct WCB inflow occurrences without clear physical justification. The adopted approach ensures that the resulting inflow-track climatology is dominated by coherent, long-lived (at least 48 hours) inflow structures that are robustly associated with WCB ascent and subsequent moisture transport.

4.2.2 Smoothing and filtering of inflow tracks

After applying the tracking algorithm, a total of 1012151 inflow tracks were generated for the period 2010-2019 over the Northern Hemisphere, with lifespans ranging from 1 hour up to more than 250 hours, where the shortest-lived tracks primarily arise before the application of any lifetime filtering. While this approach effectively captures the coherent evolution of inflow structures, artifacts may appear, particularly during the early stages of a track when inflow regions are relatively small and disorganized. Minor shifts in the shape or position of the inflow objects can lead to abrupt changes in the centroid positions, resulting in artificial zigzag patterns that do not reflect physically meaningful motion (see Fig. 4.5).

To classify the inflow tracks based on their structural characteristics in later analysis, we apply

Dynamic Time Warping (DTW) combined with K-medoids clustering. DTW is well-suited for comparing the shape of time series with temporal misalignments, but it is also sensitive to small-scale fluctuations. Such noise can mislead the similarities and result in poor clustering of otherwise similar tracks.

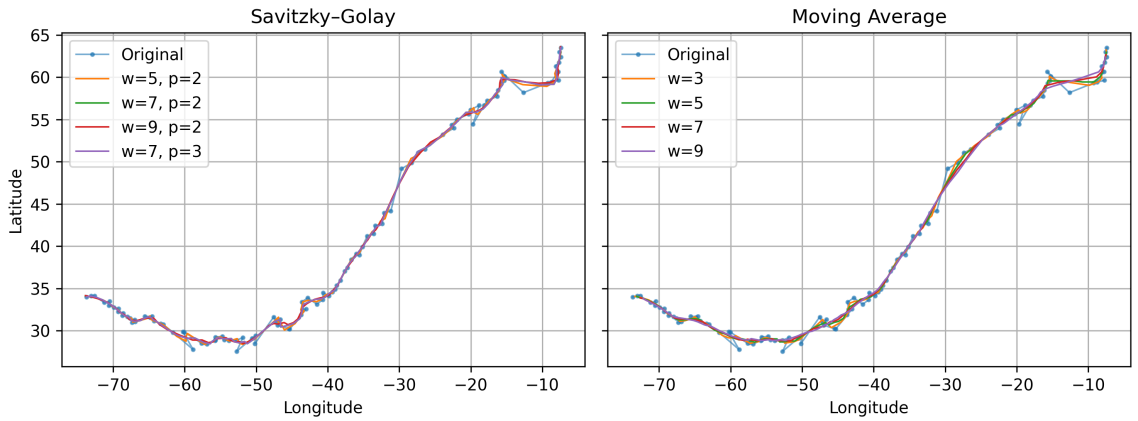

Figure 4.5: Comparison of smoothing methods applied to the inflow track starting on 19 February 2011 at 07 UTC. The left panel shows results from the Savitzky–Golay filter with varying window lengths and polynomial orders, while the right panel presents the Moving Average method with different window sizes.

To address this issue and improve the quality of subsequent analysis, we apply a smoothing procedure to the inflow tracks as a necessary pre-processing step. This step reduces high-frequency noise and suppresses artifacts while preserving the large-scale curvature, direction, and structural evolution of the tracks. The smoothing improves the robustness of DTW-based clustering, ensuring that the clustering reflects the more realistic physical behavior of the inflow tracks rather than artifacts introduced by the tracking algorithm.

Figure 4.5 illustrates the different smoothing methods evaluated for use in this study. We compared the Savitzky–Golay filter using various window lengths and polynomial orders with the Moving Average method across different window sizes. Based on visual inspection of representative inflow tracks across different parameter choices, the Savitzky–Golay filter more effectively preserves the curvature of the original tracks, while still retaining some erratic motion. Since clustering is highly sensitive to small fluctuations in track shape, robust smoothing is essential. The Moving Average method yields better noise suppression overall, but the use of a fixed window size is not well suited to the diverse lengths of inflow tracks, as different window choices for the same track can lead to different smoothing outcomes. To address this, we adopted an adaptive smoothing strategy based on the Moving Average method, where the window size is set proportionally to the track length, with a lower limit of 20 and an upper

limit of 25 time steps. Based on visual inspection of representative inflow tracks, this approach effectively suppresses high-frequency noise across tracks of varying lengths while maintaining the overall curvature and structural features that are critical for clustering. An example of the smoothed inflow tracks for the period 2010-2013 is illustrated in Appendix Fig. A.11. The full 2010-2019 period is not displayed, as more than one million identified inflow tracks would result in sever overplotting.

Filtering of smoothed inflow tracks

To focus the analysis on inflow tracks that are more likely associated with extratropical cyclones and coherent large-scale motion, we apply a selection criterion based on temporal and spatial extent. Specifically, we retain only tracks with lifespans exceeding 48 hours and spatial displacements greater than 40° in the meridional and 15° in the zonal direction between their start and end points. The histogram of inflow track lifespans for the full dataset over the period 2010-2019 is shown in Appendix Fig. A.12. Applying these criteria yields a subset of 519 inflow tracks over the period 2010-2019, corresponding to approximately 0.05% of all identified tracks, as shown in Fig. 4.6a.

There are two main regions showing a high frequency of inflow tracks over the North Atlantic and the North Pacific. The North Atlantic storm track is characterized by strong baroclinicity, pronounced meridional temperature gradients, and persistent jet stream dynamics, which favor vigorous extratropical cyclogenesis and well defined warm conveyor belt structures (Heitmann et al., 2024). In addition, the Atlantic Ocean typically exhibits relatively consistent inflow conditions, dominated by warm and moist air masses originating from subtropical latitudes and the Caribbean region (e.g., Eckhardt et al., 2004; Wenta et al., 2024). These characteristics facilitate the identification and isolation of coherent WCB events. In contrast, the North Pacific region is influenced by more complex large scale dynamics, including tropical-extratropical interactions associated with the El Niño–Southern Oscillation (ENSO), Asian monsoon circulations, and irregular continental landmasses and topography (Quinting et al., 2024). These factors lead to fundamentally different inflow regions and boundary conditions compared to the North Atlantic, making it difficult to construct a dynamically homogeneous ICON ensemble. To ensure a climatologically consistent and dynamically controlled set of initial conditions, only Atlantic cases are therefore selected for the high-resolution ensemble simulations. Specifically, Atlantic cases are constrained to inflow object initial positions located within 25°–50°N latitude and 120°–20°W longitude.

After applying all selection criteria, which require inflow track lifespans to exceed 48 hours and spatial displacements between the start and end points of the smoothed inflow tracks to

be greater than 40° in the meridional and 15° in the zonal direction, a total of 300 inflow cases remain, as shown in Figure 4.6b. These cases form the basis for the subsequent analysis.

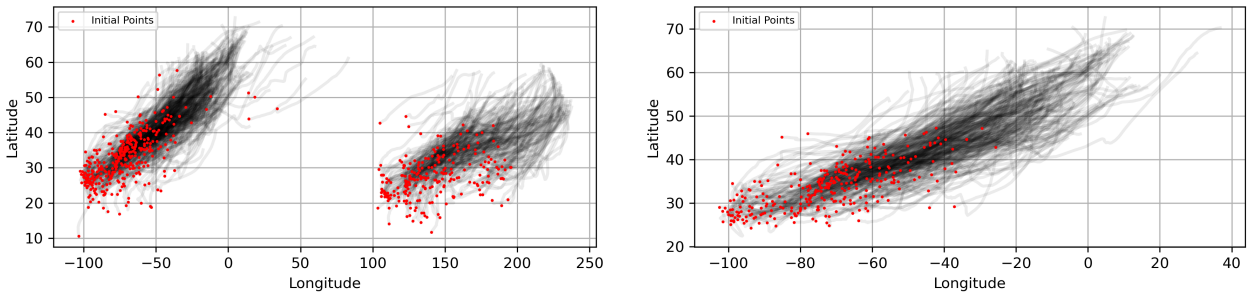

(a) (b)

Figure 4.6: Distribution of inflow tracks identified using the tracking methodology described in Section 4.2.1. (a) Subset of inflow tracks filtered to include only those with lifespans exceeding 48 hours and spatial displacements greater than 40° meridionally and 15° zonally between their first and last points. This step retains 591 tracks. (b) Final selection of inflow tracks with initial positions located over the Atlantic Ocean, constrained to the region between 25°–50°N and 120°–20°W. A total of 300 tracks are included in the final analysis set.

4.2.3 Dynamic Time Warping (DTW) with K-medoids clustering

To construct a diverse ensemble of cases, the selected inflow tracks are clustered based on their spatial and temporal characteristics. This clustering enables the identification of representative categories of WCB inflow tracks that differ in their geometric evolution, providing a structured framework to analyze variations in inflow properties and their temporal evolution over the WCB lifecycle.

Traditional K-means clustering aims to partition a dataset into k distinct clusters by minimizing the within-cluster variance. The algorithm initializes k centroids randomly, assigns each data point to the nearest centroid based on Euclidean distance, and iteratively updates the centroids by computing the mean of all points assigned to each cluster. These assignment and update steps are repeated until convergence.

However, standard K-means clustering assumes that all input vectors are of equal length and relies on Euclidean distance as the similarity metric. In our case, the inflow tracks differ in both length and duration, making Euclidean distance inadequate for capturing structural similarities between tracks. To address this limitation, we apply Dynamic Time Warping (DTW) in combination with K-medoids clustering. This approach is conceptually similar to K-means but better suited for time series data. DTW enables meaningful comparisons by aligning tracks

based on their overall shape, rather than enforcing strict point-wise alignment in time. Unlike K-means, which computes cluster centroids that may not correspond to any actual track, K-medoids selects real tracks from the dataset as cluster centers (medoids). This ensures that each cluster is represented by a physically plausible inflow track, which is particularly valuable for interpreting and analyzing the resulting groups.

Clustering sensitivity to cluster number

To evaluate clustering quality, we computed the mean intra-cluster distance, defined as the average DTW distance between each track and its corresponding medoid, and the mean inter-cluster distance, defined as the average DTW distance between the medoids of different clusters. These two metrics reflect the compactness of individual clusters and the separation between clusters, respectively. A compactness ratio was then defined as:

$$\text{compactness ratio} = \frac{\text{mean intra-cluster distance}}{\text{mean inter-cluster distance}} \tag{4.2}$$

To select an appropriate number of clusters, we evaluated the compactness ratio as defined above for cluster counts ranging from 10 to 50 (Figure 4.7). As expected, the compactness ratio generally decreases with increasing cluster number, indicating larger within-cluster similarity relative to between-cluster separation. However, a larger number of clusters also increases the risk of over-classification, where clusters may capture minor variations or noise rather than meaningful structural or physical differences. The compactness ratio exhibits a first local minimum at 24 clusters, followed by a secondary minimum around 30–32 clusters. While these configurations yield lower ratios, they may be overclassified for the purposes of case selection and interpretation.

We therefore chose 20 clusters (compactness ratio = 0.176) for the following analysis. Cluster numbers between 16 and 20 exhibit similar values, indicating no unique optimum emerges from this metric alone. The choice of 20 clusters was thus guided not only by the compactness ratio but also by a qualitative inspection of the resulting cluster structures for different cluster numbers (not shown). Compared to lower cluster numbers, 20 clusters provide a clearer separation of inflow tracks with geometric characteristics and temporal extends, avoiding the grouping of markedly different track lengths and pathways within the same cluster. Overall, this choice offers a good balance between compactness and interpretability.

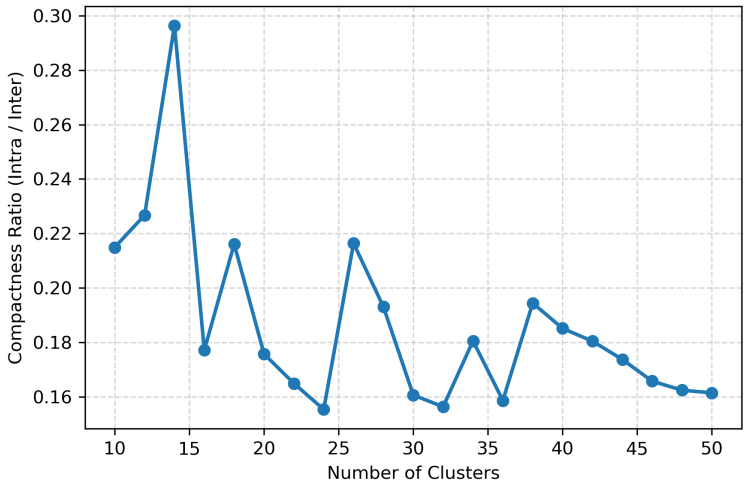

Figure 4.7: Compactness ratio function of cluster number. Lower values indicate more compact and well-separated clusters.

Clustering results

After applying the smoothing procedure and performing DTW K-medoids clustering, the final set of 300 selected cases over the Atlantic is grouped into 20 clusters. Cluster sizes vary, with the number of tracks ranging from 2 to 31 see in Table. 4.1.

Table 4.1: Number of inflow tracks per cluster obtained from the DTW K-medoids clustering.

Cluster	0	1	2	3	4	5	6	7	8	9	10	11	12	13	14	15	16	17	18	19
Tracks	20	20	21	11	13	9	11	3	10	19	26	10	2	10	22	27	31	9	20	6

Figure 4.8 shows two examples of the resulting clusters (the complete set of 20 clusters is provided in Appendix Fig. A.14). In each panel, individual inflow tracks belonging to the same cluster are shown in different colors, while the medoid track is highlighted in dashed gray, representing the most representative member in shape of the cluster. The tracks within each cluster exhibit similar overall paths and orientations, indicating that the algorithm effectively identifies coherent groups of inflow tracks.

The bar chart in Figure 4.9 shows the normalized compactness of the 20 clusters, highlighting differences in internal variability among groups. For each cluster, the cumulative distance between individual tracks and the medoid is normalized to a range from 0 to 1, where lower values indicate more compact clusters with smaller average distances to the medoid, and higher values indicate greater internal dispersion. Clusters such as 14, 7, 6, and 3 exhibit high compactness, whereas clusters 18, 5, and 9 show substantially larger internal variability. Cluster size may influence internal variability, but the normalized compactness metric largely reflects differences

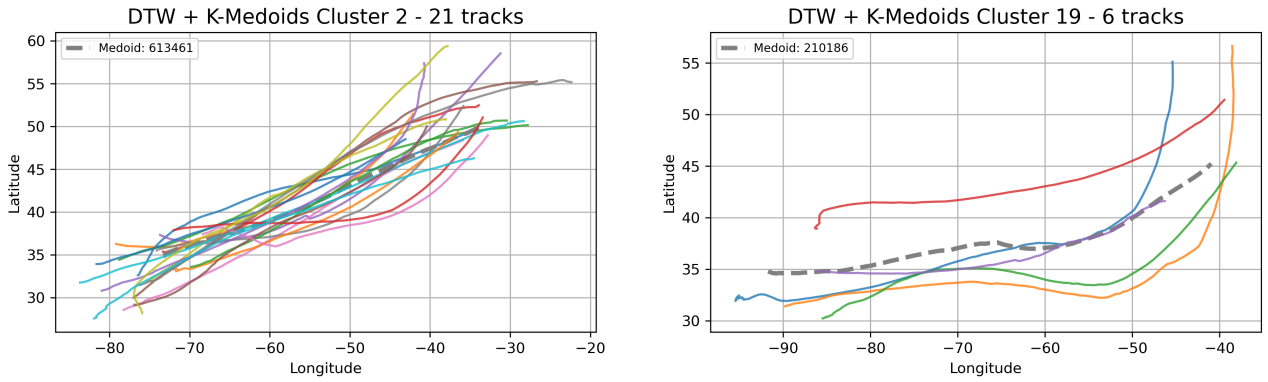

(a) (b)

Figure 4.8: Examples of inflow track clusters obtained from DTW K-medoids clustering. Panel (a) shows a cluster of 21 tracks initiating mainly near 75°W, between 30° and 40°N, exhibiting a predominantly northwestward motion. Panel (b) includes 5 tracks initiating near 85°W and 35°N, which initially move eastward before turning sharply northward.

in track geometry and temporal evolution rather than the number of tracks alone. Overall, this comparison provides a quantitative characterization of differences in internal cluster coherence.

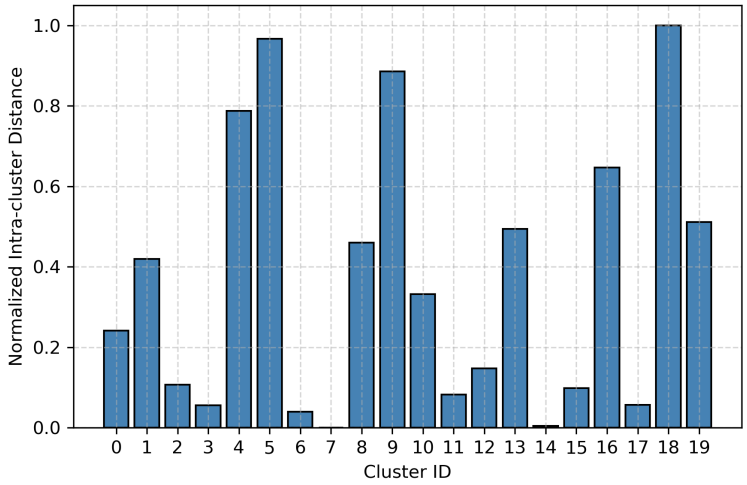

Figure 4.9: Normalized mean intra-cluster DTW distance for each cluster, based on min–max normalization. Lower values indicate more compact clusters, while higher values reflect greater internal variability.

4.2.4 Strategy for case selection

Construction of WCB characteristics along the tracks

For the selected 300 tracks initiated over the western North Atlantic, we identified WCBs along each track and retained only WCBs for which the associated outflow occurred before the end of the inflow track. This restriction ensures a consistent temporal pairing of inflow and outflow properties along the same track and avoids mixing inflow points with outflow points that are not captured within the defined inflow track time window. For each WCB trajectory, we computed the ascent timescale τ_{600} and extracted the inflow and outflow points along the trajectory. Specific humidity, condensed water, and temperature are interpolated to these inflow and outflow points, which serve as representative locations of the WCB inflow and outflow regions. Figure 4.10 illustrates the spatial characteristics of one representative inflow track, which exhibits a typical southwest-to-northeast propagation. The corresponding outflow locations mostly fall within the region of high climatological frequency for fresh outflow (Fig. 3.5), as defined and computed in Section 2.4, indicated by the red contour. The blue line shows the identified inflow track, with two red stars marking the first 48-hour time window. Green and orange dots indicate the inflow and outflow points, respectively.

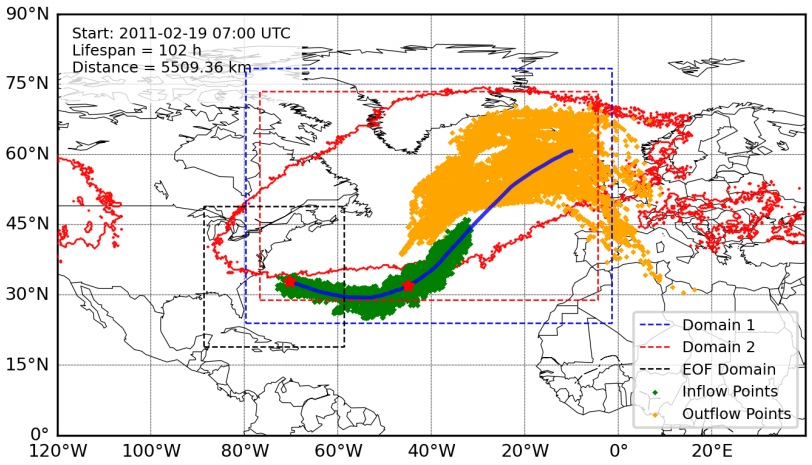

Figure 4.10: Example of a inflow track initiated over the western North Atlantic on 19 February 2011 at 07:00 UTC. The blue line shows the inflow track, while green and orange dots mark the inflow and corresponding outflow points, respectively, both occurring within the inflow track lifetime. The red contours represent the 99 % fresh outflow climatology, as described in Section 3. Two red stars indicate the 48-hour time window. The red and blue dashed squares indicate the nested domains that applied for ICON high-resolution simulations in the next chapter.

Metrics for selecting representative WCB cases

To identify a subset of inflow tracks that is representative of the diversity of WCB characteristics present in the 300 selected cases, we developed a three-dimensional physical metric space. This metric is based on key inflow track and WCB properties diagnosed in previous sections, including trajectory lifespans, the clustering of inflow tracks using K-medoids with DTW, and ascent characteristics by the median ascent timescale τ_{600} computed from all WCB trajectories within each cluster. A target sample size of 50 WCB cases was defined as a compromise between coverage of climatological WCB diversity and computational feasibility for high-resolution ensemble simulations.

The conceptual framework of this selection method is illustrated in Fig. 4.11. The three dimensions of the selection space were defined as follows: (1) the cluster assignment (i.e., the 20 groups in Appendix Fig. A.13), which represents differences in overall inflow track shape; (2) the median τ_{600} computed from all WCB trajectories of each cluster, capturing variability in vertical ascent timescales; (3) the inflow track lifespan (Fig. 4.12b), for which the logarithm of the lifespan was used to reduce the influence of the strongly right-skewed distribution, thereby preventing long-lived tracks from dominating the selection and ensuring a more balanced representation across the range of lifespans.

Each of the 300 inflow tracks was then mapped into this 3D space (black dots in Figure 4.11) and represented as a point $\mathbf{p}i = (C_i, \tau_i, \log L_i)$, where:

- C_i is the cluster ID of each track,
- τ_i is the median τ_{600} of each track,
- L_i is the logarithm of track lifespan.

To select a diverse and representative sample, we uniformly generated 50 random points (shown as green markers) within the bounds of the normalized 3D space. For each random point $\mathbf{r}_j$, we identified the closest cases $\mathbf{p}_i$ based on the Euclidean distance:

$$d(\mathbf{r}_j, \mathbf{p}_i) = \sqrt{(C_i - C_j)^2 + (\tau_i - \tau_j)^2 + (\log L_i - \log L_j)^2} \tag{4.3}$$

To avoid duplicate selections, random points were generated iteratively. When multiple random points were mapped to the same inflow track, additional points were drawn until 50 unique cases were selected. Random points were sampled uniformly within the normalized three-dimensional

metric space. The resulting 50 WCB cases constitute the final representative set, indicated by red markers in Figure 4.11 and listed in Table. 4.2. This approach ensures diversity by sampling across all clusters within the physical metric space. The corresponding two-dimensional projections of the sampling space are shown in Appendix Fig. A.13.

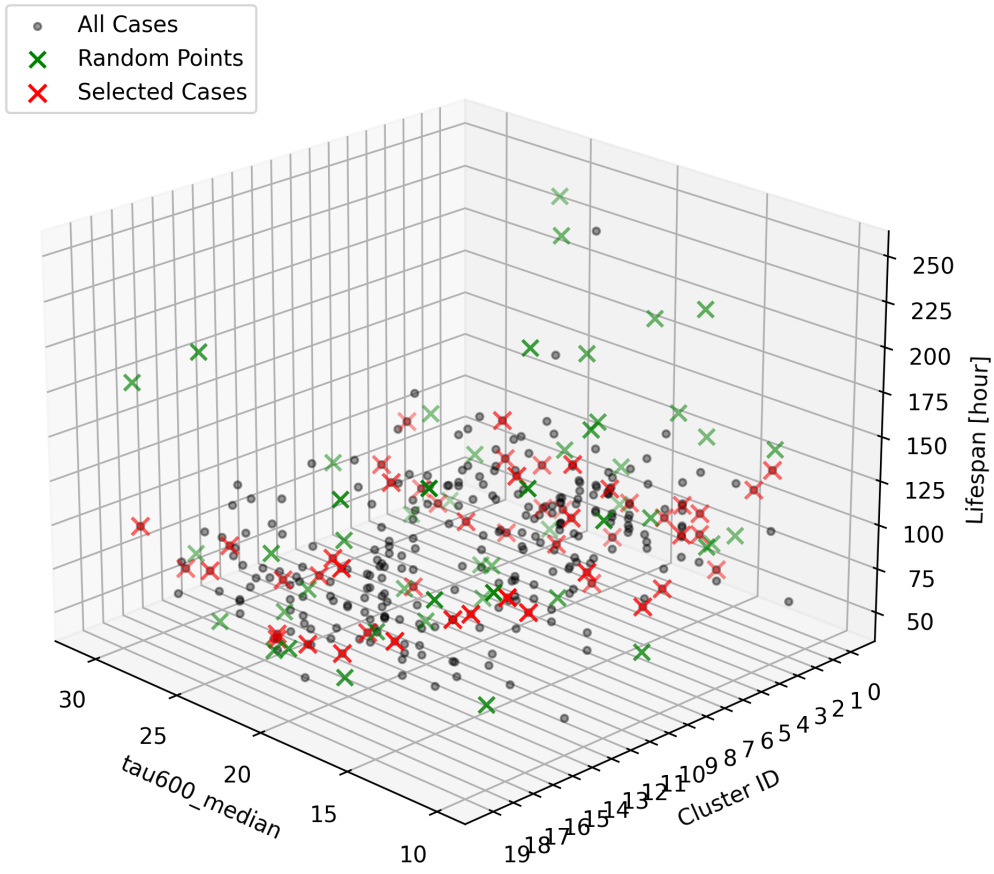

Figure 4.11: Visualization of the 3D sampling space used for case selection, based on median of $\tau 600$, cluster IDs, and Lifespan (log-scale see in Appendix). Random points (green) are sampled uniformly in this space, and the nearest 50 unique cases (red) are selected from the full set of WCB inflow tracks (gray). The corresponding two-dimensional projections of each axis pair are shown in Appendix Fig. A.13, where lifespan is displayed on a logarithmic scale.

Table 4.2: Final Selection of Inflow Tracks

Object_ID	If_Medoid	TimeStamp	tau600_median	n_WCBs	LifeSpan	Season
56258	0	2010-07-13 00:00:00	17.0	17107	86	JJA
84728	0	2010-10-25 16:00:00	14.0	24687	96	SON
103404	0	2011-01-06 20:00:00	23.0	6920	57	DJF
103682	0	2011-01-08 00:00:00	27.0	8902	91	DJF
187110	0	2011-11-15 12:00:00	26.0	13452	112	SON
192893	0	2011-12-11 06:00:00	21.0	2705	55	DJF
230440	0	2012-05-06 10:00:00	29.0	9244	110	MAM
253123	0	2012-07-18 23:00:00	23.0	4985	58	JJA
274851	0	2012-10-04 12:00:00	26.0	8288	77	SON
287884	0	2012-11-20 20:00:00	23.0	16600	67	SON
305261	0	2013-01-27 12:00:00	25.0	1579	52	DJF
307893	0	2013-02-06 12:00:00	16.0	57901	145	DJF
323229	0	2013-04-04 12:00:00	22.0	28920	106	MAM
366043	0	2013-08-25 17:00:00	12.0	36538	104	JJA
379010	0	2013-10-09 21:00:00	11.0	69321	125	SON
383125	0	2013-10-25 14:00:00	23.0	6503	73	SON
385630	0	2013-11-06 06:00:00	18.0	19285	122	SON
386582	0	2013-11-10 06:00:00	15.0	24709	94	SON
389708	0	2013-11-22 20:00:00	19.0	16590	87	SON
394818	0	2013-12-11 20:00:00	18.0	12093	75	DJF
400765	0	2014-01-06 01:00:00	27.0	13625	81	DJF
496344	0	2014-12-13 18:00:00	30.0	14852	99	DJF
558868	0	2015-07-26 19:00:00	17.0	33996	143	JJA
562147	0	2015-08-08 01:00:00	15.0	32013	96	JJA
567079	0	2015-08-25 03:00:00	18.0	5666	57	JJA
572770	1	2015-09-13 06:00:00	22.0	21215	129	SON
594822	0	2015-12-07 06:00:00	20.0	7713	72	DJF
624036	0	2016-04-01 06:00:00	11.0	31812	89	MAM
690576	0	2016-11-21 16:00:00	23.0	5710	61	SON
695212	0	2016-12-10 06:00:00	14.0	31247	101	DJF
722278	0	2017-03-29 05:00:00	20.0	63682	155	MAM
731613	0	2017-04-28 03:00:00	16.0	51205	123	MAM
741130	0	2017-05-26 10:00:00	31.0	1823	58	MAM
783234	0	2017-10-18 22:00:00	13.0	68513	120	SON
805953	0	2018-01-17 17:00:00	22.0	16788	99	DJF
810222	0	2018-02-03 21:00:00	21.0	30881	98	DJF
813677	0	2018-02-18 02:00:00	14.0	24213	105	DJF
826279	1	2018-04-02 02:00:00	27.0	6129	82	MAM
835360	0	2018-05-02 06:00:00	19.0	11516	80	MAM
883616	0	2018-10-13 03:00:00	20.0	8936	65	SON
886746	1	2018-10-24 18:00:00	12.0	58368	113	SON
891639	0	2018-11-13 19:00:00	15.0	41723	123	SON
906504	0	2019-01-02 16:00:00	13.0	43466	108	DJF
916284	0	2019-02-07 18:00:00	25.0	6257	75	DJF
921436	0	2019-02-26 14:00:00	24.0	12193	77	DJF
927193	0	2019-03-20 06:00:00	16.0	5036	51	MAM
930626	0	2019-04-01 13:00:00	15.0	36058	84	MAM
935659	0	2019-04-16 21:00:00	13.0	20013	78	MAM
937876	0	2019-04-23 11:00:00	22.0	26673	118	MAM
952734	0	2019-06-07 01:00:00	16.0	25471	97	JJA

4.3 Results

4.3.1 Statistical evaluation of the selected WCB cases

Figure 4.12a shows the monthly distribution of the 300 selected inflow cases. The distribution exhibits a pronounced seasonal cycle, with a clear maximum in winter (DJF), consistent with the climatological frequency of cyclonic activity over the North Atlantic. In contrast, summer (JJA) contributes a relatively small fraction of cases, reflecting the reduced occurrence of WCBs during this season. The transitional seasons (MAM and SON) also account for a substantial number of cases, indicating that WCB activity remains important outside the winter months. To capture this seasonal variability, cases for high-resolution simulations are selected across all seasons, rather than being restricted to winter.

The distribution of inflow track lifespans for the 300 selected cases is shown in Fig. 4.12b. Most tracks persist for 60–100 hours, with a median lifespan of approximately 83 hours and an interquartile range between roughly 65 and 105 hours. A small number of long-lived cases exceed 150 hours, potentially reflecting particularly strong WCB activity.

Figure 4.12c shows the distribution of the number of WCB trajectories associated with each of the 300 inflow tracks. The x-axis represents the number of WCB trajectories per track on a logarithmic scale, while the y-axis indicates the number of tracks falling within each bin. The number of WCB trajectories per track spans a wide range, from fewer than 500 to nearly 120000. Most tracks contain between approximately 5000 and 35000 WCB trajectories, with the highest track count (40 cases) occurring in the 13741–18680 range. A small number of tracks fall in the lower tail, with fewer than 1000 WCB trajectories, or in the upper tail, with more than 60000. This distribution highlights the substantial variability in the number of WCB trajectories across different cases, indicating potential differences in WCB occurrence among the selected tracks.

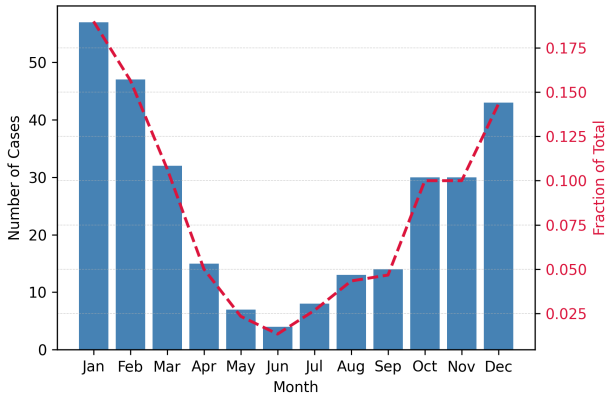

(a)

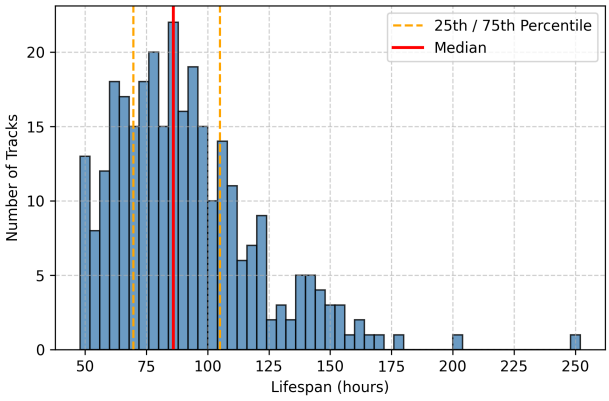

(b)

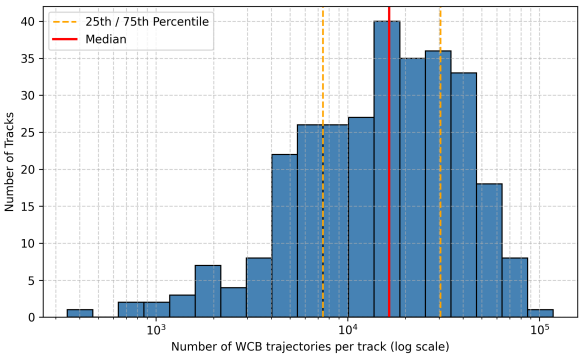

Bin Range	Track Count
344 – 468	1
637 – 866	2
866 – 1178	2
1178 – 1601	3
1601 – 2177	7
2177 – 2959	4
2959 – 4023	8
4023 – 5469	22
5469 – 7435	26
7435 – 10108	26
10108 – 13741	27
13741 – 18680	40
18680 – 25393	35
25393 – 34520	36
34520 – 46927	33
46927 – 63793	18
63793 – 86722	8
86722 – 117890	1

(c)

Figure 4.12: Statistical characterization of the 300 selected inflow tracks. Panel (a) shows the monthly distribution of track start times, with blue bars indicating the number of cases and the dashed red line showing the fraction of total cases per month, highlighting a clear seasonal cycle. Panel (b) presents the distribution of inflow track lifespans, with the 25th, median, and 75th percentiles marked with dashed orange and solid red lines, showing typical durations and outliers. Panel (c) displays the distribution of WCB trajectory counts per inflow track, grouped into a logarithmic bin ranges, with the 25th, median, and 75th percentiles marked with dashed orange and solid red lines. The table on the right side summarizes the number of tracks falling within each bin.

The final subset of 50 selected cases is subsequently analysed to assess how well it represents the broader distribution of the 300 cases, thereby providing context for the high-resolution simulations in the following chapters. The corresponding WCB inflow tracks are shown in Figure 4.13 and listed in Table. 4.2. Most tracks originate between 100°W and 40°W and south of 40°N, consistent with typical subtropical inflow regions over the western North Atlantic. A smaller number of cases initiate farther north near 45°N in the mid-Atlantic, indicating interactions with more mature or higher-latitude cyclonic systems. Together, the range of starting locations and track geometries demonstrates that the selected cases span a broad spectrum of WCB inflow configurations.

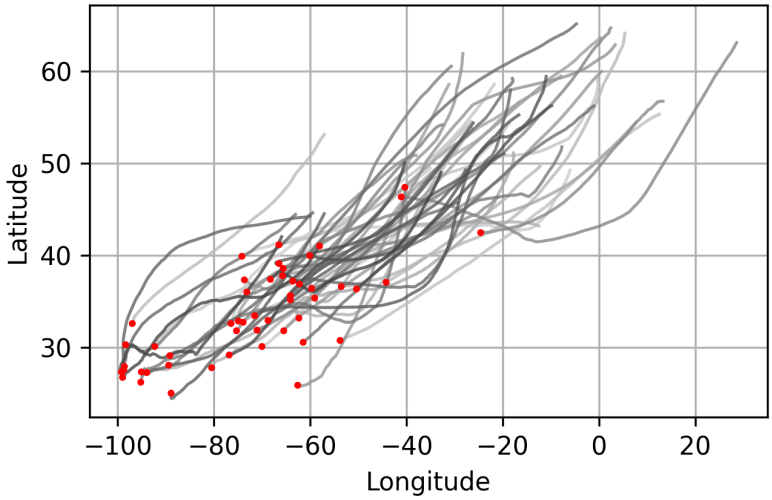

Figure 4.13: Inflow tracks of the 50 selected WCB cases, with initial positions marked in red.

First, the distribution of ascent timescales τ_{600} is compared between the full set of 300 WCB cases and the final subset of 50 selected cases (Fig. 4.14). The full dataset exhibits a broad τ_{600} distribution with a maximum around 18 hours, consistent with the climatological ascent timescale characteristics shown in Fig. 3.11a. The 50 selected cases closely reproduce both the overall shape and the full range of this distribution, including short and long ascent times. A slight shift of the peak toward shorter τ_{600} is evident for the selected cases. This results in a distribution that more closely resembles the JJA climatological pattern (Fig. 3.11a) and indicates a relatively larger contribution of summer and transitional season cases in the final set. Overall, the selection preserves the dominant ascent time variability of the full dataset.

Figure 4.15 summarizes the statistical properties of the final 50 cases and allows direct comparison with the full set of 300 inflow tracks. Panel (a) shows the monthly distribution of track initiation times. The final 50 cases largely reproduce the seasonal distribution of WCB inflow occurrence observed in the full 300-case dataset, with the largest contributions from winter and

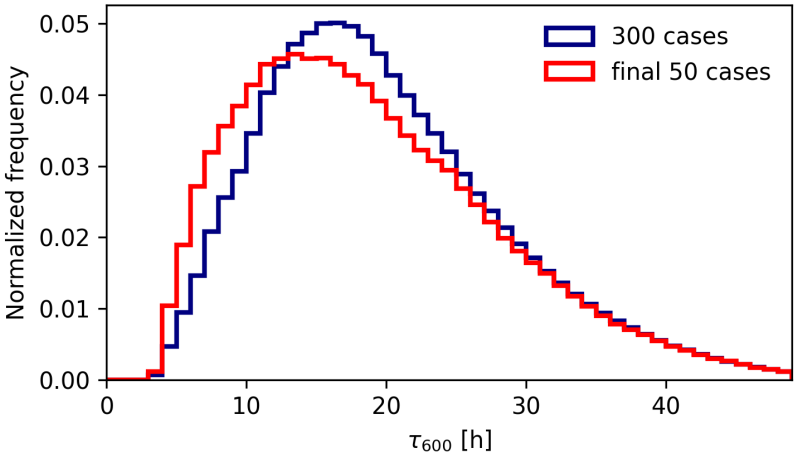

Figure 4.14: Distribution of WCB ascent timescales τ_{600} for the full set of 300 cases (navy) and the final subset of 50 selected cases (red).

the transitional seasons and a reduced contribution during summer, demonstrating that the seasonal variability is well preserved in the reduced sample.

Figure 4.15b presents the distribution of inflow track lifespans. Despite the reduced sample size, the range, median, and interquartile spread closely match those of the original 300 cases. Most tracks have lifespans between roughly 70 and 125 hours, and several long-lived cases exceeding 150 hours are retained, indicating that the selection process preserves the full spectrum of WCB inflow durations. Figure 4.15c shows the distribution of the number of WCB trajectories associated with each inflow track on a logarithmic scale. The selected cases span a wide range of WCB densities, from sparsely populated tracks to very dense ones, consistent with the variability observed in the full dataset. This demonstrates that differences in WCB intensity and track population are maintained in the reduced sample.

Additional details for each selected case are provided in Table 4.2. The final set spans the full annual cycle and covers a broad range of inflow track lifespans and ascent timescales, with median τ_{600} values ranging from 11 to 31 hours. The medoid tracks of individual clusters are not necessarily selected, as medoids represent geometric centers rather than physically representative cases. Taken together, these statistical comparisons show that the reduced set of 50 WCB cases preserves the key characteristics of the full 300 cases, including seasonal occurrence, inflow track geometry, ascent timescales, and WCB intensity. Accordingly, diagnostics of inflow and outflow properties are presented for both the full and reduced samples in the following sections to assess the robustness of the identified statistical relationships with respect to the case selection. Overall, the final 50 cases provide a suitable and diverse basis for high-resolution ensemble simulations and detailed process-based analyses in the following chapters

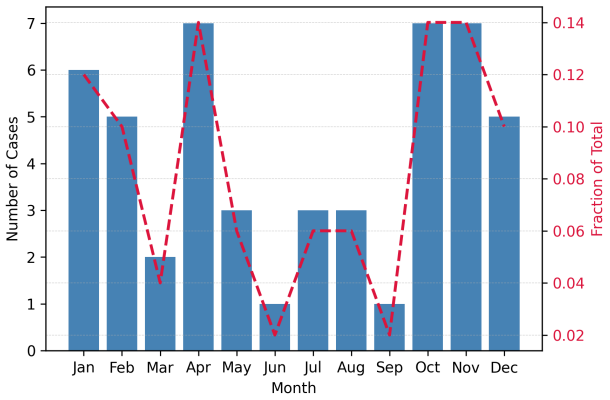

(a)

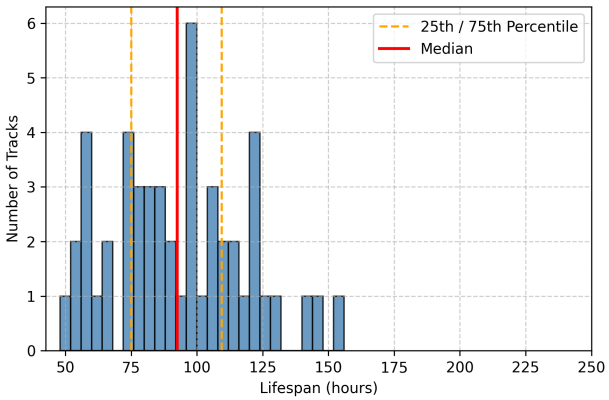

(b)

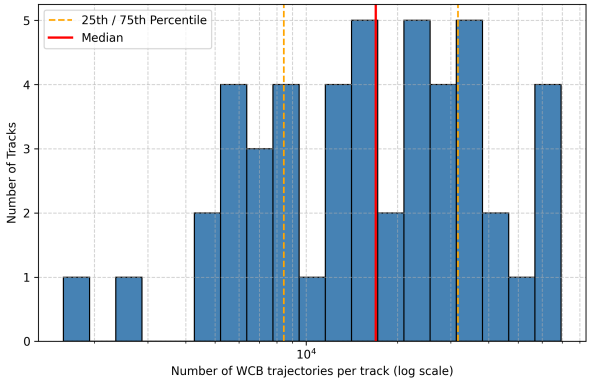

Bin Range	Track Count
1579 – 1926	1
2351 – 2868	1
4271 – 5212	2
5212 – 6360	4
6360 – 7761	3
7761 – 9471	4
9471 – 11557	1
11557 – 14102	4
14102 – 17208	5
17208 – 20998	2
20998 – 25623	5
25623 – 31266	4
31266 – 38152	5
38152 – 46555	2
46555 – 56809	1
56809 – 69320	4

(c)

Figure 4.15: Statistical characterization of the final 50 selected inflow tracks. Panel (a) shows the monthly distribution of track start times, with blue bars indicating case counts and the dashed red line showing the monthly fraction. Panel (b) presents the distribution of inflow track lifespans, with the 25th, median, and 75th percentiles marked by dashed orange and solid red lines. Panel (c) displays the number of WCB trajectories per track on a logarithmic scale, with corresponding percentiles marked. The table summarizes the number of tracks in each bin.

4.3.2 Inflow initial conditions

Temporal evolution of surface variables in the inflow region

This subsection investigates the evolution of key surface variables along the WCB inflow tracks. Figure 6.1 presents the evolution of mean sea level pressure (MSLP), sea surface temperature (SST), and 10-m meridional and zonal wind components, computed from inflow points associated with 300 tracks, as identified in Section 4.2.2. Given that the minimum-lifespan threshold in the selection criteria was 48 hours, all inflow time series are normalized to a common 48-hour scale to enable consistent comparison across cases. Figure 6.1b shows the same diagnostics for the final subset of 50 selected cases and is included to assess whether the inflow evolution identified for the full sample is preserved in the reduced dataset.

In panel (a), based on 300 WCB inflow tracks, the median MSLP exhibits a steady decline of approximately 15 hPa over 48 hours, indicative of intensifying cyclonic conditions in the inflow region. The SST decreases gradually, consistent with a poleward motion of the inflow area into cooler environments. The meridional wind (`v10`) shows a marked increase over time, reflecting strengthening poleward transport, while the zonal wind (`u10`) remains positive (westerly) but trends slightly downward toward the end of the period. Notably, the mean closely follows the median closely across most variables, suggesting near-symmetric distributions. A slight deviation between the mean and median in MSLP during the later stages may be influenced by a small subset of unusually low-pressure extratropical cyclones.

Figure 6.1b shows the same diagnostics for the final subset of 50 selected WCB cases. The overall temporal evolution of MSLP, SST, and near-surface winds is consistent with that of the full sample, indicating that the selected cases capture the characteristic inflow evolution. Minor differences include a slightly weaker MSLP decline and enhanced SST cooling, suggesting a relatively less intense but faster-moving systems within the reduced set. The interquartile spread in `v10` further indicates that cases with stronger meridional flow are well represented. Overall, the selected subset spans the relevant range of inflow conditions and provides a suitable basis for subsequent analyses.

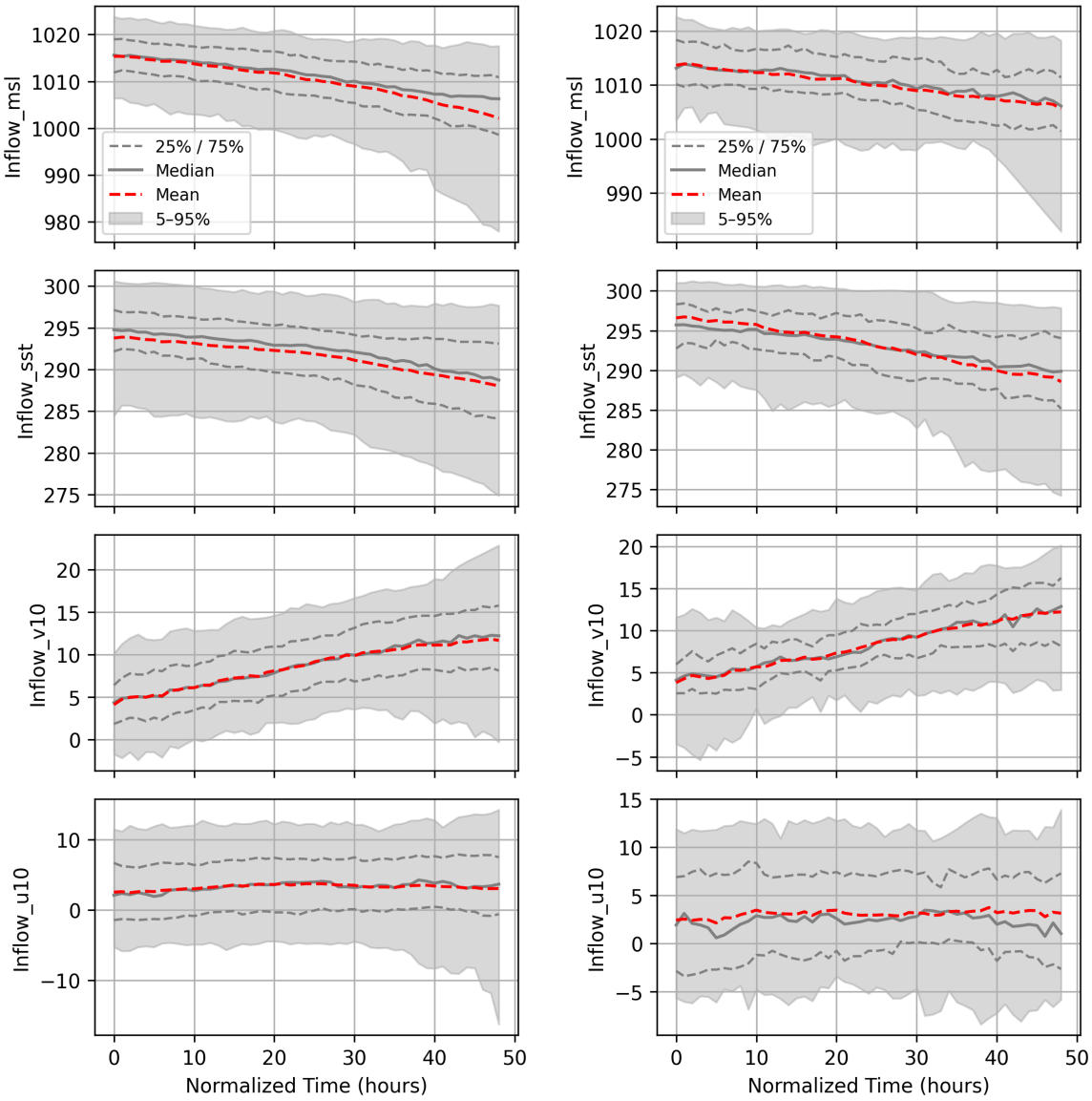

(a) Based on the full set of 300 WCB inflow tracks.

(b) Based on the final 50 selected WCB inflow cases.

Figure 4.16: Normalized 48-hour evolution of surface variables along WCB inflow trajectories. Shown are the 5–95% range (shaded), interquartile range (25–75%, dashed gray lines), median (solid gray line), and mean (dashed red line) for each variable. All time series are aligned relative to the initial inflow time.

EOF analysis of initial conditions

To further characterize the variability of the inflow environment, we apply an empirical orthogonal function (EOF) analysis to composite fields of mean sea level pressure (MSLP) and geopotential height at the dynamical tropopause (2-PVU level). These variables are chosen because they represent the dominant lower- and upper-tropospheric dynamical structures relevant to WCB trajectories, capturing the surface cyclone environment associated with inflow and the corresponding upper-level flow configuration linked to outflow, respectively. The EOF analysis is applied to the full set of 300 WCB cases in order to robustly sample the variability across a sufficiently large population, while avoiding sampling artifacts that may arise from the reduced subset.This analysis is used as a diagnostic and confirmatory tool to identify the dominant synoptic-scale patterns associated with WCB inflow conditions and to provide an objective description of inflow environment variability. For each WCB case, MSLP and 2-PVU geopotential height fields are extracted at the inflow reference time (t = 0) within a square domain extending $\pm 15^{\circ}$ in both latitude and longitude around the inflow point, yielding a $30^{\circ} \times 30^{\circ}$analysis window. The resulting inflow-centered composites allow variability across cases to be examined in a consistent synoptic framework.

Figure 4.17 summarizes the mean, median, and standard deviation of the inflow-centered MSLP and 2-PVU geopotential height fields. The composite MSLP field exhibits a pronounced meridional gradient, with lower pressure located poleward of the inflow reference point, consistent with WCB inflow occurring in the warm sector of baroclinic systems. Variability in MSLP indicates differences in cyclone position and intensity across cases.

The composite geopotential height field at the 2-PVU level also shows a clear meridional gradient. Variability is largest in the northern and eastern portions of the domain, reflecting differences in upper-level wave amplitude and position among cases. In contrast, variability near the inflow reference point is more limited, indicating that WCB inflow typically occurs beneath a dynamically consistent upper-level configuration.

To isolate the dominant modes of variability, EOF analysis is applied to the inflow-centered composite fields. The first six EOFs of MSLP explain more than 90% of the total variance, indicating that inflow variability is dominated by a small number of coherent synoptic patterns (Figure 4.18a). The leading EOF represents variability in the strength of the meridional pressure gradient surrounding the inflow region, while subsequent modes capture differences in the orientation and displacement of the synoptic-scale system relative to the inflow point. Higher-order modes explain only a small fraction of the variance and exhibit more localized structures.

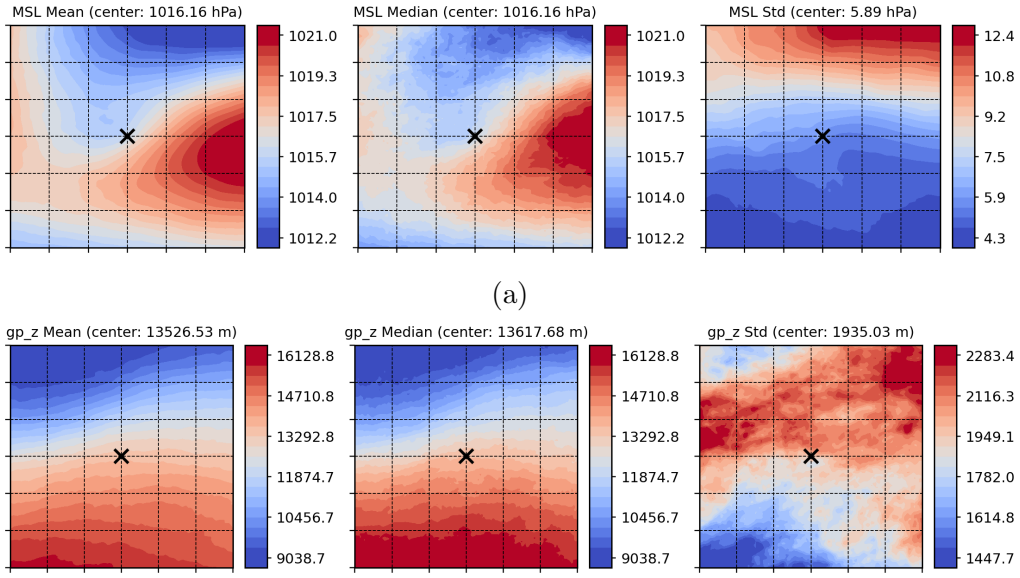

Figure 4.17: Composite statistics of (a) mean sea-level pressure (MSLP) and (b) geopotential height at the tropopause (2-PVU level), centered on the inflow points of 300 selected WCB cases. Each panel shows the mean, median, and standard deviation across all cases. The black cross marks the inflow reference point (t=0), and the center value is indicated in each panel title.

The first six EOF modes of geopotential height at the 2-PVU surface explain approximately 74% of the tota variance (Figure 4.18b). The leading mode reflects variability in the amplitude and position of the upper-level ridge–trough system above the inflow region, while subsequent modes describe shifts in wave orientation and phase. Together, these modes highlight that upper-level variability associated with WCB inflow is primarily governed by changes in large-scale jet stream structure rather than small-scale features.

Overall, the EOF analysis shows that WCB inflow environments are dominated by a small number of physically interpretable synoptic configurations at both the surface and upper levels. This supports the interpretation that the selected cases sample a dynamically consistent set of large-scale environments. The EOF results therefore provide a objective characterization of inflow environment variability and complement the statistical diagnostics presented in the previous sections.

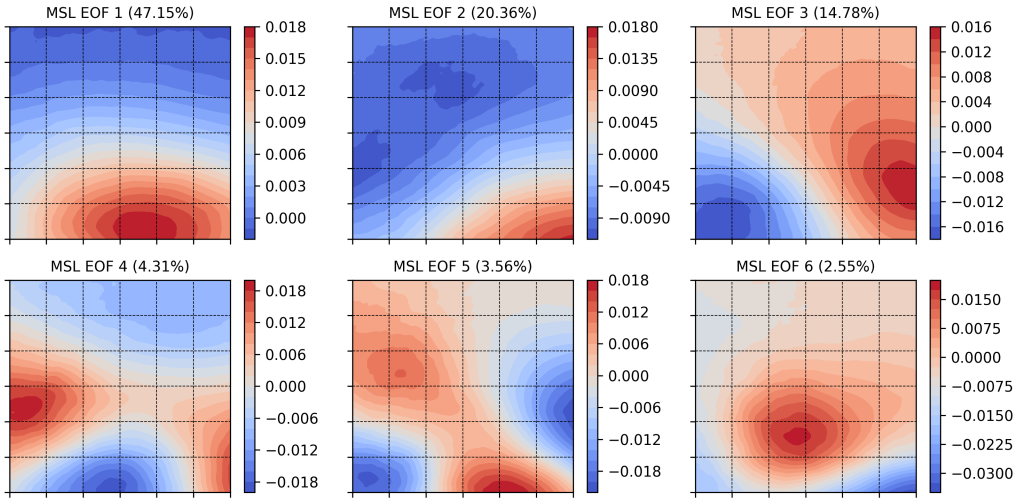

(a)

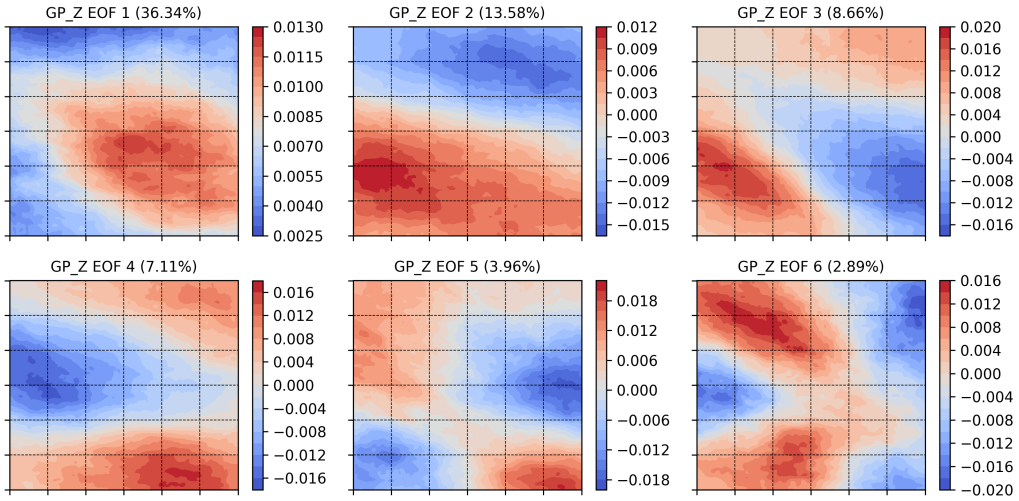

(b)

Figure 4.18: Empirical Orthogonal Function (EOF) analysis of composite fields: (a) mean sea-level pressure (MSLP), and (b) geopotential height at the dynamical tropopause (2-PVU level), based on 300 inflow-centered cases. Panels show the first six EOF patterns, along with the percentage of total variance explained by each mode.

4.3.3 Outflow moisture properties

In this subsection, we examine the moisture characteristics of WCB outflows using specific humidity (q_v) and condensed water content (q_h) at outflow points. In contrast to the climatological moisture anomalies analysis presented in Chapter 3, the focus here is on case-wise statistical distributions and correlations of inflow-outflow moisture properties derived from the full set of 300 WCB cases.

Figure 4.19 shows the spatial density of WCB outflow points derived from the two datasets, compared with the ERA5-based climatological outflow mask. For the full set of 300 cases (panel a), the outflow density broadly reproduces the climatological outflow structure over the North Atlantic and covers the core region defined by the 1% WCB occurrence frequency contour in Section 3.3. The reduced 50-case subset (panel b) exhibits a similar spatial pattern, with slightly reduced spread at the northern and eastern margins. Despite this narrower distribution, the selected cases continue to sample the dominant outflow region relevant for UTLS moisture transport, indicating that the spatial characteristics of WCB outflow are well preserved.

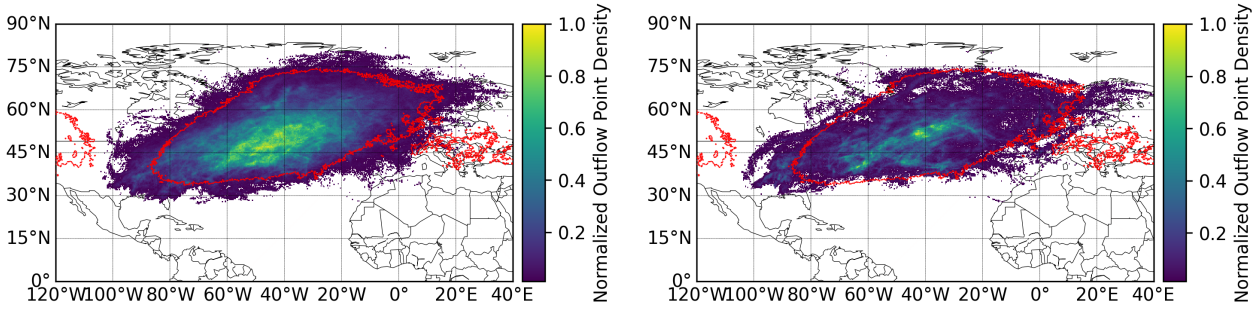

Figure 4.19: Normalized spatial density of WCB outflow points for (a) the full set of 300 inflow cases and (b) the final 50 selected cases. The color shading indicates the normalized density of outflow points, while the red contour marks the 1% WCB occurrence frequency contour derived from the ERA5-based 10-year climatological outflow mask, as defined in Chapter 3.

To assess moisture variability at the level of individual WCB events, Figure 4.20 shows the distributions of case-median water vapour (q_v) and condensate (q_h) at the outflow for the full set of 300 WCB cases (panels a, c), together with their joint correlation in logarithmic space (panel e). The distribution of median q_v spans roughly one order of magnitude across cases, with most values concentrated between $10^{-4.3}$ and $10^{-3.6}$ kg kg^{-1}, indicating substantial variability in outflow vapour content among individual WCB events. Median q_h values are systematically lower than q_v by approximately one order of magnitude, but likewise exhibit pronounced

case-to-case variability, demonstrating that condensate contributes a smaller but dynamically relevant fraction of the total outflow moisture budget. The scatter plot of median q_v versus q_h (panel e) reveals a strong positive correlation across the 300 cases, indicating that WCB events with enhanced water vapour tend to also also exhibit increased condensate content in the outflow. The corresponding distributions for the reduced subset of 50 cases (panels b, d, f) closely reproduce the range, central tendencies, and correlation structure of the full ensemble, with a modestly reduced spread attributable to the smaller sample size. This confirms that the reduced set retains the essential statistical characteristics of outflow moisture variability identified in the full dataset.

We next examine how outflow moisture depends on the ascent timescale for the selected cases. Figure 4.21 shows the distributions of total water, specific humidity, and condensed water at the end of WCB ascent as a function of their individual ascent timescale τ_{600}. Total water (Figure 4.21a) exhibits its largest values for the shortest ascent times. For the fast-ascending WCBs, specific humidity q_v is relatively low (Figure 4.21c), while condensed water dominates the total moisture content (Figure 4.21e), consistent with efficient condensation and ice formation under cold, rapidly cooling conditions (see also Section 3.3 and Schwenk and Miltenberger (2024)). Specific humidity q_v increases with increasing τ_{600}, indicating that slower ascent typically occurs at warmer temperatures, leading to reduced condensation and ice formation during ascent and a larger fraction of water remains in the vapour phase. Condensed water content is largest for fast ascent and decreases gradually with increasing τ_{600}. This behavior reflects more efficient condensation at cold temperatures during rapid ascent, followed by enhanced sedimentation and microphysical conversion of condensates, which progressively reduce the remaining condensed water in slower, warmer ascent regimes (Schwenk and Miltenberger, 2024). As a result, the relative contribution of water vapour to the total outflow moisture increases for slow-ascending WCBs, whereas fast-ascending WCBs contribute relatively more condensate to the total moisture. A similar dependence of outflow moisture on ascent timescale is evident for the reduced subset of 50 cases (panels b, d, f), indicating that the key physical controls linking ascent timescale and outflow moisture are robust across the ensemble.

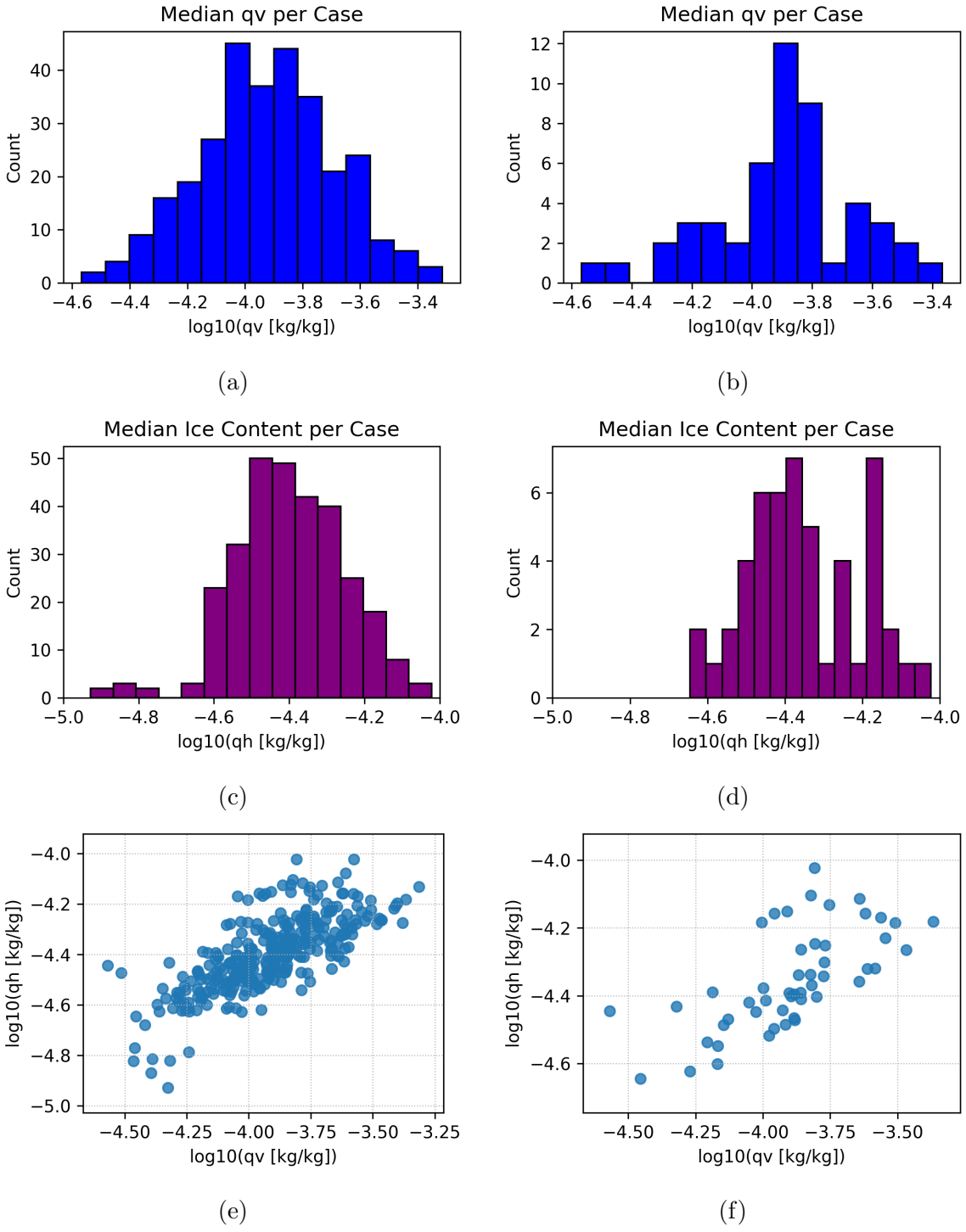

Figure 4.20: Panel (a) and (c) for histogram of median q_v and q_h in logarithmic scale and panel (e) for correlation of median q_h and q_v for 300 cases. Panel (b), (d) and (f) show the same distribution as the left column but for final 50 cases.

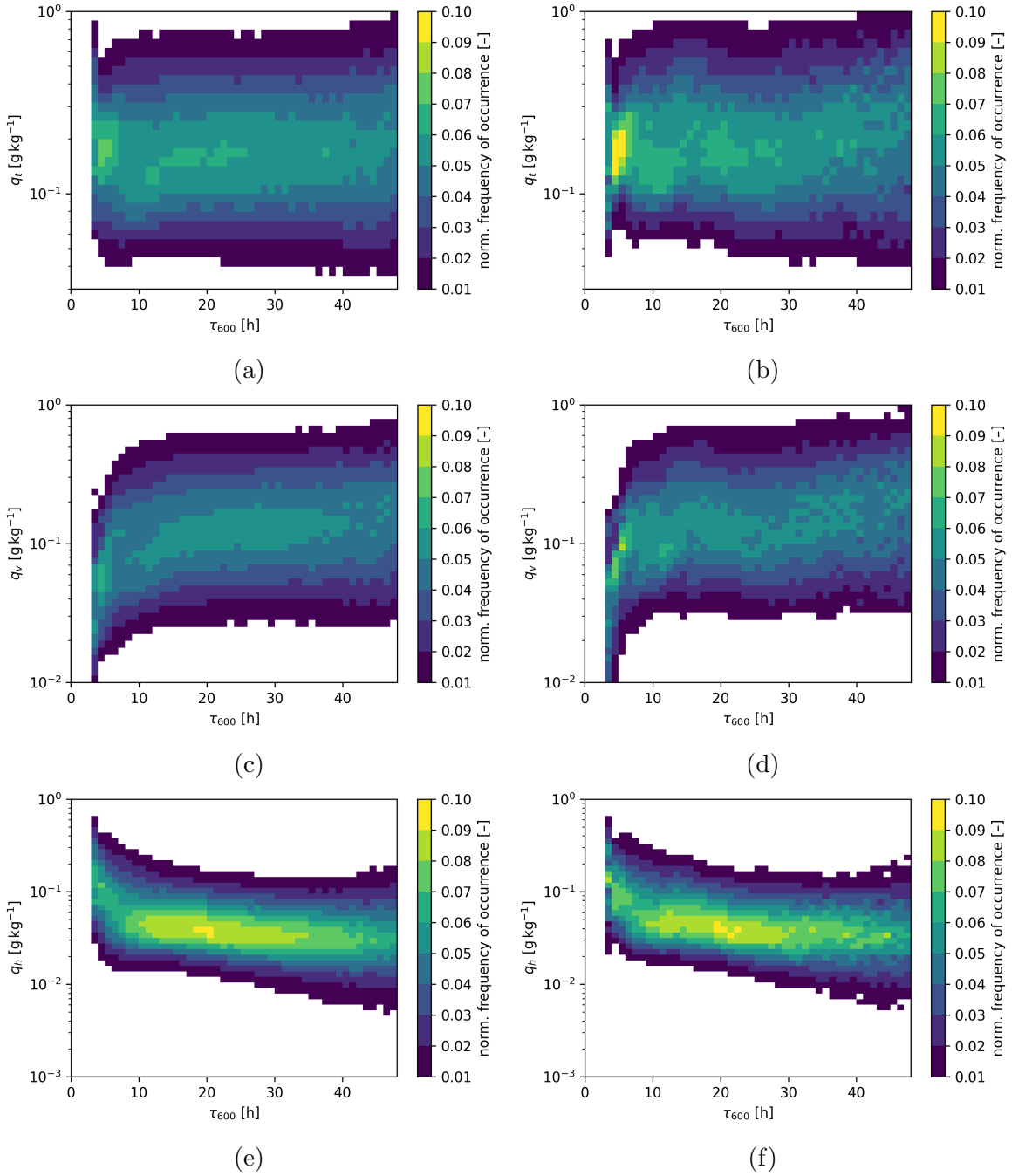

Figure 4.21: Panels (a), (c), and (e) show the distributions of total water, specific humidity, and condensed water, respectively, normalized by τ_{600}, at the end of WCB ascent as a function of τ_{600} for the full set of 300 cases. Panels (b), (d) and (f) show the same distribution for final 50 cases.

4.3.4 Correlation between inflow and outflow thermodynamic condition

In this section, we examine the relationship between inflow and outflow thermodynamic properties to assess the degree of memory retained along WCB ascent. Figure 4.22 shows normalized density plots of inflow versus outflow specific humidity (on a logarithmic scale) and temperature for the WCB ensemble.

Specific humidity exhibits a moderate positive correlation between inflow and outflow (r = 0.49), indicating that moister inflow environments tend to produce moister outflows. This relationship suggests that, despite substantial moisture loss during ascent, a large fraction of the variability in outflow vapour content is inherited from the inflow conditions, reflecting a partial retention of inflow moisture anomalies. Temperature also shows a clear positive correlation between inflow and outflow (r = 0.48, slope = 0.22). This reflects systematic cooling during ascent while preserving relative temperature differences between cases, such that warmer inflow air masses tend to remain warmer at outflow. A similar inflow–outflow relationship is evident for the reduced subset of 50 cases (panels c–d), confirming that the thermodynamic conditions and inflow-outflow correlations identified here are robust and not sensitive to the size of the ensemble.

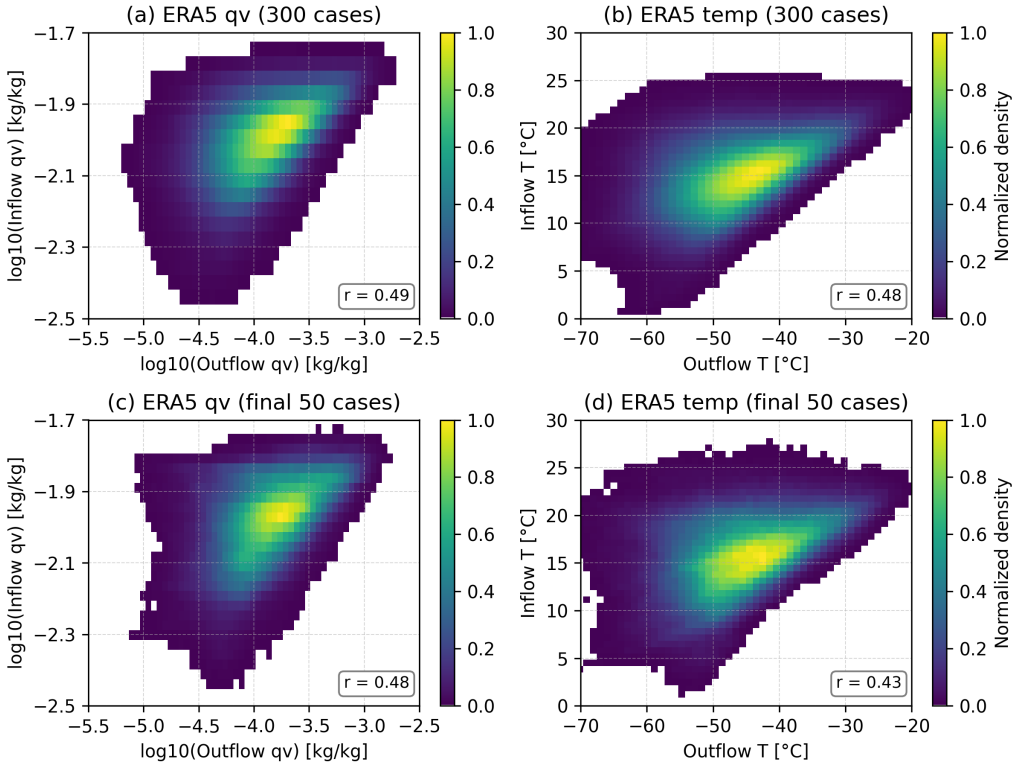

Figure 4.22: Correlations between inflow and outflow conditions for (a-b) the full 300-case ensemble and (c-d) the final 50-case subset (c–d). Panels (a, c) show specific humidity on a logarithmic scale, while panels (b, d) show temperature.

4.4 Summary

This chapter develops and validates a comprehensive framework to identify, track, and select representative WCB inflow cases, enabling a systematic assessment of how inflow variability relates to moisture transport into the UTLS. The analysis focuses on inflow-related initial conditions that seed WCB ascent and on their linkage to ascent timescale and outflow moisture properties. Building on the Eulerian inflow mask concept introduced by Heitmann et al. (2024), this study introduces a newly developed inflow-object tracking framework that enables the identification and characterization of individual WCB cases, providing the basis for a reduced yet climatologically representative case selection.

WCB inflow points are defined as the first point of the WCB ascent segment τ_{wcb} and inflated to a 100 km radius to construct spatially coherent inflow objects. These objects are tracked over time using an overlap-based criterion with a threshold of 0.3. After applying spatial constraints and requiring substantial meridional and zonal displacement over the track lifetime, a total of 300 inflow tracks are identified across all seasons over the North Atlantic.

To further reduce this dataset while retaining physical diversity, a three-dimensional selection framework is introduced. First, a combination of Dynamic Time Warping and the K-medoids method is applied to cluster the 300 cases into 20 groups based on their overall shape and curvature, regardless of differences in track lifespan. The second dimension accounts for the WCB ascent timescale (τ_{600}), while the third dimension represents track lifespans on a logarithmic scale. Uniform sampling within this metric space yields a 50-case subset that spans cluster diversity, ascent timescales, and lifespans. Seasonal distributions and track statistics confirm that this subset preserves the variability of the full dataset.

The results demonstrate that variability in the WCB inflow environment is systematically reflected in outflow moisture properties. Case-level statistics reveal a strong positive relationship between outflow water vapour and condensate content, indicating that variability in the vapour and condensed phases is tightly coupled across WCB events. Inflow–outflow correlations further show that moister inflow conditions tend to produce moister outflows, while warmer inflow air masses generally remain warmer at outflow, demonstrating a partial retention of thermodynamic characteristics along WCB ascent. The reduced subset of 50 cases reproduces these key relationships and variability patterns, confirming that it retains the essential statistical structure of the full ensemble.

The climatological analysis further indicates that different ascent timescales are associated with distinct outflow moisture signatures in terms of both water vapour and condensate con-

tent. While these results identify ascent timescale as an important parameter for outflow moisture variability, the physical mechanisms through how ascent rate modulates moisture transport and loss during ascent across different cases cannot be fully resolved at the reanalysis resolution. These process-level controls are therefore examined in detail in the following chapter using high-resolution simulations.

In summary, this chapter delivers a reproducible inflow object framework, a robust tracking and smoothing pipeline, and a physics sensible case selection strategy that yields 50 representative WCB cases. Extensive spatial, seasonal, and thermodynamic validation demonstrates that this subset captures the essential variability and key linkages between inflow conditions, ascent timescale, and outflow moisture. It therefore provides balanced and climatologically representative initial conditions for the high-resolution ICON ensemble simulations presented in the following chapters.

5 ICON Simulations of WCBs – Part 1: Case-Study Comparison of Summer and Winter WCB cases in ERA5 and the ICON Model

5.1 Introduction

Chapters 3 and 4 established a coherent climatological and statistical framework for understanding the role of warm conveyor belts (WCBs) in transporting moisture into the upper troposphere and lower stratosphere (UTLS). Using ERA5 reanalysis data, Chapter 3 quantified the contribution of WCBs to the UTLS moisture budget, while Chapter 4 demonstrated that variability in WCB inflow conditions and ascent characteristics is systematically linked to differences in outflow moisture properties. However, these analyses are based on a climatological perspective and therefore provide only limited insight into the physical processes that control moisture transport efficiency within individual WCB cases.

A central limitation of reanalysis-based diagnostics lies in the relatively coarse horizontal resolution of ERA5 (approximately 30 km) and the documented biases in UTLS moisture (e.g., Hersbach et al., 2020; Krüger et al., 2022). In high-resolution simulations, key mesoscale features such as embedded convection are more realistically represented, and cloud microphysical processes, although still parameterized, interact with a better-resolved dynamical environment. These processes play a critical role in shaping the distribution of vertical ascent, precipitation development, entrainment/detrainment of moisture (e.g., Rasp et al., 2016; Oertel et al., 2020; Schwenk and Miltenberger, 2024). Consequently, the processes controlling the efficiency of moisture transport to upper levels cannot fully resolved using reanalysis data alone.

To address these limitations, this chapter employs high-resolution simulations with the Icosahedral Nonhydrostatic (ICON) model at convection-permitting scales. These simulations explicitly resolve embedded convection within WCBs. Rather than attempting long-term, high-

resolution simulations that would require a prohibitively large ensemble to achieve climatological representativeness, a targeted case-study approach is adopted. This strategy allows for a detailed investigation of the mechanisms governing WCB moisture transport while maintaining a direct connection to the climatological context established in Chapter 3.

Building on the objectively selected and climatologically representative WCB cases identified in Section 4.2.4, this chapter investigates the physical processes governing moisture transport during WCB ascent using two contrasting high-resolution ICON simulations, representative of boreal summer and winter conditions. The analysis focuses on how differences in ascent timescale and season influence moisture loss pathways and the resulting UTLS moisture signal, and on how these process-level behaviours compare with ERA5-based diagnostics.

The analysis in this chapter is guided by the research question introduced in Section 1.5: *To what extent do mesoscale processes resolved in high-resolution ICON simulations affect UTLS moisture?* By explicitly resolving key mesoscale features, this chapter provides the physical interpretation required to link the statistical relationships identified in Chapter 4 to their underlying dynamical and thermodynamic mechanisms.

5.2 Method

5.2.1 ICON model setup

To simulate the high-resolution WCB cases, we use the Icosahedral Nonhydrostatic (ICON) modelling system, introduced in Section 2.3, with a configuration based on Schwenk and Miltenberger (2024). Each simulation is initialized from the ICON global domain at a horizontal resolution of approximately 13 km, shortly before the onset of the corresponding WCB event. The simulation period spans the full inflow track lifespan (as defined in Chapter 4) plus an additional 48 hours to capture the complete evolution of the WCB. A two-way nesting configuration is employed (see Section 2.3.1), in which two higher-resolution nests are embedded within the global domain. Two-way coupling ensures that the global domain provides lateral boundary conditions to the nests, while the nests feed back into the global field, maintaining a dynamically consistent environment (Zängl, 2013). For each WCB case, the global domain uses an R03B07 grid with a time step of 120 seconds. The two nested domains (R03B08 and R03B09) operate at higher resolutions with time steps of 60 and 30 seconds, respectively. As illustrated in Fig. 4.10, Domain 1 (R03B08, $\sim$ 6.5 km) and Domain 2 (R03B09, $\sim$ 3.3 km) fully cover the inflow track, ensuring that the main WCB ascent is resolved at convection-permitting scales.

This model setup ensures a physically consistent large-scale environment while enabling an explicit representation of convection and microphysical processes in the WCB region (Schwenk and Miltenberger, 2024). Explicitly, deep convection is parameterized only in the global domain using the Tiedtke–Bechtold scheme (e.g., Tiedtke, 1989; Bechtold et al., 2008), while only shallow convection is parameterized in the nested domains. All domains apply the standard ICON parameterizations for turbulence, gravity-wave drag (orographic and non-orographic) (e.g., Lott and Miller, 1997; Orr et al., 2010), and radiative transfer via the Rapid Radiative Transfer Model. Cloud microphysics are represented by the two-moment scheme of Seifert and Beheng (2006), which predicts both mass mixing ratios and number concentrations for cloud water, rain, ice, snow, graupel, and hail.

To track WCB air parcels in the high-resolution simulations, online trajectories are used as described in Section 2.3.4, based on the method of Miltenberger et al. (2013) and extended by Oertel et al. (2023). These trajectories are integrated directly using model wind fields, providing high temporal resolution of thermodynamic and microphysical tendencies. Trajectory output is written every 30 minutes. Initial regions are calculated along each inflow track across six vertical model levels between approximately 1000 and 800 hPa. Trajectory data are written to the highest resolution domain that contains the air parcel. If the parcel is located within Domain 2, the data are recorded in Domain 2. If it lies outside Domain 2 but within Domain 1, the data are stored in Domain 1. If the parcel is outside both nested domains, the data are written to the global domain.

5.2.2 Computation for microphysical factors

To investigate the physical processes governing the evolution of moisture during the ascent and in the WCB outflow, a Lagrangian framework is applied to derive variables that describe the temporal change of moisture within an air parcel. In the ICON output, the rates of individual microphysical processes are provided as instantaneous values, representing the local tendencies of condensation, evaporation, deposition, and other phase changes along each trajectory. To quantify the cumulative effect of these processes during the WCB ascent, the WCB segment is defined by its first and last time steps, $\tau_{\mathrm{WCB}} = [t(\mathrm{in}), t(\mathrm{out})]$, corresponding to the start and end of the ascent, respectively. For any microphysical variable X, the total change along the WCB is given by:

$$\Delta X = X(t(\mathrm{out})) - X(t(\mathrm{in})) \tag{5.1}$$

At any intermediate time $\tilde{t}$ during the ascent, the accumulated change relative to the starting point can be expressed as:

$$\Delta X(\tilde{t}) = X(\tilde{t}) - X(t(\mathrm{in})) \tag{5.2}$$

To quantify the key processes governing moisture evolution along WCB trajectories, a set of Lagrangian microphysical diagnostics is introduced in the following. These diagnostics capture how water vapour is converted into condensate, how condensate is removed through precipitation, and how the total moisture content of an air parcel changes during ascent.

Condensation Ratio (CR)

When air parcels ascend from lower to upper atmospheric levels, a portion of the contained water vapour is converted into condensate. This conversion is quantified by the condensation ratio (CR) (e.g., Barstad et al., 2007; Miltenberger, 2014; Schwenk and Miltenberger, 2024). The CR measures the fraction of available water vapour that is transformed into condensate during the ascent and is defined as:

$$\mathrm{CR}(\tilde{t}) = \frac{C_{\mathrm{hy}}(\tilde{t}) + E_{\mathrm{v}}(\tilde{t})}{\mathrm{VAP}(\tilde{t})} \tag{5.3}$$

Here, $C_{\mathrm{hy}}(\tilde{t})$ denotes the Lagrangian hydrometeor growth term, which represents the sum of all microphysical processes that convert water vapour into condensate. These processes include condensation ($\mathrm{cond}(\tilde{t})$), cloud condensation nuclei nucleation ($\mathrm{qcnuc}(\tilde{t})$), homogeneous and heterogeneous ice nucleation ($\mathrm{qihh}(\tilde{t})$), and deposition ($\mathrm{depo}(\tilde{t})$). The term $E_{\mathrm{v}}(\tilde{t})$ represents the Lagrangian vapour growth term, which accounts for the evaporation of cloud droplets and rain, as well as the sublimation of snow, graupel, hail, and ice.

The denominator, $\mathrm{VAP}(\tilde{t})$, approximates the initial vapour content of the air parcel. However, it excludes the water vapour introduced through turbulent or convective mixing ($\mathrm{qvturc}(\tilde{t}) + \mathrm{qvconv}(\tilde{t})$), as well as any residual water vapour terms $\Re(\tilde{t})$, following the approach of Schwenk and Miltenberger (2024). This ensures that the CR represents only the conversion of vapour intrinsic to the air parcel, independent of external moisture sources.

Precipitation Efficiency (PE)

After defining the CR, it is equally important to assess how effectively this condensate is subsequently removed from the air parcel as precipitation. The precipitation efficiency (PE) (e.g., Miltenberger, 2014; Dacre et al., 2023; Schwenk and Miltenberger, 2024) measures the fraction of condensate that precipitates out at a given time ($\tilde{t}$). While the CR characterizes the formation of hydrometeors from vapour, the PE describes their removal through precipitation, together providing complementary insights into the microphysical processes governing the

moisture budget during the WCB ascent. The PE is defined as:

$$\mathrm{PE}(\tilde{t}) = \frac{P(\tilde{t})}{C_{\mathrm{hy}}(\tilde{t}) + E_v(\tilde{t}) + \mathrm{HYD}(\tilde{t})} \tag{5.4}$$

Here, $\mathrm{P}(\tilde{t})$ denotes the Lagrangian net precipitation rate, which is computed as the time-integrated balance of hydrometeor mass (rain, snow, ice, graupel, and hail) entering and leaving the air parcel at time $(\tilde{t})$. This formulation ensures that only precipitation originating within the parcel is considered, rather than total surface precipitation. The terms $C_{\mathrm{hy}}(\tilde{t})$ and $E_{\mathrm{v}}(\tilde{t})$ are the Lagrangian hydrometeor and vapour growth terms, respectively, as defined in Eq. 5.3. The term $\mathrm{HYD}(\tilde{t})$represents the net initial condensate, defined analogously to $\mathrm{VAP}(\tilde{t})$, and accounts for the condensate present in the parcel at the onset of ascent.

Drying Ratio (DR)

During the ascent of an air parcel, moisture is progressively removed as altitude increases. The drying ratio (DR) is used to quantify the fractional loss of total water content within an air parcel during its ascent along a WCB trajectory (e.g., Miltenberger, 2014; Schwenk and Miltenberger, 2024). It represents the proportion of the initial total water (vapour plus condensate) that is lost through microphysical processes such as condensation, deposition, and precipitation. A higher DR indicates a more efficient removal of moisture from the air parcel, resulting in drier conditions in the outflow, whereas a lower DR suggests that a larger fraction of the initial moisture is retained. The DR is defined as:

$$\mathrm{DR} = \frac{q_{\mathrm{tot,in}} - q_{\mathrm{tot,out}}}{q_{\mathrm{tot,in}}} \tag{5.5}$$

Here, $q_{\mathrm{tot,in}}$represents the total water content (vapour plus condensate) at the beginning of the ascent, and $q_{\mathrm{tot,out}}$ is the total water content at the end of the ascent. The DR is evaluated along the WCB ascent and does not include the processes occurring near the surface prior to start of τ_{WCB}

Following Schwenk and Miltenberger (2024), the DR can be further decomposed to distinguish between different mechanisms of moisture removal. The first component, the mixing drying ratio ($\mathrm{DR_{mix}}$), quantifies the fraction of total moisture lost due to mixing processes and is defined as:

$$\mathrm{DR_{mix}} = \frac{q_{\mathrm{tcr,out}}}{q_{\mathrm{tot,in}}} \tag{5.6}$$

Here, $q_{\mathrm{tcr,out}}$ represents the reduction of total water caused by the turbulent and convective mixing with the surrounding air by the end of the ascent. This exchange reduces the parcel's total water content without necessarily involving microphysical phase changes. Consequently,

DR_{mix} characterizes the contribution of subgrid-scale and mesoscale mixing to the overall drying of the air parcel.

After the effects of mixing are accounted for, the remaining moisture in the form of hydrometeors can be further removed through precipitation. This process is described by the microphysical drying ratio (DR_{mphys}), defined as:

$$DR_{mphys} = \frac{P_{out}}{q_{tot,in} - q_{tcr,out}} \tag{5.7}$$

Here, P_{out} is the net precipitation at the end of the ascent as defined in Eq. 5.4.The term DR_{mphys} thus represents the fraction of remaining moisture that is removed by microphysical processes such as condensation growth followed by precipitation. It highlights the efficiency of the precipitation pathway in depleting the parcel's moisture content after non-microphysical mixing losses. Together, DR_{mix} and DR_{mphys} provide a physically meaningful decomposition of the total drying ration, enduring that DR_{mphys} exclusively accounts for precipitation-driven moisture loss following the effects of mixing.

Interpretation of microphysical processes

The combined interpretation of CR, PE, and DR provides a framework to distinguish between different microphysical regimes within WCBs. Again, each of these indicators reflects a specific aspect of cloud–precipitation evolution: CR represents condensation and accretion processes associated with cloud formation, PE characterizes precipitation growth through aggregation and riming, and DR captures the drying effects of sublimation and evaporation. By analyzing the joint behavior of these three components, it becomes possible to infer the dominant pathways of water transformation and removal in different WCB environments. To illustrate this, a set of theoretical edge cases can be defined by combining high and low values of CR, PE, and DR. These combinations help to conceptually interpret the range of possible microphysical states—from vigorous cloud growth and efficient precipitation production to regimes dominated by evaporation and dissipation. Together, they form a useful reference for understanding how moisture is processed and ultimately removed from ascending air parcels within WCBs.

1. High CR, High PE, High DR.
   Strong condensation and precipitation growth indicate vigorous cloud development, and high DR suggests that only a small fraction of the initial moisture is retained within the ascending air parcel. Consequently, the WCB experiences pronounced dehydration, leading to relatively dry conditions in the outflow.

2. High CR, High PE, Low DR.
   Strong condensation and precipitation growth but weak drying during the parcel's ascent. This regime represents efficient warm or mixed-phase cloud development, where microphysical conversion is active yet moisture removal is limited, resulting in substantial total water retained within the outflow.

3. High CR, Low PE, High DR.
   Strong condensation occurs, but precipitation growth is weak. A large portion of the condensate subsequently evaporates or mixes into surrounding dry air, leading to inefficient moisture retention and a relatively dry outflow despite strong condensation earlier in the ascent.

4. High CR, Low PE, Low DR.
   Represents the early or non-precipitating stage of cloud development, with vigorous condensation but limited conversion to precipitation and minimal evaporation. Most of the condensed water remains within the cloud, resulting in a moist outflow.

5. Low CR, High PE, Low DR.
   This combination is physically inconsistent. If CR is low but PE is high, there must be pre-existing condensate from an earlier phase. However, with low DR indicating limited total-water loss, substantial precipitation is unlikely to persist.

6. Low CR, Low PE, Low DR.
   Characterizes a stable, microphysically inactive regime with minimal condensation, precipitation, and evaporation. The low DR indicates that little moisture is removed during ascent, so the outflow remains relatively moist, although weak CR and PE suggest that this moisture is largely residual rather than actively processed.

5.3 Case 1: A Representative Summer WCB Event

Before turning to the broader ensemble analysis, we begin with two representative case studies from different seasons to compare ICON and ERA5 on a case-by-case basis from a process-oriented perspective. These detailed analyses provide physical insight into how both datasets capture the thermodynamic and microphysical evolution of WCBs during individual events. The first case, shown in Fig. 5.1, began on 25 August 2015 at 03 UTC, with WCB inflow trajectories originating over the subtropical western Atlantic near 37–45° N, 25-0° W. The air parcels ascended ahead of the developing cyclone and followed a northeastward path toward northern Europe. Figure 5.1 illustrates the corresponding inflow track (blue), inflow points (green), and outflow points (orange) derived from ERA5 trajectory data. The WCB inflow has a lifespan of 57 h and a total travel distance of 3457.49 km.

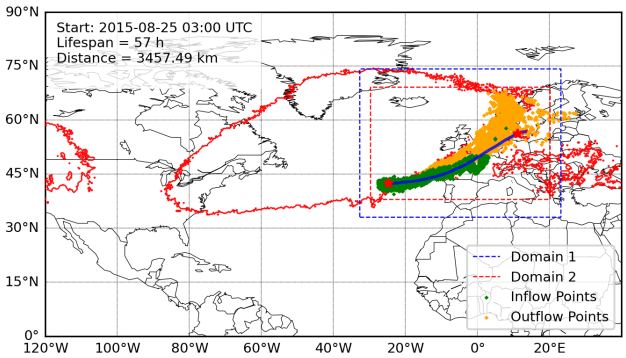

Figure 5.1: WCB event on 25 August 2015 at 03 UTC from ERA5, showing the inflow track (blue), inflow points (green), and outflow points (orange). The two stars mark the initial 48-hour time window of the inflow evolution. The nested ICON simulation domains are outlined by the blue dashed box ($\sim$ 6.5 km) and the red dashed box ($\sim$ 3.3 km).

For the analysis of correlations between inflow and outflow thermodynamic properties, only inflow and outflow points occurring within the lifetime of the inflow track are considered. This temporal constraint may lead to a underestimation of the number of valid WCB trajectories identified in the ERA5 dataset.

5.3.1 Selection of WCB trajectories

To select WCB from ICON simulations, we adopted a similar approach to select WCBs as for ERA5 dataset, with some additional refinements. First, the same trajectory-based WCB detection algorithm was applied, identifying for each trajectory the shortest time window required to complete a 600 hPa ascent (τ_{600}). The full active ascent duration, denoted by τ_{WCB}, was obtained by extending the τ_{600} segment both backward and forward in time until the vertical

velocity dropped below 8 hPa h^{-1}. The first and last points of this extended segment define the inflow and outflow of each WCB trajectory.

Second, the detected WCBs were spatially constrained to two visually determined regions of enhanced WCB activity, identified from the Eulerian high-cloud cover and sea-level pressure fields (see Appendix Fig. A.15) following Schwenk and Miltenberger (2024). In addition, a geographic displacement filter was applied, requiring each trajectory to travel at least 5° northward or 5° eastward during its ascent period (τ_{WCB}). This criterion acts as a physical quality control, ensuring that retained trajectories exhibit coherent poleward or eastward motion characteristic of WCB ascent in the warm sector, while allowing for the inclusion of rapidly ascending convective WCBs that are especially common in summer and may show limited horizontal displacement. As a result, 733 trajectories were excluded from the initial 140982 trajectories(Fig. 5.2 a). The excluded trajectories either traveled only short distances during ascent or propagated southward, away from the cyclone development region.

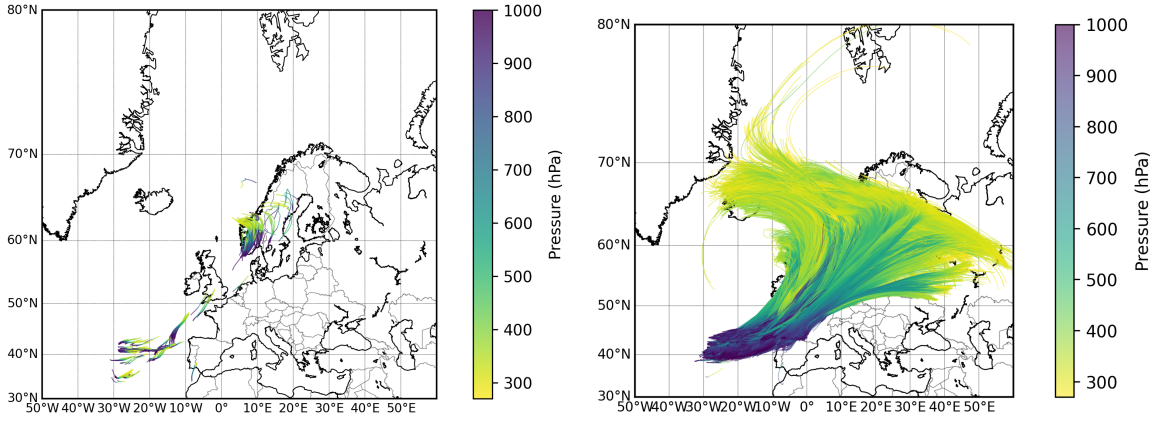

(a) (b)

Figure 5.2: (a) Trajectories excluded from the subsequent analysis. (b) Valid WCB trajectories retained after applying the selection criteria described in Section 5.3.1. ICON-simulated WCBs initialized at the same time as in ERA5 (25 August 2015 at 03 UTC).

After applying the geographic filter, the remaining WCB trajectories for this case are shown in Fig. 5.2 b. In total, 140249 trajectories remained, of which 10.4% are classified as fast-ascending ($\tau_{600} \leq 10$ h), 45.9% as normal ($10 \leq \tau_{600} \leq 30$ h), and 43.7% as slow ($\tau_{600} > 30,$ h h). The distribution of τ_{600} and τ_{WCB} for this case is shown in Fig. 5.3. Both distributions exhibit two distinct peaks, with τ_{WCB} being systematically longer than τ_{600}, consistent with the climatological patterns shown in Fig. 3.11a. With the WCB trajectories successfully identified and categorized according to their ascent timescales, we next compare the behavior of these simulated WCBs with those derived from the ERA5 dataset. This comparison serves to evaluate

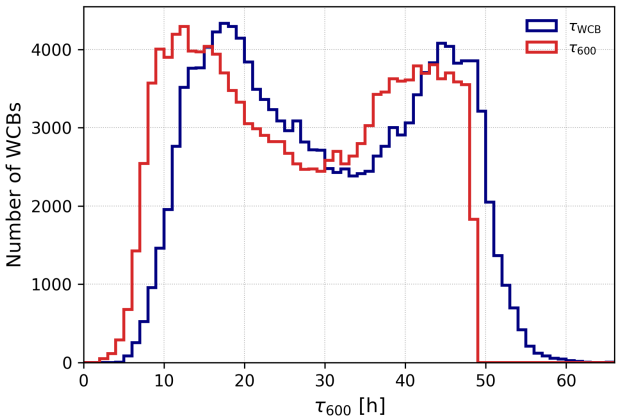

Figure 5.3: Distribution of WCB trajectory durations for the fastest ascent phase (τ_{600}, red) and for the full ascent phase (τ_{WCB}, navy).

how the explicitly resolved convection and microphysical processes in the high-resolution ICON simulations influence the structure and evolution of WCBs, relative to the more parameterized representation in ERA5. By contrasting these properties between ICON and ERA5, we aim to better understand how model resolution and physical parameterizations affect the depiction of WCB dynamics and the associated transport of moisture into the UTLS.

5.3.2 Comparison of inflow synoptic conditions

To better understand the origin of these differences and their relationship to the large-scale flow, we firxt examine the corresponding Eulerian fields from both datasets. In particular, we compare the evolution of mean sea-level pressure (MSLP) and cloud structures from high-cloud cover (HCC) to assess how variations in the synoptic environment and cyclone intensity may influence the identified WCB trajectories and their ascent characteristics. Note that the comparison is limited to the finest ICON domain (3.3 km, Domain 2 in Fig. 5.1), while the online trajectories are calculated over all domains.

Figure 5.4 shows the evolution of mean sea-level pressure (MSLP) fields from the ICON simulation (left column) and ERA5 reanalysis (middle column), together with their differences (right column) for four selected times between 25 and 27 August 2015. At the initial stage (25 August, 18:00 UTC), both datasets illustrate a broad low-pressure system centered west of the British Isles, with comparable intensity and horizontal structure. In addition, a secondary low-pressure center is evident over the North Sea near 60°N and 0° longitude, likely related to an earlier cyclonic feature and not yet fully dissipated. Over the following 24 hours, the system deepens and moves northeastward, gradually merging into a single, dominant system

while maintaining a similar synoptic-scale evolution in both ICON and ERA5. By 26 August, 18:00 UTC, subtle differences become large, with ICON showing slightly lower central pressure values and a more compact low-pressure core compared to ERA5 (see in right panel). This difference becomes more pronounced by 27 August, 06:00 UTC, when the ICON simulation develops a distinctly deeper cyclone center and stronger pressure gradients around the core region. The difference panels confirm this behavior, with negative values (blue shading) indicating that ICON produces systematically lower MSLP than ERA5 during the mature stage of the cyclone's development. The deepening of the low-pressure system in ICON suggests a more dynamically active evolution, consistent with its finer horizontal resolution and explicit representation of convection and mesoscale processes.

Figure 5.5 presents the temporal evolution of high-cloud cover (HCC) from the ICON simulation (left), ERA5 (middle), and their differences (right) for times between 25 and 27 August 2015. During the early stage (25 August, 18:00 UTC), both datasets capture a band of enhanced high-cloud cover extending from the North Atlantic toward western Europe, marking the region of outflows and cirrus clouds ahead of the surface cyclone. The overall cloud patterns are similar, although ICON simulates more localized and well-defined high-cloud structures in the core ascent and outflow region, whereas ERA5 shows broader and smoother cloud fields. By 26 August, 06:00 UTC, the high-cloud region becomes more pronounced and expands northeastward over the British Isles. At 26 August, 18:00 UTC, the two datasets begin to diverge more clearly. ICON produces a broader and more continuous high-cloud region that extends further westward over northern Britain. These features are largely absent in ERA5. This westward extension coincides with the cyclonic branch of the WCB, which is more distinctly represented in ICON. By 27 August, 06:00 UTC, ICON maintains an expansive high-cloud shield over northern Europe extending toward Iceland, while ERA5 depicts substantial dissipation. The difference panel (Fig. 5.5d) shows positive anomalies in these areas, confirming the stronger and more spatially extensive high cloud cover in ICON simulation.

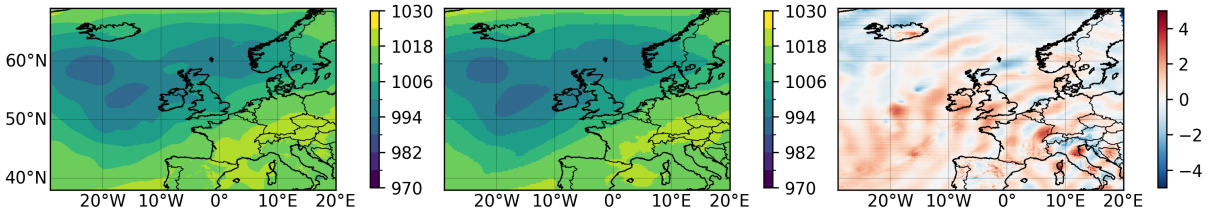

(a) 2025 August 25th, 18:00 UTC

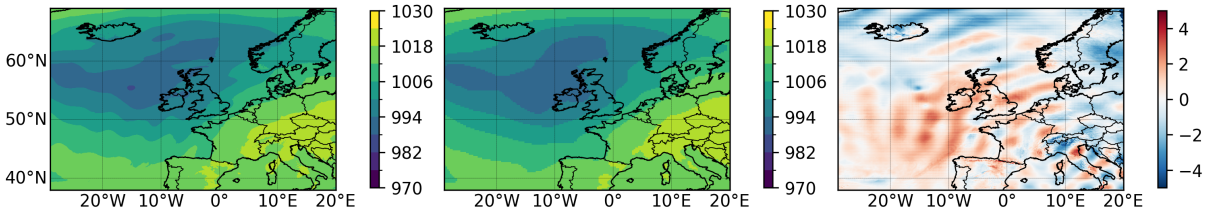

(b) 2025 August 26th, 06:00 UTC

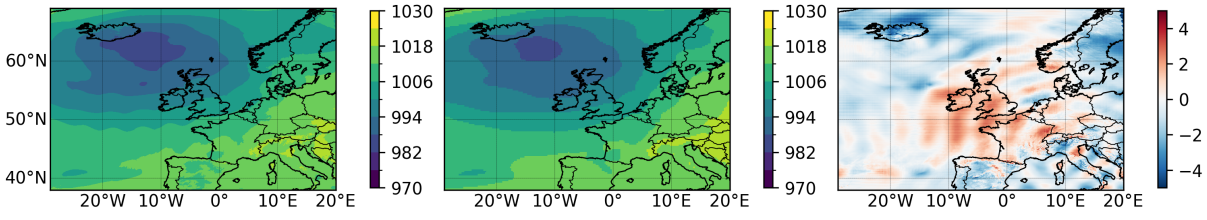

(c) 2025 August 26th, 18:00 UTC

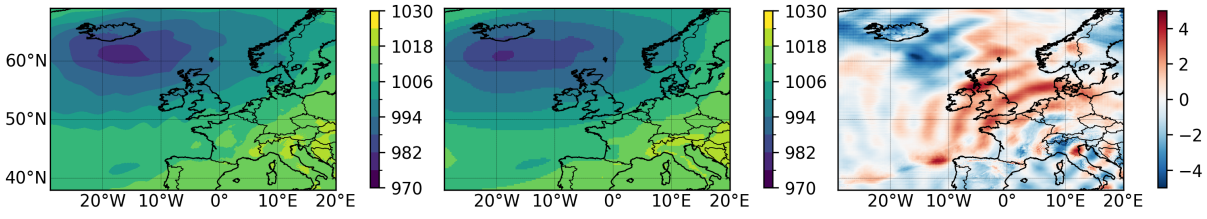

(d) 2025 August 27th, 06:00 UTC

Figure 5.4: Temporal mean sea-level pressure (MSLP) from ICON (left panels), ERA5 (middle panels), and their differences (right panels, ICON minus ERA5), shown at 12-hour intervals from 25 to 27 August 2015.

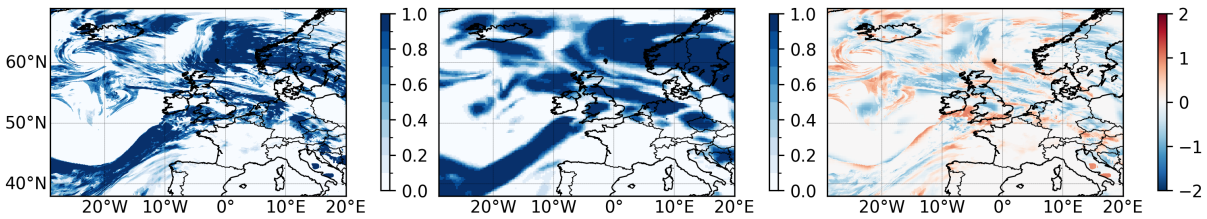

(a) 2025 August 25th, 18:00 UTC

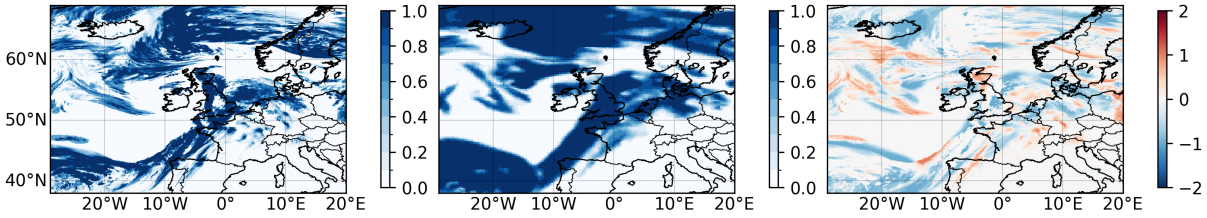

(b) 2025 August 26th, 06:00 UTC

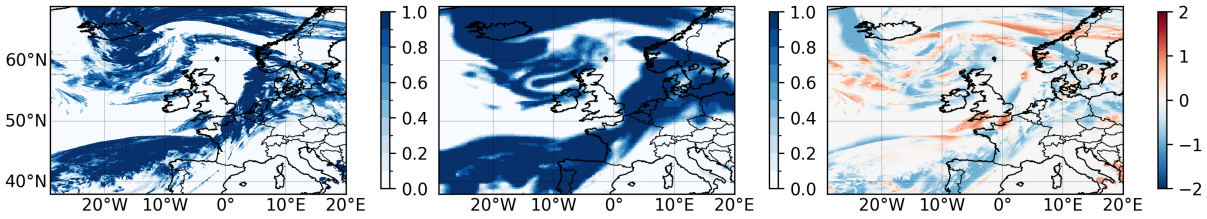

(c) 2025 August 26th, 18:00 UTC

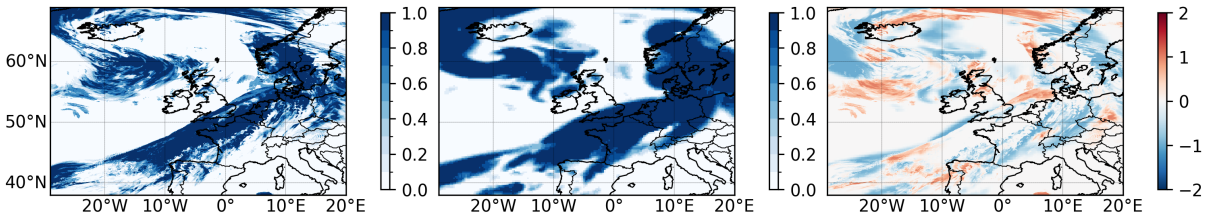

(d) 2025 August 27th, 06:00 UTC

Figure 5.5: Temporal evolution of high cloud cover (HCC) from ICON (left panels), ERA5 (middle panels), and their differences (right panels, ICON minus ERA5), shown at 12-hour intervals from 25 to 27 August 2015.

5.3.3 Comparison of ascent statistics

The distribution of ascent timescales (τ_{600}) differs markedly between the ICON simulations and the ERA5 dataset shown in Fig. 5.6a. In ERA5, the τ_{600} histogram exhibits a single, well-defined peak centered around 15–20 h, indicating a relatively uniform population of WCB trajectories dominated by large-scale, slantwise ascent. In contrast, the ICON distribution is broader and exhibits two distinct maxima with one occurring at approximately 10 to 15 h and another near 40 h. This bimodal structure reflects two ascent regimes within the high resolution model with one associated with rapid convective updrafts and the other corresponding to slower more slantwise ascent driven by synoptic scale forcing. We further project the ICON and ERA5 inflow points onto MSLP fields for the slow ascending branch at different time steps, as shown in Appendix Fig. A.16. In ERA5, slow WCB inflow points primarily appear during the early stages of the system. In contrast, ICON slow WCB inflow points are more strongly associated with a separate secondary low pressure center that is detached from the main system starting from 26 August 2015 at 18 UTC on the southern flank near 40°N and 20°W. This subset of slow WCBs is entirely absent in ERA5.

In comparison, the narrower ERA5 distribution likely arises from its parameterized vertical motions, which produce smoother and more homogenized ascent behavior. The normalized frequency distributions of WCB outflow pressure shown in Fig. 5.6b are more similar between ICON and ERA5. Both datasets peak near 300 hPa and show similar overall distributions, with a more concentrated peak in ICON and a slightly broader spread in ERA5, while the characteristic outflow level remains comparable.

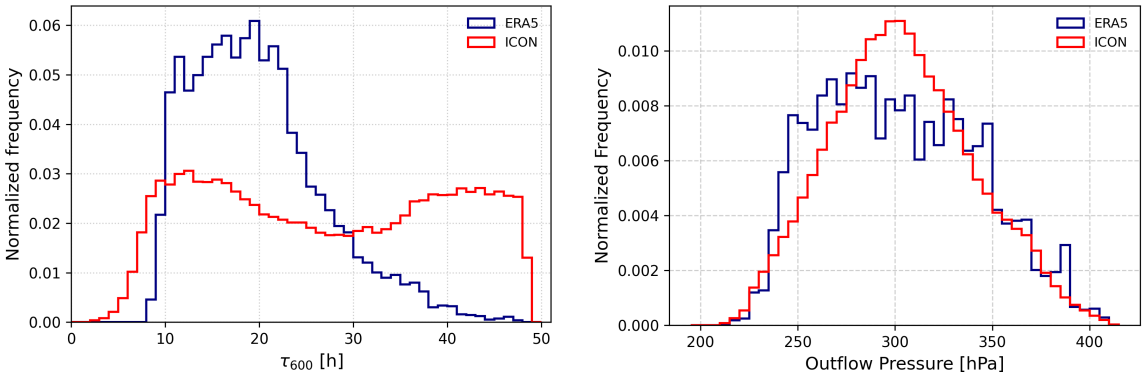

(a) (b)

Figure 5.6: Normalized frequency distributions of WCB trajectories as a function of (a) ascent timescale (τ_{600}) and (b) outflow pressure level. ICON data are shown in red and ERA5 data in navy.

Spatial distribution of WCB inflow and outflow

The Eulerian comparison indicates that ICON simulates a more dynamically active cyclone and a broader, more rapidly developing WCB system than ERA5. To examine how these large-scale differences manifest along individual air parcel pathways, we now turn to a Lagrangian analysis of the identified WCB trajectories, focusing on their outflow structure and kinematic characteristics. We first analyze the temporal evolution of outflow points (Fig. 5.7), which supports the differences in cloud evolution described above. In ICON, outflow points appear earlier than in ERA5 along the high cloud band and exhibit a faster poleward and eastward propagation, indicating a more dynamically active and faster-developing WCB. During the later stages, particularly after 26 August, 18:00 UTC, regions of enhanced HCC in ICON align closely with the simulated outflow pathways, whereas ERA5 outflows remain less extensive westward and more confined to northern Europe. These results suggest that ICON simulates a more vigorous WCB ascent with stronger cyclonic propagation and broader spatial extent in this case.

We next compare the geographic distribution of inflow and outflow points for the different ascent timescales (τ_{600}). Figure 5.8 compares the spatial distribution of (a) inflow and (b) outflow points between ICON (colored by pressure) and ERA5 (red). For ICON, the WCBs are categorized into fast-ascending ($\tau_{600} \leq 10$ h), normal-ascending ($10 < \tau_{600} < 30$ h), and slow-ascending ($\tau_{600} \geq 30$ h) groups. In the inflow region (panel a), both ICON and ERA5 indicate WCB initiation over the subtropical North Atlantic, with inflow points concentrated between 40°N–50°N and west of 30°W–0°W. The ERA5 inflow points form a narrower band compared to ICON, primarily because only points within a 5°×5° box along each inflow track were selected to ensure a consistent inflow–outflow correlation analysis.

With increasing τ_{600}, ICON inflows become more dispersed and shift northeastward, indicating that slower-ascending WCBs originate further downstream and contribute to both cyclonic and anticyclonic branches visible in the outflow region (panel b). Fast-ascending WCBs terminate mainly over northern Europe without exhibiting a distinct curvature, whereas the normal-ascending branch already shows a clear split into cyclonic and anticyclonic pathways with enhanced eastward propagation. The slow-ascending WCBs extend even further, spreading northwestward toward Greenland and eastward beyond 50°E, reflecting a broader spatial influence.

In ICON, the inflow regions associated with the normal- and slow-ascending branches extend further northeastward, covering much of the North Sea and parts of Scandinavia. As shown in Fig. 5.4, an additional low-pressure center is present over the North Sea during the early stage of cyclone development, likely associated with a previous cyclone system. This feature may

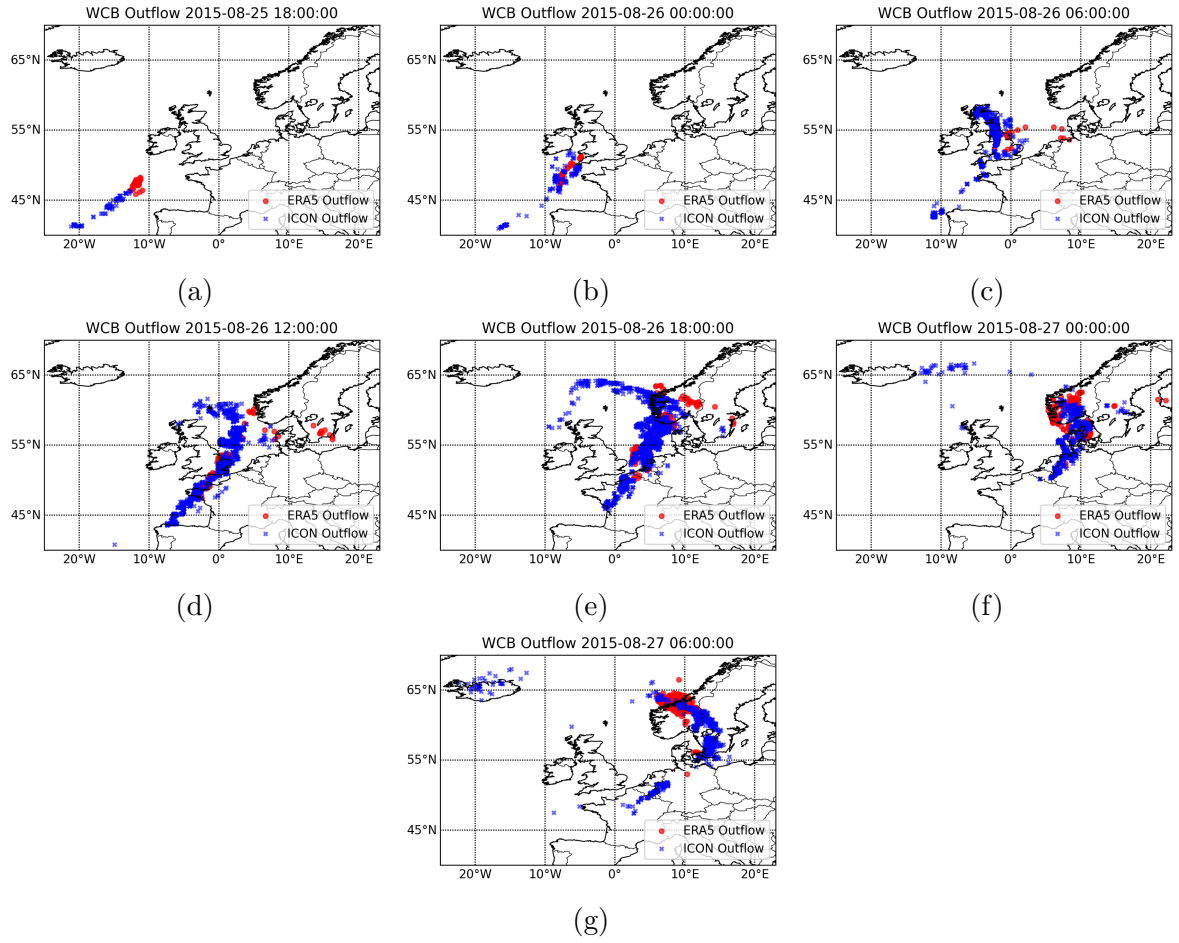

Figure 5.7: Comparison of WCB outflow locations in ERA5 and ICON at corresponding times during the event of 25–27 August 2015. Panels (a–g) show the temporal evolution of outflow points, with ERA5 outflow locations indicated in red and ICON outflow locations in blue.

influence the WCB inflow pathways in the ICON simulation, particularly for trajectories with $\tau_{600} \geq 30$ h, and could contribute to the secondary peak in slow-ascending WCBs observed in Fig. 5.6.

Overall, this comparison highlights systematic differences between ICON and ERA5, with ICON producing deeper, faster, and spatially more extensive WCBs, while ERA5 WCBs remain more confined, consistent with their smoother vertical motions and also influenced by the inflow–outflow selection applied in the analysis.

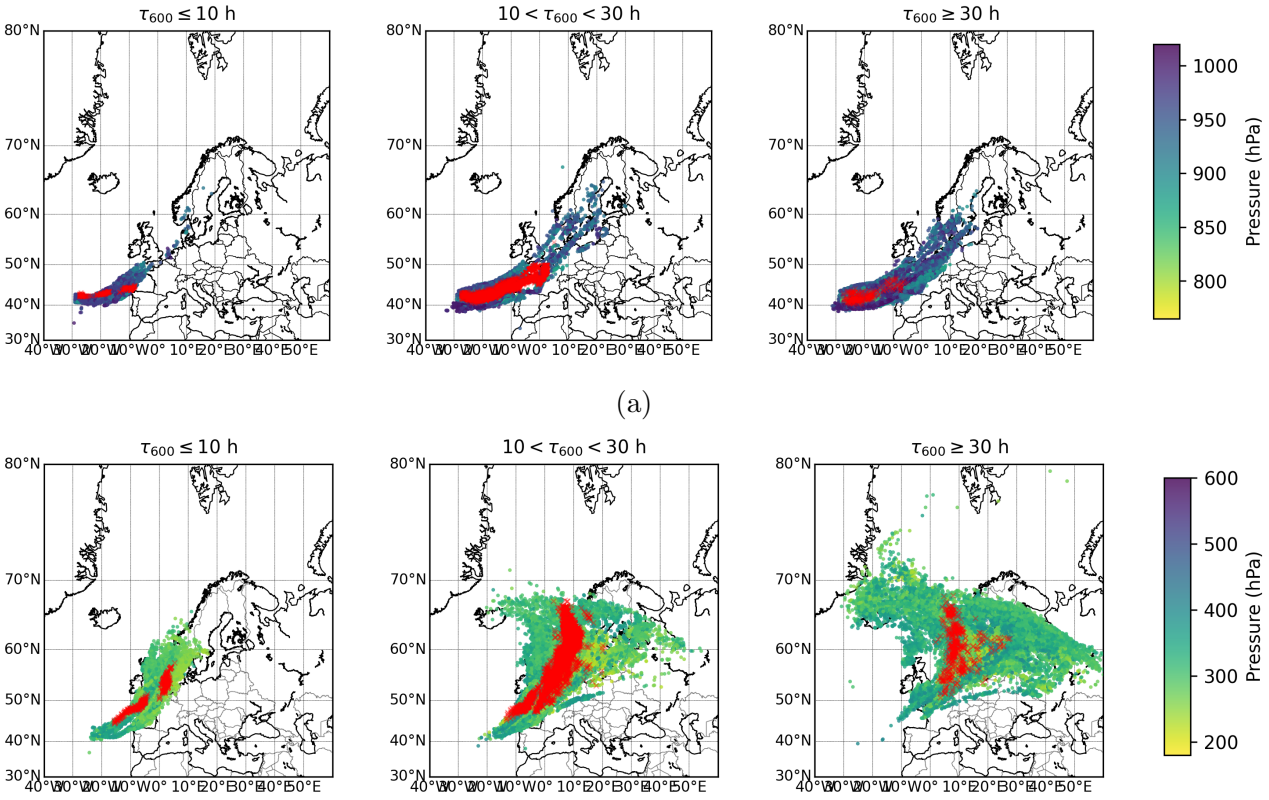

Figure 5.8: Comparison of (a) inflow and (b) outflow points between ICON (colored by pressure) and ERA5 (red) for fast-ascending WCBs ($\tau_{600} \leq 10$, left panel), normal-ascending WCBs ($10 < \tau_{600} < 30$, middle panel), and slow-ascending WCBs ($\tau_{600} \geq 30$, right panel).

5.3.4 Comparison of trajectory characteristics

Temperature and pressure evolutionn along τ_{600}

The spatial analysis of inflow and outflow distributions highlights clear structural and dynamical differences between the ICON and ERA5 WCBs. To better understand how these contrasts influence the parcel properties along individual trajectories, we now examine the thermodynamic characteristics of the WCBs at their inflow and outflow stages, focusing on differences in pressure, temperature and moisture between the two datasets.

Figure 5.9 presents the inflow and outflow pressure and temperature as a function of the ascent time τ_{600} for both ICON (red) and ERA5 (grey). At the inflow stage, fast-ascending WCBs in ICON originate on average at slightly higher temperatures and lower pressures than ERA5, indicating that the high-resolution simulations captures a somewhat warmer and deeper source region for the fast WCB air parcels. The normal- and slow-ascending WCBs exhibit similar thermodynamic characteristics in both datasets, consistent with their comparable synoptic ini-

tial conditions discussed in the previous section.

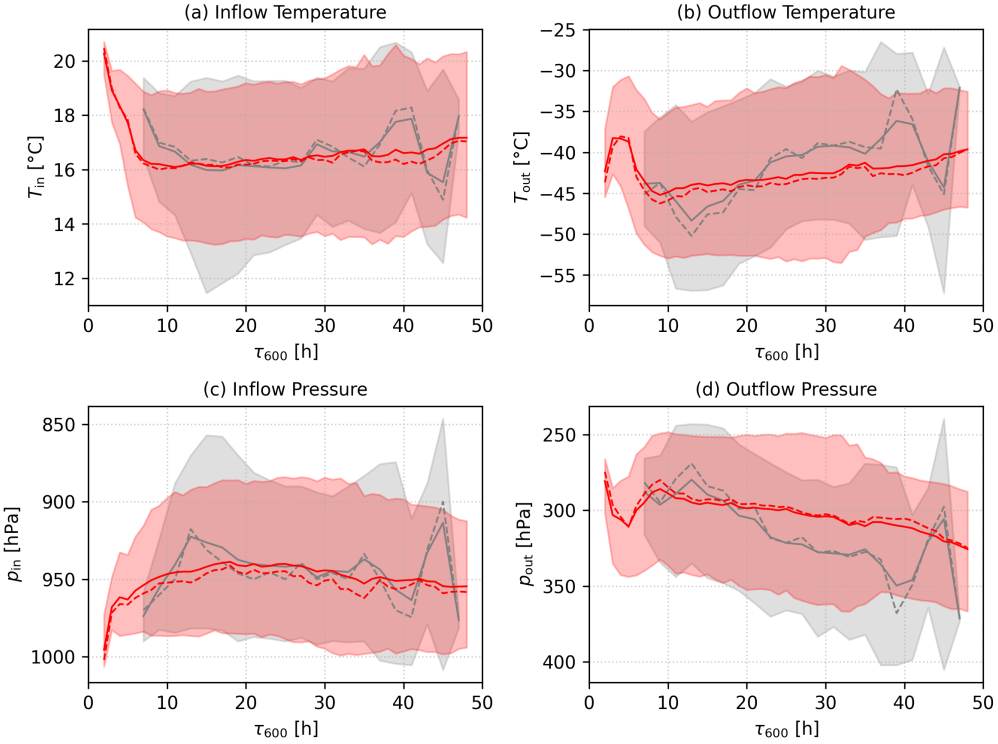

Figure 5.9: Comparison of inflow and outflow (a–b) temperature and (c–d) pressure as a function of τ_{600} for ICON (red) and ERA5 (grey). Solid (dashed) lines show mean (median) values. Shading denotes the 10th–90th percentile range.

At the outflow stage, ICON trajectories reach systematically higher levels with the temperatures 0-5°C lower than ERA5 (see the mean values comparison in Appendix Fig. A.18a-d). In addition, we compare the vertical ascent distance between ICON and ERA5 (see Appendix Fig. A.18e–f). For the normal- and slow-ascending WCBs, ICON exhibits a larger vertical displacement than ERA5, indicating that the total vertical displacement of ICON WCB air parcels is approximately 0–25 hPa larger than that in ERA5. This reflects a deeper and more vigorous vertical transport in ICON, where the explicit representation of convection facilitates faster ascent to higher altitudes and enhanced diabatic effects compared to ERA5.

Moisture evolution along τ_{600}

Figure 5.10 illustrates the evolution of total water (q_t, grey), water vapour (q_v, green), and condensate (q_h, blue) along the ascent timescale τ_{600} for (a–b) ICON inflow and outflow and (c–d) ERA5 inflow and outflow. The condensate component q_h is shown on a separate right-hand axis to facilitate comparison with the much larger magnitudes of q_v and q_t.

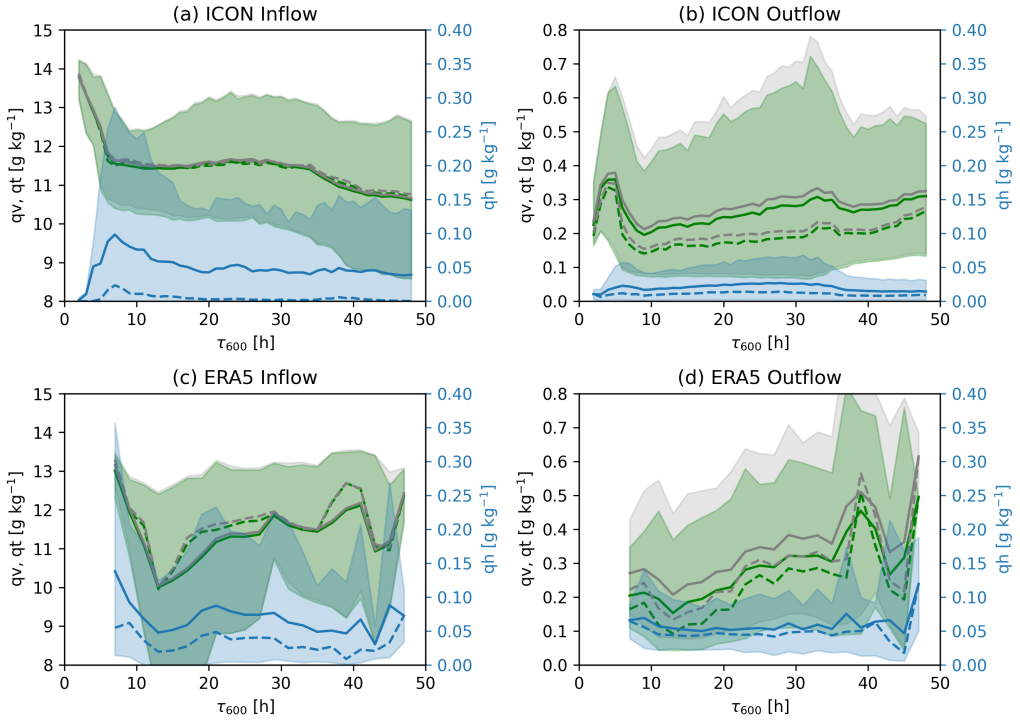

Figure 5.10: Comparison of total water (q_t, grey), water vapour (q_v, green), and condensate (q_h, blue) as a function of τ_{600} for inflow and outflow. Panels (a–b) show ICON and panels (c–d) ERA5. Solid (dashed) lines show mean (median) values. Shading denotes the 10th–90th percentile range. A separate axis on the right-hand side is used for q_h.

At the inflow stage, ICON exhibits higher total water content than ERA5 for the normal-ascending WCBs, with differences of about 0–1.4 g kg^{-1} while for fast and slow branches, ICON inflow exhibits a bit lower total moisture compared to ERA5 (see Appendix Fig. A.19a). The gradual decrease in total water with increasing τ_{600} in ICON indicates that more slowly ascending WCBs tend to originate in comparatively drier and more baroclinic environments located further downstream. The condensate mixing ratio q_h remains small at the inflow stage across most ascent timescales. A modest enhancement for the fast WCBs likely reflects early cloud formation associated with shallow convection or localized uplift in very moist near-surface air.

At the outflow stage, both datasets exhibit a substantial reduction in q_v and q_h as a result of condensation and precipitation losses during ascent. In ICON, both q_v and q_h exhibit two distinct peaks for fast WCBs and for τ_{600} around 30 h, indicating that fast-ascending WCBs transport larger amounts of moisture into the upper troposphere (see the logarithmic scale in Fig. 5.11a) into the upper troposphere. The first peak signal is less pronounced in ERA5. For $\tau_{600} > 20$ h, ICON outflow contains lower mean water vapour than ERA5, which may be related to the systematically higher outflow altitudes in ICON (Fig. 5.9d). In contrast, ICON exhibits

consistently lower condensate amounts at outflow compared to ERA5 (Appendix A.19c–d).

Overall, ICON exhibits a stronger dependence of moisture transport on ascent timescale, with enhanced inflow and outflow moisture for fast-ascending WCBs and a secondary maximum associated with slower ascent. In contrast, ERA5 shows a weaker sensitivity to ascent rate, capturing comparable outflow moisture for the normal and slow categories while lacking the enhanced signal for fast ascent.

Distribution of outflow moisture components along τ_{600}

To further examine differences in outflow moisture components between ICON and ERA5 as a function of ascent timescale, we present probability density functions of outflow moisture components normalized by τ_{600} (Fig. 5.11). In ICON, all water components (Figs. 5.11a,c,e) exhibit a pronounced maximum for the fast-ascending branch, as well as a secondary maximum around $\tau_{600} \approx 30$ h associated with the slow-ascending branch. This secondary peak indicates that a subset of WCBs linked to preceding cyclone systems contributes enhanced moisture to the outflow.

In contrast, ERA5 displays a more dispersed distribution, partly due to the smaller number of valid WCB samples. Nevertheless, the overall dependence of outflow moisture on ascent timescale in ERA5 is broadly consistent with the ICON results. However, the ERA5 condensate signal is primarily confined to the 10^{-1}–10^{-2} g kg^{-1} range, whereas the weaker 10^{-2}–10^{-3} g kg^{-1} condensate range is present in ICON condensate. This difference is likely due to the systematically higher outflow altitudes of normal- and slow-ascending WCBs in ICON compared to ERA5 (Appendix Fig. A.18), as also indicated in Fig. 5.10. Despite this, fast-ascending WCBs in ICON still reach the highest outflow levels while maintaining the largest condensate amounts.

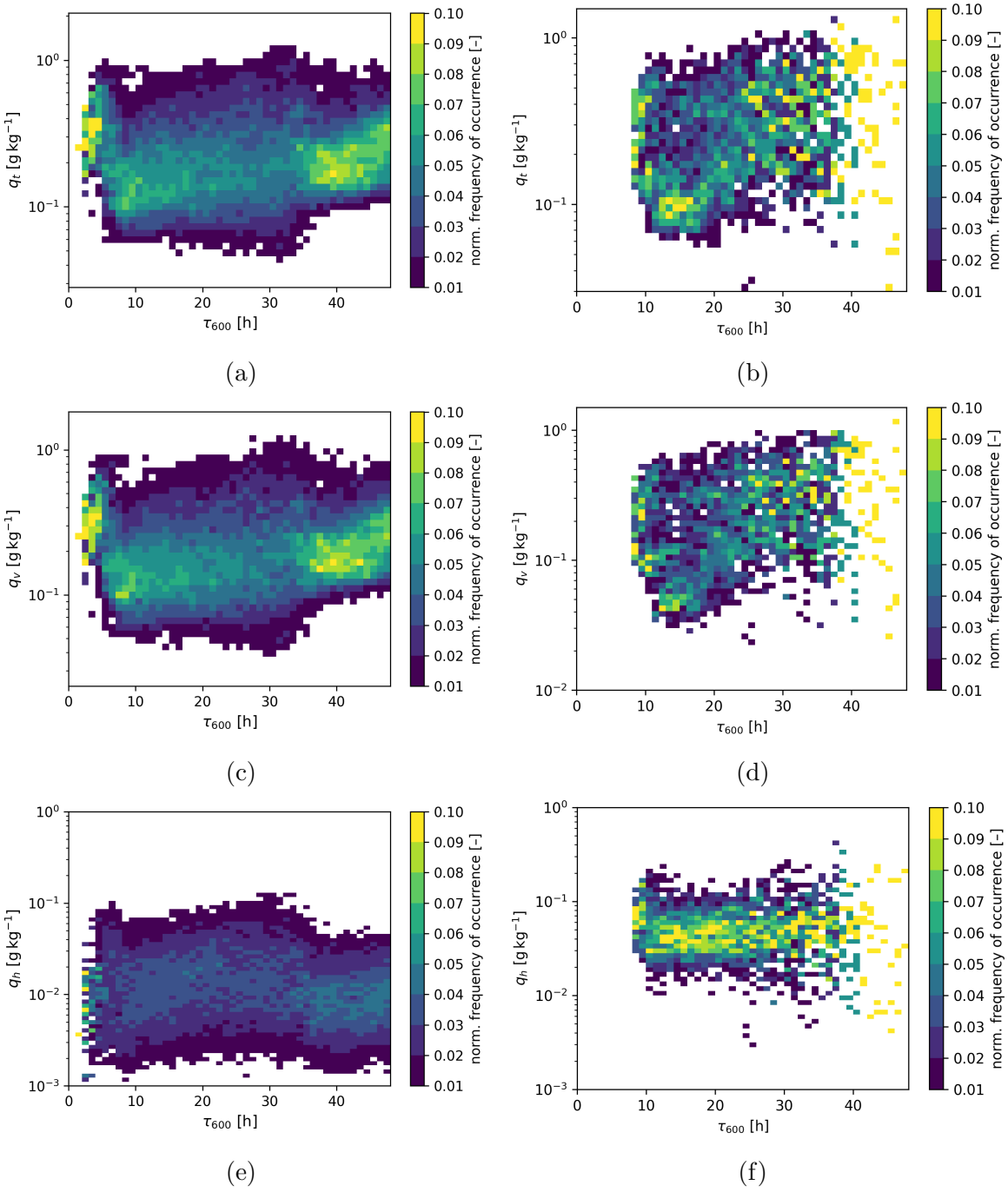

Figure 5.11: Distributions of WCB outflow total water, specific humidity, and condensate as a function of τ_{600}. Panels (a), (c), and (e) show the ICON simulation, while panels (b), (d), and (f) show ERA5.

Outflow relative humidity with respect to ice (RHi)

The relative humidity with respect to ice (RHi) was calculated following the approximation of Murphy and Koop (2005), defined as the ratio between the actual water vapour content (q_v) and the saturation vapor content over ice ($q_{si}(T)$), which depends on temperature. Figure 5.12 compares the relationship between outflow RHi and temperature for ICON (panel a) and ERA5 (panel b). ICON exhibits an overall supersaturation over 100%, with RHi increasing as temperature decreases especially exceeding the homogeneous freezing threshold (below $\sim$ -40°C). The mean RHi reahes up to 115-120% near -60°C. The wide 10–90% range further highlights the pronounced variability among ICON WCB outflows, suggesting that local supersaturation favors ice crystal growth and cirrus cloud formation. In contrast, ERA5 shows a narrower distribution with the mean values ranging between 100-105% and rarely exceeding 110%. Before reaching the homogeneous freezing threshold ($\sim$–38°C), ERA5 RHi still shows a temperature-dependent behaviour, but above this threshold the mean values remain relatively constant around 103%, indicating limited supersaturation in the colder outflow layers.

The normalised distribution of WCB outflows by RHi bins is shown in Fig. 5.12c. ICON displays a broader distribution centered near 105%, with the fast- and slow-ascending branches showing nearly similar peaks, where the slow-ascending branch exhibits a slightly higher frequency. This similarity suggests that ascent speed has only a minor influence on the resulting outflow RHi for this case. ERA5, on the other hand, shows a much narrower and sharply peaked distribution around 102-103%, with very few occurrences exceeding 110%. This constrained behaviour likely results from the microphysical schemes and saturation-adjustment approaches used in large-scale models, which limit ice supersaturation. In ERA5, once an ice cloud is present within a model grid box, the supersaturation is typically adjusted ("clipped") back to 100% or a slightly higher value (e.g., Tompkins et al., 2007; Reutter et al., 2020), since the coarse model resolution cannot efficiently resolve small-scale nucleation and depositional growth processes. Such cloud schemes suppress the larger supersaturation processes, producing a narrow RHi distribution tightly clustered around 100%. In contrast, ICON's explicit microphysics setup permits stronger and more variable supersaturation, resulting in a broader RHi distribution that aligns with the ice-supersaturated conditions observed in WCB outflows. As a result, ERA5 systematically underestimates both RHi and the frequency of ice-supersaturated regions (as shown in Fig. 5.5), a limitation that likely affects its representation of humidity conditions in WCB outflows.

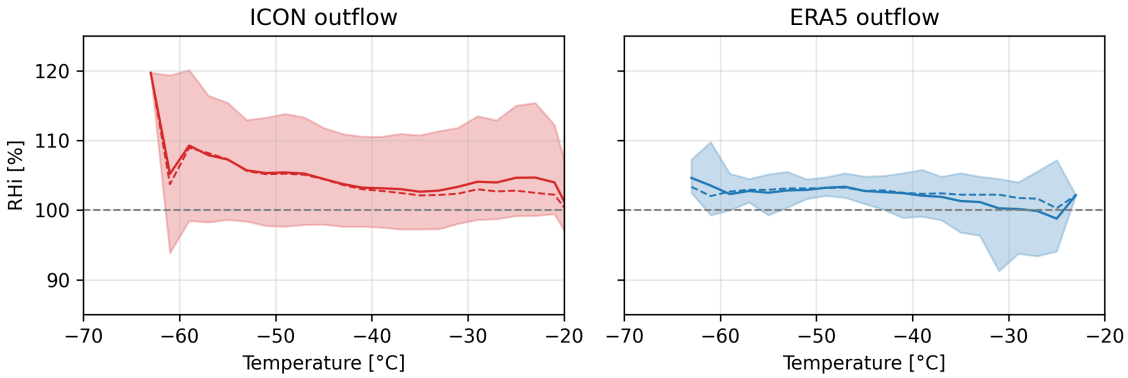

(a)

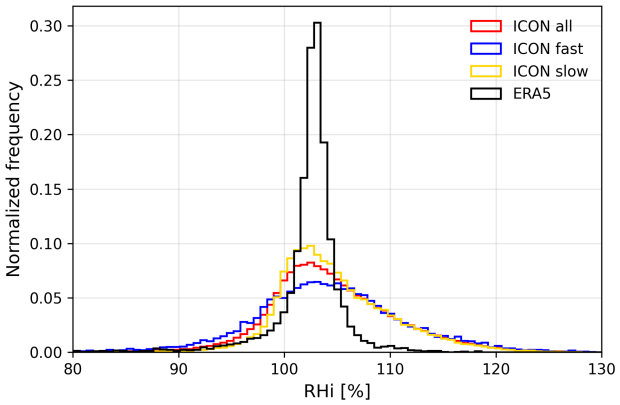

(b)

Figure 5.12: (a) Distribution of relative humidity with respect to ice (RHi) as a function of temperature in the WCB outflow for ICON (left panel) and ERA5 (right panel). Shading denotes the 10th–90th percentile range. (b) Normalized histogram of RHi at the end of ascent for ERA5 (black) and ICON (red), with ICON fast-ascending (blue) and slow-ascending (orange) WCBs shown separately.

Inflow-outflow correlations of q_v and T

Since RHi depends strongly on both specific humidity and ambient temperature, the differences observed between ICON and ERA5 in outflow RHi likely reflect variations in these underlying thermodynamic properties. To further investigate how the initial thermodynamic conditions in the WCB inflow influence the humidity state in the outflow, we analyze the correlation between inflow and outflow q_v and T in Fig. 5.13. The inflow–outflow correlation for q_v is relatively weak in ICON ($r = 0.24$, panel a), while the correlation for temperature is somewhat stronger ($r = 0.48$, panel b). When examined across different ascent timescales (figures not shown), the q_v correlation systematically decreases with the increasing ascent time, whereas the T correlation strengthens. This behaviour reflects the dominant physical processes acting during ascent. For short ascent times, limited condensation, precipitation and entrainment

allow more inflow moisture to be preserved in the outflow. As ascent time increases, however, microphysical processing and turbulent mixing progressively modify the moisture field, weakening the inflow–outflow q_v relationship. In contrast, temperature becomes more predictable with longer ascent. Rapid ascent can produce strong, abrupt latent heating, resulting in large variability in temperature changes, while slower ascent leads to a more gradual thermodynamic evolution and thus a stronger correlation between inflow and outflow temperatures.

In ERA5 (panels c–d), the correlation between inflow and outflow q_v ($r = 0.67$) is substantially stronger than in ICON ($r = 0.24$), indicating that outflow moisture in ERA5 largely reflects the initial inflow humidity. This suggests that ERA5 better preserves the large-scale moisture structure throughout the ascent. In contrast, the inflow–outflow temperature correlation in ERA5 ($r = 0.48$) is similar to that in ICON, implying that temperature evolution is governed by comparable large-scale thermodynamic constraints in both datasets. The much higher q_v correlation in ERA5 likely results from its parameterized convection and cloud schemes, which act to regulate the humidity field by adjusting it toward saturation, thereby suppressing small-scale variability. This behaviour is consistent with the uniform supersaturated RHi values in ERA5 (e.g., Fig. 5.12).

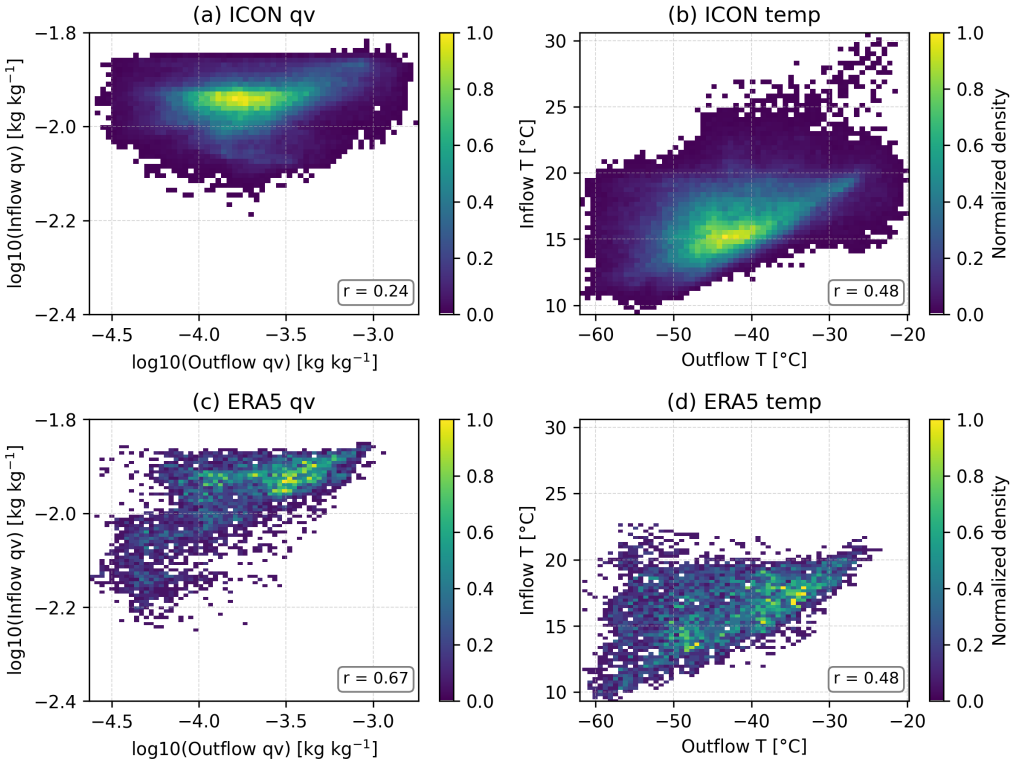

Figure 5.13: Correlations between inflow and outflow conditions for (a–b) ICON and (c–d) ERA5. Panels (a, c) show specific humidity on a logarithmic scale, while panels (b, d) show temperature.

5.3.5 Comparison of moisture loss pathways

Total moisture loss (DR)

Figure 5.14 compares the drying ratio (DR, defined in Eq. 5.5) between ICON and ERA5 as a function of ascent time τ_{600}. The DR quantifies the fraction of total water lost during WCB ascent. In both datasets, WCBs lose more than 96% of their initial total water. In ICON (panel a), DR exhibits a pronounced minimum for fast WCBs especially for $\tau_{600} < 5$, indicating that these trajectories retain relatively more moisture in the outflow. This behavior is consistent with the Fig. 5.11a that fastest WCB contain the highest total water content. This can be explained in low condensation ratio (CR) and precipitation efficiency (PE) shown in Fig. 5.15d–e. Low CR suggests that part of the water vapour is not converted into condensate, while low PE indicates that much of the condensate is not precipitated and remains within the air parcel, contributing to high outflow moisture. This feature is not captured in ERA5 (panel b), where DR decreases more gradually with ascent time.

Panel (c) shows that the DR difference between ICON and ERA5 increases with ascent time, reaching up to 0.015–0.02 for the slowest WCBs, suggesting more efficient moisture loss in ICON, particularly for slow WCBs. In both datasets, DR tends to decline with increasing τ_{600}, particularly for normal and slow WCBs. These slower WCBs ascend to lower altitudes characterized by higher temperatures and a moister environment (Fig. 5.9), indicatingthat DR is primarily controlled by thermodynamic conditions, while hydrometeor transport can also modulate the DR.

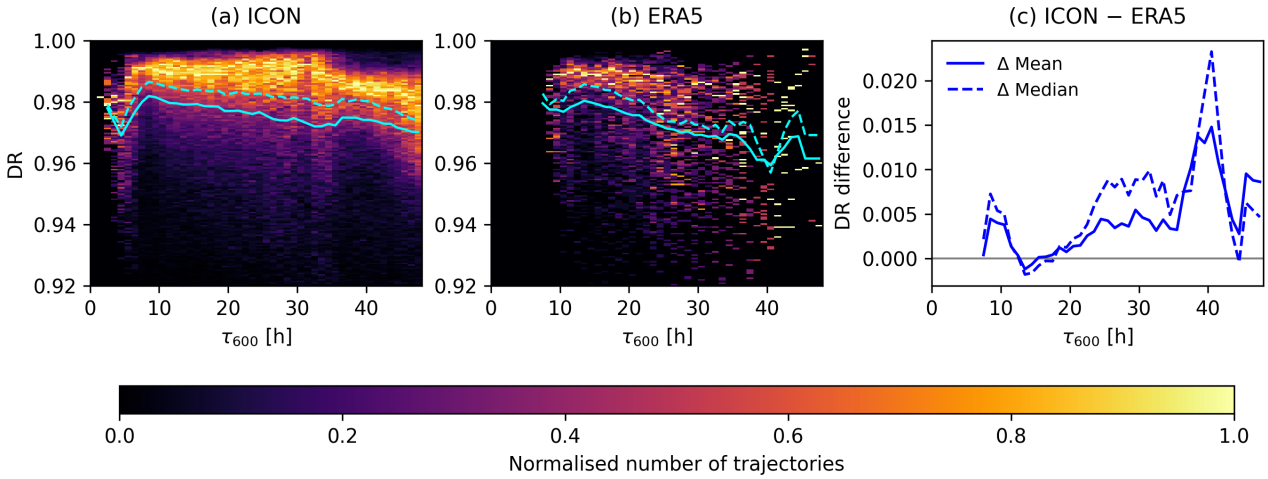

Figure 5.14: DR as the function of τ_{600} for (a) ICON simulation, (b) ERA5 data and (c) the ICON–ERA5 difference. Colors indicate the normalized number of trajectories. Solid (dashed) lines show mean (median) values.

Fractional moisture loss from mixing processes and precipitation (DR_{mix}, P_{loss})

To further investigate the processes contributing to total moisture loss, we examine diagnostics available exclusively in the ICON simulations, as ERA5 does not explicitly resolve convection or microphysical processes.

The moisture loss due to turbulence and convection is quantified by DR_{mix}(Eq. 5.6). Higher DR_{mix} indicate stronger turbulent or convective activity, as well as contributions from numerical residuals (Schwenk and Miltenberger, 2024). As shown in Fig. 5.15a, DR_{mix} exhibits a first peak for fast-ascending WCBs, primarily reflecting explicitly resolved convection. With increasing ascent time, DR_{mix} gradually rises again for normal-ascending WCBs, likely due to enhanced turbulent mixing. For slow-ascending WCBs, DR_{mix} decreases again, likely due to the presence of two distinct synoptic systems that created a wider range of ascent pathways and microphysical conditions, leading to a different DR_{mix} response in this slower branch.

The total drying ratio (DR) can be expressed as the sum of DR_{mix} and the fractional moisture loss due to precipitation, here denoted as P_{loss}, which is calculated as the ratio of the net precipitation at the outflow to the initial total water. As shown in Fig. 5.15c, P_{loss} exhibits an opposite pattern to DR_{mix}, but with much larger values, generally exceeding 0.8. This indicates that total moisture loss is primarily driven by precipitation processes, with mixing playing a secondary role.

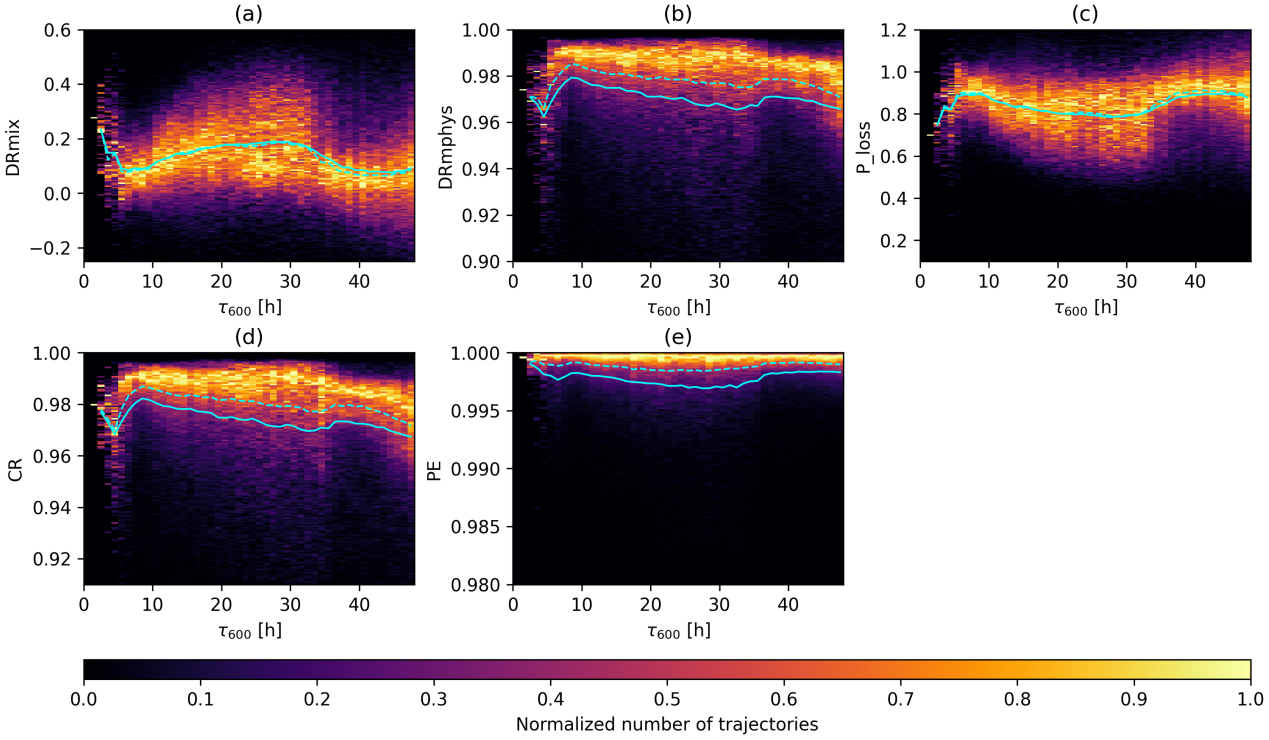

Figure 5.15: Distributions of (a) DR_{mix}, (b) DR_{mphys}, (c) moisture loss due to precipitation, (d) CR, and (e) PE as the function of τ_{600} at the end of the ascent. Colors indicate the normalized number of trajectories. Solid (dashed) lines show mean (median) values.

Fractional moisture loss from cloud microphysical processes (DR_{mphys})

As introduced in Section 5.2.2, the microphysical drying ratio (DR_{mphys}; Eq. 5.7) quantifies the moisture loss due to precipitation processes after the effects of turbulent and convective mixing have been accounted for. A value of $DR_{mphys} = 1$ does not imply that $DR_{mix} = 0$, but rather that all moisture remaining after mixing is subsequently removed by precipitation.

In Fig. 5.15b, DR_{mphys} shows its lowest values for fast-ascending WCBs, indicating that total drying in these cases is largely driven by mixing. For longer ascent times, DR_{mphys} gradually decreases with increasing τ_{600}, suggesting a reduced contribution from precipitation-related drying. Despite the influence of mixing, DR_{mphys} remains generally higher for faster WCBs, implying more efficient microphysical removal of moisture in rapidly ascending trajectories.

Microphysical efficiency: CR and PE

The following analysis examines the condensation ratio (CR) and precipitation efficiency (PE), which quantify the efficiency of vapor-to-condensate conversion and the subsequent removal of condensate by precipitation, respectively. Figure 5.15d-e show the condensation ratio (CR) and

precipitation efficiency (PE) as a function of τ_{600}. The CR exhibits a local minimum of about 0.96 for fast-ascending WCBs, indicating that rapid ascent limits the time available for vapour-to-condensate conversion. With increasing ascent time beyond 10 h, CR gradually decreases from an average of approximately 0.98 to 0.97, reflecting reduced condensation efficiency under warmer and less saturated conditions, consistent with the thermodynamic structure shown in Fig. 5.9.

In contrast, PE remains high across all ascent timescales, with only a slight reduction for normal-ascending WCBs. For the fastest WCBs, PE approaches almost 1, indicating that condensate converted during convective ascent is almost entirely precipitated out. The reduced PE around $\tau_{600} = 30$ h is also reflecting in the secondary peak of total water peak in the outflow (Fig. 5.10). Since both CR and PE contribute to $\mathrm{DR}_{\mathrm{mphys}}$, and PE remains nearly constantly as 1, the pattern of $\mathrm{DR}_{\mathrm{mphys}}$ largely follows that of CR.

Normalised process diagnostics during ascent

In this section, we present a detailed analysis of the vapor–condensate conversion and dehydration behaviour for fast-, normal-, and slow-ascending WCBs, as defined previously based on their τ_{600} distribution. To enable consistent comparison across ascent timescales, individual WCB trajectories are normalized to a common, dimensionless time range from 0 to 1, representing the relative progress along the ascent. Figure 5.16 illustrates the evolution of the normalized DR, CR and PE throughout the ascent.

The temporal evolution of CR, PE, and DR reveals when different processes dominate the moisture budget along the ascent. The CR increases monotonically for all WCB categories, reflecting ongoing vapor-to-condensate conversion. Fast-ascending WCBs show the steepest early rise in CR, indicating rapid condensation in the lower troposphere driven by strong uplift and fast saturation. In contrast, normal and slow WCBs exhibit a more gradual increase, suggesting slower condensation during ascent. The PE profiles indicate that precipitation becomes efficient early in the ascent, with values exceeding 0.8 by normalized time ~ 0.3. This suggests that condensate removal through precipitation closely follows the occurrence of condensation. Fast WCBs reach slightly lower PE in the early stages, likely due to shorter residence times for hydrometeor growth.

The normalized DR profiles reflect the cumulative effect of condensation and precipitation. Their evolution closely follows that of CR across all WCB types, indicating that vapor-to-condensate conversion governs the efficiency of moisture loss by regulating the amount of condensate available for precipitation. When decomposing DR into its components, $\mathrm{DR}_{\mathrm{mphys}}$ and

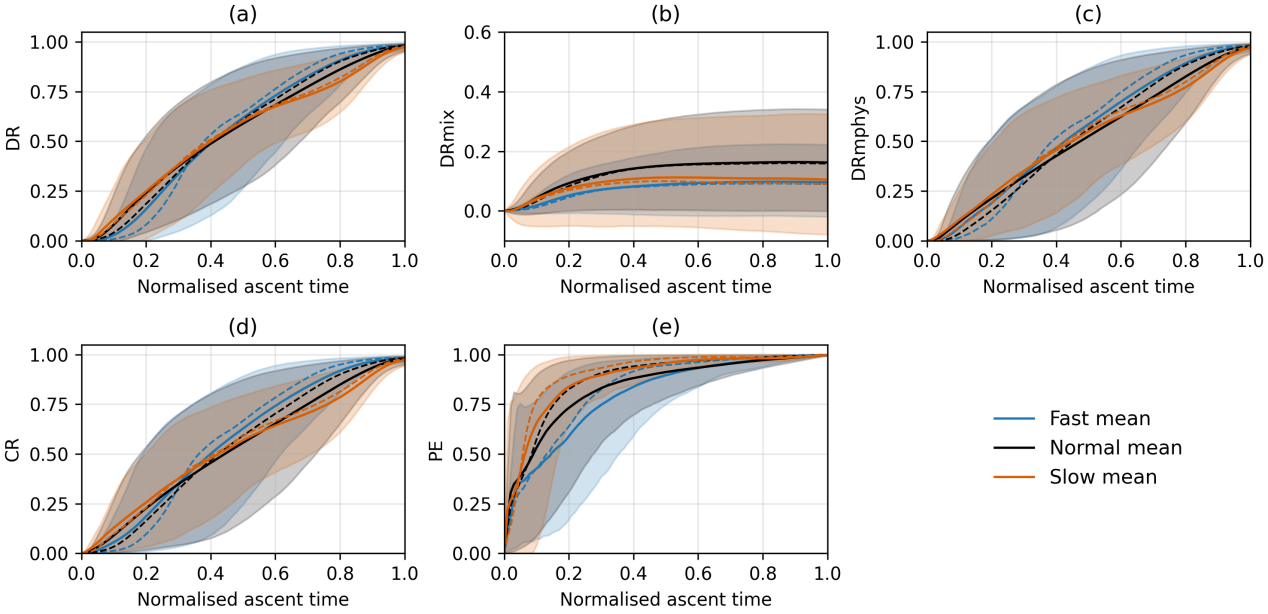

Figure 5.16: Evolution of (a) DR, (b) DR_{mix}, (c) DR_{mphys}, (d) CR, and (e) PE as a function of normalized ascent time. Solid (dashed) lines show mean (median) values. Shading denotes the 10th–90th percentile range.

DR_{mix}, distinct temporal characteristics emerge. The DR_{mix} remains near zero during the early ascent, gradually increases until the middle stage, and remains relatively stable thereafter, indicating that turbulent entrainment and detrainment are most active during the initial to mid-ascent phases, particularly in normal and slow WCBs. In contrast, fast WCBs show a weaker DR_{mix} signal, implying that their rapid ascent might limit the time for mixing with the environment.

The evolution of DR_{mphys} closely follows the CR profiles, highlighting that microphysical processes dominate the drying during the ascent. All WCBs contribute similarly at the beginning, but DR_{mphys} in fast WCBs increase more rapidly in later ascent stage, indicating that these trajectories have already reached higher altitudes where microphysical processes intensify and become more efficient. This behaviour contrasts with DR_{mix}, where normal and slow WCBs contribute more strongly in latter stage.

Relative humidity along the temperature during ascent

To connect the observed microphysical behavior with the thermodynamic environment, we examine the evolution of relative humidity with respect to water (RHw) and ice (RHi) along the ascent (τ_{WCB}) in Fig. 5.17. Examining RH as a function of temperature allows us to assess how quickly the parcels reach saturation, how long supersaturation is maintained, and how these

patterns differ across ascent-speed categories. We focus on fast and slow WCBs, as normal WCBs generally fall in between.

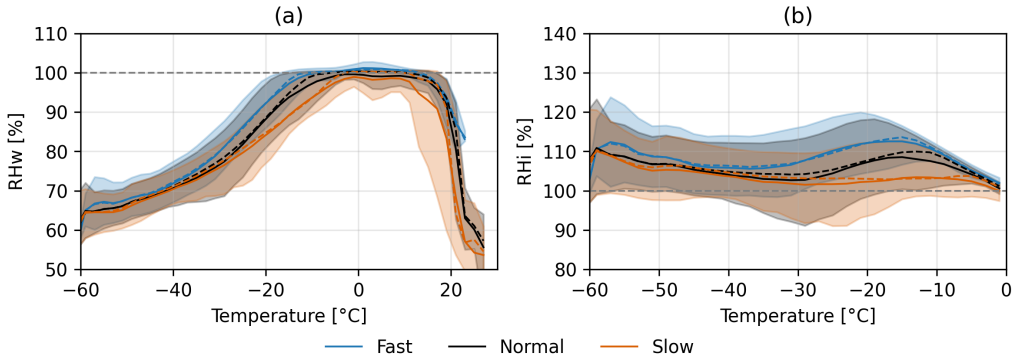

Figure 5.17: Distribution of RHw (a) and RHi (b) along the WCB ascent (τ_{WCB}) as a function of temperature. Solid (dashed) lines show mean (median) values. Shading denotes the 10th–90th percentile range.

During early ascent, when temperatures are above 0°C, RHw increases toward 100% near ∼10°C, indicating that all WCB branches reach saturation near cloud base. Supersaturation persists until about -5°C for slow WCBs and -18°C for fast WCBs, reflecting differences in how specific humidity adjusts along the ascent and possibly influenced by interpolation-related oversaturation in fast WCBs, as discussed in Schwenk and Miltenberger (2024). Once the parcels become subsaturated again, RHw declines more gradually in slow WCBs, likely due to more efficient glaciation and vapor removal via the Wegener–Bergeron–Findeisen (WBF) mechanism. As temperatures approach the homogeneous freezing threshold (∼ −38°C), RHw for all ascent categories begins to converge.

The RHi profiles show broader differences between ascent categories. Fast WCBs exhibit higher RHi values (mean ∼ 115%) throughout the mixed-phase region. This difference peaks near -15°C, where supersaturation with respect to ice is strongest in the fast group. Toward colder temperatures, glaciation and depositional growth reduce these differences, and RHi values converge near -40°C, indicating that WCBs of different ascent speeds approach similar saturation conditions below the homogeneous freezing threshold.

These differences reflect the distinct microphysical evolution in fast versus slow WCBs. Earlier and stronger supersaturation in fast WCBs is consistent with their delayed but more rapid condensational and depositional growth (see Fig. 5.16), while the slower, more gradual humidity evolution in slow WCBs reflects a more moderate microphysical response.

5.4 Case 2: A Representative Winter WCB Event

The second case study represents a wintertime WCB event, associated with a deep, baroclinically driven cyclone over the North Atlantic. It provides a typical example of strong winter WCB activity. The event originated over the central Atlantic near 46-50° N, 40-5° W on 11 December 2011 at 06 UTC. The inflow track exhibits a predominantly eastward development, with air parcels ascending rapidly ahead of the cyclone and reaching the outflow region over northern Europe. Figure 5.18 shows the corresponding inflow track (blue), inflow points (green), and outflow points (orange) derived from ERA5 trajectory data. The WCB inflow has a lifespan of 55 h and a total travel distance of 3186.74 km. Two nested domains used in the ICON simulation are indicated by the blue (∼ 6.5 km) and red (∼ 3.3 km) dashed boxes.

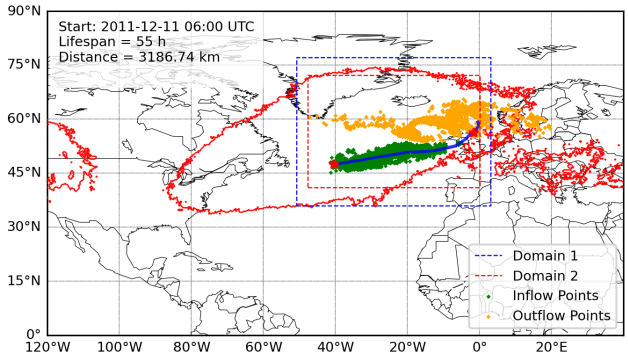

Figure 5.18: WCB event on 11 December 2011 at 06 UTC, showing the inflow track (blue), inflow points (green), and outflow points (orange). The two stars mark the initial 48-hour time window of the inflow evolution. The nested ICON simulation domains are outlined by the blue dashed box (∼6.5 km) and the red dashed box (∼3.3 km).

As in the summer case, the same geographic displacement filter was applied to the winter simulation, excluding trajectories that did not meet the minimum propagation criteria of 5° meridional or zonal displacement during their ascent period. This ensures that only trajectories representing dynamically coherent and spatially extended WCBs are retained, while those associated with short-lived, weak, or localized upward motions are removed. Eventually, 99% of the total trajectories (92215 out of the full set) are retained for further analysis, as shown in Fig. 5.19b.

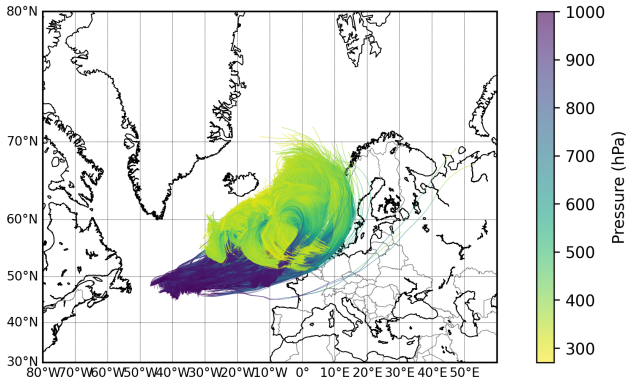

Figure 5.19: Valid WCB trajectories retained after applying the selection criteria described in Section 5.3.1. ICON simulation initialized from 11 December 2011 at 06 UTC.

5.4.1 Comparison of inflow synoptic conditions

This section compares the same Eulerian fields as discussed in the summer case, but focuses only on surface conditions. As before, only the finest ICON domain is compared with ERA5 data. The evolution of mean sea-level pressure (MSLP) over a 24-hour period beginning on 25 August 2025 at 18:00 UTC is shown for ICON (left), ERA5 (middle), and their difference (ICON minus ERA5, right). At the initial stage (Fig. 5.20a), two low-pressure systems are present over the North Atlantic. The first cyclone center is located near 38°W and 55°N, while the second, more zonally elongated low-pressure region extends around 65°N from 38°W to 8°W, spanning across Iceland and likely associated with a dissipating extratropical cyclone. After 12 hours (Fig. 5.20b), the southern cyclone intensifies and propagates northeastward, gradually merging with the northern low center system. By 27 August 06:00 UTC (Fig. 5.20c), the two systems have merged into a single, mature cyclone centered south of Iceland.

The difference fields show that ICON generally simulates a deeper cyclone core than ERA5, as reflected by negative anomalies near the central pressure minimum. In contrast, positive pressure differences along the southern and southeastern flanks suggest higher surface pressure in ICON near the warm sector. This pattern suggests that the ICON simulation produces a cyclone with a steeper pressure gradient and a more pronounced central deepening, while ERA5 depicts a broader and comparatively weaker low-pressure structure.

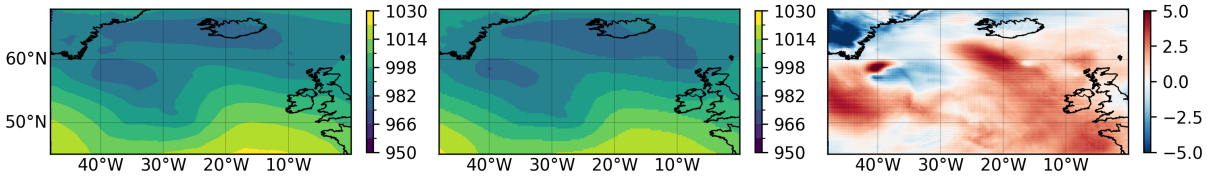

(a) 2011 December 12th, 00:00 UTC

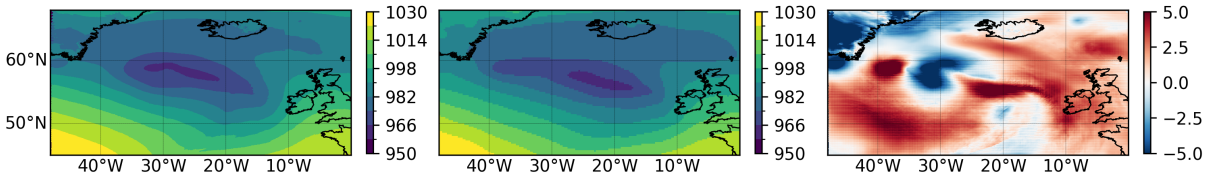

(b) 2011 December 12th, 12:00 UTC

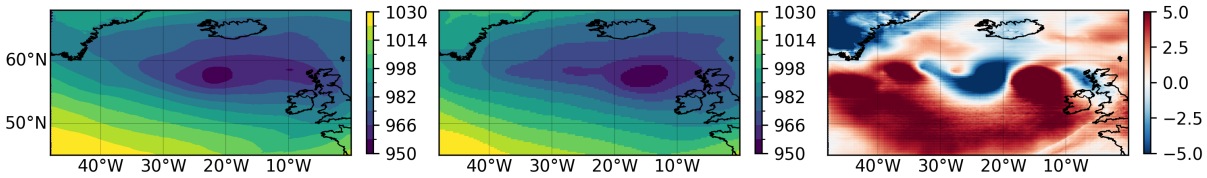

(c) 2011 December 13th, 00:00 UTC

Figure 5.20: Temporal mean sea-level pressure (MSLP) from ICON (left panels), ERA5 (middle panels), and their differences (right panels, ICON minus ERA5), shown at 12-hour intervals from 12 to 13 December 2011.

5.4.2 Comparison of ascent statistics

Fig. 5.21 compares the normalized frequency distributions of WCB occurrence between ICON and ERA5. Panel (a) shows the histogram of WCB frequency as a function of ascent timescale (τ_{600}), where the ERA5 distribution peaks at approximately 18 h, while ICON peaks slightly later, around 22 h. The ICON distribution is also broader and more gradual, indicating more extended ascent durations in the high-resolution simulations. Fast WCBs are completely missing in ERA5 for this winter case, highlighting its limited ability to capture rapid ascent. Panel (b) compares the distributions of outflow pressure. ERA5 outflows peak between 300–320 hPa, whereas ICON outflows peak at slightly higher pressures, around 340 hPa, suggesting that most ICON WCBs terminate at lower altitudes compared to ERA5.

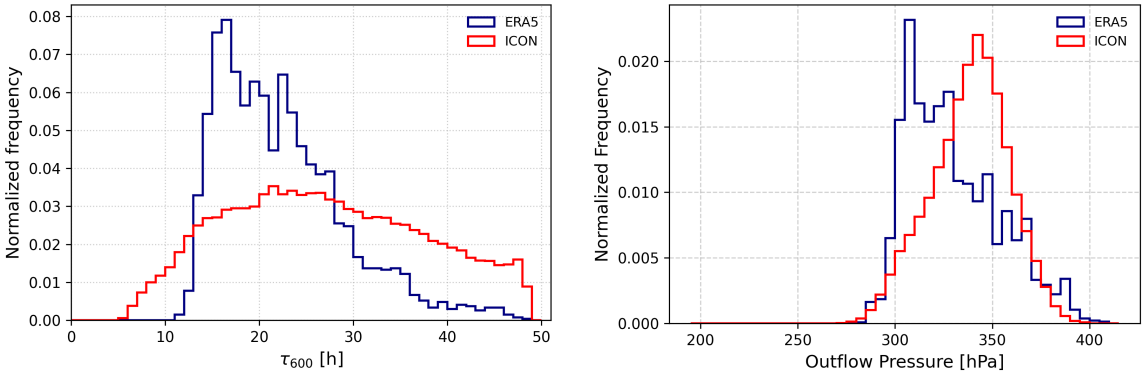

(a) (b)

Figure 5.21: Normalized frequency distributions of WCB trajectories as a function of (a) ascent timescale (τ_{600}) and (b) outflow pressure level. ICON data are shown in red and ERA5 data in navy.

Spatial distribution of WCB inflow and outflow

To further investigate differences in ascent characteristics, inflow distributions at various ascent timescales in ICON are compared with the inflow points derived from ERA5 (Fig. 5.23a). In this case, both datasets identify the main inflow region over the midlatitude North Atlantic, but ICON inflows extend slightly eastward for the normal-ascending branch and both westward and eastward for slow-ascending WCBs. For shorter ascent timescales ($\tau_{600} \leq 10$ h), inflow points cluster near 50°–55°N with relatively low density, consistent with strong frontal ascent in the warm sector(see Fig. 5.20), where air parcels rise rapidly along the surface frontal zone. As τ_{600} increases, the inflow region expands in all directions toward the central Atlantic, indicating slower, more gradual ascent within the broader baroclinic environment of the cyclone. Compared to the summer case, both ICON and ERA5 inflows occur at higher latitudes and farther west over the ocean, consistent with enhanced static stability and a more zonally oriented storm track typical of winter.

The temporal evolution of WCB outflow points (Fig. 5.22) illustrates the differences in the timing and spatial development of the outflow between ICON and ERA5. At the early stage (12 December, 12:00 UTC; Fig. 5.22a), the first outflow signatures appear in ICON over the central North Atlantic, while ERA5 shows only a few outflow points farther east. Six hours later (Fig. 5.22b–c), ICON outflows intensify and propagate rapidly northeastward toward the British Isles, indicating an earlier and faster vertical transport compared to ERA5. During the following hours (Fig. 5.22d–e), the ICON outflows continue to expand poleward, accompanied by enhanced cyclonic development, forming an elongated band that extends from the North Atlantic into northern Europe.

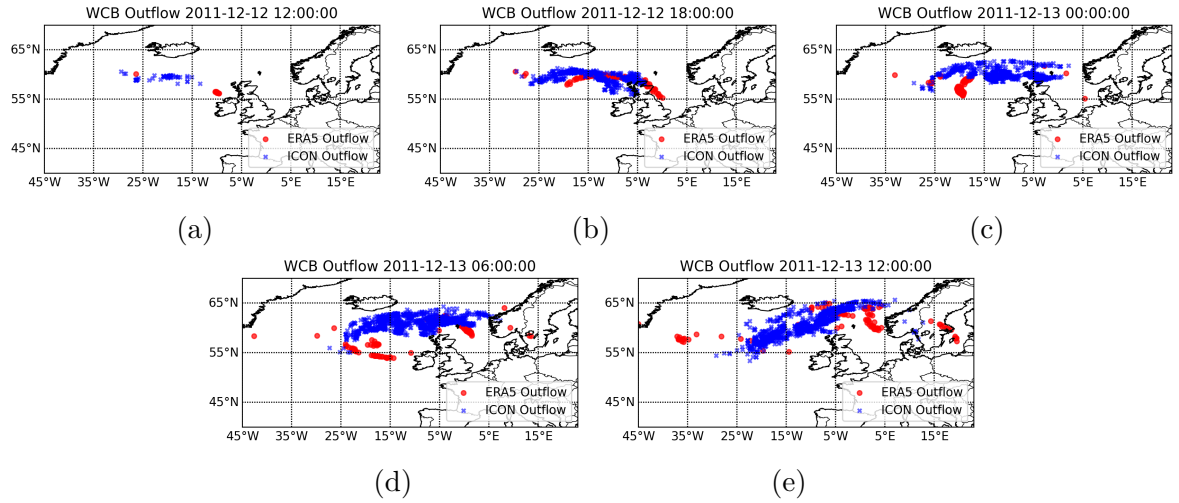

Figure 5.22: Comparison of WCB outflow locations in ERA5 and ICON at corresponding times during the event of 12-13 December 2011. Panels (a–e) show the temporal evolution of outflow points, with ERA5 outflow locations indicated in red and ICON outflow locations in blue.

In ERA5, the outflows appear more scattered, with a broader westward and eastward extent compared to ICON especially for slow WCBs. This behavior is also reflecting Fig. 5.23b, which shows the ICON WCB outflow points for different ascent times. Both ICON and ERA5 capture the main outflow structure across the North Atlantic and northern Europe, but the ERA5 outflows are less concentrated and extend further westward. In contrast, ICON displays a denser outflow region over the central North Atlantic, indicating enhanced upper-level transport and a more intense cyclone evolution. Compared to the summer case, both datasets exhibit a more poleward and zonally elongated outflow distribution during winter, reflecting enhanced baroclinicity and the seasonal shift of the midlatitude storm track.

Overall, this winter case shows a better spatial overlap of outflow points between ICON and ERA5, although ICON still represents a more intense and dynamically active WCB development.

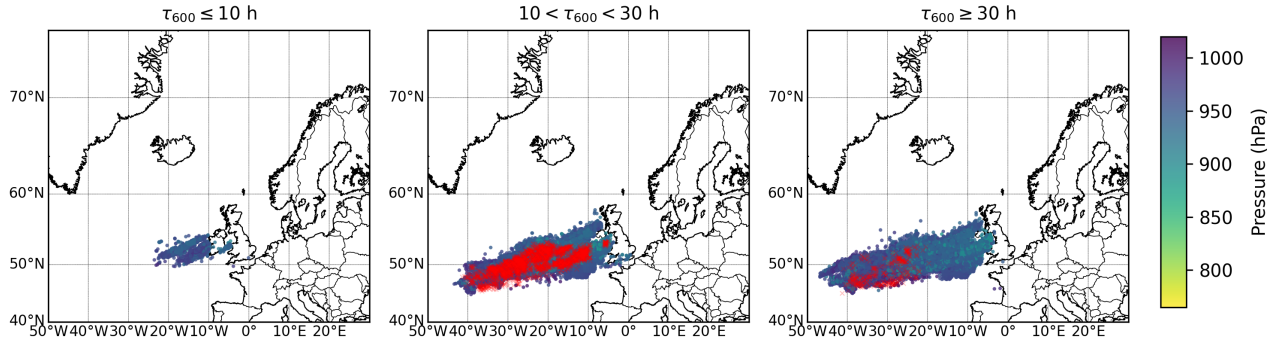

(a)

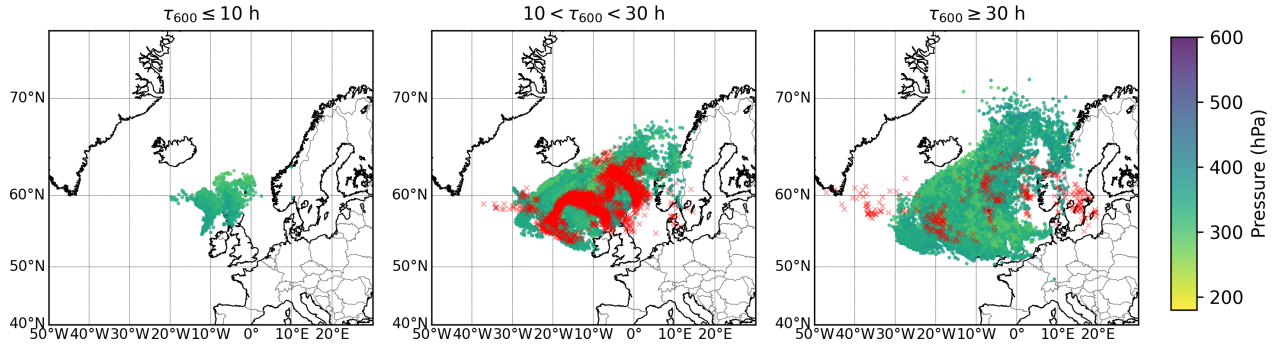

(b)

Figure 5.23: Comparison of (a) inflow and (b) outflow points between ICON (colored by pressure) and ERA5 (red) for fast-ascending WCBs ($\tau_{600} \leq 10$, left panel), normal-ascending WCBs ($10 < \tau_{600} < 30$, middle panel), and slow-ascending WCBs ($\tau_{600} \geq 30$, right panel).

5.4.3 Comparison of trajectory characteristics

Temperature and pressure evolution along τ_{600}

Figure 5.24 compares inflow and outflow temperatures and pressures as a function of the ascent timescale (τ_{600}) for the winter case. In ERA5, the minimum τ_{600} exceeds 10 h, indicating that fast-ascending WCBs are not well captured in the reanalysis. In contrast, ICON includes a limited number of trajectories with $\tau_{600} \leq 10$ h, allowing some representation of more rapid ascent.

At the inflow stage (Figs. 5.24, left panels), ICON trajectories occur at slightly higher pressures than ERA5 for $\tau_{600} > 25$ h and are systematically colder across all ascent timescales (see also Appendix Fig. A.21). This suggests that the high-resolution model captures a relatively colder and potentially more poleward source region for WCB air parcels in this winter case. As τ_{600} increases, temperatures gradually decrease while pressure levels remain relatively stable, indicating that the normal and slow ascending WCBs may originate from higher latitudes in colder environment. In contrast, ERA5 inflow pressure decreases markedly with increasing τ_{600}, while

the corresponding temperature remains more uniform.

At the outflow stage (Figs. 5.24b,d), ICON trajectories reach lower pressures and slightly higher temperatures than ERA5 for τ_{600} between 10 and 30 h. For $\tau_{600} > 30$ h, this relationship reverses, with ERA5 trajectories reaching lower pressures but higher temperatures than ICON. The slow-ascending ERA5 WCBs terminate at slightly lower pressures at the end of their τ_{WCB} compared to the normal-ascending ones. However, both datasets exhibit a similar vertical displacement across all ascent times, typically between 600 and 630 hPa (see Appendix Fig. A.21e), indicating that the outflow pressure is strongly influenced by the inflow conditions.

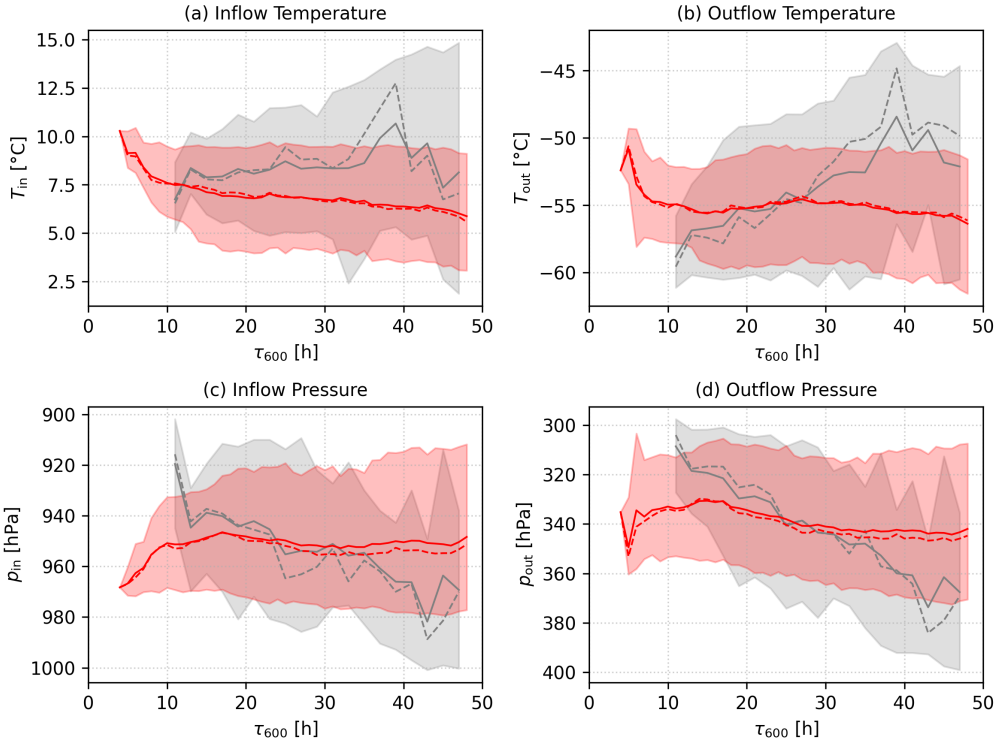

Figure 5.24: Comparison of inflow and outflow (a–b) temperature and (c–d) pressure as a function of τ_{600} for ICON (red) and ERA5 (grey). Solid (dashed) lines show mean (median) values. Shading denotes the 10th–90th percentile range.

Moisture evolution along τ_{600}

Figure 5.25 shows the dependence of total water (q_t, grey), water vapour (q_v, green), and condensate (q_h, blue) on ascent timescale (τ_{600}) for the winter case. At the inflow stage, both datasets exhibit lower q_v and q_t compared to the summer case, reflecting colder and drier wintertime conditions. ICON shows slightly lower mean and median q_v and q_t than ERA5 across

most τ_{600} values (Appendix Fig. A.22), consistent with the colder source regions of ICON WCBs (Fig. 5.24). Condensate (q_h) remains near zero in both datasets, with a slight increase at longer ascent times, as expected for unsaturated inflow air.

In the outflow, ICON exhibits peak q_v and q_t for fast-ascending WCBs, followed by a sharp decline around $\tau_{600} \sim 10$ h, after which values remain relatively constant for normal and slow ascent. In contrast, ERA5 shows increasing q_v and q_t with τ_{600}, likely because slower WCBs in ERA5 terminate at lower altitudes where ambient moisture is higher. Apart from the significantly larger moisture transport in ICON's fast-ascending WCBs, ICON outflows are generally drier than ERA5 (Appendix Fig. A.22b). Specifically, ICON water vapour is slightly higher than ERA5 for normal WCBs, but lower for slow WCBs. ICON also shows systematically lower outflow condensate than ERA5 (Appendix Fig. A.22d), consistent with its higher outflow altitudes.

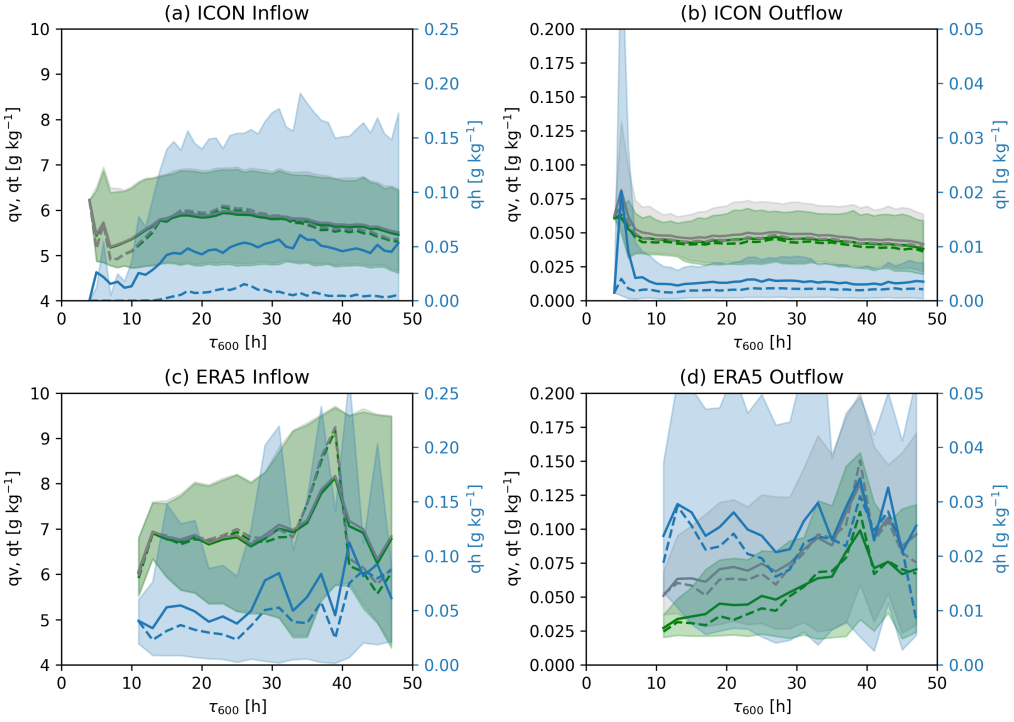

Figure 5.25: Comparison of total water (q_t, grey), water vapour (q_v, green), and condensate (q_h, blue) as a function of τ_{600} for inflow and outflow. Panels (a–b) show ICON and panels (c–d) ERA5. Solid (dashed) lines show mean (median) values. Shading denotes the 10th–90th percentile range. A separate axis on the right-hand side is used for q_h.

Overall, the winter case exhibits lower moisture content than the summer case in both ICON and ERA5. Nevertheless, the same qualitative differences remain: ICON transports more mois-

ture in fast-ascending WCBs, while ERA5 shows higher outflow condensate for normal and slow ascent.

Distribution of outflow moisture components along τ_{600}

A corresponding analysis of the outflow distributions of total water (q_h), specific humidity (q_v), and condensate (q_c) as a function of τ_{600} is shown in Fig. 5.26. Compared to the summer case, ICON shows a single dominant peak across all moisture components in fast-ascending WCBs. The distributions in ICON are characterized by generally lower values and a narrower spread.In contrast, ERA5 (Figs. 5.25b,d,f) exhibits weaker gradients along τ_{600} and more scattered distributions, particularly in the slower-ascending regime. Notably, slow-ascending WCBs in ERA5 transport higher amounts of total water, as evident in Fig. 5.25d. The condensate signal in ERA5 spans approximately 10^{-1} to 10^{-3} g kg^{-1}, whereas in ICON it is shifted about one order of magnitude lower, ranging from 10^{-2} to 10^{-4} g kg^{-1}. This difference likely reflects the lower outflow altitudes in ERA5. Overall, while ERA5 exhibits greater variability, ICON shows a stronger dependence on τ_{600}, likely due to the influence of its explicit representation of convection and microphysical processes.

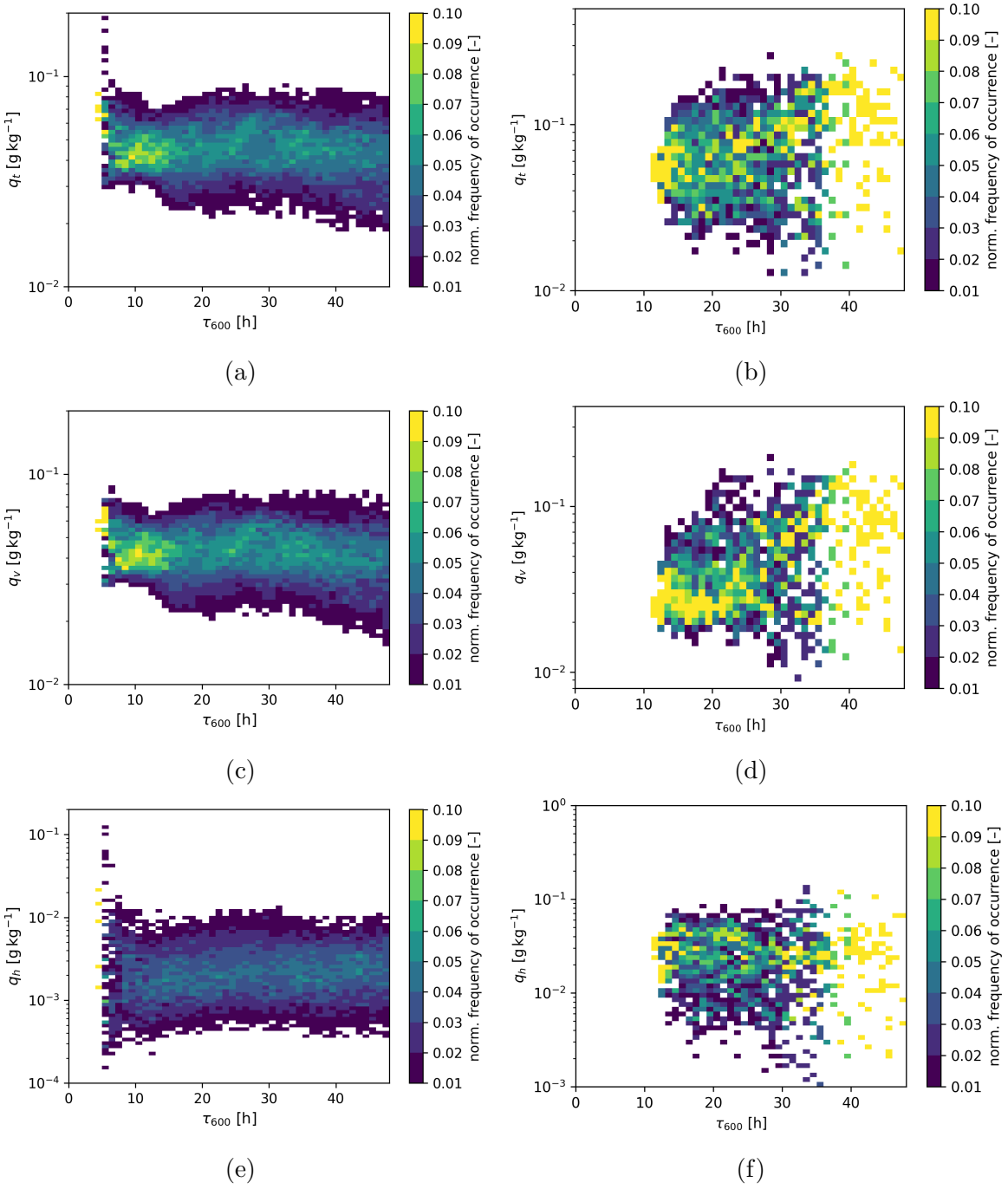

Figure 5.26: The distributions of total moisture content, specific humidity and hydrometeor content, respectively, at the end of the WCB ascent as a function of τ_{600}. Panels (a),(c),(e) are from ICON simulation and panels (b),(d),(f) are from ERA5 data.

Outflow relative humidity with respect to ice (RHi)

Figure 5.27a compares the relationship between relative humidity with respect to ice (RHi) and temperature in the WCB outflow region for ICON and ERA5, using the same axis ranges as in the summer case. Compared to summer, the winter WCB outflows all cross the homogeneous freezing threshold (~ -38°C). In ICON, RHi shows a clear temperature dependence, with values exceeding 120% near -65°C and gradually decreasing toward 100% around the homogeneous freezing threshold near -40°C. This indicates widespread ice-supersaturated conditions in ICON WCB outflow regions, favouring ice crystal growth and potential cirrus cloud formation. The broad 10-90% range further highlights substantial variability among individual WCBs, especially at colder temperatures. In contrast, ERA5 displays an almost temperature-independent RHi distribution, remaining narrowly confined between 101–103%. This suggests that homogeneous freezing processes are largely suppressed in ERA5 at temperatures below –40 °C, likely due to the model's moisture adjustment schemes as explained in Section 5.3.4.

The normalized RHi histogram in Fig. 5.27b further highlights the differences between the two datasets. ICON exhibits a broad peak near 110%, with very similar distributions for fast- and slow-ascending WCBs, indicating that the ascent timescale has only a minor influence on outflow RHi, consistent with the summer case. In contrast, ERA5 displays a much clustered distribution with a sharp peak around 103% and only a small fraction of values exceeding 110%. Compared to summer, ERA5 shows little seasonal variation and retains its near-saturation bias in the outflow region. ICON, on the other hand, displays a stronger seasonal signal, with generally higher RHi values and a broader distribution during winter. This difference suggests that ERA5 continues to underestimate ice-supersaturated conditions, particularly in colder environments, while ICON captures a more realistic spread of upper-tropospheric RHi that reflects seasonal variability in WCB outflow regions.

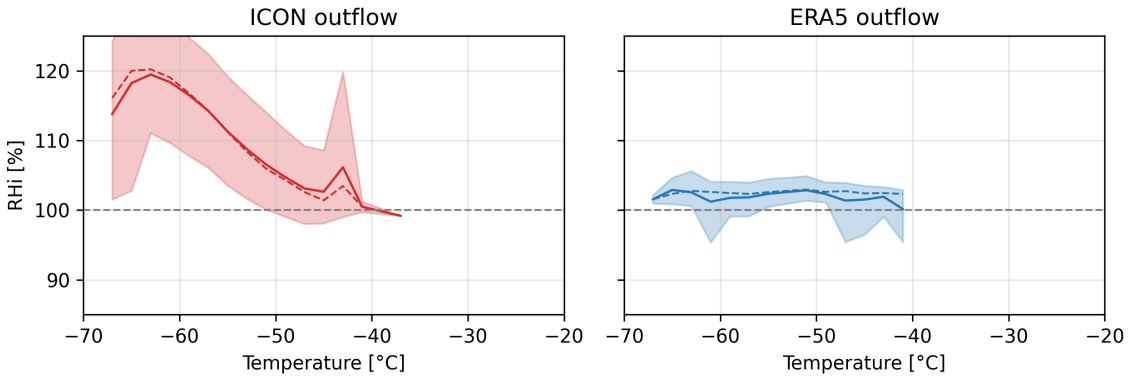

(a)

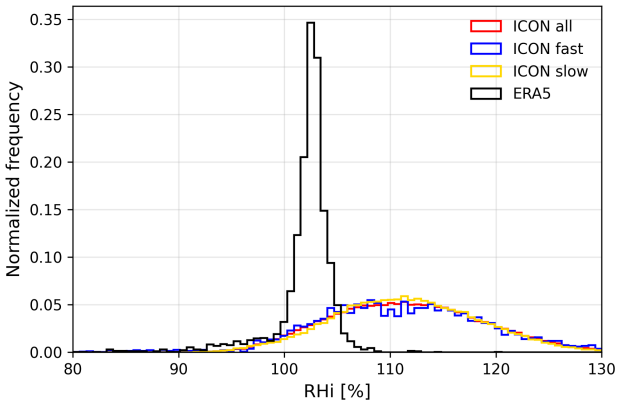

(b)

Figure 5.27: (a) Distribution of relative humidity with respect to ice (RHi) as a function of temperature in the WCB outflow for ICON (left panel) and ERA5 (right panel). Shading denotes the 10th–90th percentile range. (b) Normalized histogram of RHi at the end of ascent for ERA5 (black) and ICON (red), with ICON fast-ascending (blue) and slow-ascending (orange) WCBs shown separately.

Inflow–outflow correlations of q_v and T

For case 2, the inflow-outflow relationships for specific humidity (q_v) and temperature (T) are shown in Fig. 5.27. Similar to the summer case, both variables show stronger correlations in ERA5 than in ICON, with $r = 0.56$ for q_v and $r = 0.68$ for T, compared to $r = 0.32$ and $r = 0.48$ in ICON, respectively. The weaker correlations in ICON suggest that inflow thermodynamic properties are more substantially modified during ascent, likely due to the influence of explicitly resolved microphysical processes in the high-resolution simulations. In contrast, the higher correlations in ERA5 suggest that the outflow conditions are more directly linked to inflow values, reflecting the smoother character of reanalysis fields resulting from parameterized convection and cloud schemes. Overall, the results confirm that ERA5 exhibits a more constrained and linear inflow–outflow relationship, whereas ICON captures a broader

thermodynamic variability associated with a more physically detailed representation of WCB evolution.

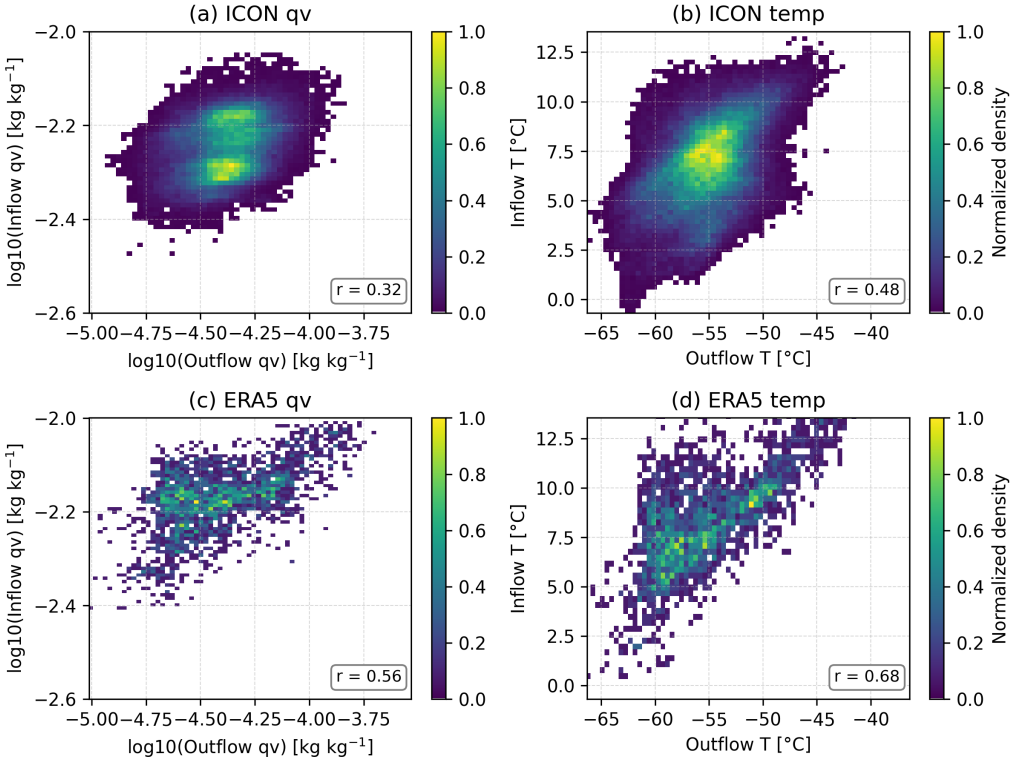

Figure 5.28: Correlations between inflow and outflow conditions for (a–b) ICON and (c–d) ERA5. Panels (a, c) show specific humidity on a logarithmic scale, while panels (b, d) show temperature.

5.4.4 Comparison of moisture loss pathways

Total moisture loss (DR)

Compared to the summer case, the winter case shows a wider range of outflow characteristics between ICON and ERA5. In ERA5, WCBs originate from a relatively moister environment (Appendix Fig. A.19a) and reach lower outflow altitudes when the ascent time exceeds 25 hours. They transport slightly more water vapour and condensate into the UTLS, except for the fast-ascending WCBs, which are not captured in ERA5. The outflow RHi shows a stronger temperature dependence, with substantially higher ice supersaturation in winter. To further assess the total moisture loss during ascent, we compare the drying ratio (DR) between the two datasets for this case (Fig. 5.29).

ERA5 shows a similar decrease in DR as in the summer case, starting from about ~ 0.991

for normal-ascending WCBs and declining to $\sim$ 0.985. ICON exhibits systematically higher DR values for the normal- and slow-ascending WCBs (Fig. 5.29c), indicating more efficient moisture loss in these trajectories. In contrast, the lowest DR for fast-ascending WCBs reflects relatively higher total water content in the outflow, which is consistent with Fig. 5.25a and likely modulated by hydrometeor transport. Unlike ERA5, the DR in ICON remains nearly constant with increasing ascent time, which aligns with the microphysical diagnostics that will be discussed in detail in the following paragraphs.

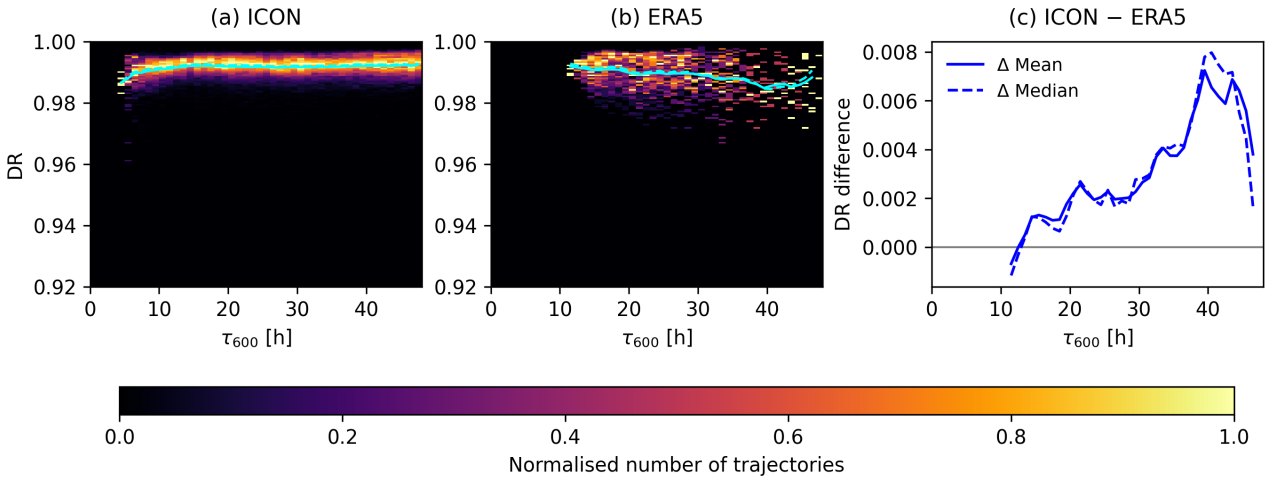

Figure 5.29: DR as the function of τ_{600} for (a) ICON simulation, (b) ERA5 data and (c) the ICON–ERA5 difference. Colors indicate the normalized number of trajectories. Solid (dashed) lines show mean (median) values.

Fractional moisture loss from mixing processes and precipitation (DR_{mix}, P_{loss})

Here, we investigate the moisture-loss contributions from individual microphysical processes, following the same approach as in the summer case and applying it to the ICON simulations. This process-level microphysical analysis provides essential context for interpreting the discrepancies identified in the ICON results for the winter case.

In this case, DR_{mix} increases with ascent time, indicating that slow-ascending WCBs lose a larger fraction of their initial moisture through mixing compared to those that ascend more rapidly.

In contrast to summer, where DR_{mphys} generally decreases with ascent time, the winter case shows the opposite trend. Here, DR_{mphys} increases from about 0.985 for the fastest-ascending WCBs to slightly above 0.99 for the slowest ones. The lowest values occur in fast-ascending

WCBs, where moisture loss is dominated by mixing, consistent with what was observed in summer. For slower WCBs, however, DR_{mphys} remains nearly constant at about 0.99, indicating that microphysical processes are the primary driver of total moisture loss in this case.

This winter behavior likely reflects the colder and more supersaturated environment in which WCB outflows locate. Under these conditions, condensation, deposition, and ice-related processes are highly efficient throughout the ascent. As a result, DR_{mphys} stays close to 0.99 across all ascent time scales. In summer, the upper atmosphere is warmer and less saturated, which enhances evaporation and sublimation, especially during slower ascents. This leads to a weaker microphysical removal and a gradual decline in DR_{mphys} with increasing τ_{600}. The presence of multiple synoptic systems in the summer case likely contributed to this broader range of ascent pathways and microphysical responses. In contrast, the more homogeneous winter case, shaped by a single dominant system, leads to a more consistent microphysical contribution to moisture loss across all WCBs.

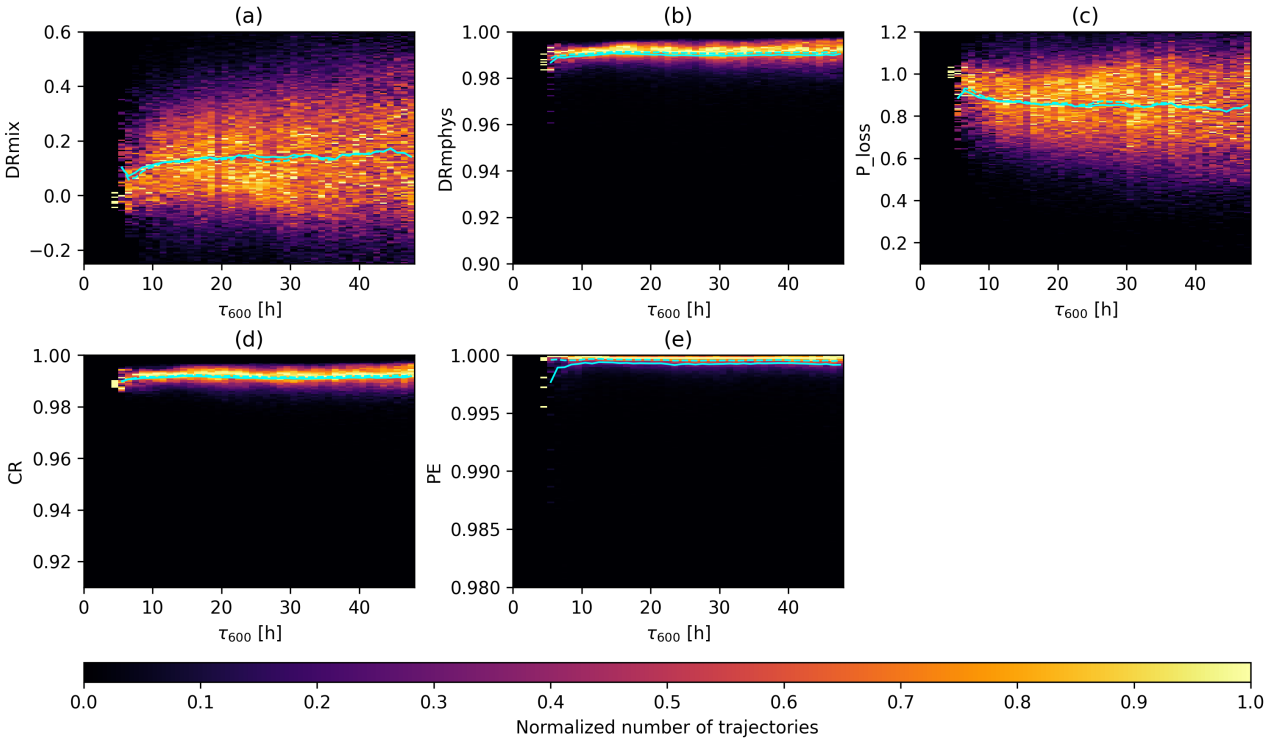

Figure 5.30: Distributions of (a) DR_{mix}, (b) DR_{mphys}, (c) moisture loss due to precipitation, (d) CR, and (e) PE as the function of τ_{600} at the end of the ascent. Colors indicate the normalized number of trajectories. Solid (dashed) lines show mean (median) values.

Microphysical efficiency metrics: CR and PE

The microphysical metrics CR and PE further highlight the distinct behaviour observed in this winter case. The fastest-ascending WCBs show the lowest CR values, reflecting the limited time available for condensational growth during rapid ascent. In contrast, slower WCBs maintain consistently high CR values above 0.99. This behaviour reflects the strong temperature dependence of CR, as the much colder environment favours high CR values and indicates highly efficient vapour-to-condensate conversion throughout the ascent.

The PE remains close to 1 across all ascent times, indicating that nearly all condensate produced along the WCB ascent is removed through precipitation. The lowest PE values occur during the fastest ascent phases, where there is little time for condensate to grow and fall out. Beyond this initial stage, PE remains nearly constant with increasing τ_{600}. This behaviour reflects the influence of the cold and strongly supersaturated winter environment, which supports efficient hydrometeor growth, particularly through deposition, and enables rapid conversion of condensate into precipitation. As a result, microphysical processes operate with very high efficiency throughout the ascent, consistent with the elevated $\mathrm{DR}_{\mathrm{mphys}}$ values observed in this case.

Normalized process diagnostics during ascent

We also analyze the temporal evolution of normalized diagnostics in the winter case, to explore how the mixing and microphysical processes vary across different WCB ascent categories. Fast WCBs show the weakest early signals across all diagnostics. During the initial 0 to 0.2 of the ascent, DR remains low because mixing-induced drying is limited during rapid uplift, and there is insufficient time for microphysical drying. Consequently, CR increases slowly, and PE remains low, reflecting minimal hydrometeor formation and fallout. Between ∼0.2-0.6 of the ascent, DR rises sharply, driven by simultaneous increases in both $\mathrm{DR}_{\mathrm{mix}}$ and $\mathrm{DR}_{\mathrm{mphys}}$. This marks the level at which fast WCBs reach colder and more saturated layers, enabling strong condensational and depositional growth and nearly complete precipitation removal.

In contrast, slow WCBs show the strongest and earliest development across all diagnostics. DR increases rapidly within the first 0.4 of the ascent, supported by substantial contributions from both $\mathrm{DR}_{\mathrm{mix}}$ and $\mathrm{DR}_{\mathrm{mphys}}$This early enhancement reflects longer residence times in mixing layers and highly efficient microphysical processes in the cold winter environment. The rapid rise in CR and PE confirms that condensation and precipitation production begin early for slow WCBs.

These characteristics demonstrate that, while fast WCBs ultimately transport the most moisture into the UTLS, slow WCBs engage in both mixing and microphysical processes much

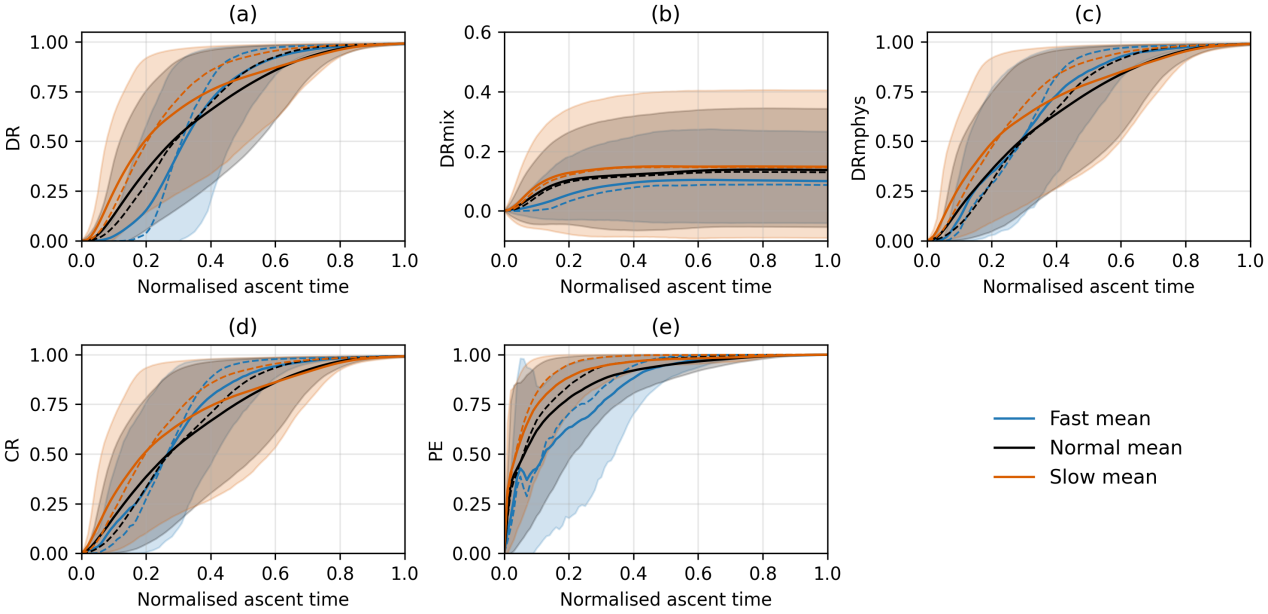

Figure 5.31: Evolution of (a) DR, (b) DR_{mix}, (c) DR_{mphys}, (d) CR, and (e) PE as a function of normalized ascent time. Solid (dashed) lines show mean (median) values. Shading denotes the 10th–90th percentile range.

earlier in their ascent, thereby strongly modulating moisture loss and precipitation efficiency throughout their evolution.

Relative humidity along the temperature during ascent

Due to the colder, drier, and more baroclinic tropospheric structure in winter, the distributions of RHw and RHi for fast and slow WCBs exhibit larger differences than in the summer case.

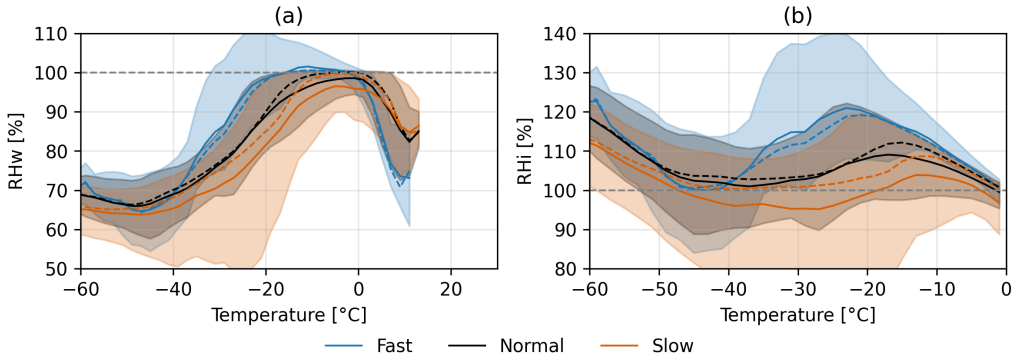

Figure 5.32: Distribution of RHw (a) and RHi (b) along the WCB ascent (τ_{WCB}) as a function of temperature. Solid (dashed) lines show mean (median) values. Shading denotes the 10th–90th percentile range.

Fast WCBs generally maintain higher RHw and RHi than slow trajectories throughout the as-

cent. Above 0 °C, RHw increases steadily as the air parcels cool and approach saturation, with fast trajectories reaching saturation with respect to liquid water more abruptly than slow ones. A subset of fast WCBs exceeds 100% RHw, peaking near –20 °C, where supersaturation with respect to liquid water is briefly maintained. Below -20°C, RHw decreases as the air continues to ascend and glaciation becomes more efficient, depleting vapor through deposition onto ice. After crossing the homogeneous freezing threshold (~ -38 °C), RHw begins to increase again due to the rapid decline in the saturation vapor pressure over liquid water at low temperatures. At this stage, although water vapour continues to be removed by deposition, the saturation vapor pressure over liquid water ($e_s^{\mathrm{liq}}(T)$) decreases more rapidly with decreasing temperature. As a result, the ratio $\frac{e}{e_s^{\mathrm{liq}}(T)}$, which defines RHw, can increase even while vapor is still being lost, leading to a secondary rise in RHw at very low temperatures.

The evolution of RHi exhibits a more distinct temperature dependence with notable differences between fast and slow WCBs compared to summer case. Within the mixed-phase cloud (0°C to -40°C), fast WCB trajectories display a pronounced increase in RHi throughout this temperature range, reaching peak values of $\sim$ 120% near -20°C. This elevated supersaturation results from the rapid ascent and associated cooling, the limited time available for microphysical adjustment allows vapor pressure to remain relatively high, while the saturation vapor pressure over ice declines with decreasing temperature, thereby driving RHi upward. In contrast, the slow WCB trajectories exhibit a more moderate RHi peak, reaching 110% near -10°C, followed by a gradual decline. The slower ascent allows more time for glaciation and depositional processes to deplete vapor, which moderates the degree of supersaturation. As a result, the moisture field remains closer to thermodynamic equilibrium, and RHi increases less dramatically compared to the fast group. This contrast highlights how ascent speed modulates the balance between cooling, saturation adjustment, and microphysical response during the mixed-phase portion of the WCB ascent.

Below -40°C, where many trajectories approach cloud top and transition toward WCB outflow (see Fig. 5.27), RHi increases again. This secondary increase reflects the rapid decline of the saturation vapor pressure over ice at very low temperatures. Although water vapour continues to be removed by depositional growth of ice, the rate at which $e_s^{\mathrm{ice}}(T)$ decreases with cooling exceeds the rate of vapor depletion, allowing RHi to increase despite ongoing condensation onto ice.

Overall, the evolution of RHw and RHi shows that ascent speed strongly controls supersaturation in this winter case, with faster trajectories exhibiting more persistent supersaturation than slower ones.

5.5 Key findings and discussions

In this chapter, we analysed two process-based case studies of WCB events, one in summer and one in winter, to investigate how ascent dynamics, thermodynamic conditions, and microphysical processes control WCB-driven moisture transport into the UTLS. We compare the ICON and ERA5 trajectories to assess how model resolution and physical parameterizations affect the representation of WCB inflow, ascent, and outflow characteristics. By combining Eulerian and Lagrangian perspectives, the main findings from these two case studies can be summarized as follows:

1. Ascent timescale is the primary control on moisture transport in both cases, but its influence is also seasonally modulated. In ICON, fast WCBs transport the largest amounts of both water vapour and condensate into the UTLS, while slow WCBs also contribute substantially to water vapour transport in summer but not in winter. In contrast, ERA5 largely misses the contribution from fast WCBs, and ERA5 exhibits increasing water vapour with τ_{600} in both seasons.

2. Thermodynamic initial conditions strongly shape moisture evolution along WCB ascent. The warmer and more heterogeneous summer initial conditions support a wide range of inflow and outflow moisture and diverse microphysical responses. In contrast, the colder and drier winter inflow condition produces lower total moisture but stronger ice supersaturation, leading to a broader spread of outflow RHi despite a narrower range of total water content.

3. Moisture loss pathways differ between seasons, as revealed by detailed microphysical diagnostics. In summer, the CR and $\mathrm{DR_{mphys}}$ decrease with increasing ascent time, indicating reduced microphysical removal and higher water vapour in the outflow. In winter, CR, $\mathrm{DR_{mphys}}$ and PE remain very high across most ascent times, leading to a high overall DR, reflecting highly efficient vapour-to-condensate conversion and precipitation removal in a cold, ice-supersaturated environment. Drying due to mixing processes plays a secondary role, but its dependence on ascent timescale varies by season. In winter, $\mathrm{DR_{mix}}$ increases slightly and steadily with τ_{600}. In summer, convective mixing contributes more strongly to moisture loss in fast WCBs compared to winter, while turbulent mixing during longer ascent times is also more pronounced in summer than in winter.

4. ERA5 broadly captures the large-scale cyclone evolution compared to ICON. However, ICON simulates a deeper low-pressure center with stronger pressure gradients and resolves mesoscale WCB structures more clearly. ERA5 underrepresents mesoscale WCB structure and moisture processing in both seasons. In the summer case, it suppresses

mesoscale features associated with an interacting low pressure center, leading to the absence of secondary WCB branches captured by ICON in slow ascent times. In winter, it underestimates both fast and slow ascending WCBs. ERA5 also systematically transports larger amounts of condensate into the WCB outflow than ICON and shows higher water vapour content for $\tau_{600} > 20$ hours in both seasons.

In summary, the two case studies show that ascent timescale is the primary control on WCB moisture transport, while moisture loss is strongly modulated by season through different thermodynamic conditions and microphysical efficiency. High-resolution, convection-permitting simulations are essential for capturing the full spectrum of WCB ascent pathways, moisture loss processes, and UTLS outflow conditions that are underestimated or missing in reanalysis data. These process-based insights provide the physical basis for the small ensemble comparisons presented in Chapter 6 and support the interpretation of ERA5-based climatological WCB diagnostics.

6 ICON Simulations of WCBs – Part 2: A Multi-Case Synthesis of ERA5 and ICON WCB Diagnostics

6.1 Introduction

This chapter compares ERA5-based warm conveyor belt (WCB) diagnostics with a small ensemble of high-resolution ICON simulations representing four WCB cases from different seasons. In contrast to the climatological analyses presented earlier in this thesis, the ERA5 diagnostics are here restricted to the same cases simulated with ICON, enabling a consistent, case-by-case comparison between the two datasets.

The primary objective of this chapter is to assess the robustness of the WCB diagnostics developed in this thesis by examining the consistency of key characteristics of WCB ascent and moisture transport across ERA5 and ICON. While ERA5 provides a statistically robust, long-term reanalysis perspective, the ICON simulations explicitly resolve mesoscale dynamical structures such as embedded convection. This comparison therefore allows a systematic evaluation of how well reanalysis-based diagnostics capture the essential features of WCB moisture transport, and to what extent high-resolution simulations reveal additional structure or systematic differences. In this context, this chapter directly addresses the final research question introduced in Section 1.5: *How robust are comparisons between ERA5-based diagnostics of WCB moisture transport from multiple high-resolution ICON simulations?*

By synthesizing results across several WCB cases, this chapter provides a critical assessment of the strengths and limitations of reanalysis-based approaches for diagnosing WCB-driven moisture transport into the UTLS, thereby complementing the climatological perspective established in Chapter 3.

6.2 Evolution of WCB inflow characteristics

We first compare the temporal evolution of temperature and pressure at WCB inflow points, defined as the first points of each τ_{WCB} segment, between the ICON ensemble and a case-matched ERA5 composite. Since inflow duration varies across individual WCB events, the time axis is normalized to a common 48-hour analysis window. This normalization enables a consistent comparison of the characteristic thermodynamic evolution sampled by WCB inflow points across many events, independent of differences in cyclone lifetime, WCB duration, or the absolute timing of inflow relative to cyclone development. The x-axis therefore represents relative rather than absolute inflow time, beginning at the first occurrence of identified inflow points in each case.

Panels a–b show the evolution of temperature and pressure at inflow points in the ICON ensemble. Inflow temperature gradually decreases from about 20°C at the beginning to ∼17°C toward the end. This trend reflects inflow air masses progressively sampling cooler environments as cyclones evolve and propagate poleward. A pronounced temperature drop occurs around 30 hours, with values decreasing to ∼12.5°C. This feature appears during the cyclone's mature stage and likely reflects frontal sharpening or enhanced intrusion of colder air into the inflow region. In contrast, inflow pressure in ICON remains relatively stable throughout the 48-hour window, with values near 940 hPa.

Compared to ICON, ERA5 inflow temperature is more stable, but exhibits a similar drop around 30 h (Fig. 6.1c–d). This suggests that in both datasets, inflow temperature is primarily governed by large-scale, well-resolved dynamics, which ERA5 captures reliably. In contrast, the evolution of inflow pressure differs markedly between the two datasets. While ICON shows relatively stable inflow pressure throughout the 48-hour window, ERA5 exhibits a pronounced pressure increase, peaking around 30 h, coinciding with the mature stage of the cyclone. This difference likely reflects the smoother representation of cyclone structure and frontal gradients in ERA5, which allows greater vertical variability in the inflow region as the large-scale pressure field evolves. In ICON, the high-resolution allows for sharper frontal structures and a more coherent inflow layer, constraining inflow points to a relatively narrow pressure range.

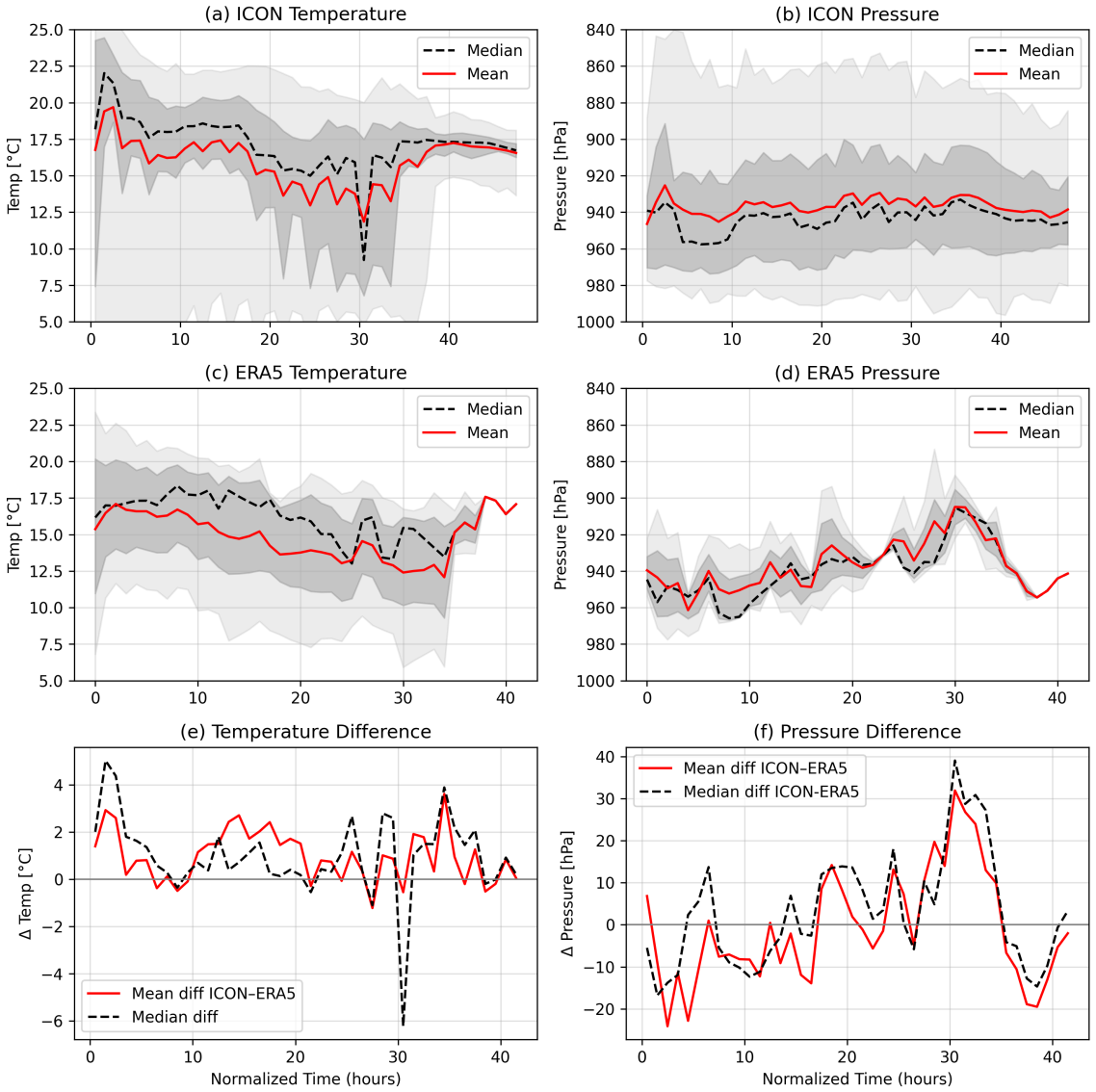

Figure 6.1

6.3 Comparison of WCB outflow characteristics

In this section, we compare the spatial characteristics of WCB outflow between the ICON simulations and the ERA5 cases in Fig. 6.2. The red contour indicates the 10-year ERA5 WCB outflow climatology introduced in Chapter 3. In both panels, color shading indicates the normalized density of outflow points.

The ICON outflow points are primarily concentrated over the North Atlantic, with distribution extending from the subtropical western Atlantic toward northeastern Europe. As discussed in the previous chapter, ICON explicitly resolves fast convective trajectories, leading to earlier outflow appearances compared to ERA5. This explains the prominent outflow band over the

western Atlantic in ICON, which is entirely absent in ERA5. Additionally, the ICON distribution extends further eastward into western Russia, indicating a broader spatial outflow reach. In contrast, ERA5 exhibits a more confined outflow pattern, underestimating both the spatial extent and the frequency of WCB outflows. This underrepresentation is particularly pronounced in regions dominated by fast, convective ascent as well as for slow-ascent WCBs embedded within large-scale, slowly evolving flows. These aspects will be discussed in the following paragraph. Overall, while both datasets capture the large-scale structure of WCB outflow regions, the ICON simulations reveal stronger regional contrasts and a more pronounced zonal extent compared to ERA5.

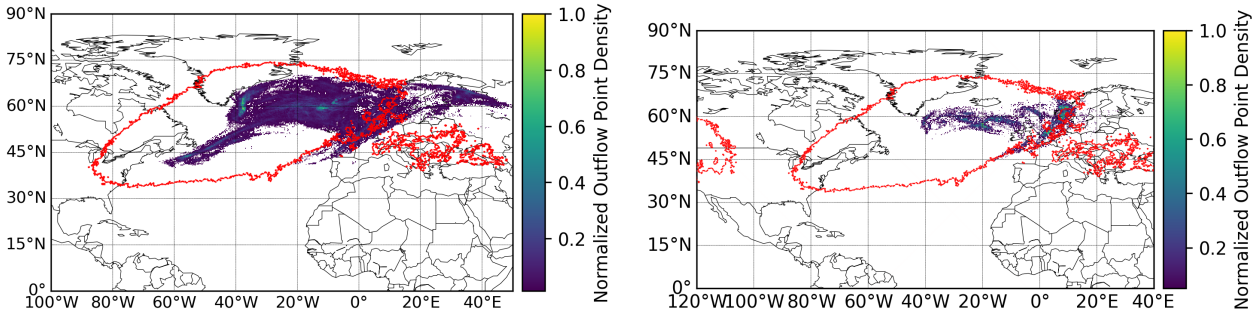

(a) ICON (b) ERA5

Figure 6.2: Normalized WCB outflow point density from (a) the ICON small ensembles and (b) the ERA5 data. Color shading indicates the relative frequency of outflow occurrence, normalized to the maximum density in each dataset. The red contour shows the 10-year ERA5 WCB outflow climatology (Chapter 3) as a reference.

Figure 6.3 compares statistical characteristics of WCB outflow between ICON and ERA5. The left panel shows the normalized frequency distribution of ascent times τ_{600}. ICON exhibits a broad distribution, with a distinct early peak representing the fastest WCBs ($\tau_{600} < 5$ h). A secondary peak in ICON aligns with the ERA5 maximum around 15–20 h. In addition, ICON shows a relatively higher frequency of slow-ascending WCBs for $\tau_{600} > 30$ h. The first bias is particularly evident in the second summer case, as shown in Appendix Fig. A.25. This case is influenced by enhanced convective activity at lower latitudes, which leads to locally rapid vertical transport embedded within the WCB inflow. Under these conditions, ICON is able to explicitly simulate convectively enhanced and rapidly ascending WCB segments, resulting in very short ascent times. In contrast, ERA5 relies on convection parameterization and smoother vertical motion fields, which distribute rapid ascent over longer time scales and therefore fail to represent the fastest ascending WCBs.

The higher frequency of slow ascending WCBs in ICON appears in both seasonal case studies. As discussed in the previous chapter, the relatively coarse resolution of ERA5 smooths

the underlying dynamical structures and limits its ability to represent more distributed ascent pathways under complex synoptic conditions. A secondary contribution to this underestimation may stem from the inflow point selection criteria used in ERA5, which restrict inflow sampling to a fixed 5°x5° box along each inflow track and require both inflow and the corresponding outflow points to occur within the lifespan of the inflow track. This constraint may exclude some WCBs that are associated with broader scale and weaker ascent. However, this effect is likely minor compared to the structural limitations in reanalysis resolution.

The right panel shows the normalized distribution of outflow pressure. Both datasets exhibits a clear maximum between 300-350 hPa and are generally consistent above 300 hPa. However, ERA5 shows a greater fraction of outflow points between 360-400 hPa, suggesting that a larger proportion of ERA5 WCBs terminate their ascent at lower altitudes compared to ICON. This difference is consistent with the smoother vertical motion fields in ERA5, which tend to weaken the vertical extent of ascent and shift outflow levels downward.

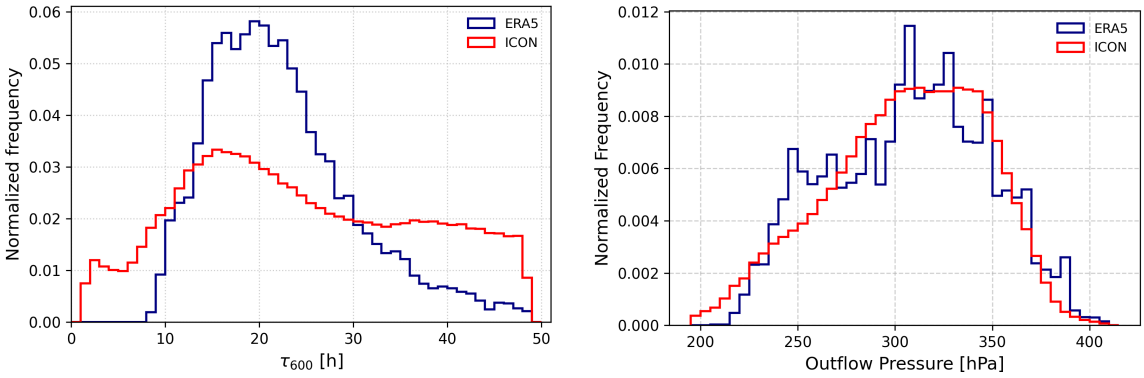

(a) (b)

Figure 6.3: Comparison of normalized frequency distributions of (a) ascent time and (b) outflow pressure between the ICON ensemble (red) and the ERA5 dataset (navy).

6.4 Comparison of trajectory characteristics

Temperature and pressure evolution along τ_{600}

We next compare the inflow and outflow pressure and temperature between ICON and ERA5 as a function of ascent time τ_{600} in Fig. 6.4, with the corresponding ICON minus ERA5 differences shown in Fig. 6.5. The inflow temperature (Fig. 6.4a) evolves similarly in both datasets, with a gradual decrease in fast WCBs followed by a weak increase toward larger ascent times.

The mean temperature difference remains small when $\tau_{600} < 20$ h. However, for slower WCBs, ICON inflow temperatures are consistently lower than those in ERA5, with differences reaching up to 4°C in Fig. 6.5a. Inflow pressure shows substantial overlap between the two datasets, as indicated by the 10–90% shading, with ICON inflow pressure slightly higher than ERA5 for $\tau_{600} > 20$. This difference is also reflected in the inflow total water, where ICON shows lower inflow values for $\tau_{600} > 20$ h in Fig. 6.7a. These results suggest that slow WCB inflow points in ICON span a wider range of initial thermodynamic conditions, while the corresponding cases in ERA5 are more tightly constrained.

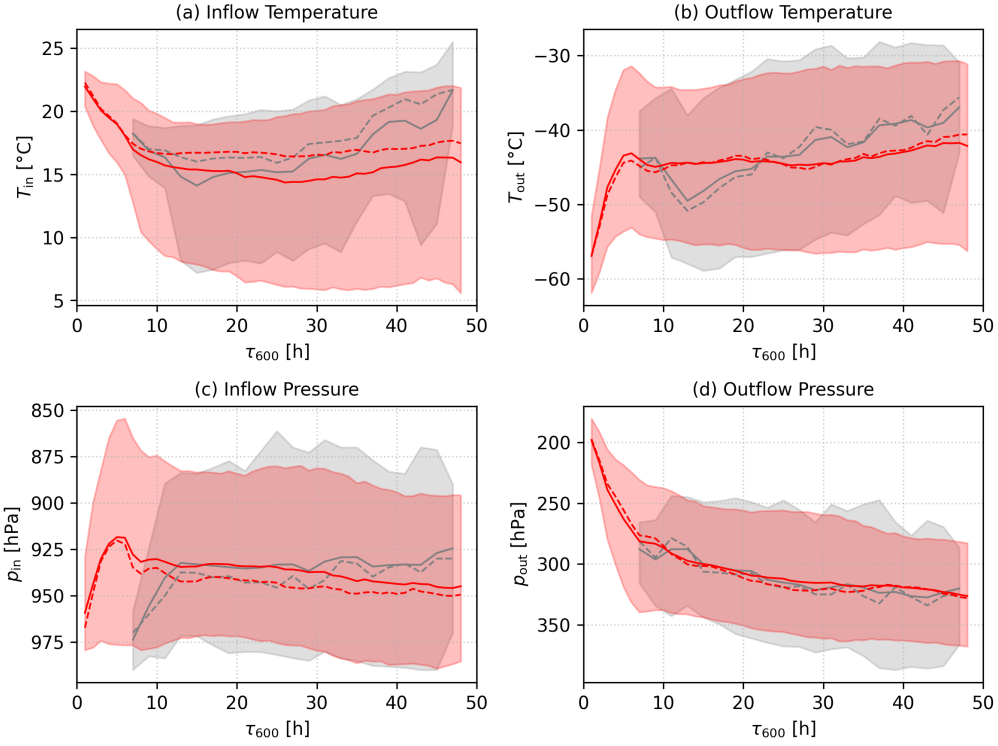

Figure 6.4: Comparison of inflow and outflow (a–b) temperature and (c–d) pressure as a function of τ_{600} for ICON (red) and ERA5 (grey). Solid (dashed) lines show mean (median) values. Shading denotes the 10th–90th percentile range.

Both datasets show overall increasing outflow temperature with ascent time (Fig. 6.4b). For $\tau_{600} < 20$, ICON produces warmer outflow temperatures, reaching up to 5 °C, and this is accompanied by lower outflow pressure compared to ERA5. When $\tau_{600} > 20$, the outflow pressures from ICON and ERA5 largely overlap, while ICON temperatures are slightly lower. The vertical displacement of WCBs, shown in Fig. 6.5e, decreases as ascent time increases. For the fastest WCBs, ICON resolves stronger vertical transport, consistent with convective enhancement, which results in the largest vertical displacements. For slower WCBs with $\tau_{600} > 20$ h, ICON still shows slightly stronger vertical transport than ERA5, reflecting its more detailed

representation of vertical motion. Notably, although the two case studies discussed in Chapter 5 show clear differences in inflow and outflow temperature and pressure between ICON and ERA5, the second summer case shown in Appendix Fig. A.30 shows a broadly similar distribution across the two datasets.

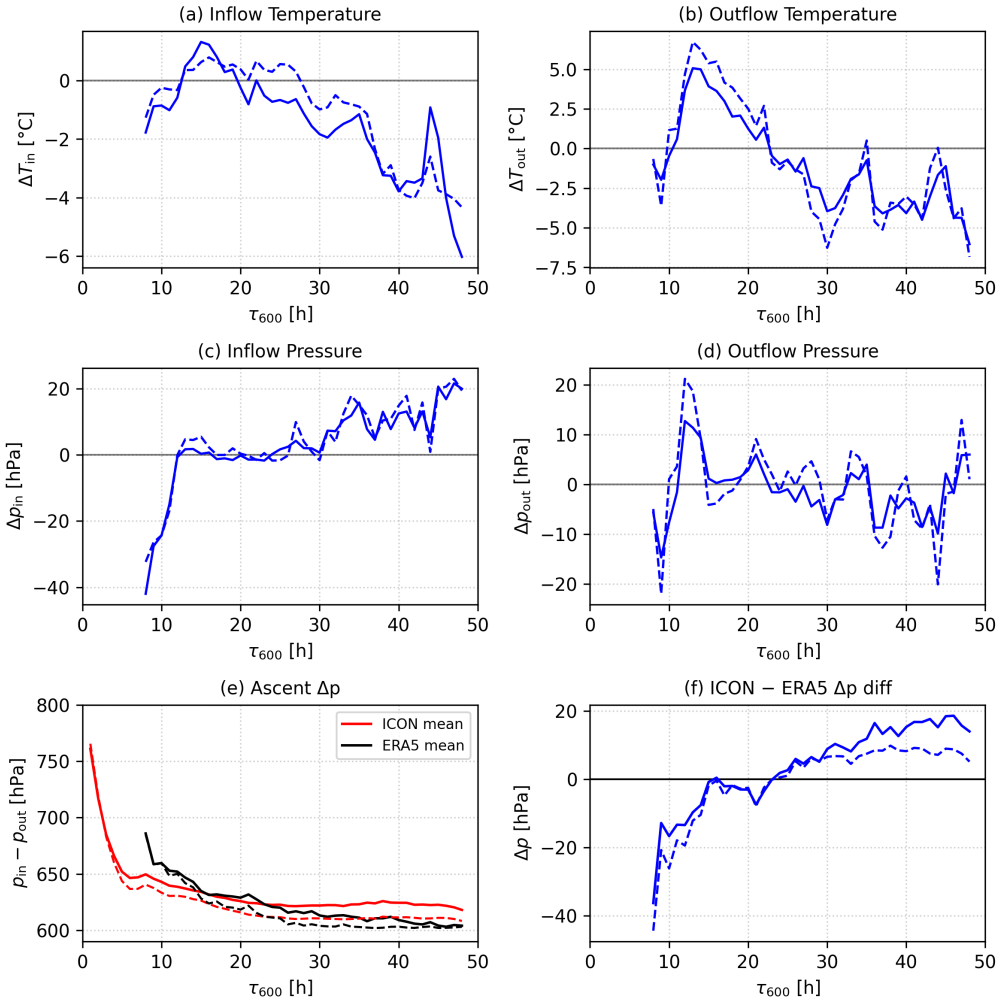

Figure 6.5: (a-d) Differences in temperature and pressure at WCB inflow and outflow points between ICON and ERA5 (ICON minus ERA5) as a function of τ_{600}. (e) Ascent pressure difference between inflow and outflow points for ICON (red) and ERA5 (black). (f) Difference in ascent pressure (ICON minus ERA5). Solid (dashed) lines show mean (median) values.

Moisture evolution along τ_{600}

The distribution of inflow and outflow moisture as a function of ascent time τ_{600} is shown in Fig. 6.6, with the corresponding ICON minus ERA5 differences in Fig. 6.7. In both datasets, inflow moisture is dominated by specific humidity q_v, with negligible contributions from con-

densate q_h. This is evident from the close agreement between total water q_t and q_v in the inflow panels, indicating that nearly all inflow moisture is in vapor form.

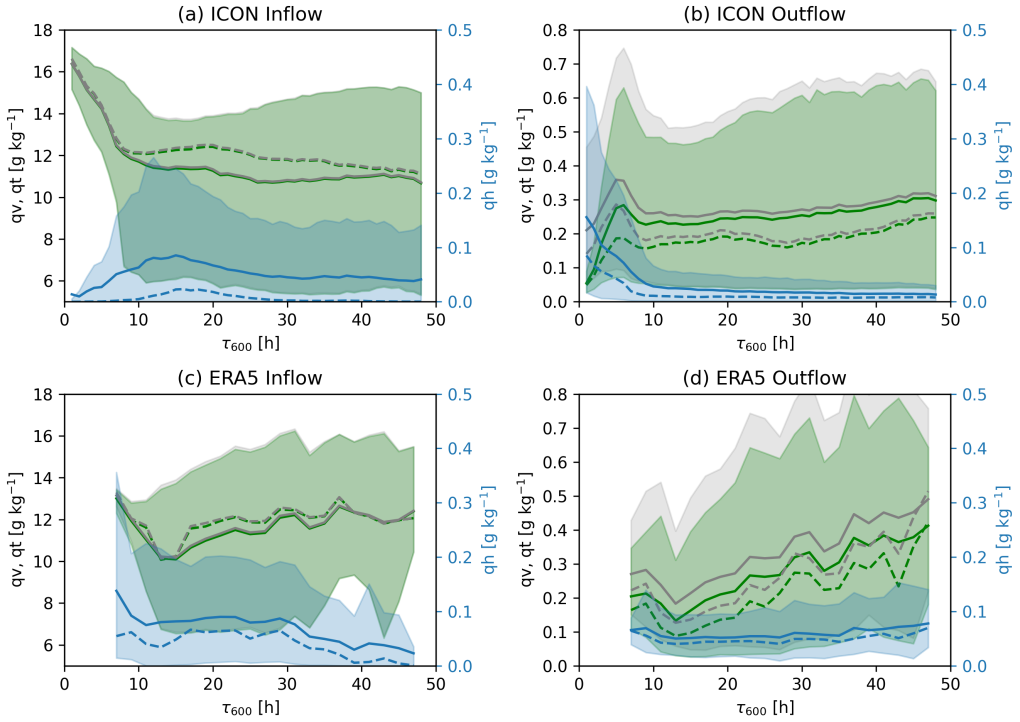

Figure 6.6: Comparison of total water (q_t, grey), water vapour (q_v, green), and condensate (q_h, blue) as a function of τ_{600} for inflow and outflow. Panels (a–b) show ICON and panels (c–d) ERA5. Solid (dashed) lines show mean (median) values. Shading denotes the 10th–90th percentile range. A separate axis on the right-hand side is used for q_h.

As discussed previously, ICON exhibits higher inflow total water than ERA5 for WCBs with $\tau_{600} < 20$ h, with differences reaching up to approximately 1.5 g kg^{-1}, whereas for slower WCBs the inflow total water in ICON is lower. A similar positive bias is found at outflow. Separating total water into vapor and condensate reveals that this outflow difference is primarily due to higher q_v in ICON, while ICON outflow condensate remains consistently lower than in ERA5. The fastest ICON WCBs carry the largest amounts of both total water and water vapour at outflow (Fig. 6.6b). In contrast, ERA5 does not capture the pronounced outflow q_v peak associated with fast WCBs, but shows its highest outflow q_h in this group. This pattern aligns with the climatological distributions in Fig. 4.21, suggesting that ERA5 systematically underrepresents the enhanced vapor signal of rapidly ascending WCBs.

For $\tau_{600} > 10$ h, the outflow water vapour increases with ascent time in both datasets, with ERA5 exceeding ICON by about 0.15 g kg^{-1} for slow WCBs. ERA5 also exhibits systematically higher outflow condensate than ICON, particularly for normal and slow WCBs, with the

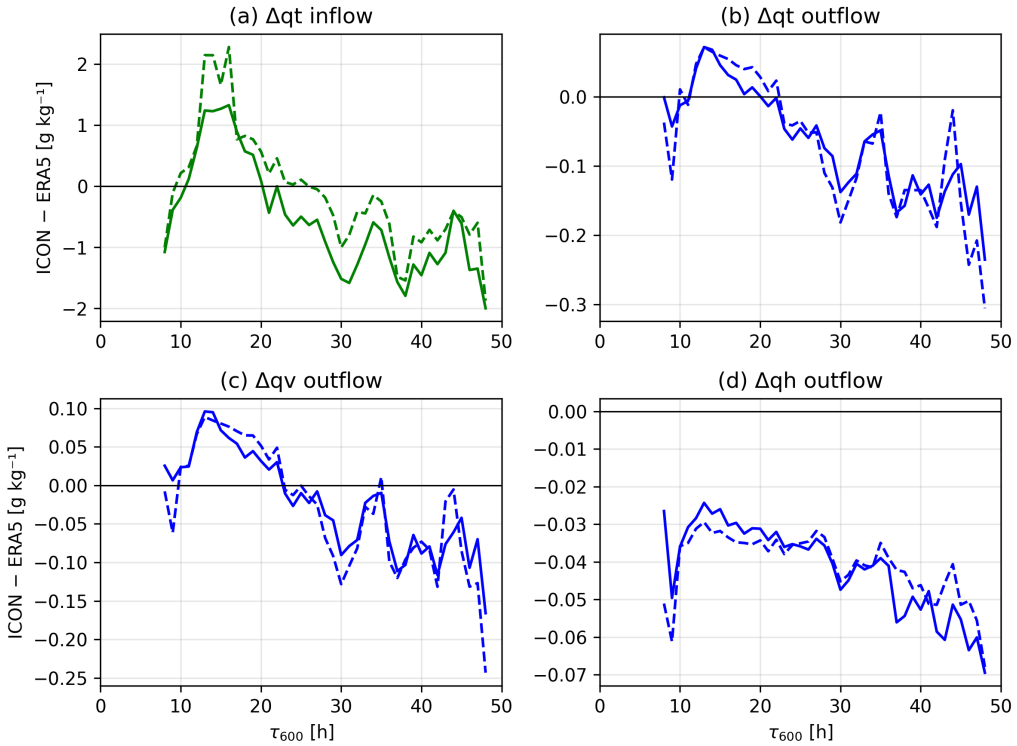

Figure 6.7: Mean differences between ICON and ERA5 (ICON minus ERA5) in (a) inflow total water, (b) outflow total water, and (c-d) outflow water vapour and condensate as a function of τ_{600}.

largest difference of approximately 0.05 g kg^{-1} for the slowest WCBs. In ICON, the outflow q_h decreases with increasing τ_{600} and stabilizes at low values, whereas in ERA5 it decreases initially and then shows a slight increase for the longest ascent times, as illustrated in Fig. 6.6.

Distribution of outflow moisture components along τ_{600}

The distributions in Fig. 6.8 provide further insight into how the outflow moisture components vary with ascent time τ_{600} when considering the ensemble. The left panels show the ICON distributions, while the right panels display the differences between ICON and the ERA5 cases.

For specific humidity, the ICON distribution exhibits a pronounced maximum at $\tau_{600} \sim 5$h. This feature is consistent with the ensemble mean peak seen in Fig. 6.6 and reflects a higher frequency of large q_v values for rapidly ascending WCBs. A second region with high frequency appears at lower q_t and q_v values and is linked to winter case, where outflow moisture is generally lower than in summer cases.

The condensate distribution shows the largest values for the fastest ascending WCBs. As ascent time increases, the occurrence of high q_h values decreases rapidly, indicating a strong

reduction in condensate along longer ascent pathways.

The difference panels on the right reveal systematic contrasts between ICON and ERA5. ICON exhibits a higher frequency of large q_v and q_h values for fast WCBs, whereas ERA5 shows a higher frequency of large q_v values for slow WCBs. For q_h, ERA5 generally displays a higher occurrence of large values, except for the fastest WCBs where ICON attains the highest condensate amounts. These contrasts are most pronounced for the normal and slow ascent regimes.

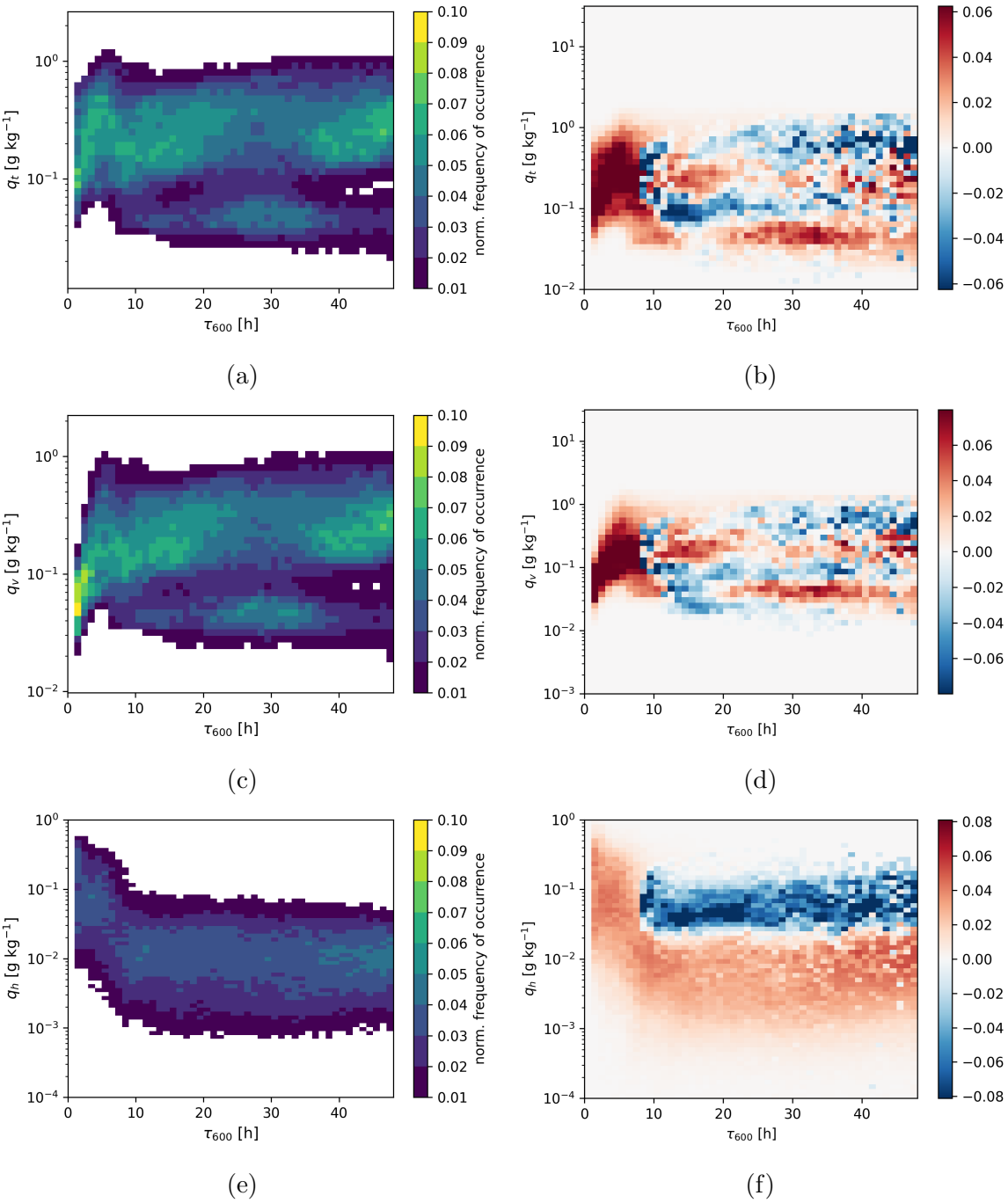

Figure 6.8: The distributions of total moisture content, specific humidity and hydrometeor content, respectively, at the end of the WCB ascent as a function of τ_{600}. Panels (a),(c),(e) are from ICON ensembles and panels (b),(d),(f) are the differences by ICON ensembles minus ERA5 cases.

Outflow relative humidity with respect to ice (RHi)

This section presents a composite comparison of RHi at WCB outflow. Figure 6.9a shows the distribution of outflow RHi as a function of temperature for ICON and ERA5. In ICON, RHi increases with decreasing temperature and reaches values of up to 115%, whereas in ERA5 it remains tightly constrained near ice saturation at around 102% across the entire temperature range. The dramatic decrease in RHi at temperatures below -65°C is mainly contributed from the second summer case (see Appendix Fig. A.35). This behavior is likely associated with fast WCBs occurring in strongly convective environments, where enhanced vertical accelerations and mixing modify the thermodynamic evolution of outflow air parcels (see Appendix Fig. A.30b,d) and thereby limit the persistence of ice supersaturation at very cold temperatures.

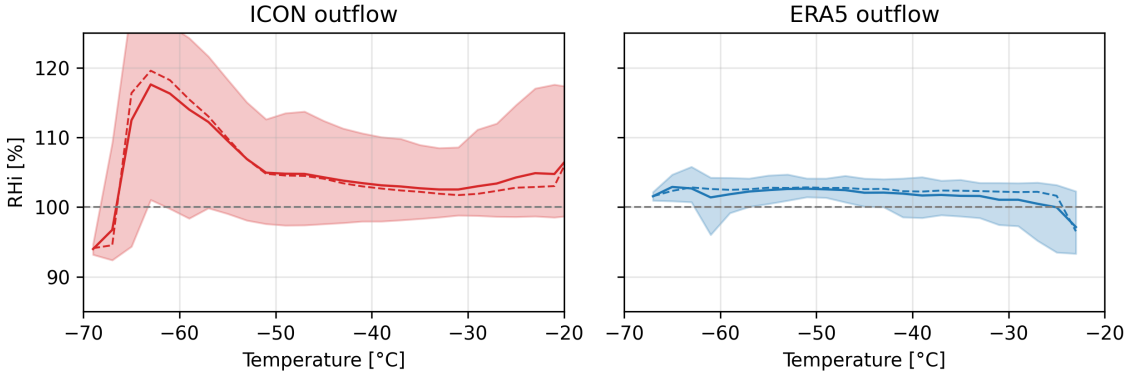

(a)

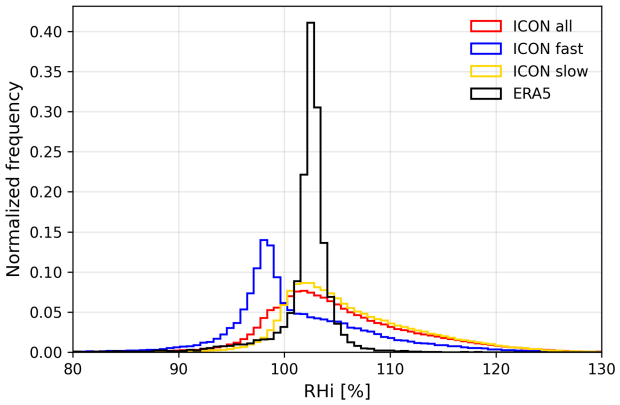

(b)

Figure 6.9: (a) Distribution of relative humidity with respect to ice (RHi) as a function of temperature in the WCB outflow for ICON ensemble (left panel) and ERA5 cases (right panel). Shading denotes the 10th–90th percentile range. (b) Normalized histogram of RHi at the end of ascent for ERA5 (black) and ICON (red), with ICON fast-ascending (blue) and slow-ascending (orange) WCBs shown separately.

Figure 6.9b shows the normalized RHi distributions for ERA5 and ICON, with the ICON ensemble further separated by ascent times. Unlike the earlier case studies, where fast and slow ascent branches in ICON showed only weak RHi differences, the ensemble analysis reveals a clear separation of outflow RHi across ascent regimes. This behavior is consistent with an additional summer case presented in the Appendix (Fig. A.35) and with previous studies such as Schwenk and Miltenberger (2024).

In ERA5, the RHi distribution shows a pronounced peak at 102.47%, with values tightly clustered near saturation. This behavior reflects the influence of the saturation adjustment scheme applied in the presence of ice cloud. As a result, only 9.03% of ERA5 WCB outflows fall below saturation, and less than 1% exceed 110%.

In contrast, the ICON ensemble shows a broader RHi distribution, with an overall peak at 101.84%. Clear differences emerge across ascent regimes. Fast WCBs ($\tau_{600} \leq 10$ h) peak at a lower RHi value of 98.04%, consistent with their reduced outflow specific humidity shown in Fig. 6.8c. Slow WCBs with $\tau_{600} \geq 30$ h tend to retain higher RHi values at outflow.

Overall, 23.68% of ICON WCB outflows are sub-saturated, with 42.12% of these belonging to the fast WCBs. Supersaturation is more frequent in ICON than in ERA5, with 21.19% of trajectories exceeding 110%, including 6.37% from fast and 37.28% from slow ascent branches. Supersaturation predominantly occurs in cold season cases (Fig. 5.12), where cold temperatures favor ice supersaturation due to thermodynamic constraints.

In summary, ERA5 captures the central tendency of outflow RHi through its saturation adjustment scheme but strongly constrains variability around ice saturation. As a result, both sub-saturated and supersaturated conditions are underrepresented, particularly during winter. In contrast, the ICON ensemble resolves a broader range of RHi values and reveals a clear dependence on ascent time, with the largest deviations from saturation occurring in the fast ascent regime.

Inflow-outflow correlation of q_v and T

To evaluate the consistency of thermodynamic transport within WCBs, we analyze the correlation between inflow and outflow conditions across all trajectories in the ICON ensemble and the ERA5 climatology (Fig. 6.10). In ERA5, both specific humidity and temperature exhibit high inflow–outflow correlations, with coefficients of 0.81 for q_v and 0.73 for T, indicating that inflow conditions largely constrain the thermodynamic state at outflow. In contrast, the ICON ensemble shows slightly weaker correlations (0.75 for q_v and 0.71 for T), also pointing to a

strong statistical link between inflow and outflow thermodynamic properties at the ensemble scale.

For individual cases, ERA5 exhibits substantially higher inflow–outflow correlations than ICON. These correlations increase slightly in the composite ERA5 analysis. This behavior reflects the more homogeneous thermodynamic evolution within individual ERA5 cases, which results from its coarser resolution and the parameterized processes such as convection and saturation adjustment. These parameterizations suppress small-scale variability and constrain the evolution of moisture and temperature along WCB trajectories, leading to more coherent inflow–outflow relationships within single events. In contrast, ICON explicitly resolves convection, turbulent mixing, and microphysical processes, which introduce greater within-case variability and thereby reduce inflow–outflow correlations for individual cases.

When ICON cases are aggregated into an ensemble, the correlations increase markedly and become comparable to those in ERA5. This results from pronounced case-to-case variability in ICON inflow humidity and temperature, which introduces strong between-case structure in the ensemble statistics. In ERA5, case-to-case variability is weaker, so aggregating many cases adds limited additional structure. Together, these results indicate that ERA5 captures inflow–outflow thermodynamic relationships comparable to those from the high resolution ensemble.

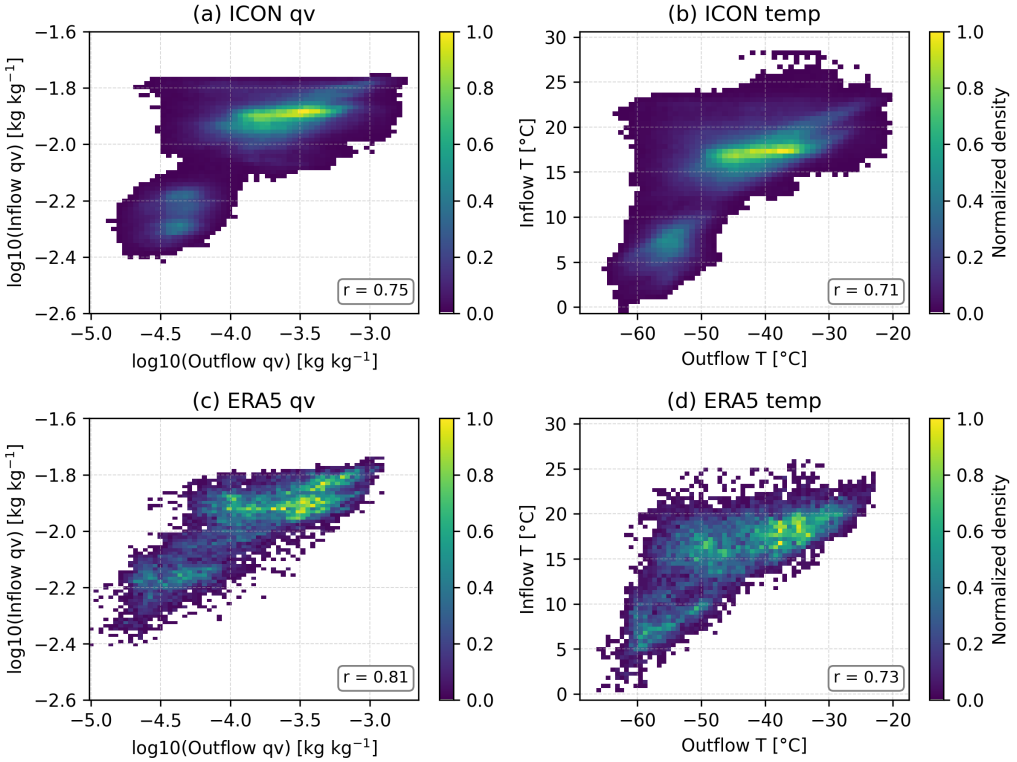

Figure 6.10: Correlations between inflow and outflow conditions for (a–b) ICON ensemble and (c–d) ERA5 cases. Panels (a, c) show specific humidity on a logarithmic scale, while panels (b, d) show temperature.

6.5 Comparison of moisture loss pathway

Total moisture loss (DR)

To quantify how moisture removal differs between the ICON ensemble and ERA5, we analysed the distribution of drying ratios (DR) as a function of τ_{600} across all available WCB cases in Fig. 6.11. In ERA5 the mean drying ratio (DR) decreases gradually from approximately 0.983 to 0.97 with increasing ascent time. ICON shows a similar decrease for $\tau_{600} > 20$ h. For fast WCBs the DR drops more sharply from around 0.99 to 0.975 and is followed by a slight increase before decreasing again.

ICON shows a higher DR than ERA5 for fast WCBs and for $\tau_{600} > 20$ h (Fig. 6.11c), indicating more efficient moisture loss along these ascent pathways, which is consistent with the higher total water retained in ERA5 slow WCBs shown in Fig. 6.7b. Overall, differences between the two datasets remain below 0.015, suggesting that ERA5 reproduces the overall moisture transport efficiency well, despite relying on parameterized convection and microphysics.

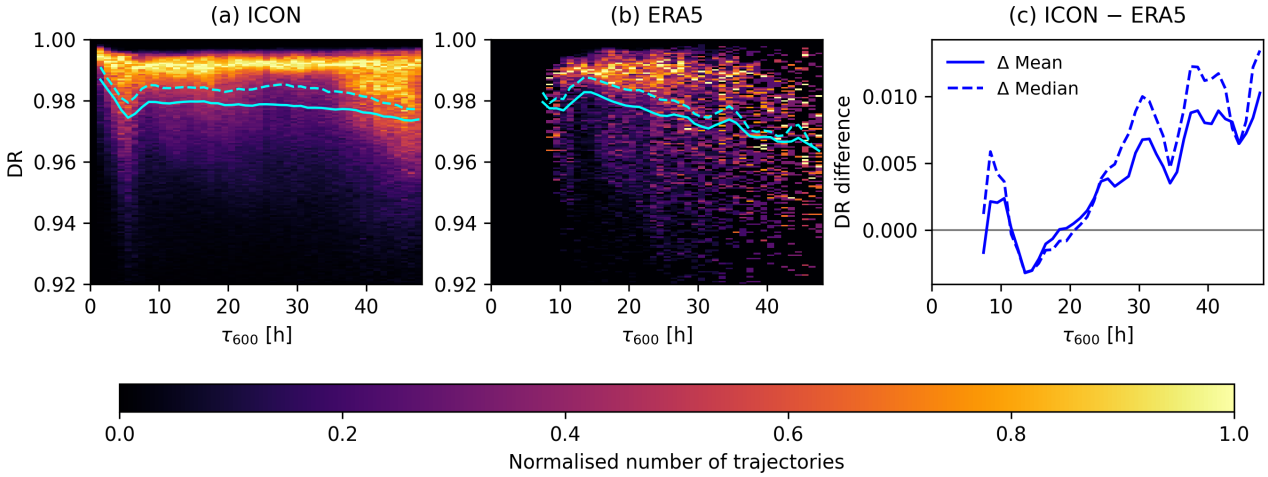

Figure 6.11: DR as the function of τ_{600} for (a) ICON simulations, (b) ERA5 data and (c) the ICON–ERA5 difference. Colors indicate the normalized number of trajectories. Solid (dashed) lines show mean (median) values.

Process-based microphysical diagnostics

To further investigate the physical processes underlying moisture removal in ICON, we analysed microphysical diagnostics as a function of τ_{600} (Fig. 6.12) for all ICON cases. For fast WCBs ($\tau_{600} < 10$ h), CR reaches high values, indicating efficient vapor-to-condensate conversion during ascent, while PE remains low, so that only a small fraction of the condensate is removed through precipitation. As a result, moisture removal during ascent is limited, leading to a relatively moist WCB outflow and reduced total DR for fast WCBs (Fig. 6.11a). In this regime, convective mixing with the environment dominates the drying efficiency, with DR_{mix} exceeding 0.2 while DR_{mphys} remains small.

For normal and slow WCBs, DR_{mix} increases with ascent time, reflecting enhanced turbulent exchange with the environment, while DR_{mphys} decreases, consistent with a gradual reduction in CR. In contrast to the fast WCBs, PE remains high, indicating that condensate formed during ascent is efficiently removed by precipitation. The reduced CR for longer ascent times implies that a larger fraction of water vapour is retained rather than converted into condensate. This behavior is consistent with the increased outflow total water content shown in Fig. 6.6b and contributes to relatively low DR values for larger ascent times. A slight reduction in DR for the longest ascent times is most pronounced in summer and the transition seasons (e.g., Figs. 5.14, Appendix Fig. A.37, and analysis in Schwenk and Miltenberger (2024)), whereas in winter DR remains high across all ascent times (Fig. 5.29). During winter, DR_{mix} exhibits only a weak dependence on τ_{600}, while DR_{mphys}, CR, and PE all remain high values, indicating efficient vapor-to-condensate conversion, strong precipitation efficiency, and comparatively weak turbulent mixing during ascent.

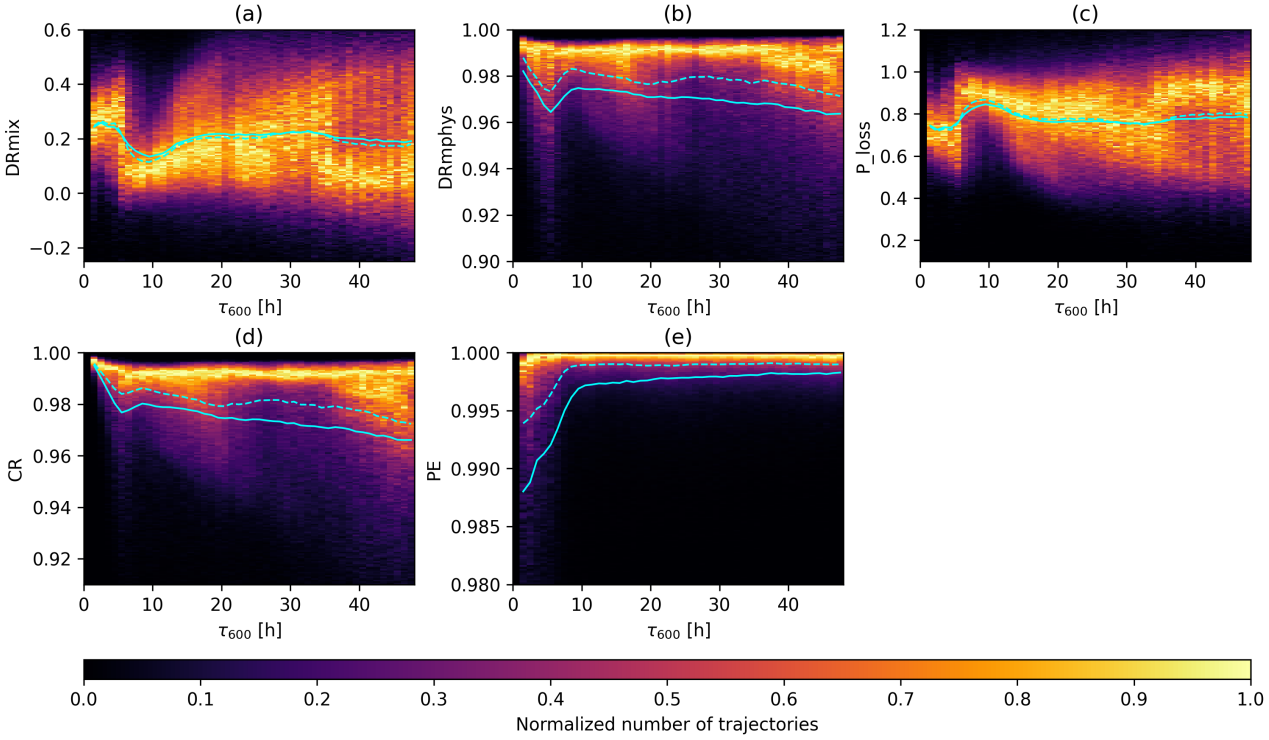

Figure 6.12: Distributions of (a) DR_{mix}, (b) DR_{mphys}, (c) moisture loss due to precipitation, (d) CR, and (e) PE as the function of τ_{600} at the end of the ascent. Colors indicate the normalized number of trajectories. Solid (dashed) lines show mean (median) values.

A summary of the normalized evolution of microphysical and mixing-related diagnostics for fast, normal, and slow WCBs is provided in Appendix Fig. A.42, with overall patterns that are consistent across all individual cases. Condensation, precipitation, and drying processes occur more rapidly during the early stages of ascent in winter and the transitional seasons, whereas summer cases exhibit a more gradual and steady evolution throughout the ascent. These differences underscore the influence of seasonal thermodynamic environments on the efficiency of WCB-associated moist processes.

The ensemble-mean evolution of RHw and RHi as a function of temperature for fast, normal, and slow WCBs (Appendix Fig. A.43) closely resembles the behavior identified in the representative case studies discussed in Chapter 5. Fast WCBs consistently exhibit stronger supersaturation, particularly with respect to ice during the mixed-phase ascent. However, at temperatures below approximately -50°C, RHi decreases to subsaturated values for fast WCBs in one summer case (see Appendix Fig. A.40). This behavior is likely linked to a pronounced slowdown during the final stages of WCB ascent, as evidenced by the shift between τ_{600} and τ_{WCB} (Appendix Fig. A.25), which reduces cooling rates relative to ice growth and allows RHi

to relax toward subsaturation. Additional drying may arise from mixing with drier stratospheric air as these trajectories approach or cross the tropopause. This feature suggests that the upper-tropospheric RHi of fast WCBs is may sensitive to case-dependent factors such as the structure of the outflow region and the distance to the tropopause.

6.6 Key findings and discussions

In this chapter, we evaluated ERA5-based WCB diagnostics using a small ensemble of high-resolution ICON simulations spanning different seasons. The comparison was designed to assess the robustness of ERA5-derived diagnostic and to identify the physical processes that control variability in WCB-driven moisture transport into the UTLS.While ERA5 provides a statistically robust representation of mean WCB inflow and outflow properties, the ICON simulations explicitly resolve embedded convection within WCBs and represent sub-grid scale microphysical processes that are not presented in the reanalysis. This allows a targeted assessment of how ascent timescale, microphysical efficiency, and seasonal thermodynamic conditions modulate moisture transport along WCBs in ICON simulation. Overall, the results show that ascent timescale is the primary control on variability in WCB moisture transport, with additional modulation by season. ERA5 captures the large-scale climatological structure of WCBs but shows systematically smaller variability associated with fast and slow ascent regimes, leading to biases in moisture transport efficiency. The main findings of this chapter are summarized as follows:

1. ERA5 underrepresents both fast and slow WCB ascent regimes compared to ICON. Fast ($\tau_{600} \leq 10$ h) and slow ($\tau_{600} \geq 30$ h) WCBs make up 12.6% and 34.2% of ICON trajectories, but only 3.1% and 15.7% in ERA5, respectively, for the simulated cases.

2. ERA5 overestimates moisture transport into the UTLS by slow WCBs. For $\tau_{600} > 20$ h, ERA5 WCBs consistently transport larger amounts of water vapour into the UTLS, with mixing ratios reaching up to 0.2 g kg^{-1}. This bias toward slower ascent regimes may lead to an overestimation of WCB influenced water vapour fluxes in the UTLS between 30° and 70°N (see Appendix Fig. A.44c,e).

3. ERA5 systematically overestimates condensate (q_h) in WCB outflow, primarily due to the saturation adjustment scheme, which constrains RHi near ice saturation and thereby limits vapor variability while enhancing condensate formation. This bias leads to a systematic overestimation of WCB influenced condensate fluxes into the UTLS, as shown in Appendix Fig. A.44d,f. Notably, the condensate flux into the UTLS associated with fast WCBs is almost entirely absent in ERA5.

4. Ascent timescale governs moisture loss pathways and transport efficiency, but ERA5 fails to capture variability associated with fast ascent. In ICON, fast WCBs exhibit the highest CR and lowest PE, so a large fraction of condensate is retained, which weakens drying and enhances moisture transport into the UTLS. For slower WCBs, increasing ascent time enhances the role of turbulent mixing while microphysical removal weakens, also leading to higher total water with longer ascent times. ERA5 reproduces the mean behavior of WCB moisture transport but fails to capture the enhanced water vapour transport associated with fast ascent.

5. Seasonal thermodynamic conditions strongly modulate WCB moisture transport pathways in the ICON simulations. During summer, WCBs transport substantially more total water into the UTLS than in winter, and fast-ascending WCBs are more frequently associated with convective ascent. The role of microphysical processes also differs by season. In winter, CR and PE are close to 1 across ascent regimes. In contrast, during summer and transitional seasons, microphysical behavior varies strongly with ascent timescale, resulting in large differences in moisture transport and drying efficiency among WCBs.

Limitations

However, there are several limitations that should be considered when interpreting these ensemble comparisons. First, the ICON ensemble is restricted to four cases due to computational constraints, and the corresponding ERA5 analysis is based on the same matched cases rather than the full subset of 50-case composite selected in Section 4.2.4. Although microphysical behavior is broadly consistent across cases, the relative frequency of fast and slow WCBs in ICON varies strongly with season. For example, fast WCBs account for only 4.21% of trajectories in the winter case but exceed 10% in summer cases. As a result, ensemble statistics may be sensitive to the small number of high-resolution cases.

Second, the selection of ERA5 WCB cases is closely tied to the inflow-track-based methodology introduced in Section 4.2.4. Requiring inflow points to lie within a fixed 5°x5° box, and both inflow and outflow points to occur within the inflow-track lifespan, ensures physical consistency but likely underestimates WCBs associated with broader, more slantwise ascent pathways farther from the cyclone center. This constraint may partly contribute to the underrepresentation of slow-ascending WCBs in ERA5

Third, except for the general WCB selection criteria (Section 1.3), the ICON WCB selection additionally relies on a visual identification of coherent WCB and outflow regions based on mean sea level pressure and total cloud cover at two different times. The sensitivity of this pro-

cedure to the choice of time windows can influence the number of identified ICON WCBs and thereby introduce differences relative to ERA5. Moreover, a geometric displacement filter was applied to retain only ICON WCBs that travel at least 5° meridionally or zonally during ascent. This criterion is particularly sensitive to fast ascending WCBs, as relaxing or tightening the filter leads to substantial changes in their representation (see Case 3 in Appendix Fig. A.26). These choices directly affect moisture transport by fast WCBs and their associated microphysical behaviour (cf. Fig. 5.10b and Appendix Fig. A.17b), and therefore must be applied with caution, especially in summer and transitional seasons when rapid ascent is most frequent.

Despite these limitations, the consistency of key signals across cases and seasons supports the robustness of the ERA5-based mean WCB climatologies, while also highlighting that high-resolution simulations are essential for capturing the seasonal variability of WCB ascent and moisture transport, particularly in fast ascent regimes.

7 Conclusions and Outlook

7.1 Summary of key contributions

This thesis investigated the role of warm conveyor belts (WCBs) in transporting moisture from the lower troposphere into the upper troposphere and lower stratosphere (UTLS), combining a climatological perspective based on ERA5 reanalysis with process-oriented insights from high-resolution, convection-permitting ICON simulations. By integrating Eulerian and Lagrangian diagnostics across multiple spatial and temporal scales, the work aimed to quantify the contribution of WCBs to the extratropical UTLS moisture budget and to identify the physical mechanisms that control the efficiency and variability of this transport.

WCBs efficiently transport moisture into the UTLS and play a climatically important role in shaping UTLS humidity, even though a large portion of the moisture is lost during ascent. However, the underlying processes governing this transport have remained incompletely quantified from both climatological and process-based perspectives. This thesis addressed this gap by combining a 10-year ERA5-based climatology with a novel inflow-object framework and targeted ICON case studies, thereby linking large-scale statistics with detailed physical process understanding. Through a systematic progression from climatological description to inflow–outflow linkage, process-resolved case studies, and a multi-case synthesis of ERA5 and ICON WCB diagnostics, this work provides a coherent and physically grounded assessment of WCB-driven moisture transport into the UTLS and evaluates the strengths and limitations of reanalysis-based diagnostics.

In Chapter 3, we examined the climatological impact of WCBs on UTLS moisture using a 10-year ERA5-based climatology, quantifying the spatial distribution, thermodynamic characteristics, and temporal evolution of WCB outflow and its contribution to the UTLS moisture budget. WCB outflow occurs preferentially in the North Atlantic and North Pacific storm tracks, with a pronounced wintertime maximum, and is typically located 1–1.5 km below the local tropopause. Although most WCB air parcels descend back into the mid-troposphere within 24–48 hours after ascent, around 15% of total outflow trajectories remain within 2 km of the tropopause, and about 5% cross into the lower stratosphere.

Despite highly efficient moisture removal during ascent, WCB outflow leaves behind persistent positive anomalies in total water content in the upper troposphere. Although WCBs represent only a small fraction of air parcels entering the UTLS, they contribute disproportionately to both water vapour and condensate transport, highlighting their role as key drivers of UTLS moisture variability. This transport is strongly modulated by season and organized along the storm tracks.

Importantly, WCB outflow is linked to coherent thermodynamic anomalies in the upper troposphere, including positive moisture anomalies and negative temperature anomalies associated with a systematic displacement of the local tropopause. These anomalies persist for up to two days after ascent, indicating that WCBs influence not only instantaneous moisture budgets but also the short-term evolution of UTLS humidity. In addition, the ERA5-based climatology reveals a sensitivity of diagnosed anomalies to the choice of vertical coordinate system and tropopause representation, underscoring the need for a physically consistent UTLS definition when quantifying cross-tropopause transport. Together, these findings establish WCBs as a key dynamical pathway shaping the extratropical UTLS moisture climatology.

Chapter 4 introduced a newly developed inflow-object framework that systematically links inflow conditions, ascent characteristics, and outflow properties within individual WCB cases. The results demonstrate that variability in WCB outflow moisture is strongly constrained by the inflow environment. Moister inflow conditions consistently lead to moister outflows, while warmer inflow air masses generally remain warmer at outflow, indicating a partial retention of thermodynamic characteristics along the WCB pathway. These findings show that outflow-based climatological diagnostics alone cannot fully explain variability in WCB moisture transport and highlight the importance of an inflow-focused perspective. By constructing spatially coherent inflow objects and tracking them over time, the framework offers a physically consistent approach to analyzing WCB life cycles and supports objective case selection. The multi-dimensional sampling yielded a reduced subset of 50 WCB cases that preserves the spatial, seasonal, and thermodynamic variability of the full 300-case dataset. Validation against ERA5 based climatological diagnostics confirms that the selected cases reproduce the key inflow-outflow relationships identified in the full ensemble, providing a robust basis for subsequent high-resolution modelling.

Chapter 5 presented two high-resolution case studies selected from Chapter 4, revealing the physical mechanisms that control moisture transport within individual WCBs. In both summer and winter cases, ascent timescale emerged as the primary factor determining transport efficiency. However, its influence is strongly modulated by the seasonal varying thermodynamic

conditions, resulting in distinct moisture loss characteristics in summer and winter. These process-based, high-resolution results show that mesoscale dynamics and microphysical processes play a crucial role in shaping WCB moisture evolution. Such processes are only partially represented in ERA5 due to its coarse resolution, highlighting the importance of convection-permitting simulations for capturing the full spectrum of WCB behavior.

Chapter 6 extended the process-based insights from Chapter 5 by evaluating ERA5-based WCB diagnostics against a small ensemble of four convection-permitting ICON simulations across different seasons. While ERA5 reproduces the mean spatial structure and overall climatological impact of WCBs on UTLS moisture, it systematically underrepresents both fast and slow ascent regimes, resulting in biases in moisture transport efficiency. These discrepancies have direct implications for UTLS moisture budgets derived from reanalysis data. ERA5 underestimates the contribution of fast-ascending WCBs and overestimates condensate across ascent regimes, as well as water vapour for slower WCBs. Consequently, ERA5 reproduces the mean climatological impact of WCBs on UTLS moisture, but the associated variability in moisture transport efficiency is not fully represented

Taken together, these results demonstrate that ascent timescale is the dominant control on WCB moisture transport into the UTLS, with seasonally dependent thermodynamic conditions and microphysical processes modulating its efficiency. These results combine climatological signals with process-level variability and provide a physically consistent framework for interpreting WCB moisture transport to the UTLS. The original contributions of this thesis include:

1. A comprehensive ERA5-based 10-year (DJF) climatology quantifying WCB outflow moisture anomalies and their contribution to UTLS water fluxes.
2. A novel inflow-object framework enabling objective inflow-outflow linkage and representative case selection.
3. A process-based analysis of WCB moisture transport using high-resolution ICON simulations across contrasting seasons.
4. A quantitative evaluation of the robustness and limitations of ERA5-based WCB diagnostics using multiple ICON simulations.

Overall, these contributions advance the understanding of WCB-driven moisture transport into the UTLS by integrating climatological and process-based perspectives within a physically consistent framework. The results show that ERA5-based climatologies robustly capture the impact of WCBs on UTLS moisture, while high-resolution simulations reveal additional variability in moisture transport efficiency that is linked to ascent characteristics and microphysical processes and is only partially represented in reanalysis data.

7.2 Limitations and outlook

Several limitations of this study should be acknowledged. The ICON ensemble is limited to a small number of cases due to computational constraints, which restricts the ability to fully assess case-to-case variability and the robustness of some diagnostics. Nevertheless, the development and validation of objective case-selection metrics in this thesis (Section 4.2.4) provide a structured pipeline for future high-resolution WCB climatology studies. Although only a limited number of selected cases were simulated here, the inflow-based sampling strategy establishes a robust and extensible framework that can be readily expanded to larger ensembles as computational resources permit.

Building on the findings of this thesis, future research can explore several important directions. First, expanding high-resolution simulations to a larger ensemble of WCB cases across all seasons and a wider range of synoptic environments would contribute to a more comprehensive high-resolution WCB climatology. This would thereby strengthen the evaluations based on reanalysis diagnostics.

Second, combining reanalysis and model output with observational datasets from field campaigns, satellites, or radar measurements would provide valuable benchmarks for assessing the realism of ERA5-based climatologies, including both UTLS moisture characteristics and associated cirrus and ice cloud conditions across the full range of WCB variability.

Finally, examining potential changes in WCB behavior under future climate conditions using time-slice experiments extending to the end of the century would provide valuable insight into how WCB outflows may influence UTLS humidity and radiative forcing in a warming climate.

A Supplementary

A.1 Supplementary for Chapter 3

A.1.1 Sensitivity test for UTLS layer definition

The UTLS layer definition as proposed in Section 3.2.3 defines the UTLS as the layer between 6 pvu and 50 hPa below the dynamical tropopause. Analysis in Section 3.3.2 indicated that the majority of WCB outflow only reaches altitudes of about 1 km below the local tropopause. Therefore, the UTLS layer definition and in particular the definition of the lower edge may impact the flux estimates presented in the previous sections. Fig. A.1 shows the DJF climatological distribution of WCB outflow height in tropopause relative pressure coordinates: Only 30.2 % of all outflow trajectories enter the UTLS layer for definition presented in Section 3.2.3. If the lower boundary of the UTLS is defined to be located 100 hPa below the dynamical tropopause, this fraction increases to 71.7 %.

In order to quantify the impact of the UTLS layer definition on flux analysis and WCB contributions, we have repeated the analysis presented in the previous two subsections placing the UTLS lower boundary at 100 hPa below the local tropopause. The results with both UTLS definitions for the year 2017 are shown in Fig. A.4. The sensitivity analysis indicates that absolute fluxes into the UTLS increase in case of a deeper UTLS layer for both total (Fig. A.2) and WCB-related fluxes (Fig. A.3). For the background this is likely due to a combination of larger vertical velocities and larger air density at lower levels in the troposphere. For WCB-fluxes the larger fraction of WCB outflow entering the UTLS plays a role in addition to the density and vertical velocity differences. Interestingly though the relative contribution of WCB trajectories to the total fluxes slightly decreases for the deeper UTLS layer definition for all fluxes (Fig. A.4, Tab. A.1). The geographic distribution of both absolute fluxes and flux contributions remains mostly unaltered. Therefore we conclude that absolute flux values are sensitive to the UTLS layer definition, but the relative contribution of WCB outflow remains almost constant.

Overall, the flux analysis confirms that WCBs are important contributors to the water budget of the UTLS during the winter season. WCB contributions are strongest in the western ocean basins, i.e. on the Southern flank in the beginning part of the storm track. Note that the

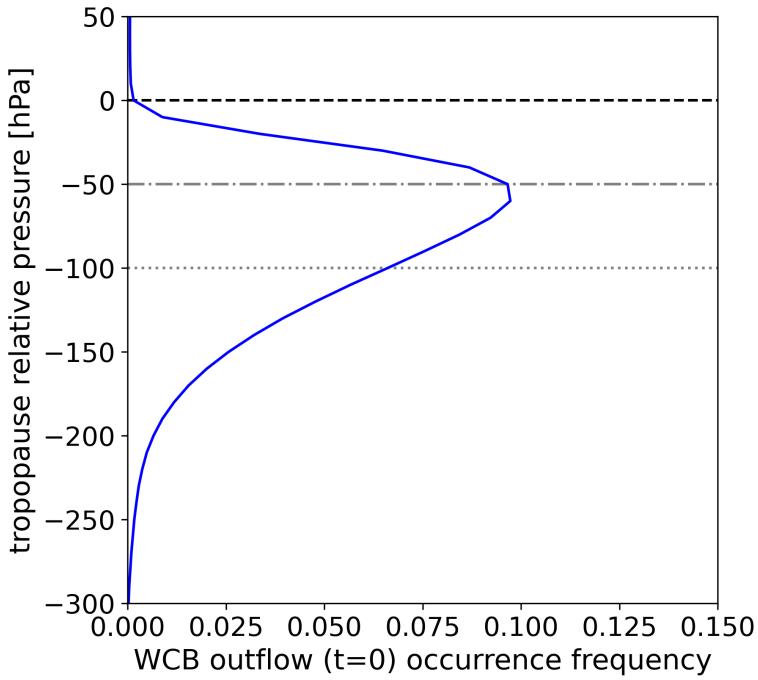

Figure A.1: Distribution of fresh WCB outflow position in a tropopause relative pressure coordinate system (DJF). Dash-dotted and dashed lines indicate the lower boundaries used in UTLS layer definitions, i.e. 50 hPa (used in main analysis) and 100 hPa (used for sensitivity test for 2017) below the local tropopause.

estimates here are rough (likely lower-bound) estimates, as fluxes due to convection are not accounted for as are contributions from air masses that ascend in the vicinity of core WCB ascent region that may not fulfill the 600 hPa in 48 h criterion.

Table A.1: Relative contribution of WCB outflow to UTLS layer fluxes. The column labeled "mean" indicates the average over regions with non-zero WCB contributions, and that labeled "peak" the maximum value in the same region.

	2010–2019		2017 (shallow UTLS)		2017 (deep UTLS)	
	mean	peak	mean	peak	mean	peak
Mass flux	3.71%	12.8%	4.39%	19.9%	3.84%	19.0%
Total moisture flux	3.78%	13.8%	4.52%	21.5%	3.97%	21.1%
Specific humidity flux	3.28%	11.7%	3.96%	18.2%	3.45%	17.4%
Condensate flux	6.33%	23.3%	7.49%	36.5%	6.19%	33.0%

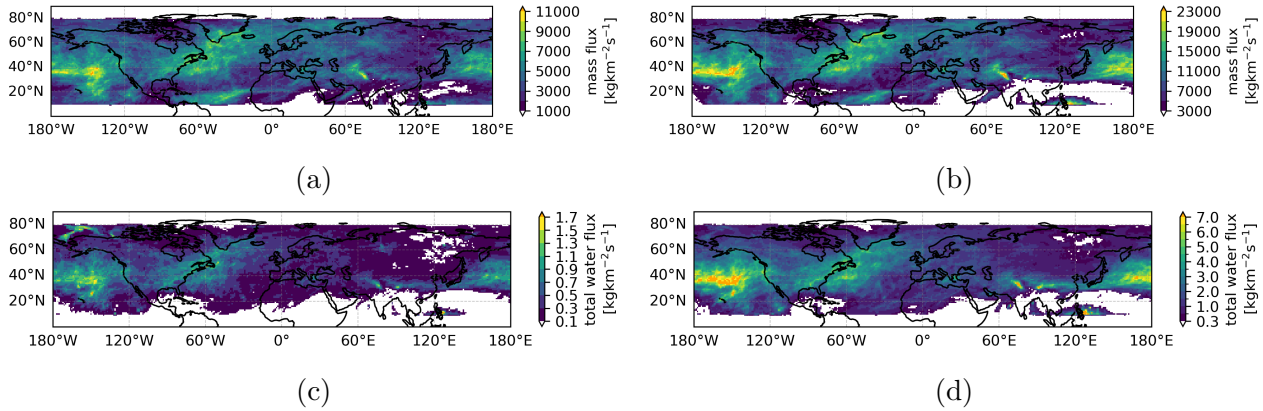

Figure A.2: Mass flux (a, b) and total water flux (c, d) into the UTLS during DJF 2017. Panels (a, d) are the same as in Fig. 3.16 but for the year 2017, i.e. the lower boundary of the UTLS layer is located at 50 hPa below the dynamical tropopause. Panels (c,d) show results from the sensitivity test, where the lower boundary of the UTLS layer is located 100 hPa below the dynamical tropopause.

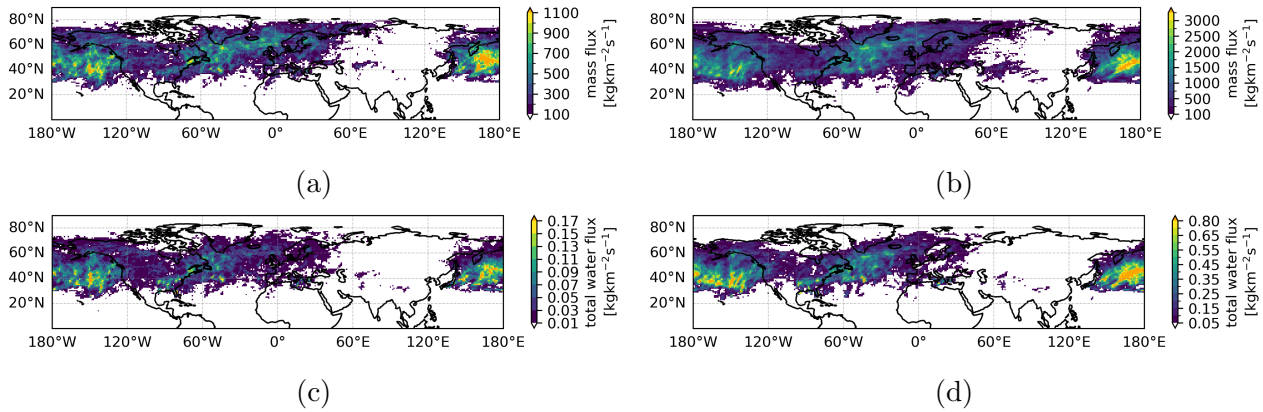

Figure A.3: WCB-related mass flux (a, b) and total water flux (c, d) into the UTLS during DJF 2017. Left panels (a, d) are the same as in Fig. 3.17 but for the year 2017, i.e. the lower boundary of the UTLS layer is located at 50 hPa below the dynamical tropopause. Panels (c,d) show results from the sensitivity test, where the lower boundary of the UTLS layer is located 100 hPa below the dynamical tropopause.

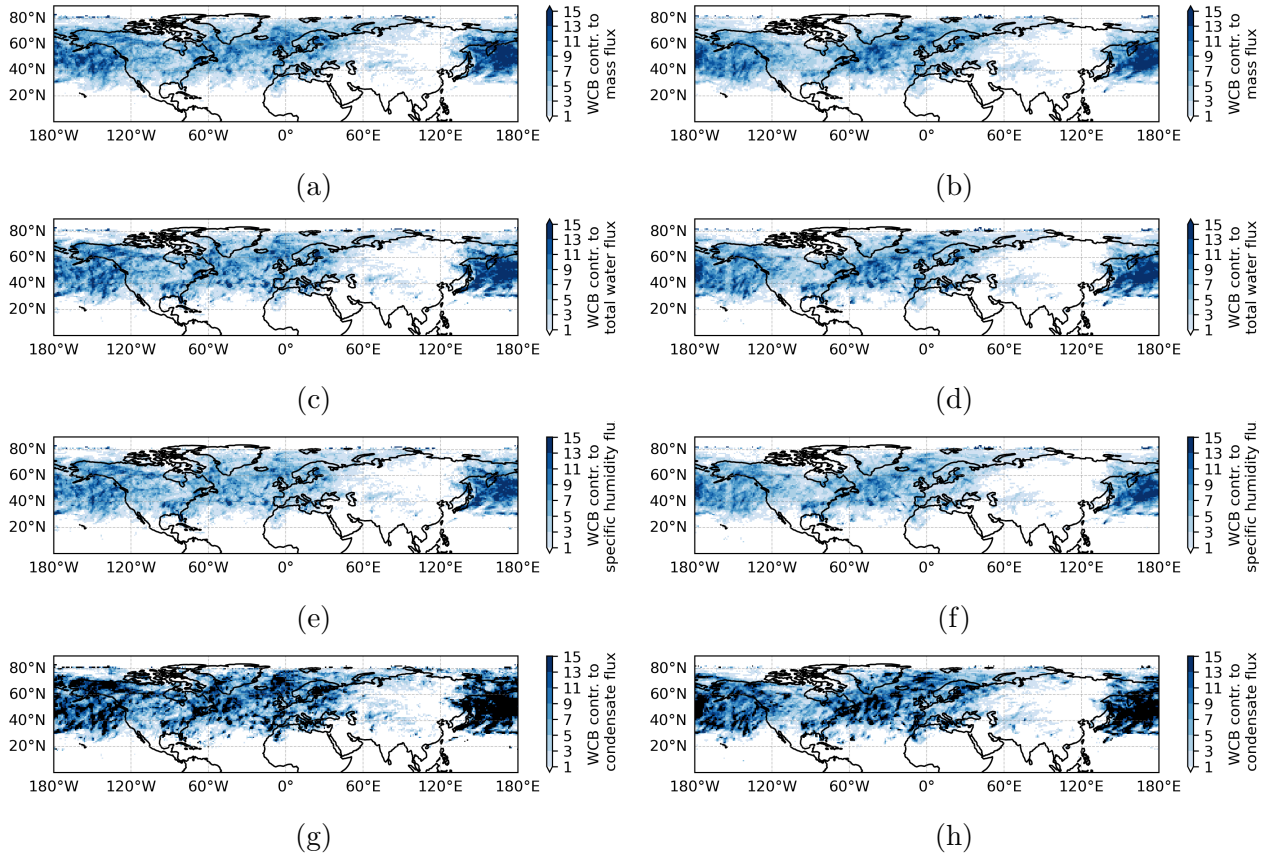

Figure A.4: Relative contribution of WCB trajectories to total fluxes into the UTLS during DJF for 2017 for the two investigated UTLS definitions. Left panels (a,c,e,d) are the same as in Fig 3.18 but for the year 2017, i.e. with the UTLS lower boundary defined as 50 hPa below the dynamic tropopause. Right panels (b,d,f,h) show results from the sensitivity test, in which the lower boundary is located 100 hPa below the dynamic tropopause. Panels (a,b) show the percentage of WCB mass flux relative to the total mass flux; (c,d) the percentage of WCB water flux relative to the total water flux; (e,f) the relative contribution of WCB water vapor flux to the total water vapor flux; and (g,h) the contribution of WCB condensate flux to the total condensate flux.

A.1.2 Evolution of WCB outflow properties after end of ascent in pressure level

In contrast to the analysis in tropopause-relative analysis, enhanced specific humidity conditions are found in the outflow for up to 12 h in pressure coordinates. This is mainly a consequence of the vertically displaced tropopause and the transport of humid air to lower pressure levels in WCB outflow. At t = 0 h, WCB outflow trajectories exhibit larger specific humidity and condensate content than the climatological background. The enhanced humidity decreases steadily over the next 12 h, likely as a result of mixing with drier environmental air or vapor deposition from remaining condensate. The background remains much drier during the first few hours, since at the corresponding pressure levels the air masses are already in the stratosphere. The background specific humidity increases from about 4 h onward, indicating the downward motion into the troposphere. After about 24 h, the median specific humidity of WCB parcels is slightly increasing, likely reflecting the more humid conditions of the mid-troposphere and mixing with this more humid environment.

Enhanced condensate is maintained for about 9 h, but the condensed mass mixing ratio decreases rapidly within the first 24 h along WCB trajectories and falls below background values after 9 h. In the background, condensate increases slightly during the first 12 h, consistent with parcels moving away from the stratosphere. Thereafter, condensate in the background shows little variation over time, likely as a consequence of the value being dominated by the fraction of cloudy versus non-cloudy background grid points at the respective pressure. “The rapid decline in condensate mixing ratio in WCB outflow is likely due to sedimentation of large ice crystals, while the increasing temperature from parcel descent may further accelerate sublimation.

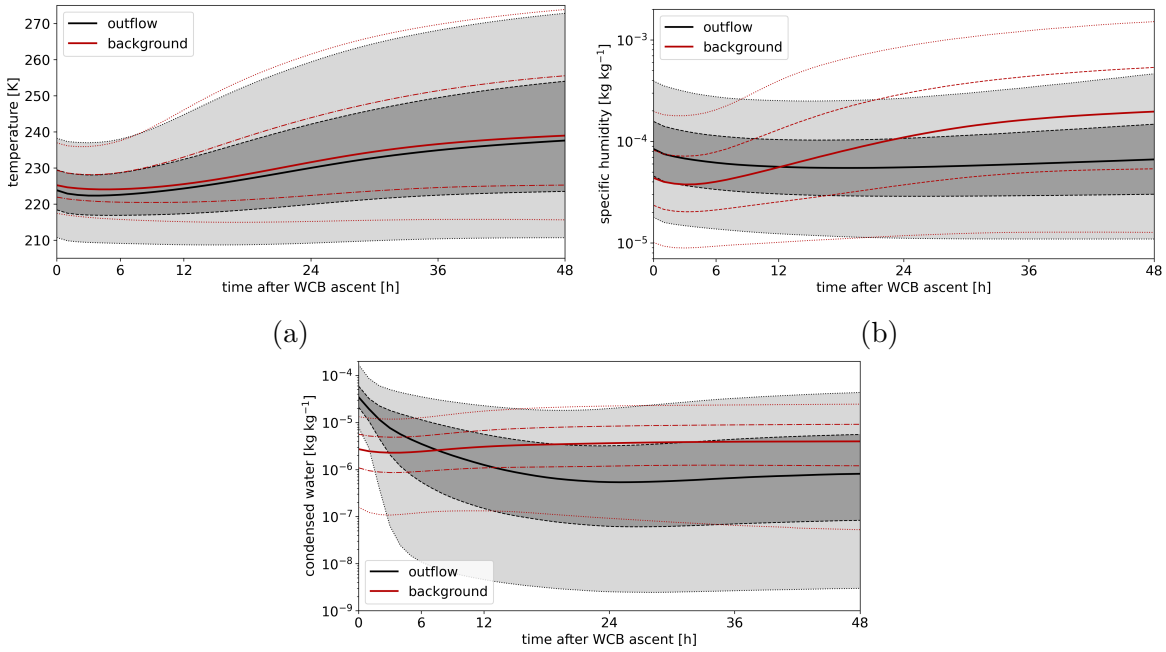

Figure A.5: Same as Fig. 3.14 but in pressure coordinates.

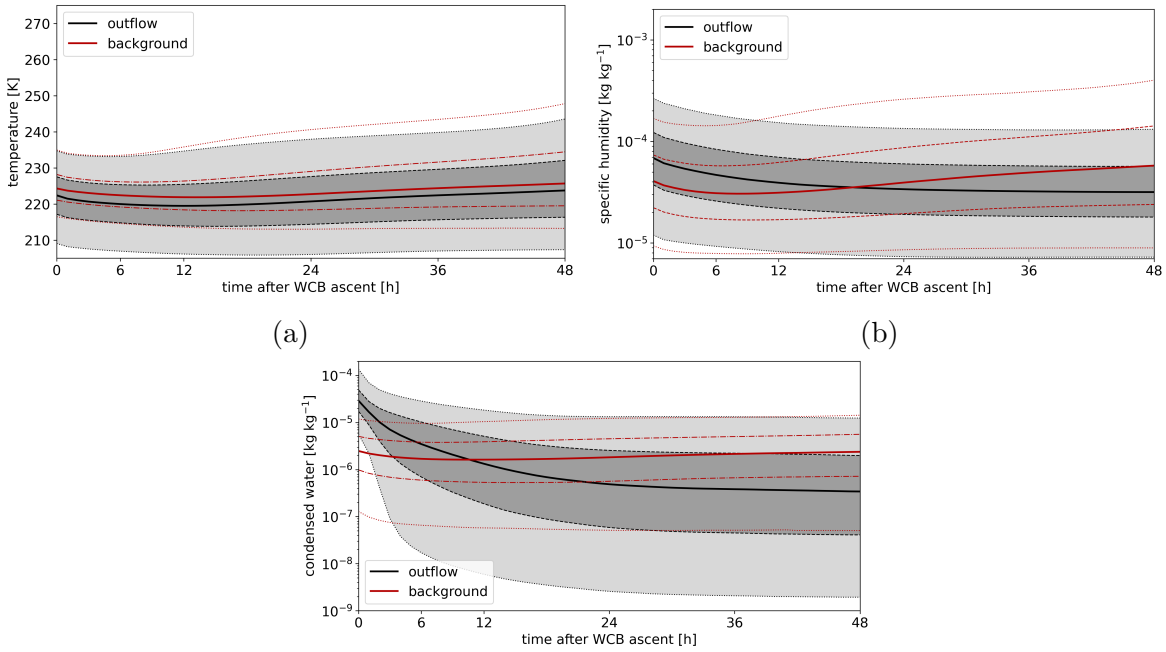

Figure A.6: Same as Fig. A.5, but only for trajectories staying within 4 km of the local tropopause over the considered 48 h period.

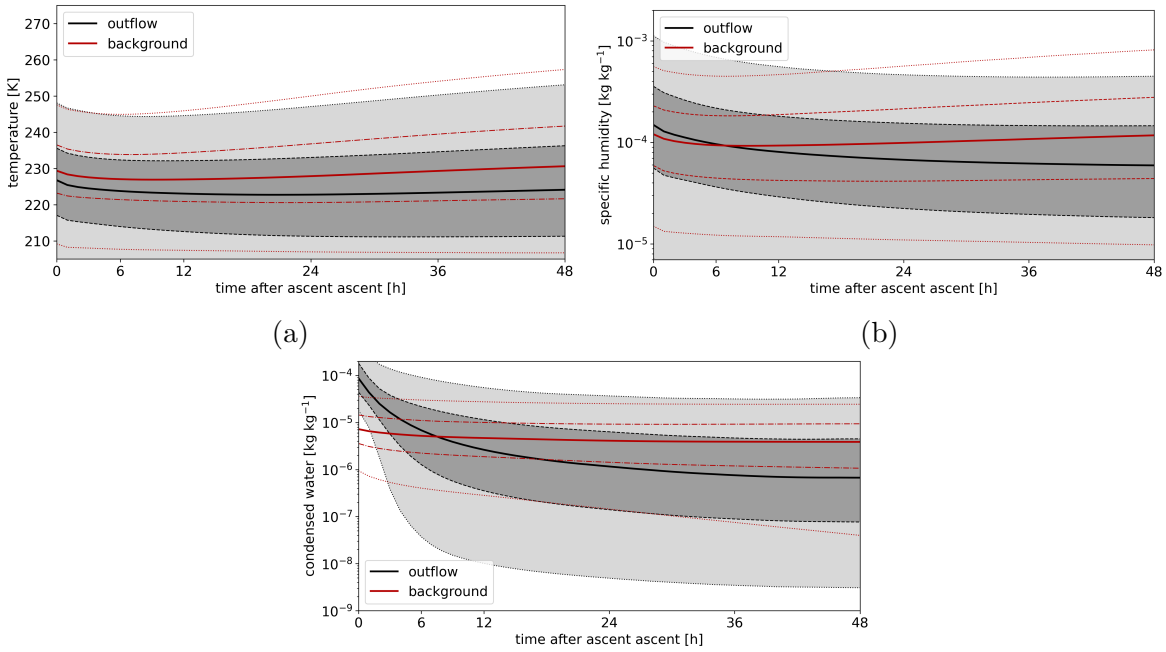

Figure A.7: Same as Fig. A.5 but for JJA.

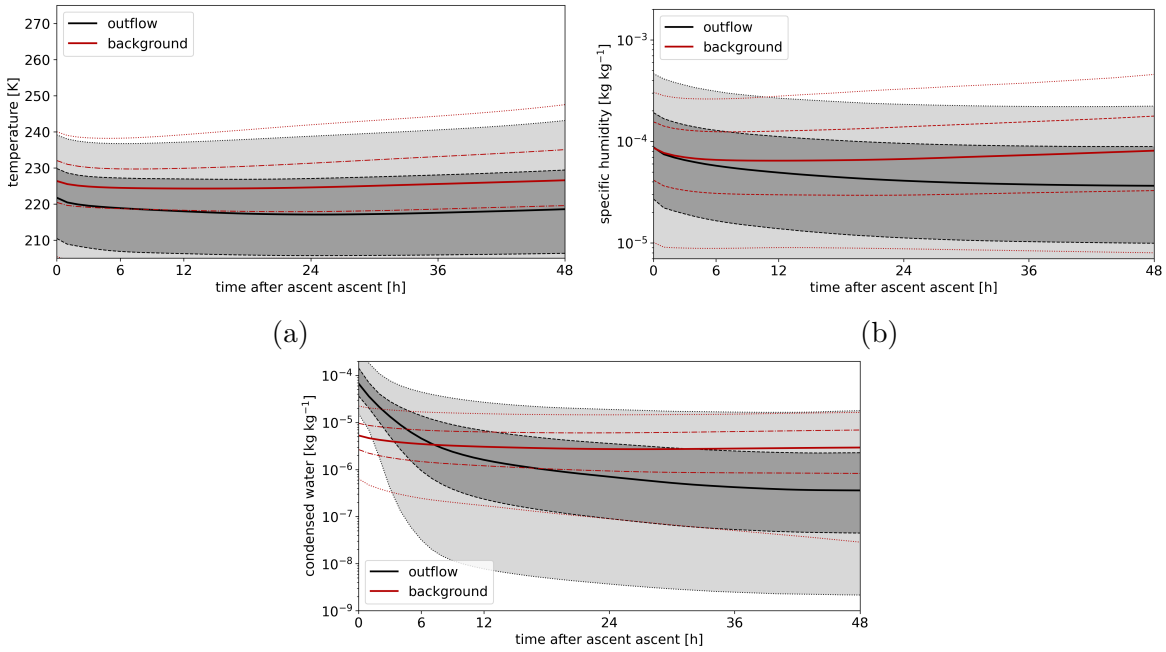

Figure A.8: Same as Fig. A.6, but for JJA.

A.1.3 Comparison of ERA5 outflow RHi with IAGOS measurements

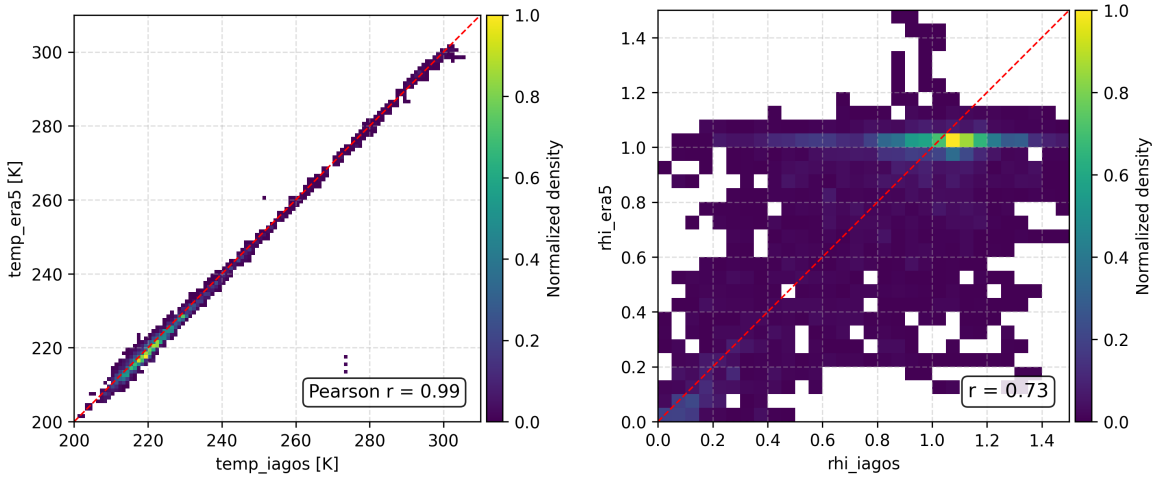

(a) (b)

Figure A.9: Correlation between ERA5 and IAGOS measurements of (a) temperature and (b) relative humidity with respect to ice (RHi) at warm conveyor belt (WCB) outflow points. Shading indicates the normalized two-dimensional density of matched data points. The red dashed line represents the 1:1 relationship. The Pearson correlation coefficient (r) is shown in each panel. Only ERA5 WCB outflow points for which corresponding IAGOS observations are available are included.

A.2 Additional plots for Chapter 4

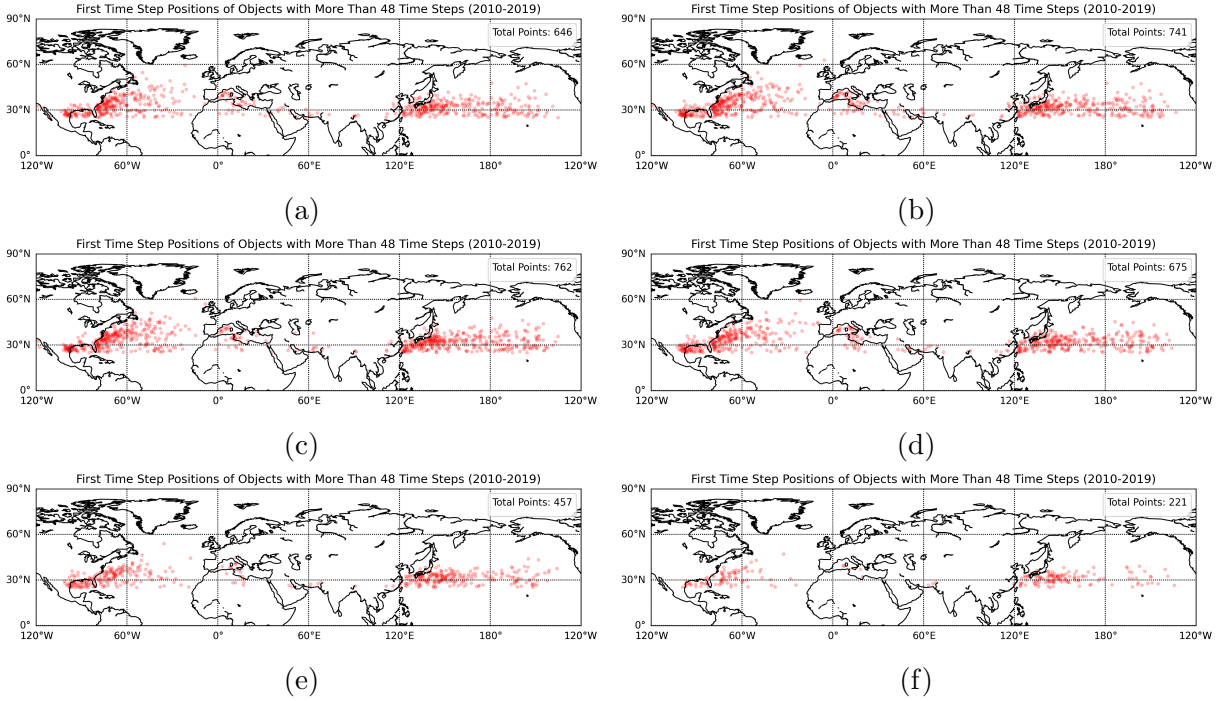

Figure A.10: Sensitivity of inflow track identification to the choice of overlap threshold. Panels (a)-(f) show the first time step positions of inflow objects with lifetimes exceeding 48 hours over the period 2010-2019 for overlap ratios ranging from 0.1 to 0.6.An overlap threshold of 0.3 yields the largest number of spatially coherent inflow tracks, while both lower and higher thresholds result in fewer retained objects.

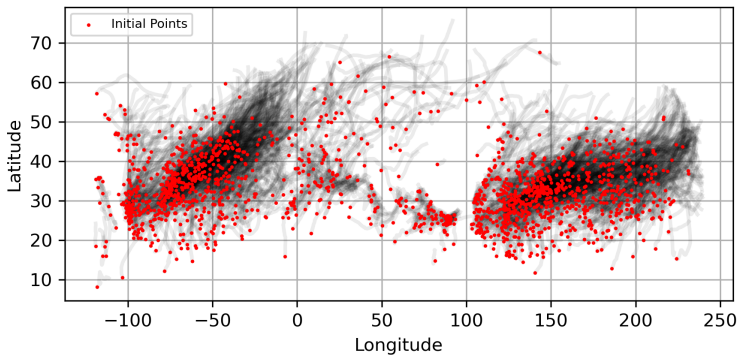

Figure A.11: Example of raw inflow tracks after application of smoothing method described in Section. 4.2.2 but without lifetime and geometric filtering for the period 2010-2013. Gray lines represent individual inflow tracks and red dots mark their initial positions. This reduced period is shown for illustrative purposes, as plotting the full 2010-2019 dataset including 1012151 tracks would result in severe overplotting and obscure individual track structures.

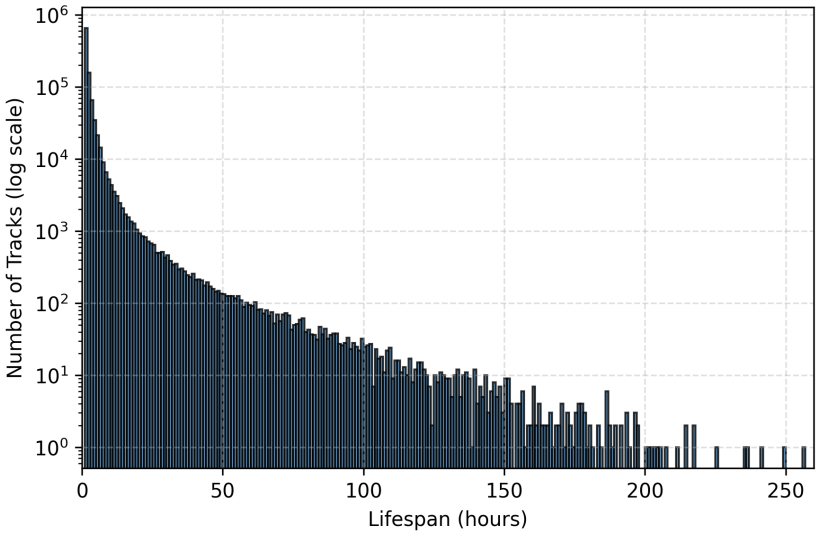

Figure A.12: Histogram of inflow track lifespans for the full, unfiltered dataset over the period 2010-2019. The number of tracks is shown on a logarithmic scale to highlight the strong dominance of short-lived inflow tracks and the long tail toward longer lifespans.

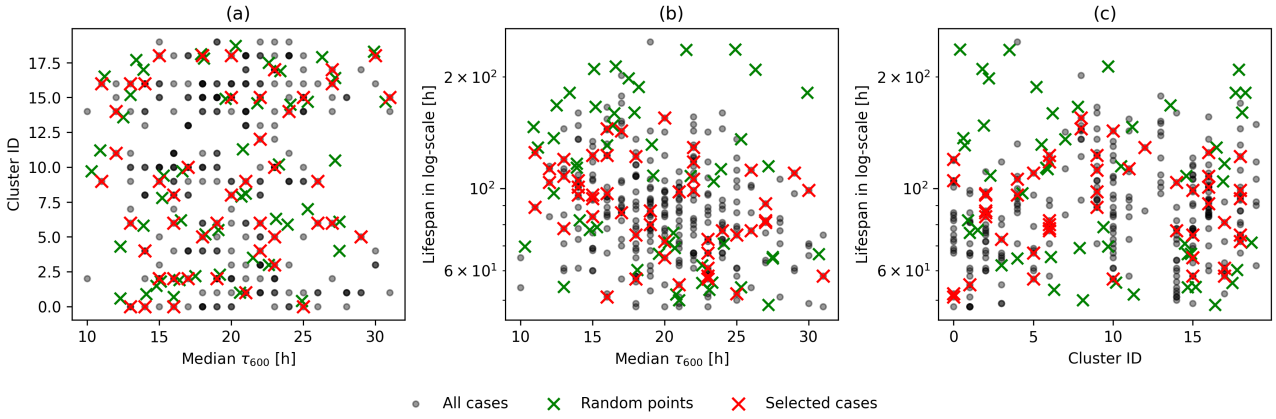

Figure A.13: Two-dimensional projections of the sampling space used for WCB case selection, corresponding to the three-dimensional metric shown in Fig. 4.11. Panels show (a) median τ_{600} versus cluster ID, (b) median τ_{600} versus lifespan, and (c) cluster ID versus lifespan, with lifespan displayed on a logarithmic scale. Gray dots indicate all WCB inflow tracks, green crosses denote randomly sampled points in the metric space, and red crosses mark the final selected cases.

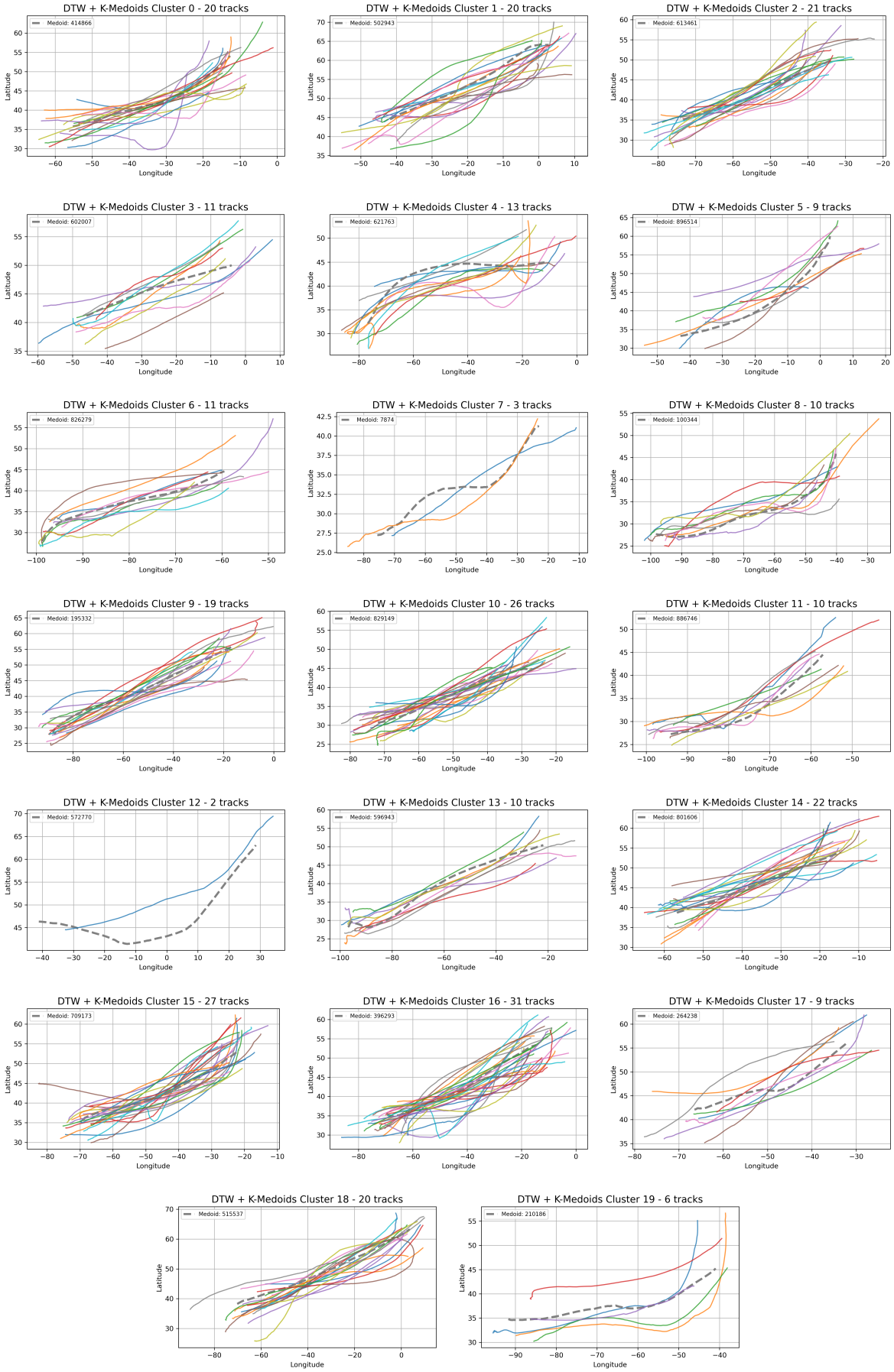

Figure A.14: Full set of 20 clusters of inflow tracks used in this study. Each subpanel shows the spatial distribution of inflow tracks belonging to one cluster, as identified by the clustering procedure described in Section. 4.2.3

A.3 Additional plots for Chapter 5

case1

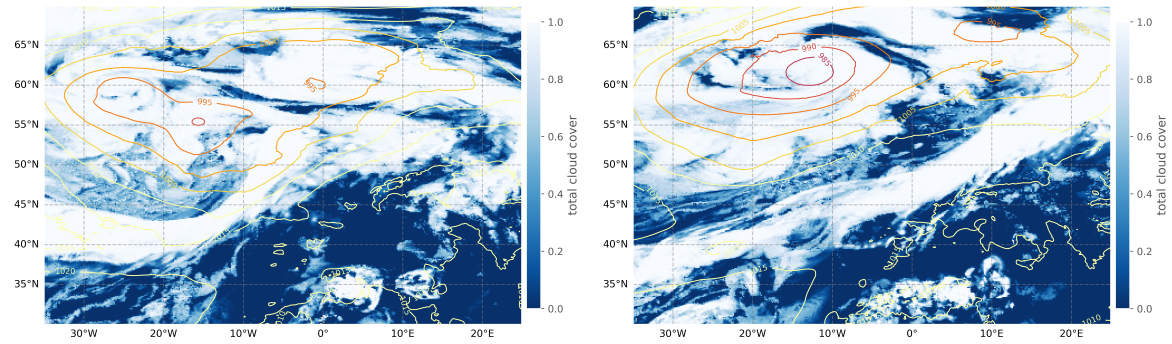

(a) (b)

Figure A.15: Example of the ICON WCBs selection based on the WCB positions at two different times. The MSLP and total cloud cover at (b) 26 August 2025 00 UTC and (b) 28 August 2025 00 UTC.

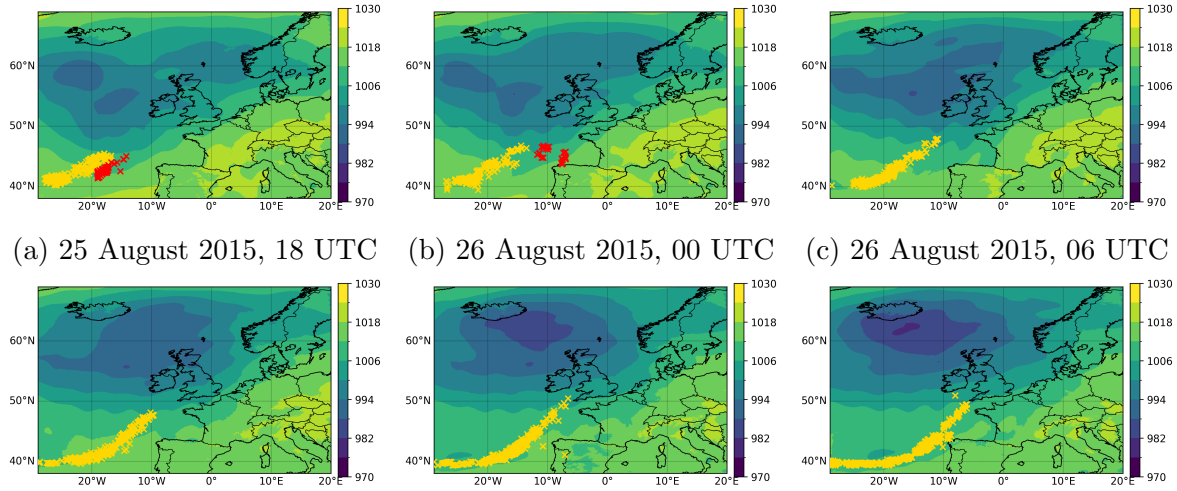

(a) 25 August 2015, 18 UTC (b) 26 August 2015, 00 UTC (c) 26 August 2015, 06 UTC

(d) 26 August 2015, 12 UTC (e) 26 August 2015, 18 UTC (f) 27 August 2015, 00 UTC

Figure A.16: Evolution of ICON inflow points overlaid on mean sea-level pressure (MSLP) in Domain 2 (3.3 km resolution) from 25 August 2015 18 UTC to 27 August 2015 00 UTC at 6-hourly intervals. Yellow (red) markers denote ICON (ERA5) inflow points associated with $\tau_{600} \geq 30$ h.

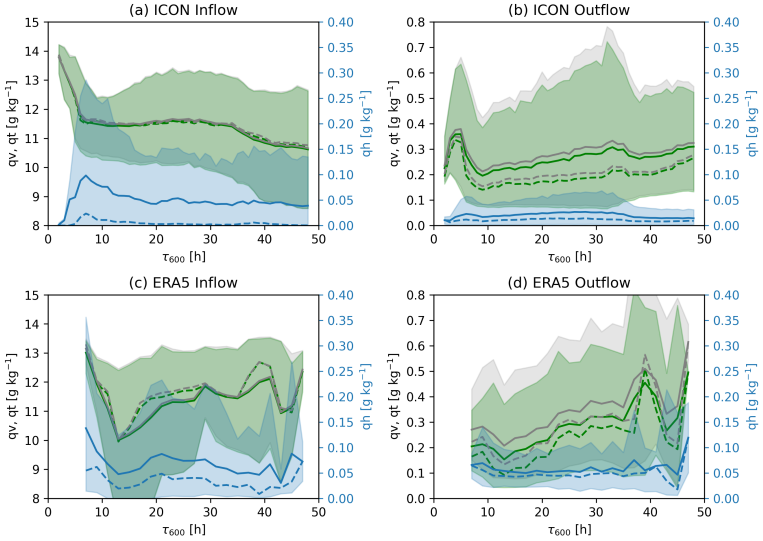

Figure A.17: Same as Fig. 5.10a–b, but without applying the geometric filter. Convective WCBs, particularly those with $\tau_{600} < 3$ h, exhibit substantially larger outflow condensate differences compared to the case where the geometric filter is applied.

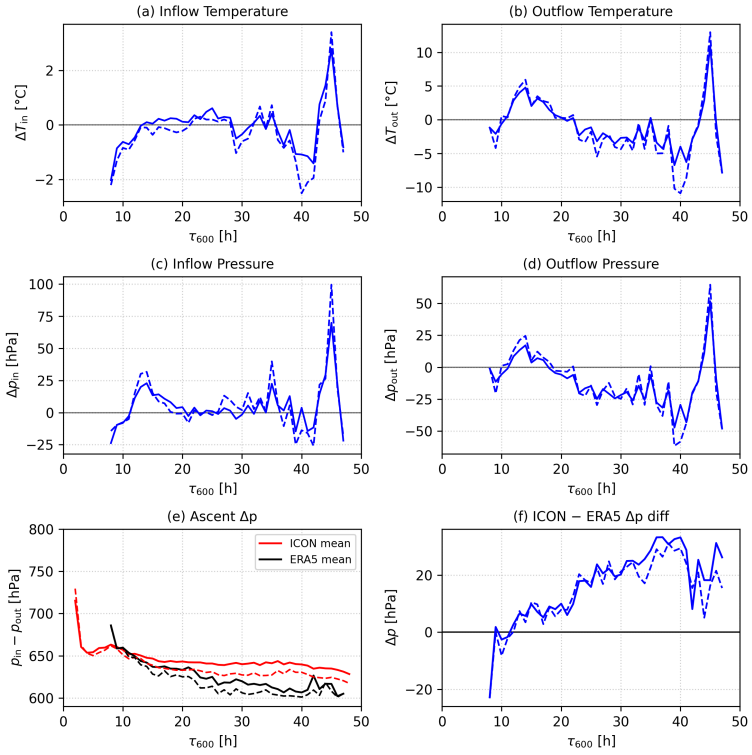

Figure A.18: (a-d) Differences in temperature and pressure at WCB inflow and outflow points between ICON and ERA5 (ICON minus ERA5) as a function of τ_{600}. (e) Ascent pressure difference between inflow and outflow points for ICON (red) and ERA5 (black). (f) ICON–ERA5 difference in ascent pressure (ICON minus ERA5). Solid (dashed) lines show mean (median) values.

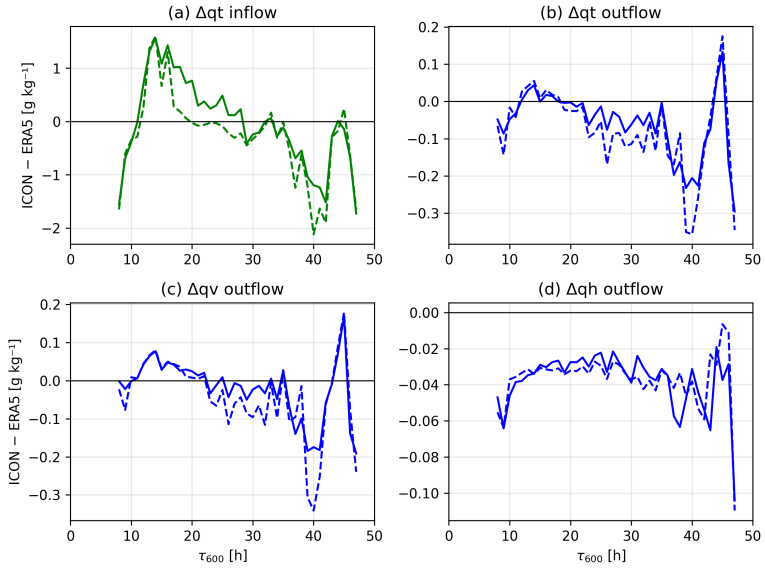

Figure A.19: Mean differences between ICON and ERA5 (ICON minus ERA5) in (a) inflow total water, (b) outflow total water, and (c-d) outflow water vapour and condensate as a function of τ_{600}.

case2

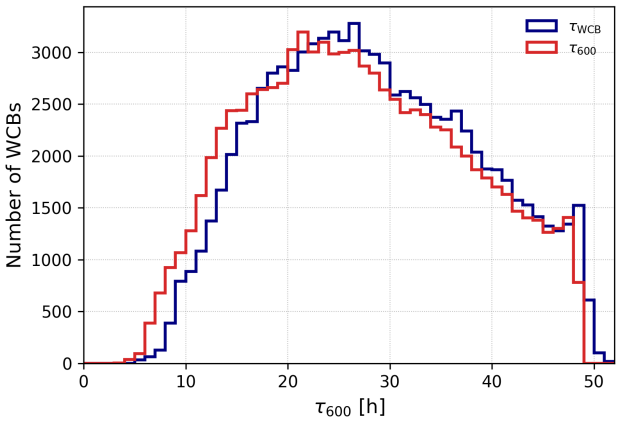

Figure A.20: Distribution of WCB trajectory durations for the fastest ascent phase (τ_{600}, red) and for the full ascent phase (τ_{WCB}, navy).

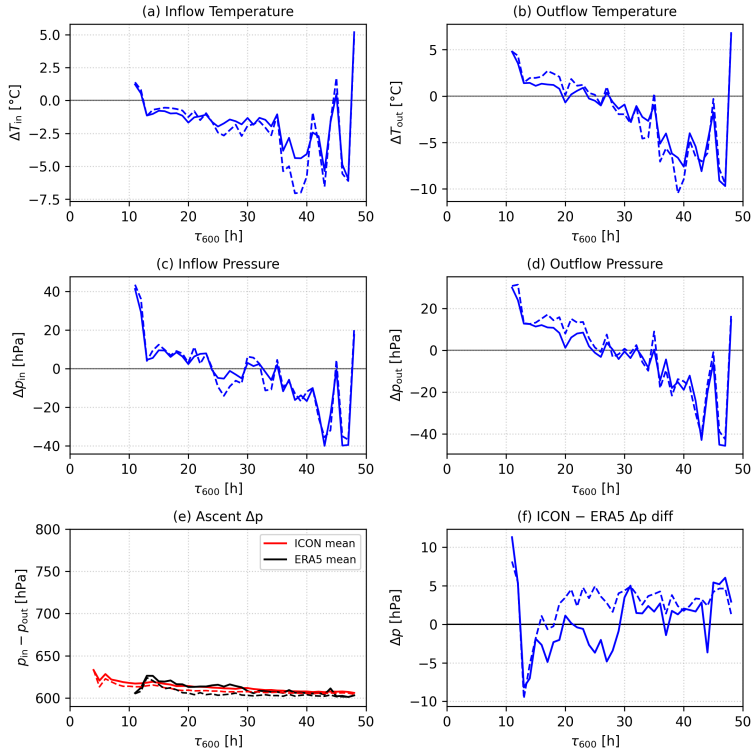

Figure A.21: (a–d) Differences in temperature and pressure at WCB inflow and outflow points between ICON and ERA5 (ICON - ERA5) as a function of τ_{600}. (e) Ascent pressure difference between inflow and outflow points for ICON (red) and ERA5 (black). (f) ICON-ERA5 difference in ascent pressure (ICON - ERA5). Solid (dashed) lines show mean (median) values.

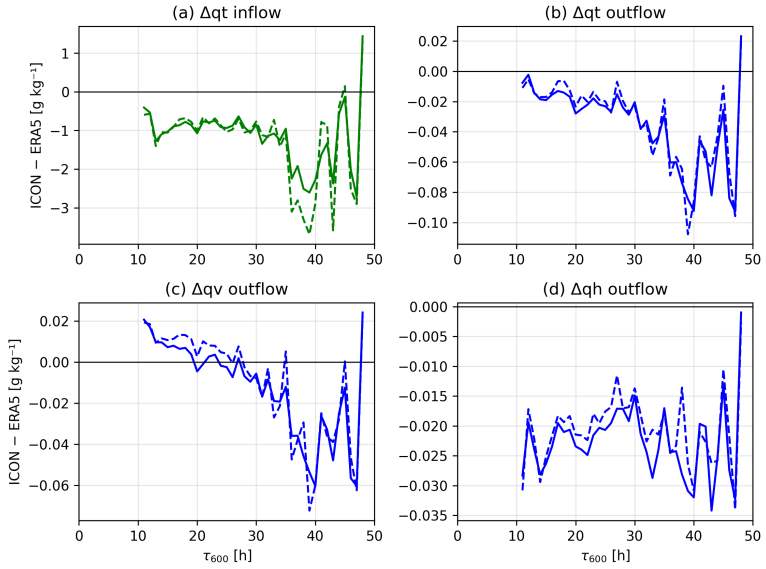

Figure A.22: Mean differences between ICON and ERA5 (ICON - ERA5) in (a) inflow total water, (b) outflow total water, and (c-d) outflow water vapour and condensate as a function of τ_{600}.

case3

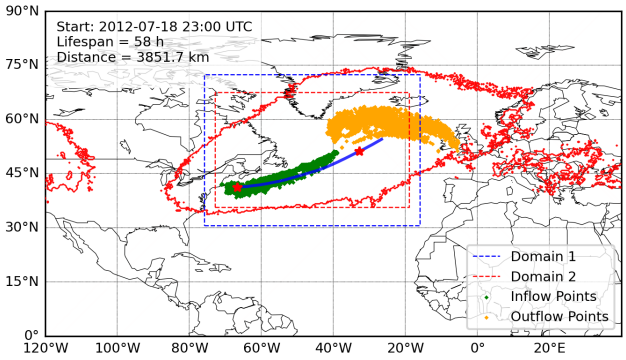

Figure A.23: WCB event on 18 July 2012 at 23 UTC, showing the inflow track (blue), inflow points (green), and outflow points (orange). The two stars mark the initial 48-hour time window of the inflow evolution. The nested ICON simulation domains are outlined by the blue dashed box (∼6.5 km) and the red dashed box (∼3.3 km).

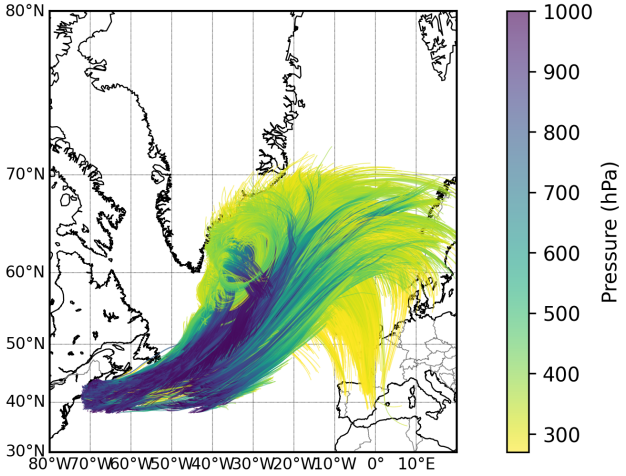

Figure A.24: Valid WCB trajectories retained after applying the selection criteria described in Section 5.3.1. ICON simulation initialized from 18 July 2012 at 18 UTC.

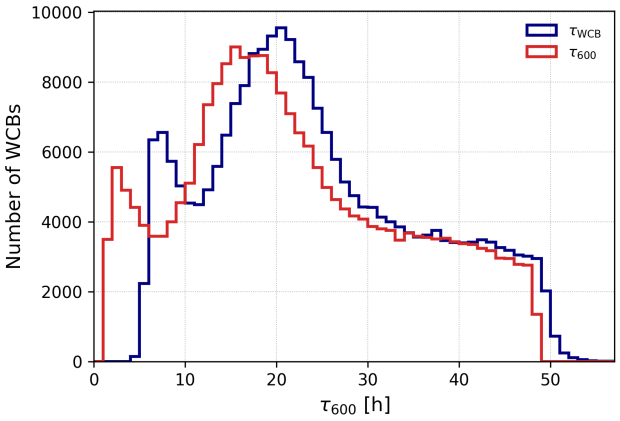

Figure A.25: Distribution of WCB trajectory durations for the fastest ascent phase (τ_{600}, red) and for the full ascent phase (τ_{WCB}, navy).

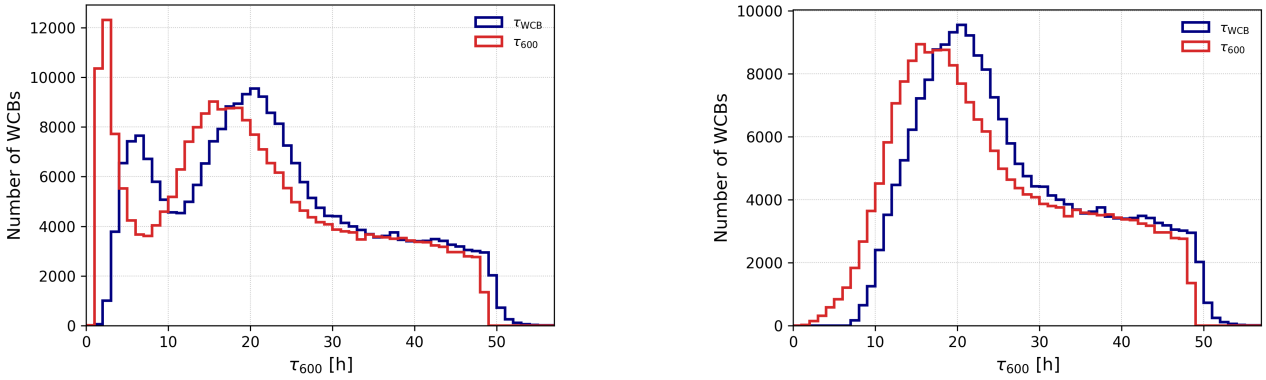

(a) (b)

Figure A.26: Illustration of how different geometric filter choices affect the number of fast ascending WCBs. Panel (a) shows results without applying any geometric filter. Panel (b) shows results when a stricter filter is applied, requiring at least 10° meridional and 20° zonal displacement during ascent.

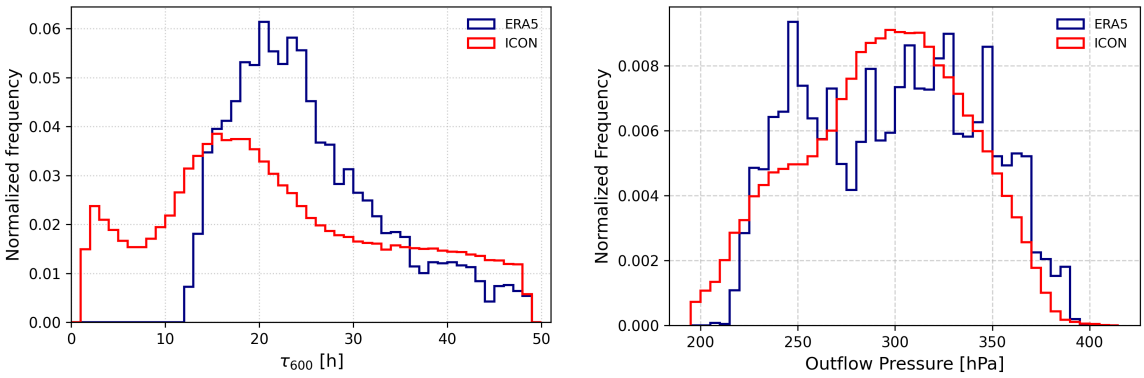

(a) (b)

Figure A.27: Normalized frequency distributions of WCB trajectories as a function of (a) ascent timescale (τ_{600}) and (b) outflow pressure level. ICON data are shown in red and ERA5 data in navy.

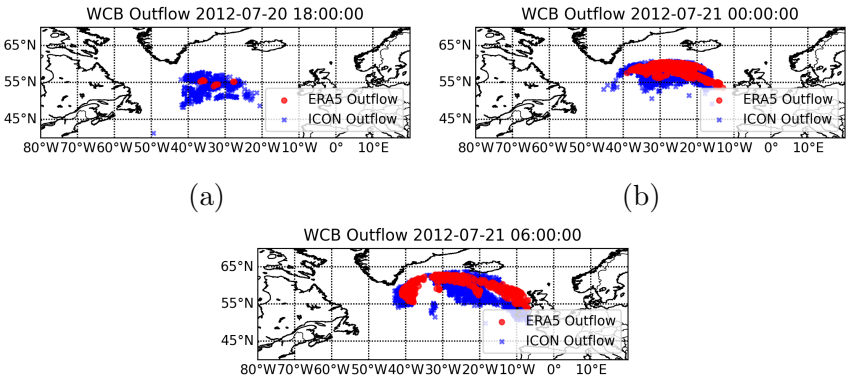

(a) (b)

(c)

Figure A.28: Comparison of WCB outflow locations in ERA5 and ICON at corresponding times during the event of 20-21 July 2012. Panels (a–c) show the temporal evolution of outflow points, with ERA5 outflow locations indicated in red and ICON outflow locations in blue.

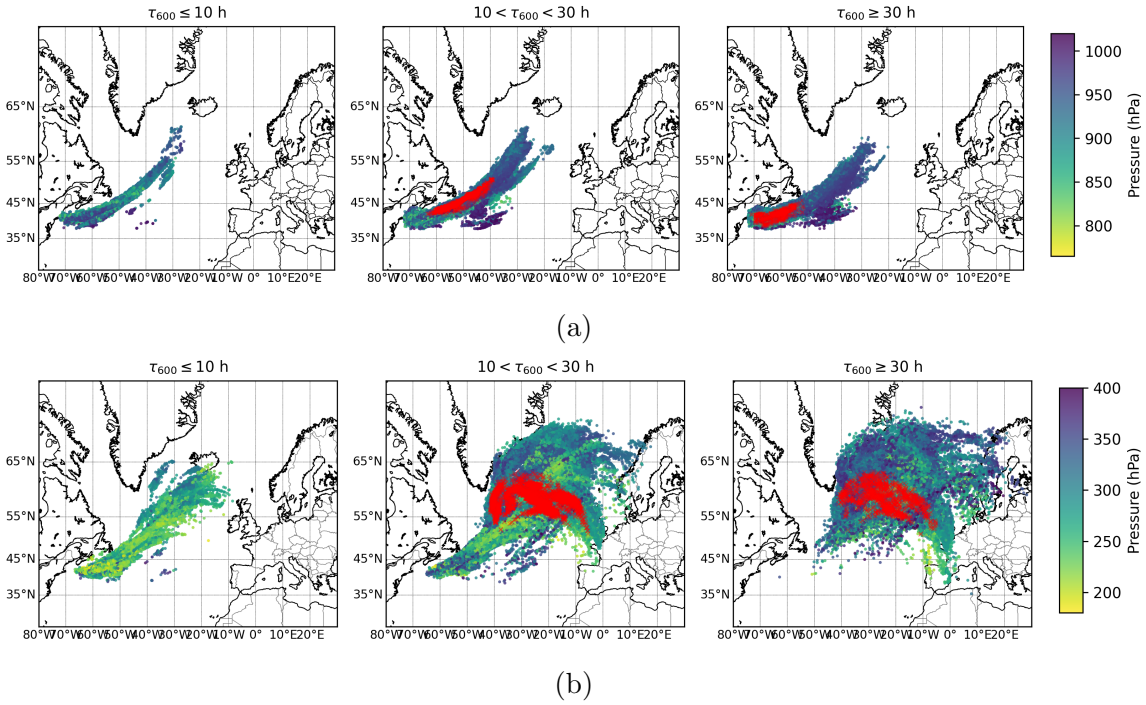

Figure A.29: Comparison of (a) inflow and (b) outflow points between ICON (colored by pressure) and ERA5 (red) for fast-ascending WCBs ($\tau_{600} \leq 10$, left panel), normal-ascending WCBs ($10 < \tau_{600} < 30$, middle panel), and slow-ascending WCBs ($\tau_{600} \geq 30$, right panel).

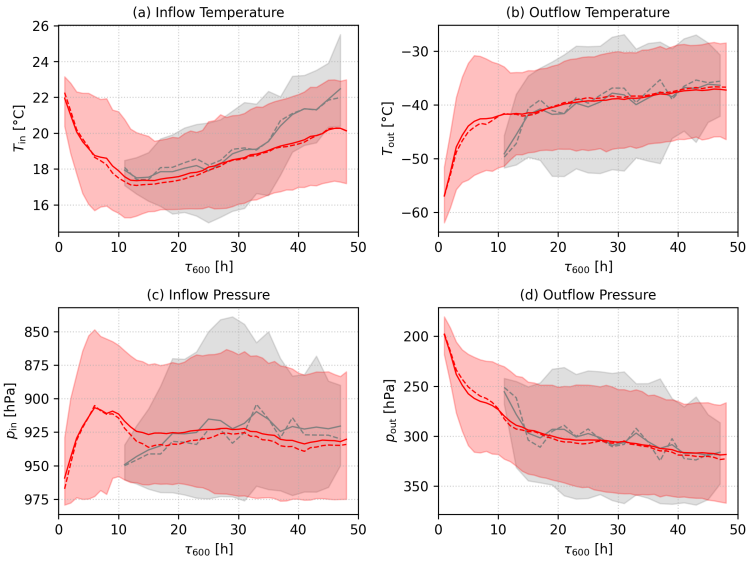

Figure A.30: Comparison of inflow and outflow (a–b) temperature and (c–d) pressure as a function of τ_{600} for ICON (red) and ERA5 (grey). Solid (dashed) lines show mean (median) values. Shading denotes the 10th–90th percentile range.

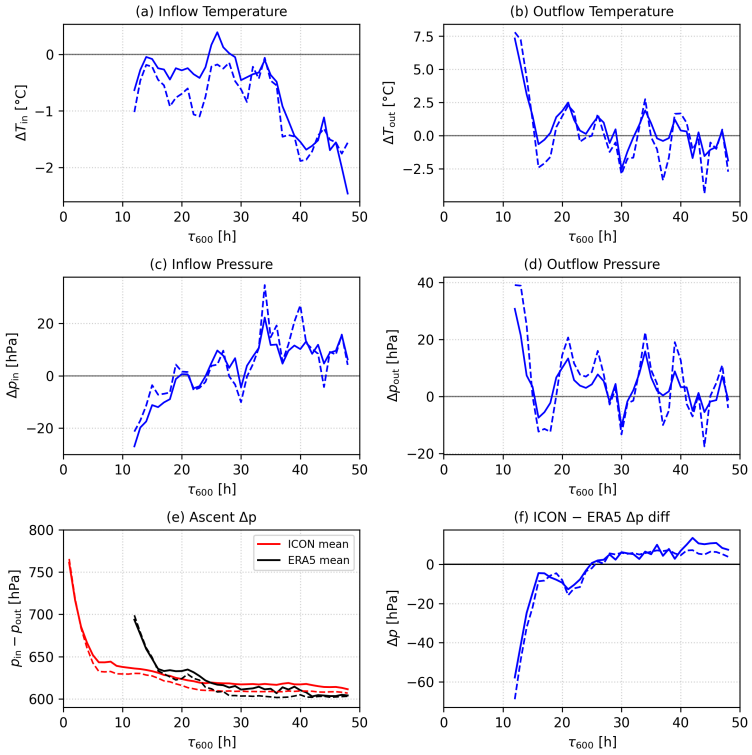

Figure A.31: (a-d) Differences in temperature and pressure at WCB inflow and outflow points between ICON and ERA5 (ICON minus ERA5) as a function of τ_{600}. (e) Ascent pressure difference between inflow and outflow points for ICON (red) and ERA5 (black). (f) Difference in ascent pressure (ICON minus ERA5). Solid (dashed) lines show mean (median) values.

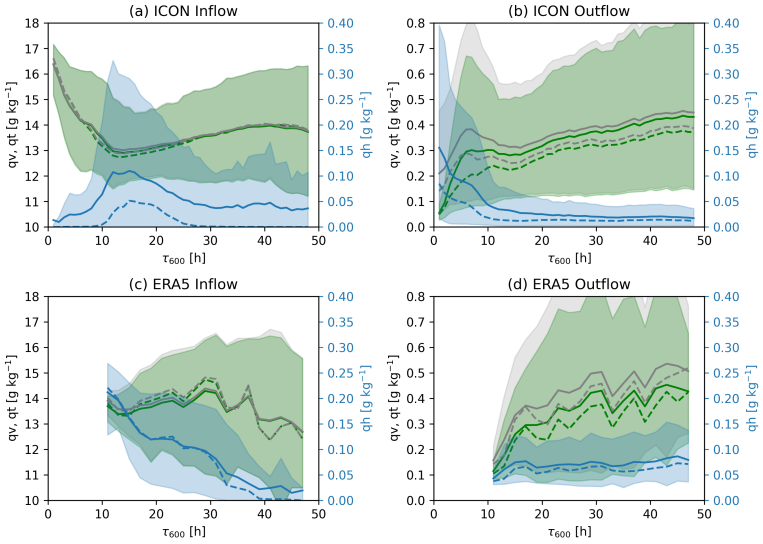

Figure A.32: Comparison of total water (q_t, grey), water vapour (q_v, green), and condensate (q_h, blue) as a function of τ_{600} for inflow and outflow. Panels (a–b) show ICON and panels (c–d) ERA5. Solid (dashed) lines show mean (median) values. Shading denotes the 10th–90th percentile range. A separate axis on the right-hand side is used for q_h.

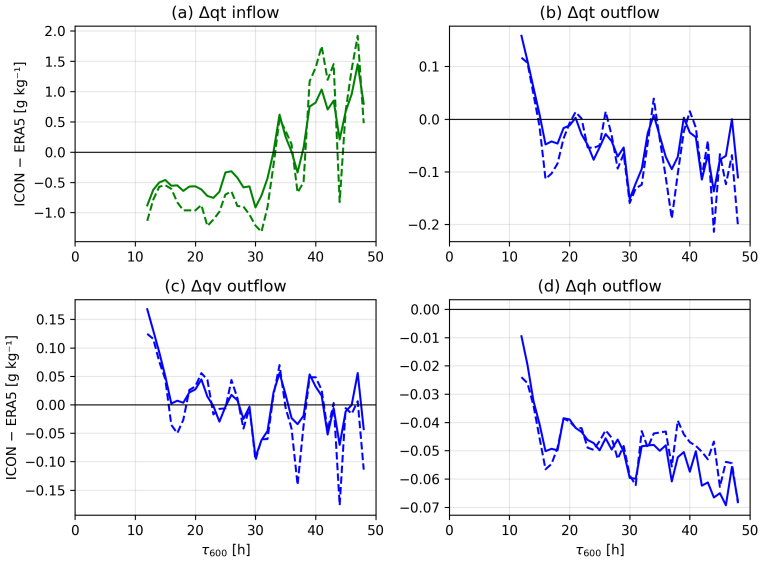

Figure A.33: Mean differences between ICON and ERA5 (ICON minus ERA5) in (a) inflow total water, (b) outflow total water, and (c-d) outflow water vapour and condensate as a function of τ_{600}.

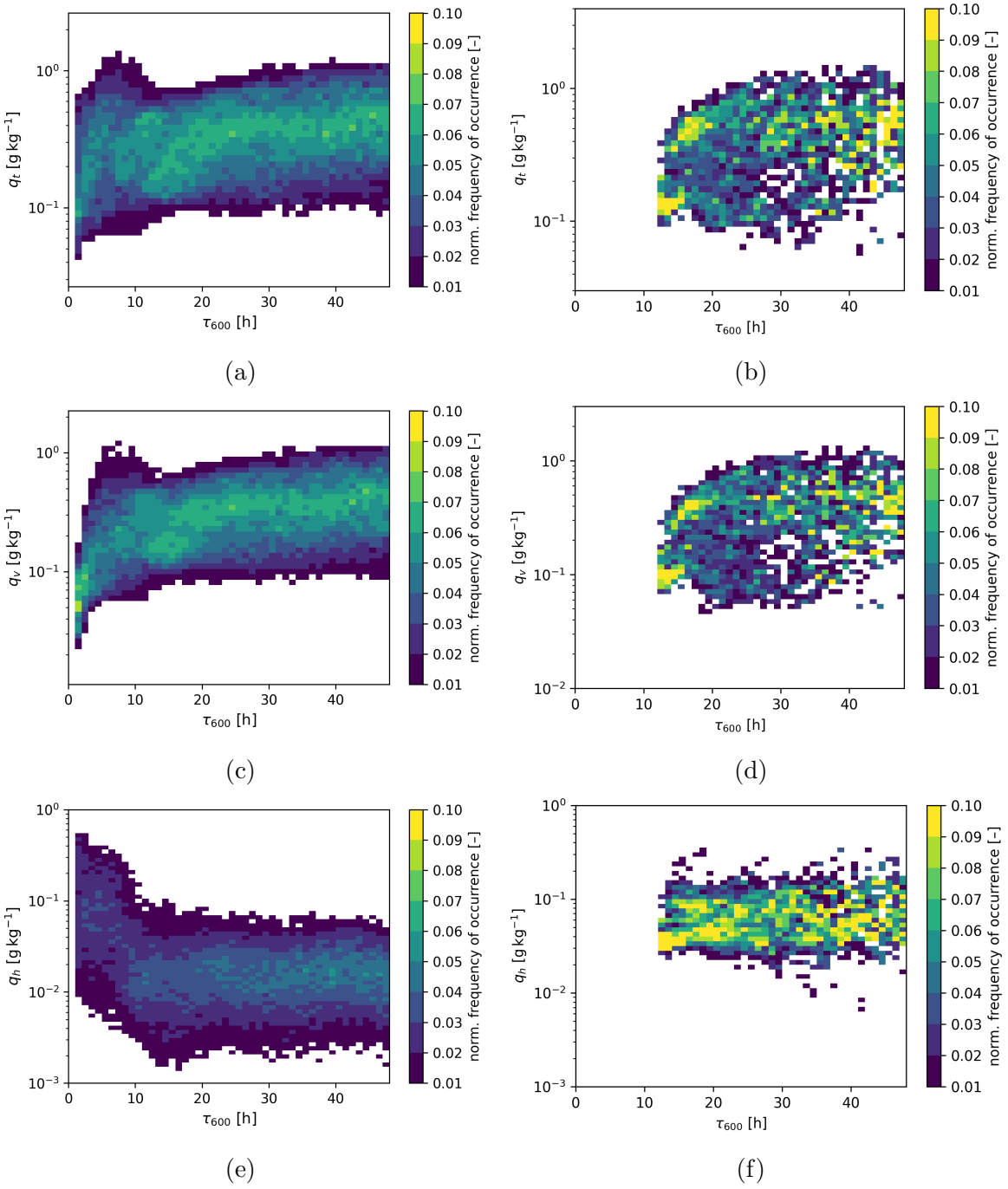

Figure A.34: Distributions of WCB outflow total water, specific humidity, and condensate as a function of τ_{600}. Panels (a), (c), and (e) show the ICON simulation, while panels (b), (d), and (f) show ERA5.

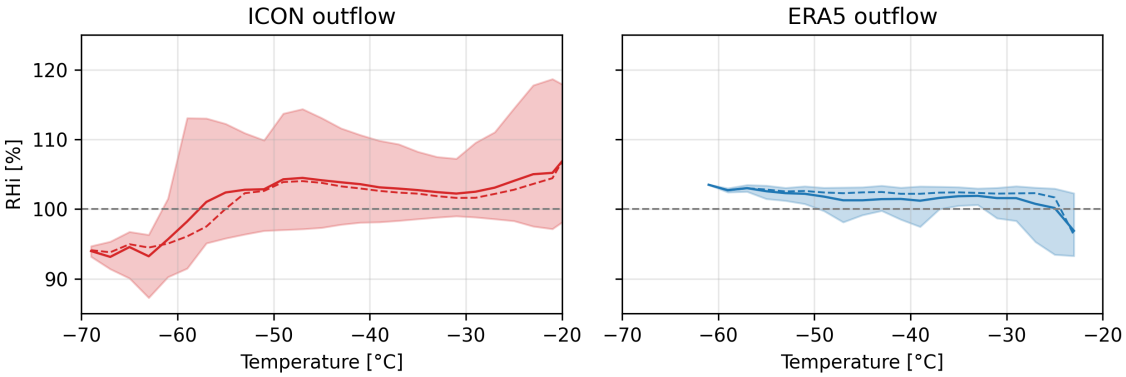

(a)

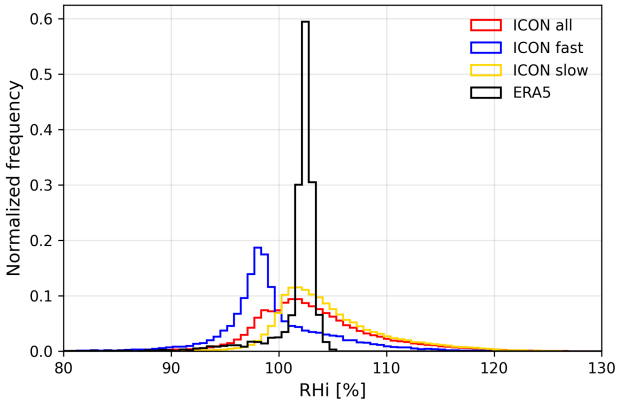

(b)

Figure A.35: (a) Distribution of relative humidity with respect to ice (RHi) as a function of temperature in the WCB outflow for ICON (left panel) and ERA5 (right panel). Shading denotes the 10th–90th percentile range. (b) Normalized histogram of RHi at the end of ascent for ERA5 (black) and ICON (red), with ICON fast-ascending (blue) and slow-ascending (orange) WCBs shown separately.

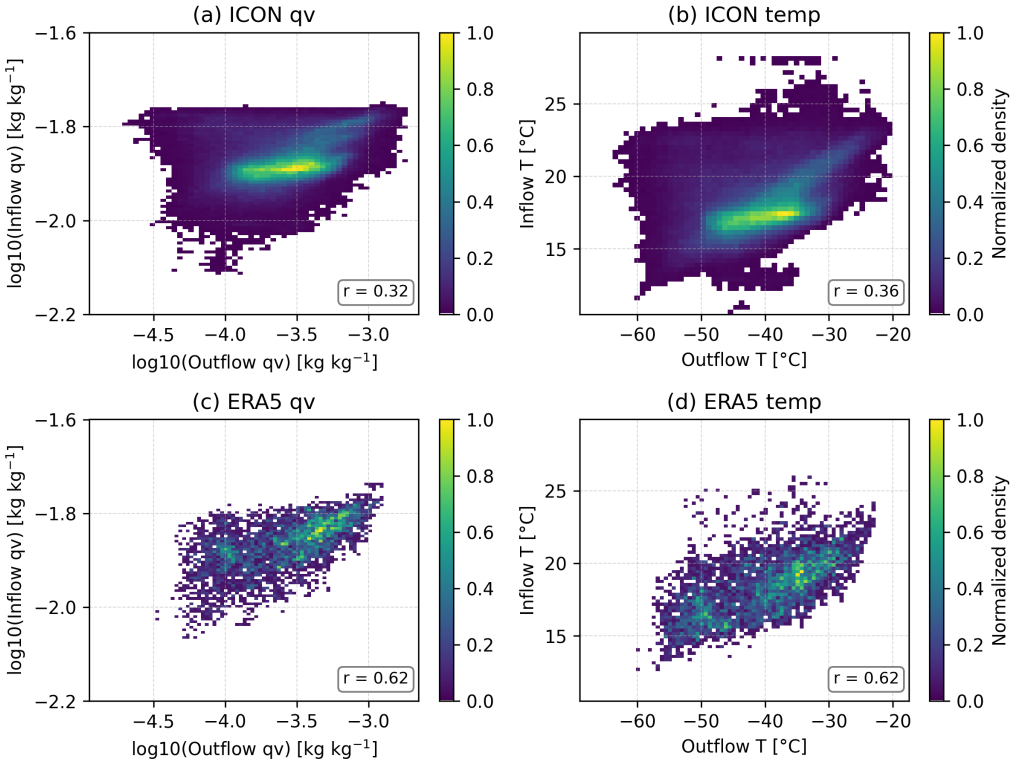

Figure A.36: Correlations between inflow and outflow conditions for (a–b) ICON and (c–d) ERA5. Panels (a, c) show specific humidity on a logarithmic scale, while panels (b, d) show temperature.

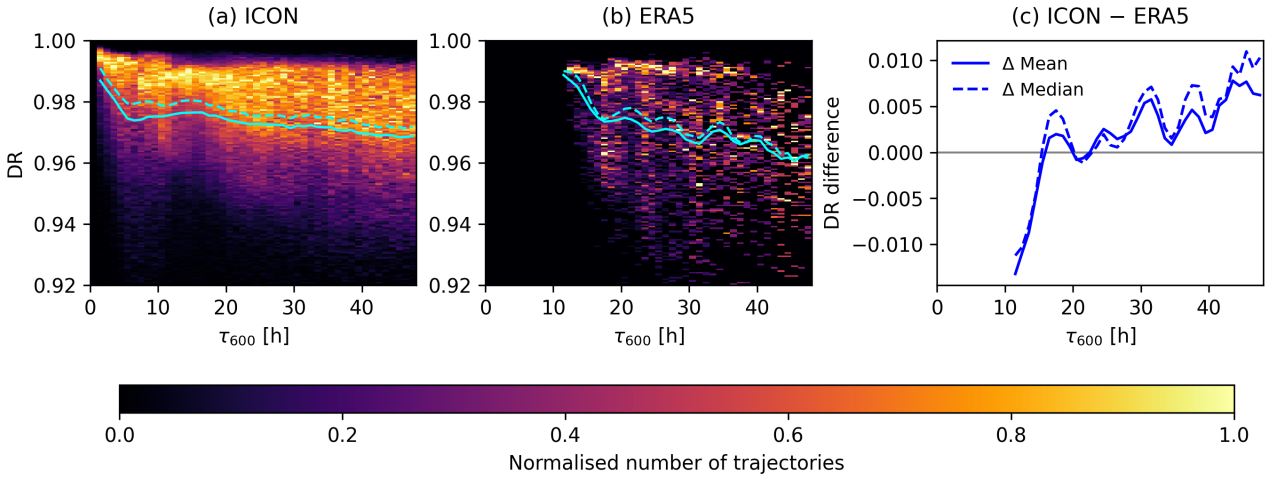

Figure A.37: DR as the function of τ_{600} for (a) ICON simulation, (b) ERA5 data and (c) the ICON–ERA5 difference. Colors indicate the normalized number of trajectories. Solid (dashed) lines show mean (median) values.

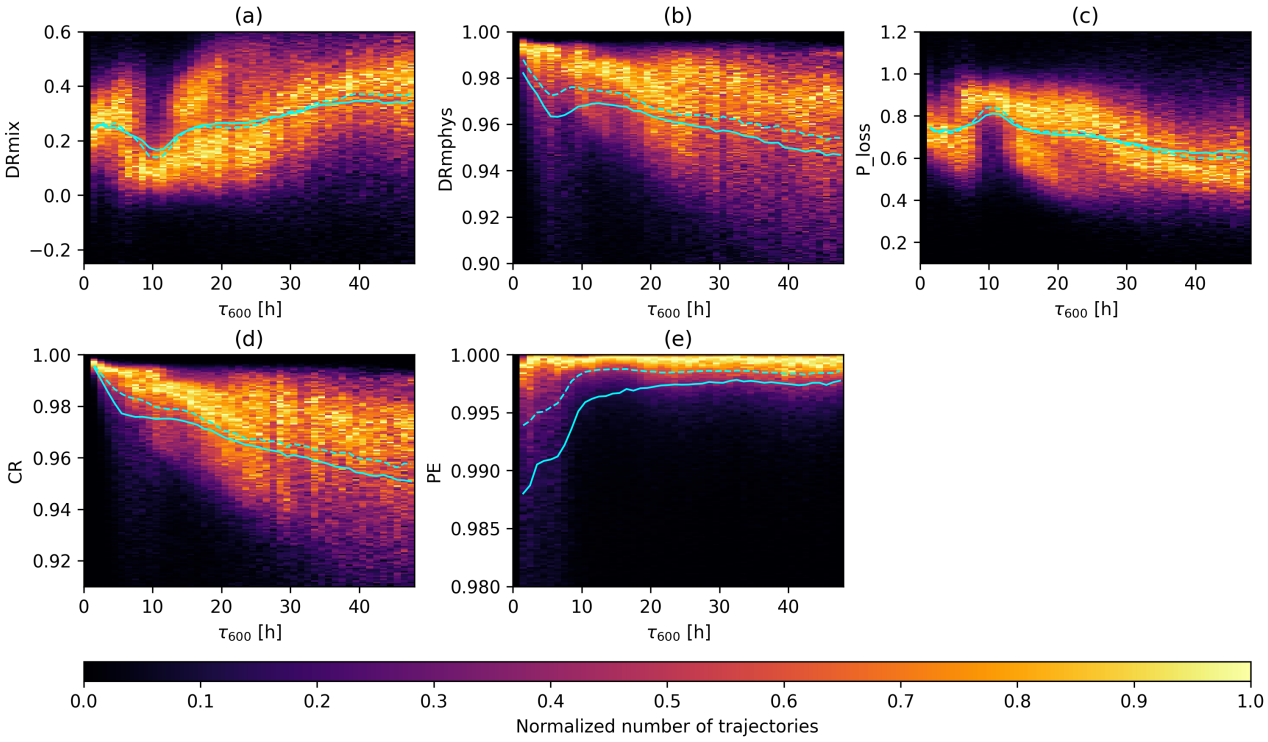

Figure A.38: Distributions of (a) DR_{mix}, (b) DR_{mphys}, (c) moisture loss due to precipitation, (d) CR, and (e) PE as the function of τ_{600} at the end of the ascent. Colors indicate the normalized number of trajectories. Solid (dashed) lines show mean (median) values.

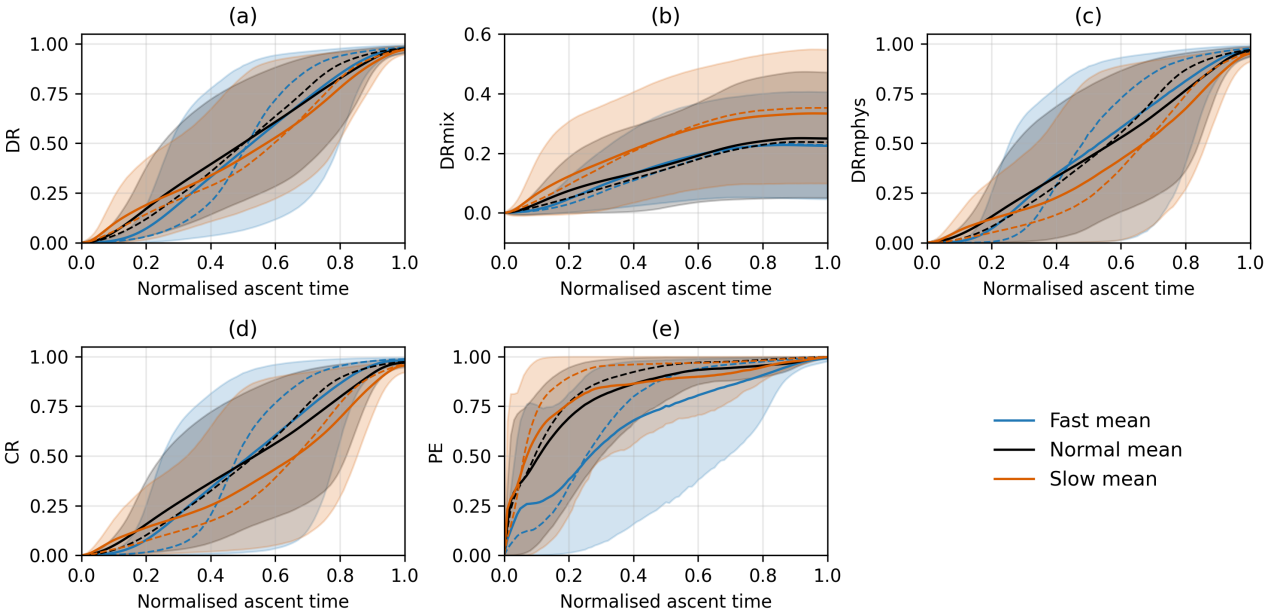

Figure A.39: Evolution of (a) DR, (b) DR_{mix}, (c) DR_{mphys}, (d) CR, and (e) PE as a function of normalized ascent time. Solid (dashed) lines show mean (median) values. Shading denotes the 10th–90th percentile range.

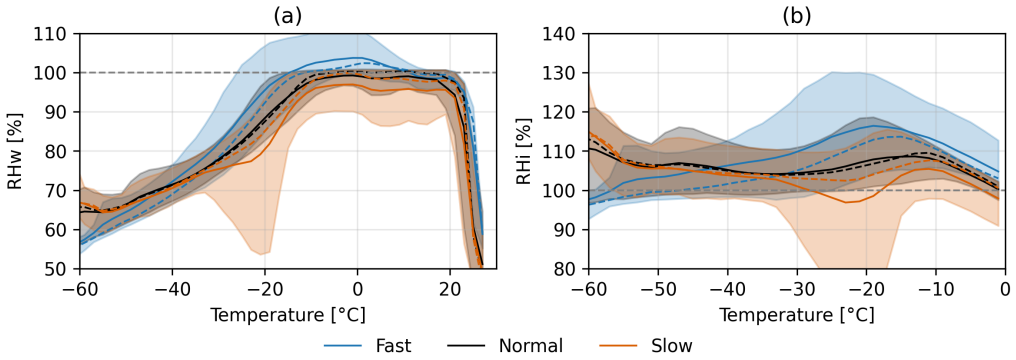

Figure A.40: RHw and RHi along the ascent but limited to temperatures lower than 0°. Shading includes 10% and 90% of the data.

A.4 Additional plots for Chapter 6

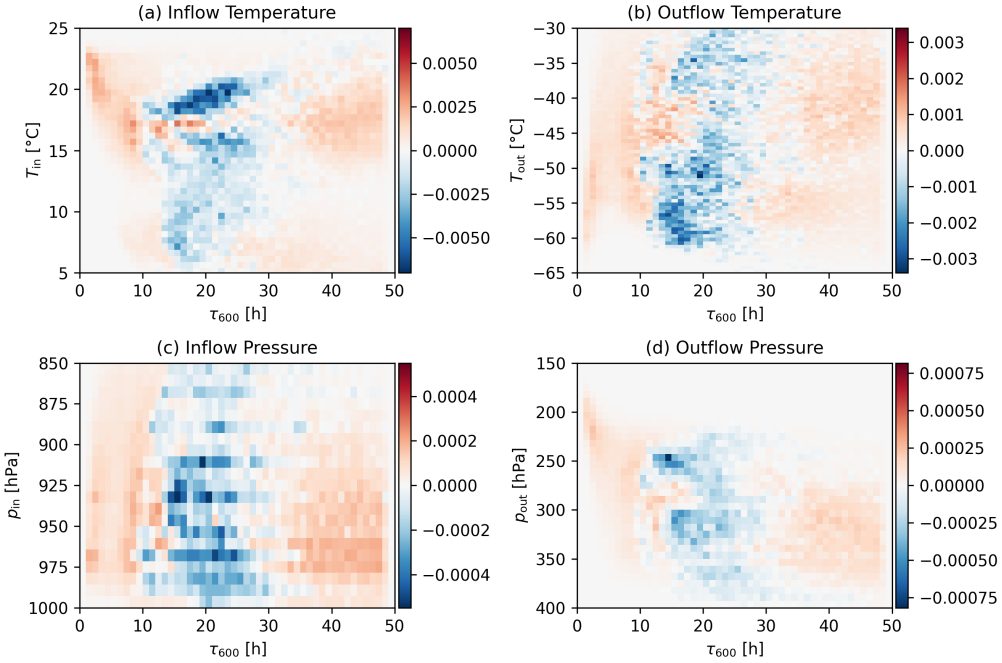

Figure A.41: Probability density differences between ICON and ERA5 for (a-b) inflow and outflow temperature and (c-d) inflow and outflow pressure, as a function of τ_{600}. Positive values (red) indicate higher frequency in ICON, while negative values (blue) indicate higher frequency in ERA5.Strong anomalies at the shortest ascent times reflect convectively enhanced vertical transport that is explicitly resolved in ICON but absent in ERA5. ERA5 exhibits a higher relative frequency of WCBs with ascent times between 10-30 h, whereas ICON dominates for longer ascent times, particularly in the pressure distributions. These patterns are consistent with the composite differences discussed in the Chapter 6 and highlight differences in how each dataset represents the distribution of WCB ascent characteristics.

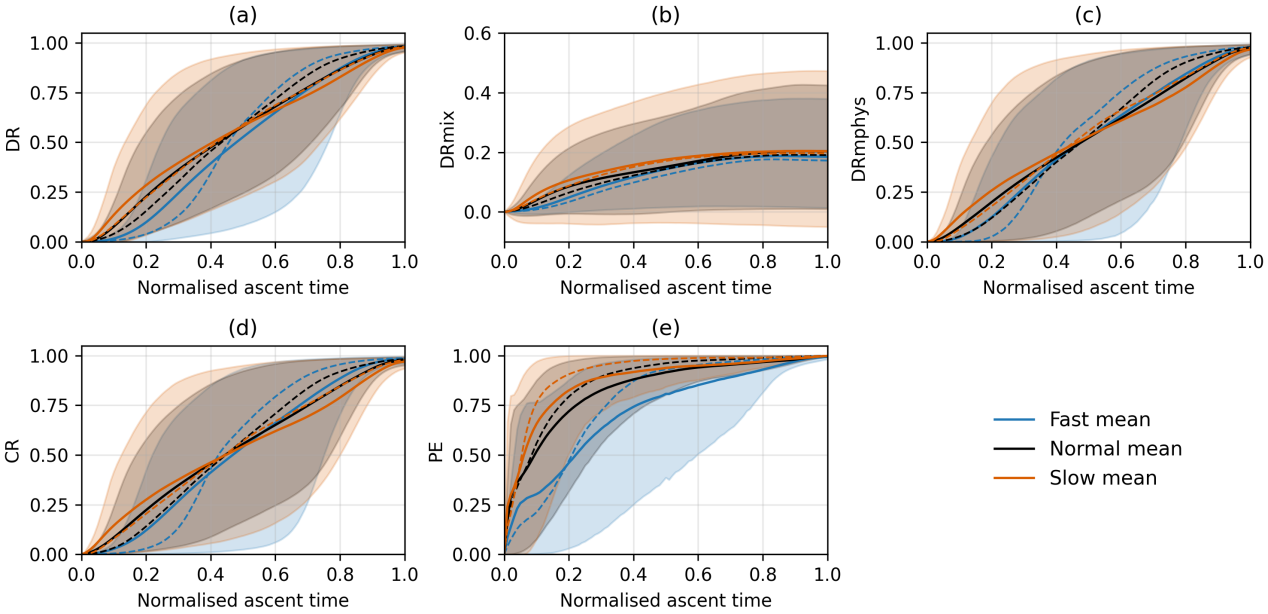

Figure A.42: Evolution of (a) DR, (b) DR_{mix}, (c) DR_{mphys}, (d) CR, and (e) PE as a function of normalized ascent time. Solid (dashed) lines show mean (median) values. Shading denotes the 10th–90th percentile range.

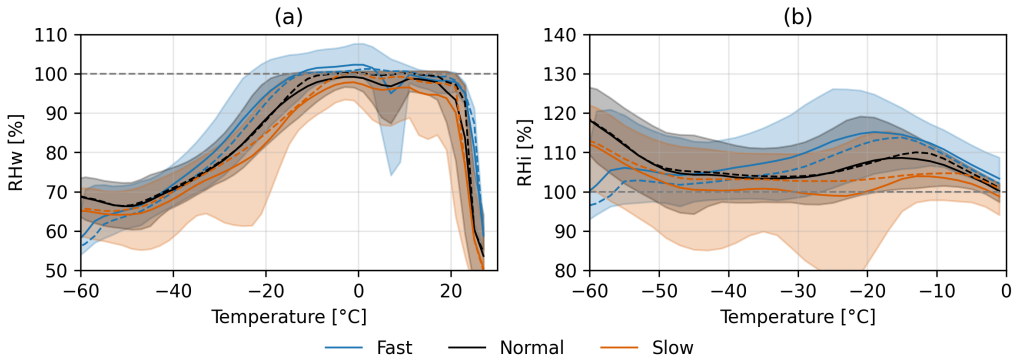

Figure A.43: Distribution of RHw (a) and RHi (b) along the WCB ascent (τ_{WCB}) as a function of temperature. Solid (dashed) lines show mean (median) values. Shading denotes the 10th–90th percentile range.

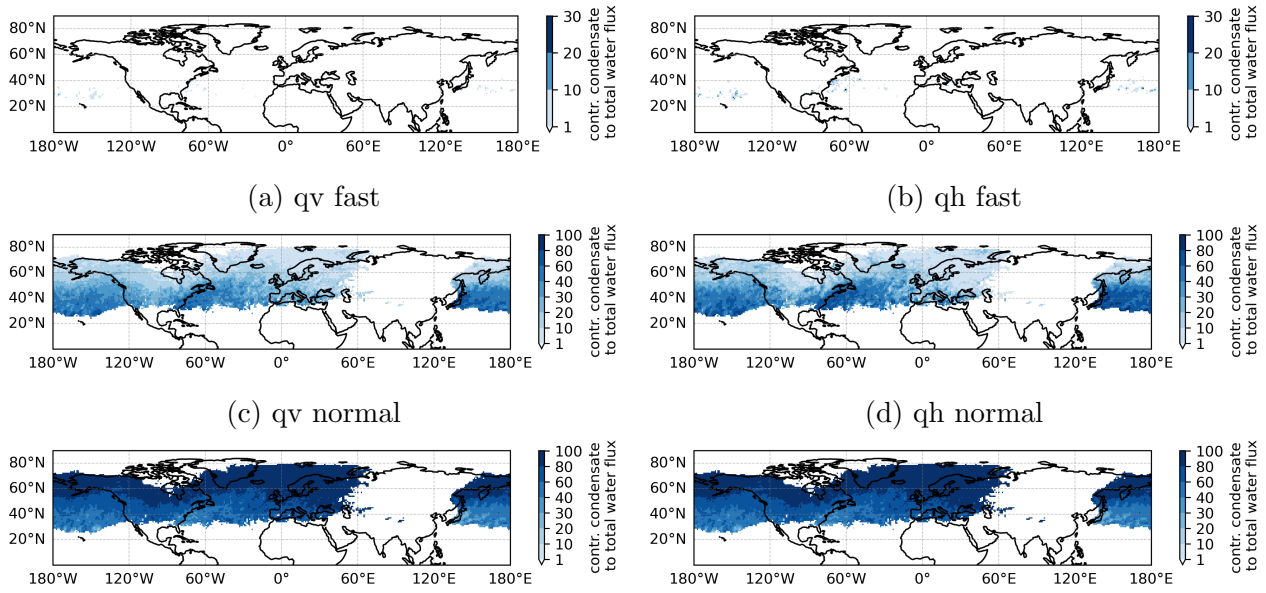

(a) qv fast

(b) qh fast

(c) qv normal

(d) qh normal

(e) qv slow

(f) qh slow

Figure A.44: Relative contribution of WCB trajectories to total fluxes into the UTLS during DJF 2010-2019 (same as in Fig 3.18) but separated by ascent time into fast, normal, and slow branches. The UTLS layer is defined in Chapter 3.2.2. Panels (a, c, e) show the percentage contribution of water vapor (q_v) flux relative to the total q_v flux, while panels (b, d, f) show the corresponding percentage contribution of condensate (q_h) flux relative to the total q_h flux.

B Bibliography

Farhang Ahmadi-Givi, GC Graig, and RS Plant. The dynamics of a midlatitude cyclone with very strong latent-heat release. *Quarterly Journal of the Royal Meteorological Society*, 130 (596):295–323, 2004.

Roger G Barry and Richard J Chorley. *Atmosphere, weather and climate*. Routledge, 2009.

Idar Barstad, Wojciech W Grabowski, and Piotr K Smolarkiewicz. Characteristics of large-scale orographic precipitation: Evaluation of linear model in idealized problems. *Journal of Hydrology*, 340(1-2):78–90, 2007.

P Bechtold, E Bazile, F Guichard, P Mascart, and E Richard. A mass-flux convection scheme for regional and global models. *Quarterly Journal of the Royal Meteorological Society*, 127 (573):869–886, 2001.

Peter Bechtold, Martin Köhler, Thomas Jung, Francisco Doblas-Reyes, Martin Leutbecher, Mark J Rodwell, Frederic Vitart, and Gianpaolo Balsamo. Advances in simulating atmospheric variability with the ecmwf model: From synoptic to decadal time-scales. *Quarterly Journal of the Royal Meteorological Society: A journal of the atmospheric sciences, applied meteorology and physical oceanography*, 134(634):1337–1351, 2008.

Gufran Beig, Jurgen Scheer, Martin G Mlynczak, and Philippe Keckhut. Overview of the temperature response in the mesosphere and lower thermosphere to solar activity. *Reviews of Geophysics*, 46(3), 2008.

Hanin Binder. *Warm conveyor belts: cloud structure and role for cyclone dynamics and extreme events*. PhD thesis, ETH Zurich, 2017.

Hanin Binder, Maxi Boettcher, Hanna Joos, and Heini Wernli. The role of warm conveyor belts for the intensification of extratropical cyclones in northern hemisphere winter. *Journal of the Atmospheric Sciences*, 73(10):3997–4020, 2016.

Hanin Binder, Hanna Joos, Michael Sprenger, and Heini Wernli. Warm conveyor belts in present-day and future climate simulations–part 2: Role of potential vorticity production for cyclone intensification. *Weather and Climate Dynamics*, 4(1):19–37, 2023. doi: 10.5194/wcd-4-19-2023.

Maxi Boettcher, Andreas Schäfler, Michael Sprenger, Harald Sodemann, Stefan Kaufmann, Christiane Voigt, Hans Schlager, Donato Summa, Paolo Di Girolamo, Daniele Nerini, et al. Lagrangian matches between observations from aircraft, lidar and radar in an orographic warm conveyor belt. *Atmospheric Chemistry and Physics Discussions*, 2020:1–32, 2020.

Michael Boy, Erik S Thomson, Juan-C Acosta Navarro, Olafur Arnalds, Ekaterina Batchvarova, Jaana Bäck, Frank Berninger, Merete Bilde, Zoé Brasseur, Pavla Dagsson-Waldhauserova, et al. Interactions between the atmosphere, cryosphere, and ecosystems at northern high latitudes. *Atmospheric Chemistry and Physics*, 19(3):2015–2061, 2019.

Melissa Leah Breeden, Andrew Hoell, John Robert Albers, and Kimberly Slinski. The monthly evolution of precipitation and warm conveyor belts during the central southwest asia wet season. *Weather and Climate Dynamics*, 4(4):963–980, 2023.

KA Browning and NM Roberts. Structure of a frontal cyclone. *Quarterly Journal of the Royal Meteorological Society*, 120(520):1535–1557, 1994. doi: 10.1002/qj.49712052006.

KA Browning and NM Roberts. Variation of frontal and precipitation structure along a cold front. *Quarterly journal of the royal meteorological society*, 122(536):1845–1872, 1996.

Keith A Browning. Organization of clouds and precipitation in extratropical cyclones. In *Extratropical cyclones: the Erik Palmén memorial volume*, pages 129–153. Springer, 1990.

Simone Brunamonti, Linda Füzér, Teresa Jorge, Yann Poltera, Peter Oelsner, Susanne Meier, Ruud Dirksen, Manish Naja, Suvarna Fadnavis, Jagadishwor Karmacharya, et al. Water vapor in the asian summer monsoon anticyclone: Comparison of balloon-borne measurements and ECMWF data. *Journal of Geophysical Research: Atmospheres*, 124(13):7053–7068, 2019. doi: 10.1029/2018JD030000.

Neal Butchart. The brewer-dobson circulation. *Reviews of geophysics*, 52(2):157–184, 2014.

Toby N Carlson. Airflow through midlatitude cyclones and the comma cloud pattern. *Monthly Weather Review*, 108(10):1498–1509, 1980.

Jennifer L Catto, Erica Madonna, Hanna Joos, Irina Rudeva, and Ian Simmonds. Global relationship between fronts and warm conveyor belts and the impact on extreme precipitation. *Journal of Climate*, 28(21):8411–8429, 2015.

JL Catto. Extratropical cyclone classification and its use in climate studies. *Reviews of Geophysics*, 54(2):486–520, 2016. doi: 10.1002/2016RG000519.

CB Chang, DJ Perkey, and CW Kreitzberg. A numerical case study of the effects of latent heating on a developing wave cyclone. *Journal of Atmospheric Sciences*, 39(7):1555–1570, 1982.

Edward Charlesworth, Felix Plöger, Thomas Birner, Rasul Baikhadzhaev, Marta Abalos, Nathan Luke Abraham, Hideharu Akiyoshi, Slimane Bekki, Fraser Dennison, Patrick Jöckel, James Keeble, Doug Kinnison, Olaf Morgenstern, David Plummer, Eugene Rozanov, Sarah Strode, Guang Zeng, Tatiana Egorova, and Martin Riese. Stratospheric water vapor affecting atmospheric circulation. *Nature Communications*, 14(1):3925, 2023. doi: 10.1038/s41467-023-39559-2. URL `https://doi.org/10.1038/s41467-023-39559-2`.

Anubhav Choudhary and Aiko Voigt. Impact of grid spacing, convective parameterization and cloud microphysics in icon simulations of a warm conveyor belt. *Weather and Climate Dynamics*, 3(4):1199–1214, 2022.

HL Clark, RS Harwood, A Billingham, and HC Pumphrey. Cirrus and water vapor in the tropical tropopause layer observed by upper atmosphere research satellite (uars). *Journal of Geophysical Research: Atmospheres*, 108(D24), 2003.

Thierry Corti, Beiping P Luo, Qinjun Fu, Holger Vömel, and Thomas Peter. The impact of cirrus clouds on tropical troposphere-to-stratosphere transport. *Atmospheric Chemistry and Physics*, 6(9):2539–2547, 2006.

HF Dacre, O Martinez-Alvarado, and KI Hodges. Precipitation efficiencies in a climatology of southern ocean extratropical cyclones. *Journal of Geophysical Research: Atmospheres*, 128 (24):e2023JD039239, 2023.

Martin Dameris. Stratosphere/troposphere exchange and structure— tropopause. *Elsevier*, 2015.

Maurice B Danard. On the influence of released latent heat on cyclone development. *Journal of Applied Meteorology and Climatology*, 3(1):27–37, 1964.

AE Dessler, MR Schoeberl, T Wang, SM Davis, and KH Rosenlof. Stratospheric water vapor feedback. *Proceedings of the National Academy of Sciences*, 110(45):18087–18091, 2013.

Oliver GA Driver, Marc EJ Stettler, and Edward Gryspeerdt. The ice supersaturation biases limiting contrail modelling are structured around extratropical depressions. *Atmospheric Chemistry and Physics*, 25(22):16411–16433, 2025.

Sabine Eckhardt, Andreas Stohl, Heini Wernli, Paul James, Caroline Forster, and Nicole Spichtinger. A 15-year climatology of warm conveyor belts. *Journal of climate*, 17(1):218–237, 2004. doi: 10.1175/1520-0442(2004)017⟨0218:AYCOWC⟩2.0.CO;2.

Kerry A Emanuel. *Atmospheric convection*. Oxford university press, 1994.

Encyclopædia Britannica. Cyclogenesis. https://www.britannica.com/science/cyclogenesis. Accessed 2025-10-09. Diagram illustrating stages of frontal cyclone development.

Encyclopædia Britannica. Atmospheric structure: Layers of the atmosphere showing temperature variation with height. https://www.britannica.com/science/atmosphere. Retrieved October 6, 2025.

Marc Federer, Lukas Papritz, Michael Sprenger, and Christian M Grams. Synoptic perspective on the conversion and maintenance of local available potential energy in extratropical cyclones. *Weather and Climate Dynamics*, 6(1):211–230, 2025.

S Fueglistaler, AE Dessler, TJ Dunkerton, I Folkins, Q Fu, and Philip W Mote. Tropical tropopause layer. *Reviews of Geophysics*, 47(1), 2009.

M Gauss, G Myhre, G Pitari, MJ Prather, ISA Isaksen, TK Berntsen, Guy P Brasseur, FJ Dentener, RG Derwent, DA Hauglustaine, et al. Radiative forcing in the 21st century due to ozone changes in the troposphere and the lower stratosphere. *Journal of Geophysical Research: Atmospheres*, 108(D9), 2003. doi: 10.1029/2002JD002624.

Andrew Gettelman, P Hoor, LL Pan, WlJ Randel, Michaela I Hegglin, and T Birner. The extratropical upper troposphere and lower stratosphere. *Reviews of Geophysics*, 49(3), 2011. doi: 10.1029/2011RG000355.

Michael Ghil and Valerio Lucarini. The physics of climate variability and climate change. *Reviews of Modern Physics*, 92(3):035002, 2020.

Andrea E Gordon, Cameron R Homeyer, Jessica B Smith, Rei Ueyama, Jonathan M Dean-Day, Elliot L Atlas, Kate Smith, Jasna V Pittman, David S Sayres, David M Wilmouth, et al. Airborne observations of upper troposphere and lower stratosphere composition change in active convection producing above-anvil cirrus plumes. *Atmospheric Chemistry and Physics*, 24(13):7591–7608, 2024.

Christian M Grams, Heini Wernli, Maxi Böttcher, Jana Čampa, Ulrich Corsmeier, Sarah C Jones, Julia H Keller, Claus-Jürgen Lenz, and Lars Wiegand. The key role of diabatic processes in modifying the upper-tropospheric wave guide: a north atlantic case-study. *Quarterly Journal of the Royal Meteorological Society*, 137(661):2174–2193, 2011.

Christian M Grams, Linus Magnusson, and Erica Madonna. An atmospheric dynamics perspective on the amplification and propagation of forecast error in numerical weather prediction models: A case study. *Quarterly Journal of the Royal Meteorological Society*, 144(717): 2577–2591, 2018.

Kevin M Grise, David WJ Thompson, and Thomas Birner. A global survey of static stability in the stratosphere and upper troposphere. *Journal of Climate*, 23(9):2275–2292, 2010.

Ziyan Guo and Annette Miltenberger. Climatology of warm conveyor belt contributions to utls moisture in era5 between 2010 and 2019. *Journal of Climate*, 38(22):6505–6525, 2025.

Steven C Hardiman, Ian A Boutle, Andrew C Bushell, Neal Butchart, Mike JP Cullen, Paul R Field, Kalli Furtado, James C Manners, Sean F Milton, Cyril Morcrette, et al. Processes controlling tropical tropopause temperature and stratospheric water vapor in climate models. *Journal of Climate*, 28(16):6516–6535, 2015.

TW Harrold. Mechanisms influencing the distribution of precipitation within baroclinic disturbances. *Quarterly Journal of the Royal Meteorological Society*, 99(420):232–251, 1973.

Dennis L Hartmann. *Global physical climatology*, volume 103. Newnes, 2015.

Katharina Heitmann, Michael Sprenger, Hanin Binder, Heini Wernli, and Hanna Joos. Warm conveyor belt characteristics and impacts along the life cycle of extratropical cyclones: case studies and climatological analysis based on era5. *Weather and Climate Dynamics*, 5(2): 537–557, 2024. doi: 10.5194/wcd-5-537-2024.

Hans Hersbach. Global reanalysis: goodbye era-interim, hello era5. *ECMWF newsletter*, 159: 17, 2019.

Hans Hersbach, Bill Bell, Paul Berrisford, Shoji Hirahara, András Horányi, Joaquín Muñoz-Sabater, Julien Nicolas, Carole Peubey, Raluca Radu, Dinand Schepers, et al. The era5 global reanalysis. *Quarterly journal of the royal meteorological society*, 146(730):1999–2049, 2020.

Matthew H Hitchman and Shellie M Rowe. On the formation of tropopause folds and constituent gradient enhancement near westerly jets. *Journal of the Atmospheric Sciences*, 78 (7):2057–2074, 2021.

Martin P Hoerling, Todd K Schaack, and Allen J Lenzen. Global objective tropopause analysis. *Monthly Weather Review*, 119(8):1816–1831, 1991. doi: 10.1175/1520-0493(1991)119⟨1816:GOTA⟩2.0.CO;2.

S. Hofer, K. Gierens, and S. Rohs. How well can persistent contrails be predicted? an update. *Atmospheric Chemistry and Physics*, 24(13):7911–7925, 2024. doi: 10.5194/acp-24-7911-2024. URL `https://acp.copernicus.org/articles/24/7911/2024/`.

Lars Hoffmann and Reinhold Spang. An assessment of tropopause characteristics of the era5 and era-interim meteorological reanalyses. *Atmospheric Chemistry and Physics Discussions*, 2021:1–44, 2021.

Lars Hoffmann, Gebhard Günther, Dan Li, Olaf Stein, Xue Wu, Sabine Griessbach, Yi Heng, Paul Konopka, Rolf Müller, Bärbel Vogel, et al. From era-interim to era5: the considerable impact of ecmwf's next-generation reanalysis on lagrangian transport simulations. *Atmospheric Chemistry and Physics*, 19(5):3097–3124, 2019.

James R Holton and Gregory J Hakim. *An introduction to dynamic meteorology*, volume 88. Academic press, 2013.

James R Holton, Peter H Haynes, Michael E McIntyre, Anne R Douglass, Richard B Rood, and Leonhard Pfister. Stratosphere-troposphere exchange. *Reviews of geophysics*, 33(4):403–439, 1995. doi: 10.1029/95RG02097.

Cameron R Homeyer and Kenneth P Bowman. A 22-year evaluation of convection reaching the stratosphere over the united states. *Journal of Geophysical Research: Atmospheres*, 126 (13):e2021JD034808, 2021.

Brian John Hoskins and Kevin Ivan Hodges. A new perspective on southern hemisphere storm tracks. *Journal of climate*, 18(20):4108–4129, 2005.

Robert A Houze Jr, Darren C Wilton, and Bradley F Smull. Monsoon convection in the himalayan region as seen by the trmm precipitation radar. *Quarterly Journal of the Royal Meteorological Society: A journal of the atmospheric sciences, applied meteorology and physical oceanography*, 133(627):1389–1411, 2007.

Shineng Hu and Geoffrey K Vallis. Meridional structure and future changes of tropopause height and temperature. *Quarterly Journal of the Royal Meteorological Society*, 145(723): 2698–2717, 2019.

Yoichi Inai, Ryo Fujita, Toshinobu Machida, Hidekazu Matsueda, Yousuke Sawa, Kazuhiro Tsuboi, Keiichi Katsumata, Shinji Morimoto, Shuji Aoki, and Takakiyo Nakazawa. Seasonal characteristics of trace gas transport into the extratropical upper troposphere and lower stratosphere. *Atmospheric Chemistry and Physics*, 19(10):7073–7103, 2019.

Eric Jensen and Leonhard Pfister. Transport and freeze-drying in the tropical tropopause layer. *Journal of Geophysical Research: Atmospheres*, 109(D2), 2004.

Eric J Jensen, Owen B Toon, Leonard Pfister, and Henry B Selkirk. Dehydration of the upper troposphere and lower stratosphere by subvisible cirrus clouds near the tropical tropopause. *Geophysical Research Letters*, 23(8):825–828, 1996.

Eric J Jensen, Glenn Diskin, R Paul Lawson, Sara Lance, T Paul Bui, Dennis Hlavka, Matthew McGill, Leonhard Pfister, Owen B Toon, and Rushan Gao. Ice nucleation and dehydration

in the tropical tropopause layer. *Proceedings of the National Academy of Sciences*, 110(6): 2041–2046, 2013.

H Joos and Heini Wernli. Influence of microphysical processes on the potential vorticity development in a warm conveyor belt: a case-study with the limited-area model COSMO. *Quarterly Journal of the Royal Meteorological Society*, 138(663):407–418, 2012. doi: 10.1002/qj.934.

Hanna Joos. Warm conveyor belts and their role for cloud radiative forcing in the extratropical storm tracks. *Journal of Climate*, 32(16):5325–5343, 2019. doi: 10.1175/JCLI-D-18-0802.1.

Hanna Joos, Michael Sprenger, Hanin Binder, Urs Beyerle, and Heini Wernli. Warm conveyor belts in present-day and future climate simulations–part 1: Climatology and impacts. *Weather and Climate Dynamics*, 4(1):133–155, 2023a. doi: 10.5194/wcd-4-133-2023.

Hanna Joos, Michael Sprenger, Hanin Binder, Urs Beyerle, and Heini Wernli. Warm conveyor belts in present-day and future climate simulations–part 1: Climatology and impacts. *Weather and Climate Dynamics*, 4(1):133–155, 2023b.

AS Kentarchos and GJ Roelofs. A model study of stratospheric ozone in the troposphere and its contribution to tropospheric oh formation. *Journal of Geophysical Research: Atmospheres*, 108(D12), 2003.

Patrick Konjari, Christian Rolf, Martina Krämer, Armin Afchine, Nicole Spelten, Irene Bartolome Garcia, Annette Miltenberger, Nicolas Emig, Philipp Joppe, Johannes Schneider, et al. Stratospheric hydration and ice microphysics of a convective overshoot observed during the tpex campaign over sweden. *Atmospheric Chemistry and Physics*, 25(23):18031–18050, 2025.

Martina Krämer, Christian Rolf, Nicole Spelten, Armin Afchine, David Fahey, Eric Jensen, Sergey Khaykin, Thomas Kuhn, Paul Lawson, Alexey Lykov, et al. A microphysics guide to cirrus–part ii: climatologies of clouds and humidity from observations. *Atmospheric Chemistry and Physics Discussions*, 2020:1–63, 2020.

Stefanie Kremser, Larry W Thomason, Marc von Hobe, Markus Hermann, Terry Deshler, Claudia Timmreck, Matthew Toohey, Andrea Stenke, Joshua P Schwarz, Ralf Weigel, et al. Stratospheric aerosol—observations, processes, and impact on climate. *Reviews of Geophysics*, 54(2):278–335, 2016.

K. Krüger, A. Schäfler, M. Wirth, M. Weissmann, and G. C. Craig. Vertical structure of the lower-stratospheric moist bias in the ERA5 reanalysis and its connection to mixing processes. *Atmospheric Chemistry and Physics*, 22(23):15559–15577, 2022. doi: 10.5194/acp-22-15559-2022. URL `https://acp.copernicus.org/articles/22/15559/2022/`.

A Kunz, P Konopka, R Müller, and LL Pan. Dynamical tropopause based on isentropic potential vorticity gradients. *Journal of Geophysical Research: Atmospheres*, 116(D1), 2011.

Anne Kunz, Nicole Spelten, Paul Konopka, Rolf Müller, Richard M Forbes, and Heini Wernli. Comparison of fast in situ stratospheric hygrometer (FISH) measurements of water vapor in the upper troposphere and lower stratosphere (UTLS) with ECMWF (re) analysis data. *Atmospheric chemistry and physics*, 14(19):10803–10822, 2014. doi: 10.5194/acp-14-10803-2014.

Hsiao-Lan Kuo. On formation and intensification of tropical cyclones through latent heat release by cumulus convection. *Journal of Atmospheric Sciences*, 22(1):40–63, 1965.

J Lelieveld, PJ Crutzen, and Ch Brühl. Climate effects of atmospheric methane. *Chemosphere*, 26(1-4):739–768, 1993.

F Lott and MJ Miller. A new subgrid-scale orographic drag parametrization: Its formulation and testing, qj roy. meteor. soc., 123, 101–127, 1997.

F-J Lübken and U Von Zahn. Thermal structure of the mesopause region at polar latitudes. *Journal of Geophysical Research: Atmospheres*, 96(D11):20841–20857, 1991.

Franz-Josef Lübken. Physics in the mesosphere/lower thermosphere: A personal perspective. *Frontiers in Astronomy and Space Sciences*, 9:1000766, 2022.

Patrick Ludwig, Joaquim G Pinto, Simona A Hoepp, Andreas H Fink, and Suzanne L Gray. Secondary cyclogenesis along an occluded front leading to damaging wind gusts: Windstorm kyrill, january 2007. *Monthly Weather Review*, 143(4):1417–1437, 2015.

Tim Lüttmer, Annette Miltenberger, and Peter Spichtinger. On the impact of ice formation processes and sedimentation on cirrus origin classification in warm conveyor belt outflow. *Atmospheric Chemistry and Physics*, 25(17):10245–10265, 2025.

Erica Madonna, Heini Wernli, Hanna Joos, and Olivia Martius. Warm conveyor belts in the ERA-Interim dataset (1979–2010). part i: Climatology and potential vorticity evolution. *Journal of climate*, 27(1):3–26, 2014. doi: 10.1175/JCLI-D-12-00720.1.

Oscar Martínez-Alvarado, Laura H Baker, Suzanne L Gray, John Methven, and Robert S Plant. Distinguishing the cold conveyor belt and sting jet airstreams in an intense extratropical cyclone. *Monthly Weather Review*, 142(8):2571–2595, 2014.

Oscar Martínez-Alvarado, Suzanne L Gray, and John Methven. Diabatic processes and the evolution of two contrasting summer extratropical cyclones. *Monthly Weather Review*, 144 (9):3251–3276, 2016.

Marie Mazoyer, Didier Ricard, Gwendal Rivière, Julien Delanoë, Philippe Arbogast, Benoit Vié, Christine Lac, Quitterie Cazenave, and Jacques Pelon. Microphysics impacts on the warm conveyor belt and ridge building of the nawdex iop6 cyclone. *Monthly Weather Review*, 149 (12):3961–3980, 2021.

Marie Mazoyer, Didier Ricard, Gwendal Rivière, Julien Delanoë, Sébastien Riette, Clotilde Augros, Mary Borderies, and Benoit Vie. Impact of mixed-phase cloud parameterization on warm conveyor belts and upper-tropospheric dynamics. *Monthly Weather Review*, 151(5): 1073–1091, 2023.

Annette K Miltenberger. *Lagrangian perspective on dynamic and microphysical processes in orographically forced flows*. PhD thesis, ETH Zurich, 2014.

Annette K Miltenberger, Stephan Pfahl, and Heini Wernli. An online trajectory module (version 1.0) for the non-hydrostatic numerical weather prediction model cosmo. *Geoscientific Model Development Discussions*, 6(1):1223–1257, 2013.

Annette K Miltenberger, Tim Lüttmer, and Christoph Siewert. Secondary ice formation in idealised deep convection—source of primary ice and impact on glaciation. *Atmosphere*, 11 (5):542, 2020.

Hugh Morrison, Marcus van Lier-Walqui, Ann M Fridlind, Wojciech W Grabowski, Jerry Y Harrington, Corinna Hoose, Alexei Korolev, Matthew R Kumjian, Jason A Milbrandt, Hanna Pawlowska, et al. Confronting the challenge of modeling cloud and precipitation microphysics. *Journal of advances in modeling earth systems*, 12(8):e2019MS001689, 2020. doi: 10.1029/2019MS001689.

Philip W Mote, Karen H Rosenlof, Michael E McIntyre, Ewan S Carr, John C Gille, James R Holton, Jonathan S Kinnersley, Hugh C Pumphrey, James M Russell III, and Joe W Waters. An atmospheric tape recorder: The imprint of tropical tropopause temperatures on stratospheric water vapor. *Journal of Geophysical Research: Atmospheres*, 101(D2):3989–4006, 1996. doi: 10.1029/95JD03422.

Daniel M Murphy and Thomas Koop. Review of the vapour pressures of ice and supercooled water for atmospheric applications. *Quarterly Journal of the Royal Meteorological Society: A journal of the atmospheric sciences, applied meteorology and physical oceanography*, 131 (608):1539–1565, 2005.

National Center for Atmospheric Research (NCAR). Upper troposphere and lower stratosphere (utls): Atmospheric chemistry observations and modeling (acom) laboratory. `https://www.acom.ucar.edu/utls/`. Retrieved October 7, 2025.

Paul J Neiman and MA Shapiro. The life cycle of an extratropical marine cyclone. part i: Frontal-cyclone evolution and thermodynamic air-sea interaction. *Monthly Weather Review*, 121(8):2153–2176, 1993.

Annika Oertel, Maxi Boettcher, Hanna Joos, Michael Sprenger, Heike Konow, Martin Hagen, and Heini Wernli. Convective activity in an extratropical cyclone and its warm conveyor belt–a case-study combining observations and a convection-permitting model simulation. *Quarterly Journal of the Royal Meteorological Society*, 145(721):1406–1426, 2019. doi: 10.1002/qj.3500.

Annika Oertel, Maxi Boettcher, Hanna Joos, Michael Sprenger, and Heini Wernli. Potential vorticity structure of embedded convection in a warm conveyor belt and its relevance for large-scale dynamics. *Weather and Climate Dynamics*, 1(1):127–153, 2020.

Annika Oertel, Michael Sprenger, Hanna Joos, Maxi Boettcher, Heike Konow, Martin Hagen, and Heini Wernli. Observations and simulation of intense convection embedded in a warm conveyor belt–how ambient vertical wind shear determines the dynamical impact. *Weather and Climate Dynamics*, 2(1):89–110, 2021.

Annika Oertel, Annette K Miltenberger, Christian M Grams, and Corinna Hoose. Interaction of microphysics and dynamics in a warm conveyor belt simulated with the icosahedral nonhydrostatic (ICON) model. *Atmospheric Chemistry and Physics*, 23(15):8553–8581, 2023. doi: 10.5194/acp-23-8553-2023.

Annika Oertel, Annette K Miltenberger, Christian M Grams, and Corinna Hoose. Sensitivities of warm conveyor belt ascent, associated precipitation characteristics and large-scale flow pattern: Insights from a perturbed parameter ensemble. *Quarterly Journal of the Royal Meteorological Society*, page e4986, 2025.

Andrew Orr, Peter Bechtold, John Scinocca, Manfred Ern, and Marta Janiskova. Improved middle atmosphere climate and forecasts in the ecmwf model through a nonorographic gravity wave drag parameterization. *Journal of Climate*, 23(22):5905–5926, 2010.

Douglas J Parker, Peter Willetts, Cathryn Birch, Andrew G Turner, John H Marsham, Christopher M Taylor, Seshagirirao Kolusu, and Gill M Martin. The interaction of moist convection and mid-level dry air in the advance of the onset of the indian monsoon. *Quarterly Journal of the Royal Meteorological Society*, 142(699):2256–2272, 2016.

Kenneth E Parsons and Phillip J Smith. An investigation of extratropical cyclone development using a scale-separation technique. *Monthly weather review*, 132(4):956–974, 2004.

Sverre Petterssen. Weather analysis and forecasting. *(No Title)*, 1956.

Stephan Pfahl, Erica Madonna, Maxi Boettcher, Hanna Joos, and Heini Wernli. Warm conveyor belts in the ERA-Interim dataset (1979–2010). part ii: Moisture origin and relevance for precipitation. *Journal of Climate*, 27(1):27–40, 2014. doi: 10.1175/JCLI-D-13-00223.1.

Stephan Pfahl, Paul A O'Gorman, and Martin S Singh. Extratropical cyclones in idealized simulations of changed climates. *Journal of Climate*, 28(23):9373–9392, 2015.

Matthew DK Priestley and Jennifer L Catto. Future changes in the extratropical storm tracks and cyclone intensity, wind speed, and structure. *Weather and Climate Dynamics Discussions*, 2021:1–40, 2021.

F. Prill, D. Reinert, D. Rieger, and G. Zängl. Icon tutorial 2023, 2023.

Julian F Quinting, Christian M Grams, Edmund Kar-Man Chang, Stephan Pfahl, and Heini Wernli. Warm conveyor belt activity over the pacific: modulation by the madden–julian oscillation and impact on tropical–extratropical teleconnections. *Weather and Climate Dynamics*, 5(1):65–85, 2024.

Veerabhadran Ramanathan and Anand Inamdar. The radiative forcing due to clouds and water vapor. *Frontiers of climate modeling*, pages 119–151, 2006.

William Randel and Mijeong Park. Diagnosing observed stratospheric water vapor relationships to the cold point tropical tropopause. *Journal of Geophysical Research: Atmospheres*, 124 (13):7018–7033, 2019.

Stephan Rasp, Tobias Selz, and George C Craig. Convective and slantwise trajectory ascent in convection-permitting simulations of midlatitude cyclones. *Monthly Weather Review*, 144 (10):3961–3976, 2016. doi: 10.1175/MWR-D-16-0112.1.

Shira Raveh-Rubin. Dry intrusions: Lagrangian climatology and dynamical impact on the planetary boundary layer. *Journal of Climate*, 30(17):6661–6682, 2017. doi: 10.1175/JCLI-D-16-0782.1.

Philipp Reutter and Peter Spichtinger. The frosty frontier: redefining the mid-latitude tropopause using the relative humidity over ice. *Atmospheric Chemistry and Physics*, 25 (22):16303–16314, 2025.

Philipp Reutter, Patrick Neis, Susanne Rohs, and Bastien Sauvage. Ice supersaturated regions: properties and validation of era-interim reanalysis with iagos in situ water vapour measurements. *Atmospheric chemistry and physics*, 20(2):787–804, 2020.

Herbert Riehl and Sidney Teweles Jr. A further study on the relation between the jet stream and cyclone formation. *Tellus*, 5(1):66–79, 1953.

Martin Riese, Felix Ploeger, Alexandru Rap, Bärbel Vogel, Paul Konopka, Martin Dameris, and Piers Forster. Impact of uncertainties in atmospheric mixing on simulated UTLS composition and related radiative effects. *Journal of Geophysical Research: Atmospheres*, 117(D16), 2012. doi: 10.1029/2012JD017751.

Christian Rolf, Bärbel Vogel, Peter Hoor, Armin Afchine, Gebhard Günther, Martina Krämer, Rolf Müller, Stefan Müller, Nicole Spelten, and Martin Riese. Water vapor increase in the lower stratosphere of the northern hemisphere due to the asian monsoon anticyclone observed during the TACTS/ESMVal campaigns. *Atmospheric Chemistry and Physics*, 18(4):2973–2983, 2018. doi: 10.5194/acp-18-2973-2018.

Karen H Rosenlof. How water enters the stratosphere. *Science*, 302(5651):1691–1692, 2003.

CE Rössler, T Paccagnella, and St Tibaldi. A three-dimensional atmospheric trajectory model: Application to a case study of alpine lee cyclogenesis. *Meteorology and Atmospheric Physics*, 50(4):211–229, 1992.

F Sherwood Rowland. Stratospheric ozone depletion. *Philosophical Transactions of the Royal Society B: Biological Sciences*, 361(1469):769–790, 2006.

Takeaki Sampe and Shang-Ping Xie. Large-scale dynamics of the meiyu-baiu rainband: Environmental forcing by the westerly jet. *Journal of Climate*, 23(1):113–134, 2010.

Sebastian Schemm, Michael Sprenger, and Heini Wernli. When during their life cycle are extratropical cyclones attended by fronts? *Bulletin of the American Meteorological Society*, 99(1):149–165, 2018.

Friedrich A Schott and Julian P McCreary Jr. The monsoon circulation of the indian ocean. *Progress in Oceanography*, 51(1):1–123, 2001.

David M Schultz, Lance F Bosart, Brian A Colle, Huw C Davies, Christopher Dearden, Daniel Keyser, Olivia Martius, Paul J Roebber, W James Steenburgh, Hans Volkert, et al. Extratropical cyclones: A century of research on meteorology's centerpiece. *Meteorological monographs*, 59:16–1, 2019.

Cornelis Schwenk and Annette Miltenberger. The role of ascent timescales for warm conveyor belt (WCB) moisture transport into the upper troposphere and lower stratosphere (UTLS). *Atmos. Chem. Phys.*, 24:14073–14099, 2024. doi: 10.5194/acp-24-14073-2024.

Cornelis Schwenk, Annette Miltenberger, and Annika Oertel. Microphysical parameter choices modulate ice content and relative humidity in the outflow of a warm conveyor belt. *Atmospheric Chemistry and Physics*, 25(18):11333–11361, 2025.

Dian J Seidel, Rebecca J Ross, James K Angell, and George C Reid. Climatological characteristics of the tropical tropopause as revealed by radiosondes. *Journal of Geophysical Research: Atmospheres*, 106(D8):7857–7878, 2001.

Axel Seifert and Klaus Dieter Beheng. A two-moment cloud microphysics parameterization for mixed-phase clouds. part 1: Model description. *Meteorology and atmospheric physics*, 92(1): 45–66, 2006.

Christian Seiler. A climatological assessment of intense extratropical cyclones from the potential vorticity perspective. *Journal of Climate*, 32(8):2369–2380, 2019.

Hyodae Seo, Larry W O'Neill, Mark A Bourassa, Arnaud Czaja, Kyla Drushka, James B Edson, Baylor Fox-Kemper, Ivy Frenger, Sarah T Gille, Benjamin P Kirtman, et al. Ocean mesoscale and frontal-scale ocean–atmosphere interactions and influence on large-scale climate: A review. *Journal of climate*, 36(7):1981–2013, 2023.

Ming Shangguan, Wuke Wang, and Shuanggen Jin. Variability of temperature and ozone in the upper troposphere and lower stratosphere from multi-satellite observations and reanalysis data. *Atmospheric Chemistry and Physics*, 19(10):6659–6679, 2019.

Napier Shaw and Rudolf Gustav Karl Lempfert. *The Life History of Surface Air Currents: A Study of the Surface Trajectories of Moving Air...* Darling & Son, 1906.

W Napier Shaw. The meteorological aspects of the storm of february 26–27, 1903. *Quarterly Journal of the Royal Meteorological Society*, 29(128):233–262, 1903.

Michaela Sickmöller, Richard Blender, and Klaus Fraedrich. Observed winter cyclone tracks in the northern hemisphere in re-analysed ECMWF data. *Quarterly Journal of the Royal Meteorological Society*, 126(563):591–620, 2000. doi: 10.1002/qj.49712656311.

Adrian Simmons, Cornel Soci, Julien Nicolas, Bill Bell, P. Berrisford, Rossana Dragani, Johannes Flemming, Leopold Haimberger, Sean Healy, Hans Hersbach, Andras Horányi, Antje Inness, J. Munoz-Sabater, Raluca Radu, and Dinand Schepers. Global stratospheric temperature bias and other stratospheric aspects of era5 and era5.1. *ECMWF Technical Memoranda*, 859, 2020. doi: 10.21957/rcxqfmg0.

Victoria A Sinclair, Mika Rantanen, Päivi Haapanala, Jouni Räisänen, and Heikki Järvinen. The characteristics and structure of extra-tropical cyclones in a warmer climate. 2020. doi: 10.5194/wcd-1-1-2020.

Bojan Škerlak, Michael Sprenger, and Heini Wernli. A global climatology of stratosphere–troposphere exchange using the ERA-Interim data set from 1979 to 2011. *Atmospheric Chemistry and Physics*, 14(2):913–937, 2014. doi: 10.5194/acp-14-913-2014.

Bojan Škerlak, Michael Sprenger, Stephan Pfahl, Evangelos Tyrlis, and Heini Wernli. Tropopause folds in era-interim: Global climatology and relation to extreme weather events. *Journal of Geophysical Research: Atmospheres*, 120(10):4860–4877, 2015.

Susan Solomon. Stratospheric ozone depletion: A review of concepts and history. *Reviews of geophysics*, 37(3):275–316, 1999.

Susan Solomon, Karen H Rosenlof, Robert W Portmann, John S Daniel, Sean M Davis, Todd J Sanford, and Gian-Kasper Plattner. Contributions of stratospheric water vapor to decadal changes in the rate of global warming. *science*, 327(5970):1219–1223, 2010. doi: 0.1126/science.118248.

Peter Spichtinger, Klaus Gierens, and Heini Wernli. A case study on the formation and evolution of ice supersaturation in the vicinity of a warm conveyor belt's outflow region. *Atmospheric Chemistry and Physics*, 5(4):973–987, 2005. doi: 10.5194/acp-5-973-2005.

Elisa Spreitzer, Roman Attinger, Maxi Boettcher, Richard Forbes, Heini Wernli, and Hanna Joos. Modification of potential vorticity near the tropopause by nonconservative processes in the ecmwf model. *Journal of the atmospheric sciences*, 76(6):1709–1726, 2019.

Michael Sprenger and Heini Wernli. A northern hemispheric climatology of cross-tropopause exchange for the ERA15 time period (1979–1993). *Journal of Geophysical Research: Atmospheres*, 108(D12), 2003. doi: 10.1029/2002JD002636.

Michael Sprenger and Heini Wernli. The LAGRANTO lagrangian analysis tool – version 2.0. *Geoscientific Model Development*, 8(8):2569–2586, 2015. doi: 10.5194/gmd-8-2569-2015.

Michael Sprenger, Mischa Croci Maspoli, and Heini Wernli. Tropopause folds and cross-tropopause exchange: A global investigation based upon ecmwf analyses for the time period march 2000 to february 2001. *Journal of Geophysical Research: Atmospheres*, 108(D12), 2003.

Michael Sprenger, Heini Wernli, and Michel Bourqui. Stratosphere–troposphere exchange and its relation to potential vorticity streamers and cutoffs near the extratropical tropopause. *Journal of the atmospheric sciences*, 64(5):1587–1602, 2007.

Robert J States and Chester S Gardner. Thermal structure of the mesopause region (80–105 km) at 40° n latitude. part i: Seasonal variations. *Journal of the Atmospheric Sciences*, 57 (1):66–77, 2000.

Graeme L Stephens. Cloud feedbacks in the climate system: A critical review. *Journal of climate*, 18(2):237–273, 2005.

Andreas Stohl. A 1-year lagrangian "climatology" of airstreams in the northern hemisphere troposphere and lowermost stratosphere. *Journal of Geophysical Research: Atmospheres*, 106 (D7):7263–7279, 2001. doi: 10.1029/2000JD900570.

Andreas Stohl, P Bonasoni, P Cristofanelli, W Collins, Johann Feichter, Andreas Frank, C Forster, Evangelos Gerasopoulos, H Gäggeler, P James, et al. Stratosphere-troposphere exchange: A review, and what we have learned from staccato. *Journal of Geophysical Research: Atmospheres*, 108(D12), 2003.

MICHAEL Tiedtke. A comprehensive mass flux scheme for cumulus parameterization in large-scale models. *Monthly weather review*, 117(8):1779–1800, 1989.

Emily N Tinney and Cameron R Homeyer. A 13-year trajectory-based analysis of convection-driven changes in upper troposphere lower stratosphere composition over the united states. *Journal of Geophysical Research: Atmospheres*, 126(3):e2020JD033657, 2021.

Emily N Tinney and Cameron R Homeyer. Climatology, sources, and transport characteristics of observed water vapor extrema in the lower stratosphere. *Atmospheric Chemistry and Physics*, 23(22):14375–14392, 2023. doi: 10.5194/acp-23-14375-2023.

Adrian M Tompkins, Klaus Gierens, and Gaby Rädel. Ice supersaturation in the ecmwf integrated forecast system. *Quarterly Journal of the Royal Meteorological Society: A journal of the atmospheric sciences, applied meteorology and physical oceanography*, 133(622):53–63, 2007.

Kevin E Trenberth, John T Fasullo, and Jeffrey Kiehl. Earth's global energy budget. *Bulletin of the american meteorological society*, 90(3):311–324, 2009.

Katharina Turhal, Felix Plöger, Jan Clemens, Thomas Birner, Franziska Weyland, Paul Konopka, and Peter Hoor. Variability and trends in the potential vorticity (pv)-gradient dynamical tropopause. *Atmospheric Chemistry and Physics*, 24(23):13653–13679, 2024.

UCAR Center for Science Education. The troposphere. `https://scied.ucar.edu/learning-zone/atmosphere/troposphere`, 2023. Accessed: 6 October 2025.

Robert A Vincent. The dynamics of the mesosphere and lower thermosphere: A brief review. *Progress in Earth and Planetary Science*, 2(1):4, 2015.

John M Wallace and Peter V Hobbs. *Atmospheric science: an introductory survey*, volume 92. Elsevier, 2006.

Tao Wang, Dong L Wu, Jie Gong, and Victoria Tsai. Tropopause laminar cirrus and its role in the lower stratosphere total water budget. *Journal of Geophysical Research: Atmospheres*, 124(13):7034–7052, 2019.

Marta Wenta, Christian M Grams, Lukas Papritz, and Marc Federer. Linking gulf stream air–sea interactions to the exceptional blocking episode in february 2019: a lagrangian perspective. *Weather and Climate Dynamics*, 5(1):181–209, 2024.

Heini Wernli. A lagrangian-based analysis of extratropical cyclones. ii: A detailed case-study. *Quarterly Journal of the Royal Meteorological Society*, 123(542):1677–1706, 1997. doi: 10.1002/qj.49712354211.

Heini Wernli and Huw C Davies. A lagrangian-based analysis of extratropical cyclones. i: The method and some applications. *Quarterly Journal of the Royal Meteorological Society*, 123 (538):467–489, 1997.

Heini Wernli and Suzanne L Gray. The importance of diabatic processes for the dynamics of synoptic-scale extratropical weather systems—a review. *EGUsphere*, 2023:1–151, 2023.

Heini Wernli and Cornelia Schwierz. Surface cyclones in the ERA-40 dataset (1958–2001). part i: Novel identification method and global climatology. *Journal of the Atmospheric Sciences*, 63(10):2486–2507, 2006. doi: 10.1175/JAS3766.1.

Heini Wernli and Michael Sprenger. Identification and era-15 climatology of potential vorticity streamers and cutoffs near the extratropical tropopause. *Journal of the atmospheric sciences*, 64(5):1569–1586, 2007.

Heini Wernli, Maxi Boettcher, Hanna Joos, Annette K Miltenberger, and Peter Spichtinger. A trajectory-based classification of ERA-Interim ice clouds in the region of the north atlantic storm track. *Geophysical Research Letters*, 43(12):6657–6664, 2016. doi: 10.1002/2016GL068922.

Meryl Wimmer, Gwendal Rivière, Philippe Arbogast, Jean-Marcel Piriou, Julien Delanoë, Carole Labadie, Quitterie Cazenave, and Jacques Pelon. Diabatic processes modulating the vertical structure of the jet stream above the cold front of an extratropical cyclone: sensitivity to deep convection schemes. *Weather and Climate Dynamics*, 3(3):863–882, 2022.

World Meteorological Organization. Definition of the tropopause. *WMO Bull.*, 6:136, 1957.

Xiangde Xu, Chungu Lu, Xiaohui Shi, and Yihui Ding. Large-scale topography of china: A factor for the seasonal progression of the meiyu rainband? *Journal of Geophysical Research: Atmospheres*, 115(D2), 2010.

A Zahn, E Christner, PFJ van Velthoven, A Rauthe-Schöch, and CAM Brenninkmeijer. Processes controlling water vapor in the upper troposphere/lowermost stratosphere: An analysis of 8 years of monthly measurements by the IAGOS-CARIBIC observatory. *Journal of Geophysical Research: Atmospheres*, 119(19):11–505, 2014. doi: 10.1002/2014JD021687.

Gunther Zängl. Icon: The icosahedral nonhydrostatic modelling framework of dwd and mpi-m. In *Proc. ECMWF Seminar on Numerical Methods for Atmosphere and Ocean Modelling*, 2013.

Günther Zängl, Daniel Reinert, and Florian Prill. Grid refinement in icon v2. 6.4. *Geoscientific Model Development Discussions*, 2022:1–32, 2022.

Acknowledgments